

# **Schichtsilicate als effiziente Bausteine für funktionelle Nanokomposite**

## **Dissertation**

zur Erlangung des akademischen Grades eines

**Doktor der Naturwissenschaften (Dr. rer. nat.)**

im Fach Chemie

an der Fakultät Biologie, Chemie und Geowissenschaften

der Universität Bayreuth

vorgelegt von

**Daniel Alexander Kunz**

geboren in Weiden in der Oberpfalz

Bayreuth, 2013

Die vorliegende Arbeit wurde in der Zeit von April 2008 bis Januar 2013 in Bayreuth am Lehrstuhl für Anorganische Chemie I unter Betreuung von Herrn Prof. Dr. Josef Breu angefertigt.

Vollständiger Abdruck der von der Fakultät für Biologie, Chemie und Geowissenschaften der Universität Bayreuth genehmigten Dissertation zur Erlangung des akademischen Grades eines Doktors der Naturwissenschaften (Dr. rer. nat.).

Dissertation eingereicht am: 06.02.2013

Zulassung durch die Promotionskommission: 13.02.2013

Wissenschaftliches Kolloquium: 08.05.2013

Amtierender Dekan: Prof. Dr. Beate Lohnert

Prüfungsausschuss:

Prof. Dr. J. Breu (Erstgutachter)

Prof. Dr. G. Papastavrou (Zweitgutachter)

Prof. Dr. A. Fery (Vorsitz)

Prof. Dr. V. Altstädt

NIHIL TAM DIFFICILE EST,

QUIN QUAERENDO INVESTIGARI POSSIT.

*Nichts ist derart schwer, als dass es nicht erforscht werden könnte.*

(Terenz, Heautontimorumenos)





Meiner Familie.

Inhaltsverzeichnis

1	Summary .....	1
2	Zusammenfassung .....	3
3	Einleitung .....	5
3.1	Schichtsilicate im Kontext der Energieproblematik.....	5
3.2	Schichtsilicate als effiziente Bausteine für funktionelle Nanokomposite .....	6
3.2.1	Allgemeines.....	6
3.2.2	Synthetische Schichtsilicate .....	8
3.2.3	Schichtsilicate als Füllstoffe .....	10
3.2.4	Mechanische Eigenschaften von Nanoplättchen .....	11
3.3	Mesotechnologische Anwendungen – Schichtsilicat-Nanokomposite.....	18
3.3.1	Gasbarriere.....	18
3.3.2	Quasi-Epitaxie zur Steigerung der OLED-Effizienz .....	23
3.4	Problemstellung: Vom Festkörper zur Mesotechnologie .....	25
4	Synopsis.....	27
4.1	Hochreiner Natrium-Fluorohectorit.....	28
4.2	Deformationsmessungen an einzelnen Schichtsilicattaktoiden.....	30
4.3	Mechanische Eigenschaften einer einzelnen Silicatlamelle .....	32
4.4	Lokal-aufgelöste mechanische Eigenschaften von Graphen, Graphenoxid und chemisch erzeugtem Graphen .....	34
4.5	Flexible Nanokomposit-Beschichtung zur Anwendung in der Optoelektronik .....	36
4.6	Polarisierte Emission durch templatgesteuerte Quasi-Epitaxie .....	38
5	Verwendete Literatur.....	40
6	Ergebnisse .....	44
6.1	Hochreiner Natrium-Fluorohectorit.....	44

---

6.1.1	Nanoplatelets of Sodium Hectorite Showing Aspect Ratios of $\approx 20000$ and Superior Purity.....	45
6.1.2	Supporting Information .....	51
6.2	Deformationsmessungen an dünnen Schichsilicattaktoiden .....	60
6.2.1	Deformation Measurements on Thin Clay Tactoids.....	61
6.2.2	Supporting Information .....	66
6.3	Mechanische Eigenschaften einer einzelnen Silicatlamelle durch kontrollierte Faltung.....	68
6.3.1	In-plane Modulus of Singular 2:1-Clay Lamellae Applying a Simple Wrinkling Technique .....	69
6.3.2	Supporting Information .....	74
6.4	Lokal-aufgelöste mechanische Eigenschaften von Graphen, Graphenoxid und chemisch erzeugtem Graphen.....	82
6.4.1	Space-Resolved In-Plane Moduli of Graphene and Graphene Oxide Applying a Simple Wrinkling Procedure .....	83
6.4.2	Supporting Information .....	89
6.5	Flexible Nanokomposit-Beschichtung zur Anwendung in der Optoelektronik.....	103
6.5.1	Clay-Based Nanocomposite Coating for Flexible Optoelectronics Applying Commercial Polymers.....	104
6.5.2	Supporting Information .....	110
6.6	Polarisierte Emission durch templatgesteuerte Quasi-Epitaxie.....	113
6.6.1	Quasi-Epitaxy of $[\text{Ru}(\text{bpy})_3]^{2+}$ by Confinement in Clay Nanoplatelets Yields Polarized Emission .....	115
6.6.2	Supporting Information .....	133
7	Publikationsliste.....	139
7.1	Publikationen.....	139
7.2	Konferenzbeiträge .....	140

7.3	Pressemitteilungen .....	140
8	Danksagung.....	141
9	Erklärung des Verfassers.....	143

## 1 Summary

A concept for the progressive generation of efficient polymer layered silicate nanocomposites is described within this thesis. These nanocomposites require the optimization of four crucial factors, the aspect ratio and the mechanical properties of the nanofiller, as well as its compatibilization with and texturizing within the polymer matrix.

Firstly, an important issue was the synthesis of a highly pure, coarse-grained layered silicate that fulfilled the requirements as nanofiller. A combination of melt synthesis followed by long-term annealing provided a unique material showing unprecedented activation with respect to intracrystalline reactivity. Due to annealing huge particle sizes in the range of 20  $\mu\text{m}$  and high material purity could be obtained. In a mild anisotropic top down process the aspect ratio of this layered silicate could be maximized via delamination caused by osmotic swelling. Hereby aspect ratios of about 20000 were realized. In combination with further outstanding physical properties like homogeneous charge density and high optical transparency that material offered an ideal platform as filler for sophisticated nanocomposites in the in the field of sensitive optoelectronics packaging.

A further central aspect of this work was the mechanical characterization of single nanoplatelets for their application in nanocomposites. Two AFM-based methods were developed enabling the analysis of monolayers up to platelets of about 80 nm thickness. A nanoscale bending test offered new insights into the bending stiffness of clay platelets that are suitable for extrusion-based composites. For applications in nanocomposite coatings the mechanical performance of a single clay lamella was of crucial importance. Via a controlled wrinkling process on a deformable polymeric substrate the in-plane modulus of singular layered silicate lamellae could be extracted very efficiently.

Because of the efficiency and high resolution of the wrinkling metrology the in-plane moduli of inhomogeneous graphene oxide and chemically derived graphene could be obtained with sub-micron spatial resolution. Comparison with chemical vapor deposited graphene revealed the real capability of such materials implemented as fillers in nanocomposites. Furthermore, the wrinkling method could be applied to discern quickly and unambiguously between monolayer and bilayer graphene.

With a simple but efficient organophilization of the silicate lamellae described above a time-saving phase transfer into an organic solvent and an interface-optimized compounding with commercially available polyurethane precursor polymers could be achieved. In a subsequent bottom up process these nanoscale building blocks could be oriented on the mesoscale applying a cost-effective texturizing process yielding a nanocomposite coating with ultra-high gas barrier. Extremely low oxygen transmission rates, high transparency and flexibility enable an application for efficient packaging of sensitive and flexible OLEDs.

Furthermore, due to the high charge homogeneity of the synthesized layered silicate transition metal complexes could be oriented on its interfaces yielding polarized emission. That novel approach could be applied to synthesize efficient, polarized, flexible and at the same time resistant nanocomposite OLEDs.

This work is written in the style of a cumulative thesis. A detailed description of the results can be found within the attached publications.

## 2 Zusammenfassung

Im Rahmen der vorliegenden Dissertation ist es gelungen, ein Konzept zu erarbeiten, das eine Route für die sukzessive Generierung effizienter Nanokomposite von der Synthese eines nanoskaligen Schichtsilicat-Füllstoffs bis zur möglichen High-End Anwendung beschreibt. Bei der Optimierung von Polymer-Schichtsilicat-Nanokompositen treten vor allem vier zentrale Faktoren in den Vordergrund, das sind das Aspektverhältnis und die mechanischen Eigenschaften des Nanofüllstoffs, sowie dessen Kompatibilisierung mit der Polymermatrix und Texturierung in derselben.

Zunächst stand die Synthese eines hochreinen, grobkristallinen Schichtsilicats im Fokus, das obigen Anforderungen genügt. Hierbei lieferte eine Kombination aus Schmelzsynthese und Langzeittempern ein einzigartiges Material, das eine starke Erhöhung der intrakristallinen Reaktivität zeigte. Darüber hinaus konnten durch das Tempern Partikelgrößen von etwa 20  $\mu\text{m}$  und eine hohe Materialreinheit erreicht werden. In einem milden anisotropen „Top Down“ Prozess konnte das Aspektverhältnis dieses Schichtsilicats durch osmotische Quellung mit resultierender Delaminierung maximiert werden. Dadurch ließen sich Werte im Bereich von 20 000 realisieren. Kombiniert mit weiteren herausragenden physikalischen Eigenschaften wie einer homogenen Ladungsdichte und einer hohen optischen Transparenz bot dieses Material eine ideale Plattform als Füllstoff in anspruchsvollen Nanokompositen für den Sektor sensibler Opto-Elektronik.

Einen weiteren zentralen Aspekt in dieser Arbeit bildete die mechanische Charakterisierung einzelner Nanoplättchen für deren spätere Anwendung in Nanokompositen. Es wurden zwei AFM-basierte Methoden erarbeitet, die eine Analytik von Monolagen bis hin zu Teilchendicken von ca. 80 nm erlauben. Ein nanoskaliger Biegetest bot neuartige Einblicke in die Biegesteifigkeit von Schichtsilicatplättchen, welche für Spritzgusskomposite geeignet sind. Für Anwendungen im Bereich von Nanokompositbeschichtungen war darüber hinaus die mechanische Belastbarkeit einzelner Schichtsilicatlamellen von großer Bedeutung. Durch kontrollierte Faltenbildung auf einem deformierbaren Polymersubstrat ließ sich der in-plane Modul von einzelnen Schichtsilicatlamellen sehr effizient extrahieren.

In diesem Zuge wurde die hohe Auflösung der Faltungs-Methode durch eine orts aufgelöste mechanische Charakterisierung inhomogener Graphenoxid- und chemisch hergestellter Graphenmonolagen herausgestellt und mit CVD-Graphen verglichen. Dies gab Rückschlüsse auf die reale Leistungsfähigkeit derartiger Materialien in Nanokompositen und kann zukünftig beim Screening nach milderen, homogenen Oxidationsprozessen unterstützen. Des Weiteren erlaubte diese Methode eine sehr schnelle und einfache Unterscheidung zwischen Graphenmonolagen und -bilagen.

Eine einfache aber effektive Organophilierung der Schichtsilicatlamellen ermöglichte einen zeitsparenden Phasentransfer in ein organisches Lösungsmittel und eine grenzflächenoptimierte Compoundierung mit kommerziellen Polyuretan-Precursor-Polymeren. In einem nachfolgenden „Bottom Up“ Prozess konnten diese nanoskaligen Bausteine mittels eines effizienten Texturierungsverfahrens in Precursor-Polymeren auf der Meso-Skala orientiert und zu einem Nanokomposit-Hochbarrierefilm verarbeitet werden. Extrem niedrige Sauerstofftransmissionsraten, die hohe Transparenz und die Flexibilität der Beschichtungen erlauben einen Einsatz in der wirksamen Verkapselung sensibler, flexibler OLEDs.

Weiterhin konnten durch die hohe Ladungshomogenität des eingangs vorgestellten Schichtsilicats Übergangsmetallkomplexe so auf dessen Oberfläche orientiert werden, dass eine polarisierte Emission gemessen werden konnte. Dieser neue Ansatz der Quasi-Epitaxie könnte dazu beitragen, effiziente, polarisiert emittierende, flexible und zugleich resistente Nanokomposit-OLEDs herzustellen.

Bei der vorliegenden Arbeit handelt es sich um eine kumulative Dissertation. Die Ergebnisse werden daher thematisch getrennt in den einzelnen Publikationen beschrieben.



### 3 Einleitung

#### 3.1 *Schichtsilicate im Kontext der Energieproblematik*

Das Streben nach Energieeffizienz stellt eines der Schlüsselemente in der Zeit steigender Ressourcenknappheit dar, das in den letzten Jahren den Weg für ein rasantes Vorantreiben der Entwicklungen im Bereich der Materialwissenschaften ebnete. Vor allem zwei zentrale Überlegungen kristallisierten sich heraus, die Forschung nach Methoden zur alternativen Energieversorgung und die nach effizienter Nutzung der existierenden Ressourcen. Erstere konzentriert sich hauptsächlich auf die Energieerzeugung durch natürliche Ressourcen wie z.B. Wind, Wasser-, und vor allem solarer Energie. Trotz der Entwicklung neuer Solarzellen auf Siliciumbasis mit immer besserem Wirkungsgrad und auch der intensiven Forschung an kostengünstigeren, energieeffizienteren organischen Solarzellen<sup>[1]</sup> bleibt ein zentrales bis dato ungelöstes Problem: die Energiespeicherung. So können momentan derartige Energiequellen zwar zur haushaltseigenen Zusatzversorgung herangezogen werden, sind aber für eine komplett von fossilen und atomaren Quellen unabhängige Energieversorgung noch nicht nutzbar. Daher ist eine *zusätzliche* nachhaltige Nutzung existierender Energieressourcen von größter Bedeutung. Diese erstreckt sich von der Gewichtsreduktion im Automobilsektor bis hin zum Einsatz energieeffizienter Geräte aus der Elektronikindustrie. Hier haben funktionelle Kompositwerkstoffe seit Jahren vor allem in der Polymertechnologie sehr intensive Aufmerksamkeit erreicht. Als geeignete Füllstoffe für Polymermatrizen zur Eigenschaftsverbesserung haben sich Schichtsilicate und andere Schichtverbindungen wie z.B. Graphit-basierte Materialien erwiesen. Schichtsilicat-Komposite werden seit der Mitte des vorigen Jahrhunderts intensiv erforscht und haben durch die Nanotechnologie und nicht zuletzt durch den Graphen-Boom eine Renaissance erfahren.

### 3.2 *Schichtsilicate als effiziente Bausteine für funktionelle Nanokomposite*

#### 3.2.1 Allgemeines

Aufgrund ihrer vielfältig nutzbaren und attraktiven kolloidchemischen Eigenschaften erreichten Schichtsilicate in den letzten Jahrzehnten große Aufmerksamkeit im Sektor der Materialchemie und Nanotechnologie mit Anwendungsbereichen von mechanischer Verstärkung,<sup>[2-4]</sup> über eine Verbesserung der elektrischen Eigenschaften<sup>[5]</sup> und Flammsechutzeigenschaften,<sup>[6,7]</sup> bis hin zu einer effizienteren Gasbarrieretechnologie.<sup>[8,9]</sup> Schichtsilicate zeichnen sich durch einen tafeligen Habitus mit schichtartigem Aufbau aus (**Abbildung 1a**). Einzelne Plättchen, auch als Taktoide bezeichnet, bestehen aus parallel gestapelten Silicatlamellen (**Abbildung 1b**), die wiederum einen Sandwich-Aufbau aus einer Lage kantenverknüpfter Oktaeder besitzen, an die eckenverknüpfte Tetraeder apikal ankondensiert sind (**Abbildung 1c**). Aufgrund dieser Struktur werden derartige Tonminerale auch als 2:1 Schichtsilicate bezeichnet, zu denen auch der in dieser Arbeit verwendete Hectorit zählt.

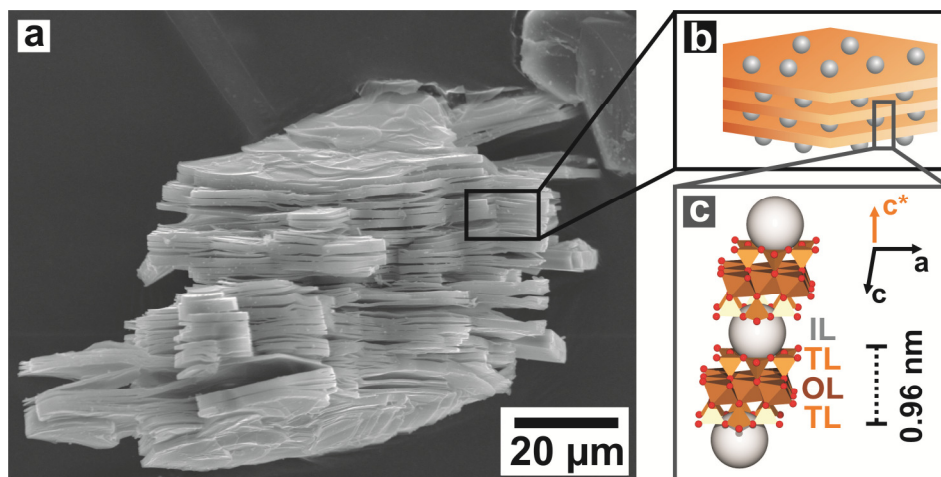


**Abbildung 1.** Vom Fundamentalpartikel zur atomaren Struktur. a) REM Aufnahme eines Hectorit-Taktoids, b) schematische Darstellung der lamellaren Struktur mit Zwischenschichtkationen, c) repräsentativer Ausschnitt aus der Schichtsilicat-Kristallstruktur.

Durch isomorphe Substitution innerhalb der Sandwich-Struktur, d.h. durch den Austausch höher valenter Kationen durch niedervalentere in Tetraeder- und/oder Oktaederschicht,

entsteht bei vorgegebener Ladung des Anionengerüsts (22 negative Ladungen pro Formeleinheit) eine negative Überschussladung (Schichtladung). Diese wird durch die Interkalation mobiler Kationen, der Zwischenschichtkationen, kompensiert. Die physikochemischen Eigenschaften der Schichtsilicate hängen dabei im Wesentlichen von der Verteilungsdichte der Zwischenschichtkationen, also der Schichtladung, und der Art ab. Letztere bestimmen den Schichtabstand und somit die interlamellare Wechselwirkung und Kohäsion.<sup>[10,11]</sup> Durch die Natur des Zwischenschichttraumes geht auch, bis auf wenige Ausnahmen wie z.B. Glimmer, die 3D-Phasenbeziehung verloren. Verantwortlich dafür sind planare Fehlorderungen, d.h. Rotation und Translation der einzelnen Lamellen gegeneinander, die u.a. durch unpassende Ionenradien der Zwischenschichtkationen, sowie durch Unterbesetzungen entstehen.<sup>[12]</sup>

Das wohl herausragende Alleinstellungsmerkmal der Schichtsilicate ist deren intrakristalline Reaktivität und darin insbesondere das Quellverhalten. Der Hydrationsenthalpie der Zwischenschichtkationen geschuldet, vermögen diese bei unterschiedlichen relativen Feuchten (r.h.) unterschiedliche Mengen an Wassermolekülen zu koordinieren und somit den Schichtabstand aufzuweiten.<sup>[13]</sup> Der Grad der Aufweitung wird durch ein kompetitives Gleichgewicht von attraktiven und repulsiven Kräften bestimmt. Dabei wirken Coulombanziehung und van der Waals Wechselwirkungen der Quellung entgegen, wohingegen eine betragsmäßig hohe Hydrationsenthalpie die Quellung begünstigt.

Somit lassen sich bei geeigneter Wahl von Schichtladung und Zwischenschichtkation unterschiedliche Quellungszustände bei gegebener Luftfeuchte realisieren, wobei die Quellung, vor allem bei synthetischen Schichtsilicaten (**Kapitel 3.2.2**) stufenförmig verläuft.<sup>[14]</sup> Bei Kontakt mit deionisiertem Wasser kann die Quellung schließlich so stark sein (osmotische Quellung), dass die Kohäsion der Silicatlamellen innerhalb eines Taktoids überwunden wird und dieser spontan in die einzelnen Silicatlamellen desintegriert. Dieser Vorgang wird als Delaminierung bezeichnet.<sup>[15]</sup> Aus der Sicht der Anwendung als nanoskaliger Füllstoff eignen sich gequollene Taktoide nur bedingt, da die interkalierten Wassermoleküle als Gleitfilm wirken können und die Scherfestigkeit des Füllstoffs somit dramatisch reduzieren (**Kapitel 4.2**). Alternativ können entweder maßgeschneiderte einzelne Silicatlamellen (**Kapitel 4.3 und 4.5**) oder schersteife Taktoide<sup>[14]</sup> eingesetzt werden.

Deren Generierung ist dank der hohen intrakristallinen Reaktivität der Schichtsilicate, also

der Zugänglichkeit zur Substitution der vorliegenden Zwischenschichtkationen gegen andere anorganische oder organische Spezies, relativ leicht möglich.<sup>[14]</sup> Treibende Kraft ist hierbei die erhöhte Selektivität v.a. organischer Kationen gegenüber z.B.  $\text{Na}^+$  und der Entropiegewinn im Falle der Interkalation höherwertiger Kationen. Allerdings gilt zu beachten, dass Kationenaustauschreaktionen auch einen erheblichen Einfluss auf das Zetapotential des Schichtsilicates haben können, was im Extremfall zur Ladungsneutralisierung und Flockung oder zur Umladung der Silicatoberfläche führen kann.<sup>[16,17]</sup> Außerdem sollten die Ladungsdichten des Wirtsmaterials<sup>a</sup> und des Intercalats weitgehend übereinstimmen. Durch geeignete Modifikation (Organophilierung) lassen sich delaminierte Schichtsilicate auch gezielt in wässrigen Medien flocken und in organische Lösungsmittel transferieren (**Kapitel 4.5**).

### 3.2.2 Synthetische Schichtsilicate

Schichtsilicate sind in der Natur als Tonminerale allgegenwärtig. Aufgrund ihrer Genese unter geologischen Bedingungen weisen diese klastischen Materialien stets ein gewisses Maß an Inhomogenitäten auf. Sie enthalten mineralische Akzessorien wie z.B. Quarz oder eisenhaltige oxidische Verbindungen, welche sich kaum oder nur durch aufwändige Reinigungsprozesse entfernen lassen. Strukturelles Eisen sorgt darüber hinaus für eine typisch bräunliche Färbung der Plättchen, die für optische Anwendungen im positivsten Fall unästhetisch ist, aber auch thermische Abbaureaktionen begünstigen kann. Weiterhin bedingen Heterogenitäten in der Ladungsdichte eine inhomogene intrakristalline Reaktivität und damit Inhomogenitäten im Quellverhalten. Ein dritter schwerwiegender Nachteil ist die kleine Partikelgröße (maximal 300 nm Durchmesser bei Montmorillonit), welche zusammen mit den erwähnten Inhomogenitäten die Verwendung natürlicher Schichtsilicate für High-End Nanokomposite stark limitiert.

---

<sup>a</sup> Für eine einzelne Schichtsilicatlamelle ergibt sich eine Ladungsdichte von etwa einer negativen Ladung pro  $\text{nm}^2$  auf jeder Seite.

Daher gibt es seit über fünf Jahrzehnten das Bestreben, Schichtsilicate kontrolliert im Labor zu synthetisieren.<sup>[18]</sup> Bereits 1970 wurde über eine Hectoritsynthese im geschlossenen Platintiegel berichtet.<sup>[19]</sup> Gängige Syntheseprotokolle nanoskaliger Hectorite stützten sich aber meist auf eine hydrothermale Umsetzung. Diese lieferten zwar phasenreine Materialien, jedoch mit sehr kleinen Partikelgrößen (20-50 nm), ähnlich ihren natürlichen Vertretern.<sup>[20]</sup> Sie sind seit mehreren Jahrzehnten unter Handelsnamen wie Laponit<sup>b</sup> kommerziell erhältlich. Verbesserungen in den Partikelgrößen konnten erst durch Hochtemperatursynthesen erzielt werden. Allerdings zeigte sich in Festphasenreaktionen wie beispielsweise die von *Tateyama* et al., dass durch die geringen Diffusionsraten keine Phasenreinheit erreicht wurde.<sup>c,[21]</sup> In der patentierten Schmelzsynthese eines quellfähigen Fluorotänioliths<sup>d</sup> von *Masato* und *Kenichiro* (JP11199111AA) werden durch Umsetzung von u.a. binären Fluoriden und Talk laut Hersteller Partikelgrößen im Bereich von 10-50 µm realisiert.

Seit etwa einem Jahrzehnt werden am Lehrstuhl Anorganische Chemie I der Universität Bayreuth Syntheseprotokolle für Schichtsilicate entwickelt, die durchwegs Plättchen mit erheblich größeren Partikeldurchmessern und homogener Ladungsdichte liefern.<sup>[22-24]</sup> Dabei zeigte sich, dass die intrakristalline Reaktivität von Schichtladung<sup>[13,25]</sup> und Art des Zwischenschichtkations<sup>[14]</sup> abhängt. Bisher war es jedoch noch nicht gelungen, ein absolut phasenreines Material zu synthetisieren, meist wurden geringste Anteile an kristalliner und amorpher Nebenphase im Bereich von etwa 5 % detektiert. Höchstwahrscheinlich ließ sich ein Natrium-Fluorohectorit beispielsweise aufgrund der amorphen Nebenphase trotz Applizierung starker Scherkräfte nicht vollständig delaminieren.<sup>[14]</sup> Ein in der Arbeitsgruppe synthetisierter neuartiger Li-Fluorohectorit war bis dato das einzige Material, welches in deionisiertem Wasser spontan delaminierte, allerdings nicht vollkommen phasenrein war.<sup>[24]</sup> In **Kapitel 4.1** wird die Synthese eines hochreinen Na-Fluorohectorits beschrieben, die durch eine Kombination aus Schmelzsynthese und Langzeittempern erreicht wurde.

---

<sup>b</sup> Handelsname Laponite von Laporte Industries Ltd., Widnes/UK; seit 1985.

<sup>c</sup> Handelsname Somasif (ME100) von CO-OP Chemicals Ltd., Japan.

<sup>d</sup> Hochgeladenes (Schichtladung ~1) trioktaedrisches Schichtsilicat, von Topy Co. Ltd., Japan.

### 3.2.3 Schichtsilicate als Füllstoffe

Der Einsatz von maßgeschneiderten Schichtsilicaten als funktionelle Füllstoffe in Polymermatrizen bedingt hohe Materialanforderungen. Durch ein in dieser Arbeit beschriebenes Konzept können zukünftig effiziente Nanokomposite für High-End-Anwendungen generiert werden. Dazu müssen vor allem vier zentrale Faktoren optimiert werden. Diese sind zum einen ein maximiertes Aspektverhältnis, des Weiteren optimale mechanische Eigenschaften des Füllstoffs<sup>e</sup>, ein perfektes Grenzflächenmanagement zur Kompartibilisierung des Füllstoffs mit der Matrix, sowie eine zeit- und kosteneffiziente Verarbeitung, die eine Texturierung<sup>f</sup> der Nanoplättchen garantiert.

Die Maximierung des Aspektverhältnisses spielt für optimierte Füllstoffanwendungen eine zentrale Rolle. So wirkt es sich signifikant auf die mechanischen Eigenschaften des generierten Nanokomposits,<sup>[26]</sup> sowie auf die erreichbare Textur der Plättchen und damit auf dessen Performance als Gasbarrierebeschichtung (**Kapitel 3.3.1**) aus. Ein großes Aspektverhältnis verbessert naturgemäß die Textur der Plättchen, wodurch mit synthetischen Hectoriten selbsttragende Filme durch einen Sedimentationsprozess mit nachfolgendem Evaporationsprozess hergestellt werden können.<sup>[27]</sup> Um eine Aggregation der Nanoplättchen bei der Verarbeitung mit der Polymermatrix zu verhindern, ist ein perfektes Grenzflächenmanagement eminent wichtig. Nur maßgeschneiderte Plättchen mit einer kompatiblen Oberflächenmodifikation ermöglichen eine optimierte Dispersion in der Matrix. Besonders signifikant für die mechanische Verstärkung des Nanokomposits ist zusätzlich eine gezielte Einbindung des Modifikators in die Matrix. Dies kann prinzipiell über chemische Bindungen oder physikalische Wechselwirkungen erfolgen. Zuletzt sind auch die mechanischen Eigenschaften eines einzelnen Plättchens für den nach *Halpin Tsai*<sup>[28]</sup> zu erwartenden Verstärkungsgrad des Nanokomposits von essentieller Bedeutung. Da diese einen zentralen Punkt in dieser Arbeit einnehmen, wird nachfolgend detaillierter auf die Plättchenmechanik eingegangen.

---

<sup>e</sup> Der Füllstoff sollte über maximierte Elastizitätskonstanten und hohe Scherstabilität verfügen.

<sup>f</sup> Parallele Orientierung der Plättchen zueinander in der Ebene.

### 3.2.4 Mechanische Eigenschaften von Nanoplättchen

#### 3.2.4.1 Allgemeines

Wie bereits geschildert, zeichnet sich die Anisotropie der Bindungsverhältnisse von Schichtsilicaten und auch anderen, beispielsweise graphitischen Nanoplättchen vom strukturellen Aufbau bis zum Habitus ab. Der intrinsisch-anisotrope Charakter wirkt sich natürlich auch auf deren mechanische Eigenschaften aus. Ein einzelnes Plättchen kann daher keineswegs als isotropes Material gesehen werden und erfordert eine richtungsabhängige mechanische Charakterisierung. Bei der Deformation von einzelnen lamellaren Plättchen muss auch das *Hookesche* Gesetz allgemeiner durch eine lineare Tensorgleichung der vierten Stufe ausgedrückt werden. Auf der Basis der Symmetrie des Verzerrungs- und Spannungstensors lassen sich die ursprünglichen 81 Komponenten des Elastizitätstensors zunächst auf 36 reduzieren, was eine Überführung in eine Matrixgleichung ermöglicht. Die Elastizitätskonstanten werden in einer 6 x 6-Matrix geschrieben, die Verzerrung und die Spannung in der *Voigtschen* Notation als sechskomponentige Vektoren:

$$\begin{pmatrix} \sigma_1 \\ \sigma_2 \\ \sigma_3 \\ \sigma_4 \\ \sigma_5 \\ \sigma_6 \end{pmatrix} = \begin{pmatrix} c_{11} & c_{12} & c_{13} & c_{14} & c_{15} & c_{16} \\ c_{21} & c_{22} & c_{23} & c_{24} & c_{25} & c_{26} \\ c_{31} & c_{32} & c_{33} & c_{34} & c_{35} & c_{36} \\ c_{41} & c_{42} & c_{43} & c_{44} & c_{45} & c_{46} \\ c_{51} & c_{52} & c_{53} & c_{54} & c_{55} & c_{56} \\ c_{61} & c_{62} & c_{63} & c_{64} & c_{65} & c_{66} \end{pmatrix} \cdot \begin{pmatrix} \varepsilon_1 \\ \varepsilon_2 \\ \varepsilon_3 \\ \varepsilon_4 \\ \varepsilon_5 \\ \varepsilon_6 \end{pmatrix} \quad (1)$$

Die Bedingung, dass das Gesamtmoment der applizierten Kraft auf das Material gleich Null ist, erniedrigt ihre Anzahl schließlich auf 21 voneinander symmetrieunabhängige Konstanten.<sup>[29]</sup> Je höher die Symmetrie des untersuchten Materials ist, desto weiter vereinfachen sich diese.

Für monokline Symmetrie, wie etwa beim Glimmer (2M<sub>1</sub> Polytyp), existiert eine Symmetrieebene im Material und man unterscheidet folglich 13 voneinander unabhängige Elastizitätskonstanten:<sup>[29,30]</sup>

$$\begin{pmatrix} C_{11} & C_{12} & C_{13} & 0 & C_{15} & 0 \\ & C_{22} & C_{23} & 0 & C_{25} & 0 \\ & & C_{33} & 0 & C_{35} & 0 \\ & & & C_{44} & 0 & C_{46} \\ & & & & C_{55} & 0 \\ & & & & & C_{66} \end{pmatrix} \quad (2)$$

Von diesen werden  $C_{11}$ ,  $C_{22}$ ,  $C_{66}$  und  $C_{12}$  primär von den starken kovalenten Bindungen innerhalb der Schichten beeinflusst. Bei trioktaedrischen Schichtsilicaten wie Biotiten und dem Hectorit bestehen aufgrund der pseudo-hexagonalen Symmetrie keine signifikanten Unterschiede der Elastizitätskonstanten in der Ebene vor. Die anderen Elastizitätskonstanten hängen in erster Linie von den schwächeren Wechselwirkungen zwischen den Lamellen ab und sind stärker von Temperatur, Druck und Interkalat beeinflussbar.<sup>[30]</sup> Die Elastizität entlang der Stapelachse wird dabei durch die  $C_{33}$  Konstante wiedergegeben.

Um nun die elastischen Eigenschaften einzelner Plättchen entlang der beiden stark unterschiedlichen Hauptrichtungen, d.h. in der Ebene (in-plane Modul) oder senkrecht dazu (Biegemodul), zu untersuchen, eignet sich die Rasterkraftmikroskopie dank der extrem hohen Sensitivität auf Meso- und Nanoskala hervorragend. Da es für die in den **Kapiteln 4.2 bis 4.4** vorgestellten Forschungsarbeiten eine tragende Rolle spielt, wird im Folgenden die prinzipielle Funktionsweise eines Rasterkraftmikroskops (AFM) vorgestellt.

#### 3.2.4.2 Mechanische und topographische Untersuchungen mit dem AFM

Die Vielseitigkeit im Anwendungsspektrum eines AFMs wird durch einen Blick auf den Aufbau deutlich. **Abbildung 2** zeigt die wesentlichen Bausteine eines typischen AFMs.



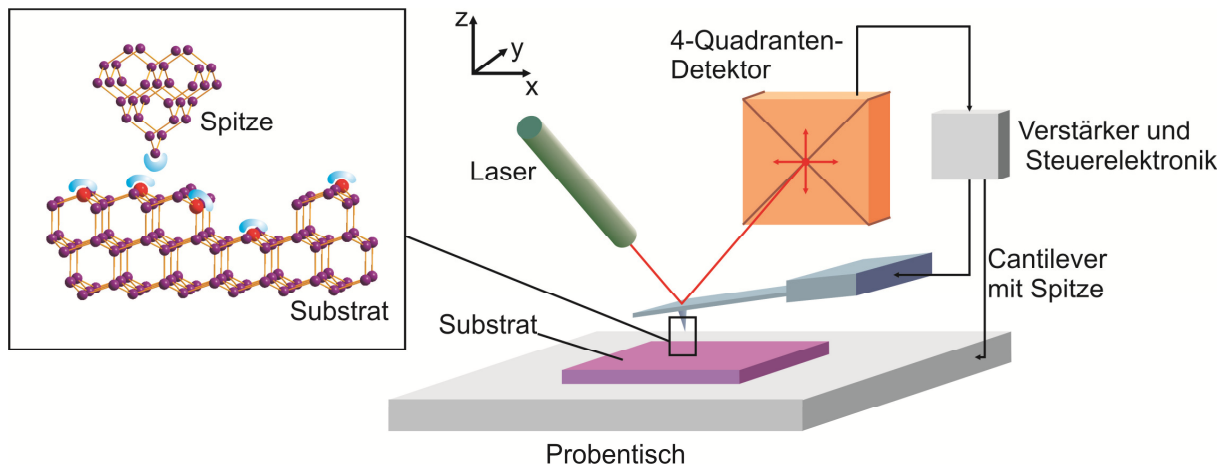


**Abbildung 2. Aufbau eines Rasterkraftmikroskops (AFM) mit Ausschnittsvergrößerung zur Visualisierung der Wechselwirkungen (blau) der Cantileverspitze (Si) in der Nähe des Substrats (Si).**

Die Hauptkomponente des AFMs bildet eine mikroskopisch kleine Blattfeder, der Cantilever, mit einer scharfen Spitze am Ende. Bei einer Interaktion der Spitze mit dem Substrat verbiegt sich dieser. Die Deformation wird optisch erfasst, wobei ein auf die Rückseite des Cantilevers fokussierter Laserstrahl reflektiert und über eine Vier-Quadranten-Photodiode detektiert wird. Auf diese Weise können sowohl vertikale als auch torsionale Deformationen aufgelöst werden. Piezo-Scanner kontrollieren die Bewegung des Cantilevers (und des Proben­tisches). Während die Spitze über die Probe rastert wird die zwischen Probe und Spitze wirkende Kraft anhand der Cantileverdeflektion gemessen. Trägt man diese gegen die Position auf der Probe auf, entsteht eine topographische Aufnahme der Probenoberfläche. Alternativ kann die z-Position der Cantileverhalterung herangezogen werden, während die zwischen Probe und Spitze wirkende Kraft über eine Rückkopplungsschleife konstant gehalten wird. Da diese Kraft sowohl eine Funktion des Abstands zwischen Spitze und Probe ist, als auch von deren Materialeigenschaften abhängig ist, entsteht ein Bildkontrast.

Generell unterscheidet man zwischen langreichweitigen und kurzreichweitigen Kräften. Bei letzteren handelt es sich um repulsive elektrostatische Kräfte, Kräfte kovalenter Bindungen, metallische Adhäsion und auch Reibungskräfte. Langreichweitige Kräfte sind *van der Waals* Kräfte, Coulomb-Wechselwirkungen und Kapillarkräfte. Der Einfachheit halber wird im Folgenden die Spitze-Probe-Wechselwirkung durch eine interatomare *Lennard-Jones* Kraft beschrieben:<sup>[31,32]</sup>

$$F(D) = -\frac{A}{D^7} + \frac{B}{D^{13}} \quad (3)$$

In der Realität gehorcht jedoch die attraktive Kraft zwischen den Oberflächen einer Gesetzmäßigkeit von  $-D^{-n}$  mit  $n \leq 3$  und nicht  $n = 7$ . Der repulsive Teil ist ebenfalls weitaus komplexer als der durch die *Lennard-Jones* Kraft beschriebene. Für eine einfache, qualitative Beschreibung des Mechanismus der Akquisition von Kraft-Abstandskurven ist eine derartige Abhängigkeit wie in **Gleichung (3)** jedoch ausreichend.

Wie in **Abbildung 3a** dargestellt wird der Cantilever mit der Federkonstante  $k_c$  nun entlang der vertikalen Achse (z-Achse) an die Probenoberfläche angenähert und dessen Verbiegung  $\delta_c$  bestimmt. Für die Kraft zwischen Spitze und Probe gilt dabei das *Hookesche Gesetz*:<sup>[31,32]</sup>

$$F_{Hooke} = k_c \delta_c \quad (4)$$

Die Entfernung  $Z$ , welche der Z-Piezo kontrolliert, ist nicht der Abstand  $D$  zwischen Spitze und Probe, sondern zwischen Probe und Ruheposition des Cantilevers. Diese beiden Strecken unterscheiden sich um die Cantileververbiegung  $\delta_c$  und um die Probendeformation  $\delta_p$  (**Abbildung 3a**).<sup>[31,32]</sup>

$$D = Z - (\delta_c + \delta_s) \quad (5)$$

Zu jeder Distanz  $Z$  verbiegt sich der Cantilever so weit ( $\delta_c$ ) bis die elastische Kraft des Cantilevers gegengleich der Spitze-Probe-Wechselwirkungskraft ist und sich das System im Gleichgewicht befindet. Es gilt:<sup>[31,32]</sup>

$$F(D) = -F_{Hooke} = -k_c \delta_c = -k_c (Z - D) \quad (6)$$

Die beiden Größen  $Z$  und  $\delta_c$  werden mit dem AFM gemessen. Die Beziehung zwischen der Spitze-Probe-Wechselwirkung und der resultierenden Kraft-Abstandskurve ist in **Abbildung 3b** zu sehen.  $\delta_c$  ist exemplarisch für den Punkt c eingezeichnet.

Wird der Cantilever an das Substrat angenähert, so wird die grüne Gerade (Elastizität des Cantilevers nach Gleichung (4)) in **Abbildung 3b** nach links verschoben. Ist der Abstand noch sehr groß, verbleibt der Cantilever in seiner Ruheposition. So verbleibt er bis mit weiterer Annäherung die Spitze eine *van der Waals*-Anziehung erfährt. Auf der Trajektorie von Punkt c nach Punkt b verbiegt sich der Cantilever um einen Betrag von  $\delta_c$  bis sich das System wieder im Gleichgewicht befindet. Hier muss gelten<sup>[31,32]</sup>:

$$\frac{\partial^2 U_{tot}}{\partial (\delta_c)^2} = \frac{\partial F(D)}{\partial D} > 0 \Rightarrow k_c > \frac{\partial F(D)}{\partial D} \quad (7)$$

$U_{tot}$  stellt die gesamte innere Energie des Systems dar. An Punkt b ist der Kraftgradient größer als  $k_c$ . Folglich wird der Cantilever instabil und springt nach Punkt b'. Diese Diskontinuität wird als „jump-to-contact“ bezeichnet. Ab hier befindet sich die Spitze im Kontakt mit der Probe. Dehnt sich der Z-Piezo weiter aus, so verbiegt sich der Cantilever aufgrund der *Coulomb*-Abstoßung konkav. Der Anstieg in diesem Bereich ist durch die mechanischen Eigenschaften der Probe und des verwendeten Cantilevers bestimmt.

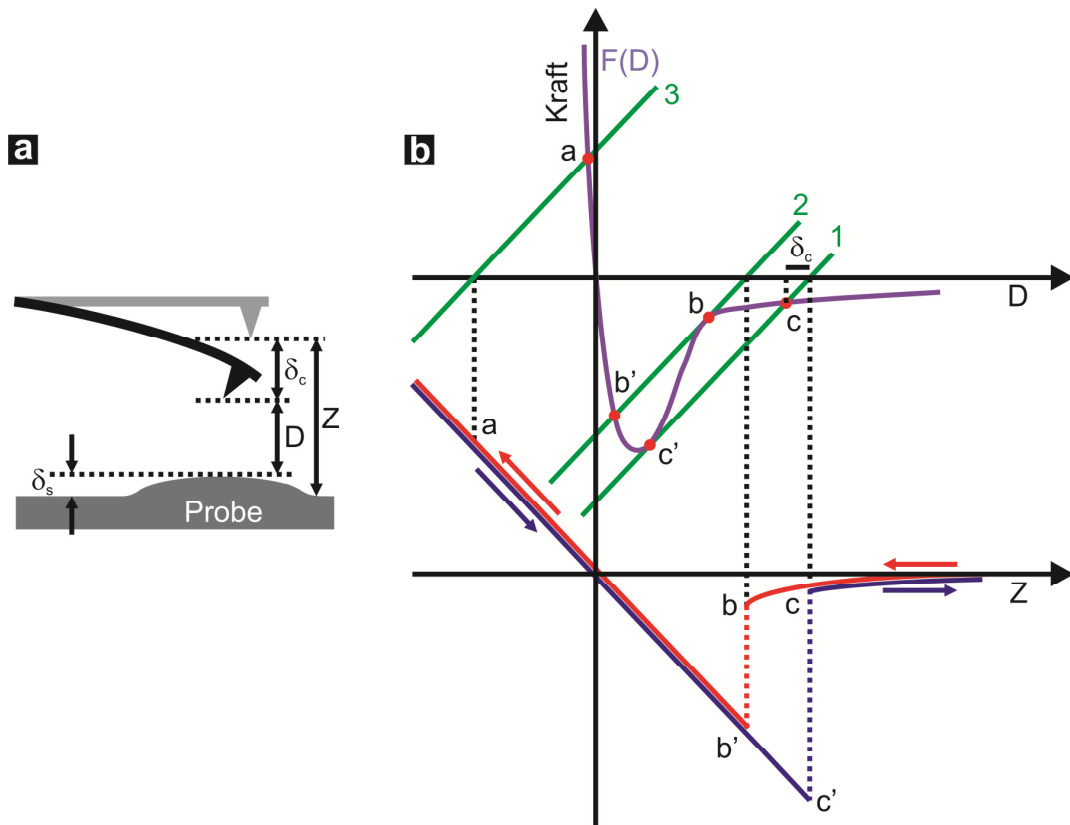


Abbildung 3. a) Schema zur Wechselwirkung zwischen Spitze und Probe; b) graphische Konstruktion einer Kraft-Abstandskurve aus der Spitze-Probe-Wechselwirkung; nach Ref.<sup>[31]</sup>

Beim Rückzug folgt die Spitze der Trajektorie von Punkt a nach Punkt c' (Gleichgewicht). Dann kann die Adhäsionskraft die elastische Kraft des Cantilevers nicht mehr kompensieren und er springt von Punkt c' nach Punkt c zurück. Diese Instabilität wird analog „jump-off-contact“ genannt.<sup>[31,32]</sup>

Die oben beschriebenen Punkte werden bei der sogenannten Kraftspektroskopie, d.h. der mechanischen Charakterisierung, während jeder einzelnen Messung durchlaufen (siehe **Kapitel 4.2**) und dementsprechend eine Kraft-Abstands-Kurve aufgenommen. Darüber hinaus sind die in bestimmten Bereichen wirkenden Kräfte auch für korrekte topographische Analysen von Bedeutung (siehe **Kapitel 4.3** und **4.4**).

Bei der Generierung von Oberflächenbildern mit dem AFM unterscheidet man prinzipiell zwei verschiedene Betriebsmodi, den statischen und den dynamischen. Dabei wird stets ein Regelparameter festgehalten und dessen Veränderung während der Messung registriert.<sup>[33]</sup> Im statischen Fall differenziert man zwischen dem so genannten Kontakt-Modus („contact mode“) und dem Nicht-Kontakt-Modus („non-contact mode“). Bei letzterem wird die Spitze des Cantilevers lediglich in die Nähe der Probenoberfläche gebracht und Wechselwirkungen detektiert. Aufgrund der geringen lateralen Auflösung wird dieses Setup nur sehr selten in den Materialwissenschaften genutzt. Im Kontakt-Modus wird die Spitze in Kontakt mit der Probe über diese gezogen, wobei direkt die Cantileververbiegung gemessen wird. Erfolgt keine weitere Nachregelung, spricht man vom „constant height mode“. Um bei unebenen Proben eine zu starke Belastung der Probe und Spitze zu vermeiden, ist ein weiteres Feature zugänglich. Die im Kontakt-Modus wirkenden Wechselwirkungskräfte gehorchen dem Hookeschen Gesetz, so dass eine direkte Proportionalität zwischen der Kraft und dem Betrag der Verbiegung, also der Höhe der Probe relativ zum Ausgangspunkt besteht. Dadurch kann die relative Position des Cantilevers zur Probe über eine Rückkopplungsschleife zu einer konstanten Kraft zwischen Spitze und Probe nachgeregelt werden. Dies bezeichnet man als „constant force mode“. Ein analoges Setup wurde bei den in **Kapitel 4.4** beschriebenen Leitfähigkeitsmessungen gewählt.

In den letzten Jahren haben sich dynamische Betriebsmodi zum Standard für topographische Analysen etabliert, da sie sich für eine Vielzahl von Probenoberflächen eignen und gleichzeitig über eine hohe Ortsauflösung verfügen. Dabei wird der Kontakt zwischen Cantilever und Probe minimiert um Schäden auf beiden Seiten vorzubeugen. Der wichtigste Betriebsmodus ist hierbei der intermittierende Kontakt-Modus („intermittent contact mode“, „tapping mode<sup>TM</sup>“). Hier wird der Cantilever nahe seiner Resonanzfrequenz angeregt. Die Annäherung des annahmeweise mit seiner Eigenfrequenz  $\omega_0$  schwingenden Cantilevers an die Probenoberfläche ändert dessen Resonanzfrequenz aufgrund der attraktiven und repulsiven Kräfte zwischen Spitze und Probe. Folglich erfährt auch die Schwingungsamplitude eine Änderung und nimmt den Wert der neuen Resonanzkurve bei der Anregungsfrequenz des Oszillators an (**Abbildung 4a**), gestrichelte Linien). Dadurch würde die neue Amplitude kleiner als die freie Amplitude (Schnittpunkte mit der gepunkteten senkrechten Linie) sein. Ist die Anregungsfrequenz  $\omega_{\text{exc}}$  jedoch, wie oben erwähnt, etwas von  $\omega_0$  verschieden, kann die Amplitu-

de, je nach der Position der neuen Resonanzfrequenz relativ zur Eigenfrequenz des freien Oszillators, kleiner oder größer werden. Eine implementierte Rückkopplungsschleife (Amplitudenmodulation) korrigiert dies üblicherweise und hält die Amplitude konstant.

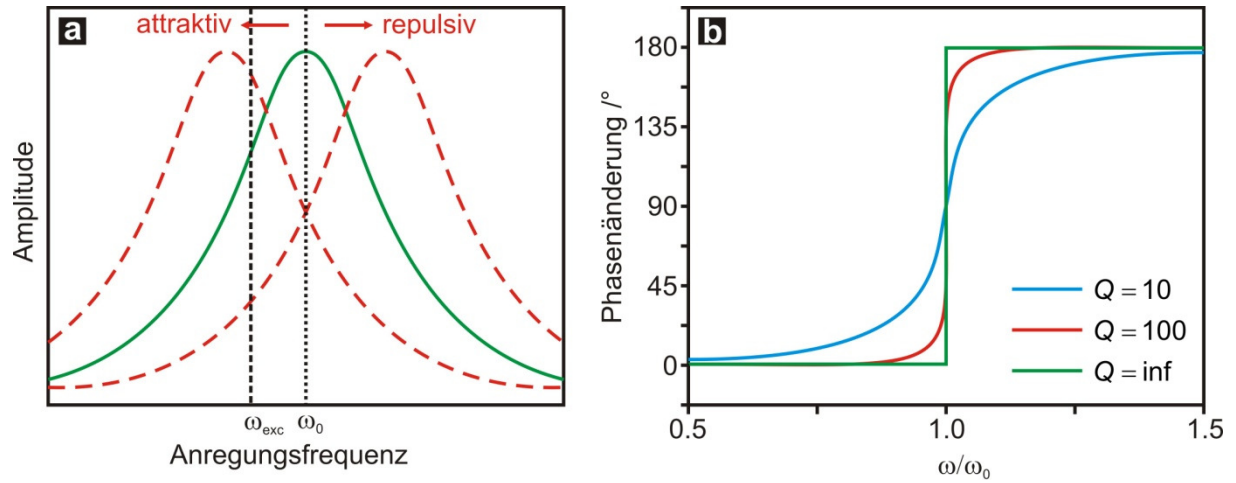


Abbildung 4. a) Resonanzkurve für einen freien harmonischen Oszillator (grüne Linie) und einer Oszillation beeinflusst von attraktiven und repulsiven Kräften (gestrichelte rote Linien); b) Phasenänderung eines gedämpften harmonischen Oszillators als Funktion der Ansteuerfrequenz; für den Idealfall ( $Q = 0$ ) ergibt sich ein scharfer Übergang von  $0^\circ$  nach  $180^\circ$  bei  $\omega = \omega_0$ . Nach Garcia et al. [34]

Die Verwendung des intermittierenden Kontakt-Modus erhöht darüber hinaus die Qualität extrahierbarer Informationen aus einer Messung. Beispielsweise können Änderungen in der Phase des oszillierenden Cantilevers Probeneigenschaften zugeordnet werden. Die Lösung für einen gedämpften harmonischen Oszillator  $z$  ist als die Summe eines transienten und eines stationären Terms definiert: [34]

$$z = B \exp(-\alpha t) \cos(\omega_{\text{exc}} t + \beta) + A \cos(\omega t - \phi) \quad (8)$$

Nach einer Zeit  $2Q/\omega_0$ , wobei  $Q$  einen Gütefaktor zur Beschreibung der Dämpfungseffizienz darstellt, wird die Bewegung vom stationären (zweiten) Term dominiert und die Phasenänderung ergibt sich zu: [34]

$$\tan \phi = \frac{\omega \omega_0 / Q}{\omega_0^2 - \omega^2} \quad (9)$$

Hierbei ist  $\phi$  der Winkel, bei dem die Triebkraft die Auslenkung leitet. Wie bereits erwähnt, ändert die Dämpfung die Resonanzfrequenz des Cantilevers (**Abbildung 4a**). Aus dieser Phasenverschiebung sind Materialeigenschaften der untersuchten Probe extrahierbar und visualisierbar, welche in der topographischen Aufnahme verborgen bleiben. Der prominen-

teste Fall sind qualitative mechanische Eigenschaften. Wie aus **Abbildung 4b** ersichtlich wird, können Materialien mit unterschiedlichen (mechanischen) Eigenschaften, also unterschiedlichen Dämpfungsfaktoren, innerhalb einer Probe signifikante Phasenänderungen hervorrufen.

Für sämtliche im Rahmen dieser Arbeit durchgeführten topographischen Aufnahmen wurde der intermittierende Kontakt-Modus herangezogen (**Kapitel 4.1 bis 4.5**).

### 3.3 *Mesotechnologische Anwendungen – Schichtsilicat-Nanokomposite*

Optimierte Füllstoffeigenschaften ebnen den Weg zu High-End Nanokompositen. Im Folgenden werden nun zwei Anwendungsbeispiele zur Verwendung von Schichtsilicaten diskutiert, eine flexible Hochbarrierebeschichtung und ein neuer Ansatz zur Effizienzsteigerung von OLEDs durch quasi-epitaktische Orientierung phosphoreszierender Emitter auf Schichtsilicatoberflächen.

#### 3.3.1 Gasbarriere

Effiziente und dünne Beschichtungssysteme mit einer hohen Gasbarriere gegenüber Sauerstoff und Wasserdampf stellen wichtige Wachstumsfelder in einer kontinuierlich expandierenden Industrie dar. Dabei erfüllen die Beschichtungen ein breites Feld an Anforderungen, angefangen bei der Verpackung von Convenience Produkten bis hin zu High-Tech Anwendungen wie der Verkapselung flexibler Displays oder organischer Photovoltaik. Die Barriereanforderungen (Sauerstoff- und Wasserdampf-Transmissionsraten, OTR, WVTR) an die jeweiligen Systeme unterscheiden sich jedoch um Größenordnungen (**Abbildung 5**).

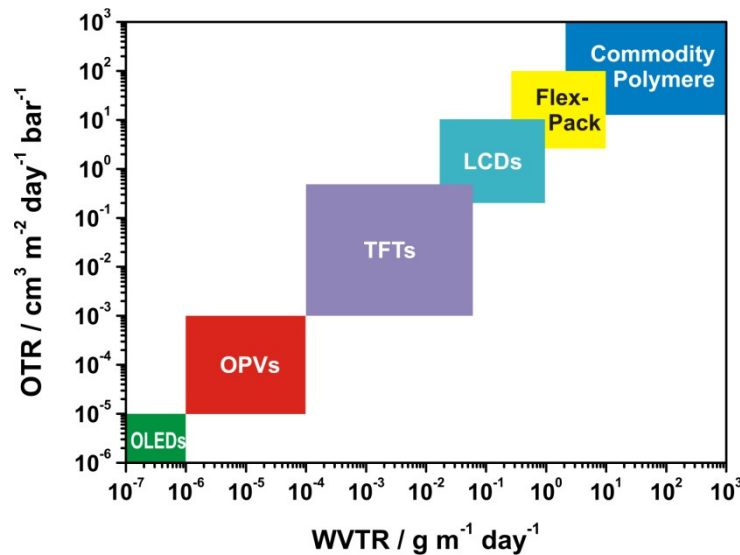


Abbildung 5. Geforderte Sauerstoff- (OTR) und Wasserdampftransmissionsraten (WVTR) für repräsentative Barriereanwendungen. Ergänzt nach Ref.<sup>[35]</sup>

Gerade in der Elektronikindustrie herrscht ein erheblicher Bedarf an flexiblen Hochbarrierebeschichtungen für biegsame elektronische Devices, wie flexible OLEDs, vor.<sup>[36]</sup> Diese zeichnen sich gegenüber konventionellen OLEDs durch ein breiteres Anwendungsspektrum, höhere Haltbarkeit und Schlagfestigkeit aus – Displaybruch ist beispielsweise mit Hauptursache bei Displayschäden und nicht zuletzt ein zentraler Sicherheitsaspekt. Bis jetzt existiert allerdings aber noch keine befriedigende Lösung für flexible Barrierebeschichtungen, die den hohen Anforderungen der sensiblen OLED-Materialien entsprechen ( $\text{OTR} < 10^{-5} \text{ cm}^3 \text{m}^{-2} \text{day}^{-1} \text{bar}^{-1}$ ,  $\text{WVTR} < 10^{-6} \text{ g m}^{-1} \text{day}^{-1}$ ).

Erfahrungsgemäß zeigen reine Commodity-Polymere als Verpackungsmaterialien relativ hohe Gasdurchflussraten (Permeabilitäten), was nicht zuletzt auf ein nicht unerhebliches freies Volumen in amorphen Polymeren zurückzuführen ist, sowie geringe Kratzfestigkeit. Eine effiziente Barriertechnologie hingegen erhöht die Lebensdauer des Produktes ungemein. Von besonderer Relevanz für industrielle Anwendungen sind einfach durchzuführende Beschichtungsverfahren, d.h. das Veredeln eines preisgünstigen Substrats mit einer Barrierebeschichtung.

Die resultierende Gesamtpermeabilität  $P$  ergibt sich aus einer Linearkombination aus den Einzelpermeabilitäten von Substrat ( $P_s$ ) und Beschichtung ( $P_B$ ). Die Größen  $l$ ,  $l_s$  und  $l_B$  stellen die Dicke des beschichteten Films, des Substrates und der Beschichtung selbst dar:

$$\frac{l}{P} = \frac{l_B}{P_B} + \frac{l_S}{P_S} \quad (10)$$

$$P = \frac{J_\infty \cdot l}{\Delta p}, \text{ wobei } J_\infty = \frac{\Delta m}{\Delta t \cdot A} \quad (11)$$

Die Permeabilität  $P$  ist eine Materialkonstante des Massenflusses im Gleichgewicht ( $J_\infty$ ), die Triebkraft ist hierbei die Partialdruckdifferenz des Permeants.  $J_\infty$  setzt sich aus dem Massenunterschied  $\Delta m$  pro Zeit  $\Delta t$  und Fläche  $A$  zusammen. Die Permeabilität  $P$  wird immer in Bezug auf eine Filmdicke  $l$  angegeben, während die ebenfalls oftmals verwendete Transmission  $T$  den Absolutwert des Massenstroms darstellt:

$$T = \frac{P}{l} \quad (12)$$

Neben der im Allgemeinen linearen Korrelation der Massentransmission mit der Membrandicke ist der Stofftransport durch eine Membran ein äußerst komplexer Vorgang. Zwei wesentliche Aspekte beeinflussen die Permeabilität erheblich, das ist zum einen die Löslichkeit des Permeanten in der Matrix und zum anderen die Diffusion. Außer dem ersten Fickschen Gesetz der Diffusion kann noch eine Vielzahl anderer Prozesse auftreten, die den Stofftransport accelerieren oder retardieren. Der Stofftransport kann durch das Einbringen texturierter impermeabler Nanoobjekte in die Beschichtungsmatrix („Tortuous Path“ Modell) und das freie Volumen, sofern die Beschichtung polymerer Natur ist, signifikant beeinflusst werden. Da Letzteres nicht Gegenstand der in dieser Arbeit vorgestellten Studien war, sei an dieser Stelle nur auf einen aussagekräftigen Übersichtsartikel von *Choudalakis et al.* verwiesen.<sup>[37]</sup>

Grundlegende Studien zum „Tortuous Path“ Modell wurden bereits 1967 von *Nielsen* publiziert.<sup>[38]</sup> Seine Theorie beruht auf der Annahme, dass sich der Diffusionsweg von Molekülen durch das parallele und gegeneinander versetzte Einbringen von impermeablen unendlich langen Bändern mathematisch und physikalisch verlängert.

$$P_{rel} = \frac{P}{P_0} = \frac{1-\phi}{1+0.5\alpha\phi} \quad (\phi \ll 1 \text{ und } \alpha\phi < 1) \quad (13)$$



Hierbei setzt sich die relative Permeabilität  $P_{rel}$  aus dem Quotienten der Permeabilitäten aus Barrieremembran  $P$  und der reinen Matrix  $P_0$  zusammen und hängt im Wesentlichen vom Aspektverhältnis  $\alpha$  des Füllstoffs und dessen Volumenanteil  $\phi$  ab. Dieses Modell gilt vor allem für sehr kleine Plättchen-Volumenfraktionen ( $\phi \ll 1$ ) mit kleinem Aspektverhältnis ( $\alpha\phi < 1$ ) und wurde in den nachfolgenden Jahren mit diversen Ansätzen verfeinert<sup>[39-41]</sup> und zum Teil mit empirischen Daten und finite Elemente Berechnungen unterfüttert.<sup>[42,43]</sup> Als repräsentativstes Modell, v.a. im Hinblick auf Aspektverhältnis und realistische Abschätzung, hat sich die *Cussler*-Theorie bewährt.<sup>[40]</sup> Hierbei gilt:

$$P_{rel} = \frac{P}{P_0} = \left( 1 + \mu \frac{\alpha^2 \phi^2}{1 - \phi} \right)^{-1} \quad (\phi \ll 1 \text{ und } \alpha\phi > 1) \quad (14)$$

Das *Cussler* Modell beschreibt halbverdünnte Systeme mit größeren Aspektverhältnissen am besten. Zusätzlich wird ein Geometrieparameter  $\mu$  eingeführt, der die Plättchenform beschreibt. Im Falle der Schichtsilicate entspräche  $\mu$  einem Wert von 4/9 (hexagonale Plättchen).<sup>[36]</sup> In **Abbildung 6a** und **b** sind ausgewählte relative Permeationsisothermen in Abhängigkeit von Füllstoffgehalt und Aspektverhältnis gemäß *Cussler* gezeigt. Diese Erweiterung der *Nielsen*-Theorie in den halbverdünnten Volumenanteil-Bereich führt dazu, dass die einzelnen Plättchen nicht mehr als unabhängig angesehen werden können, was zu einer reflektiven Diffusion führt, wie sie schematisch in **Abbildung 6c** dargestellt ist.

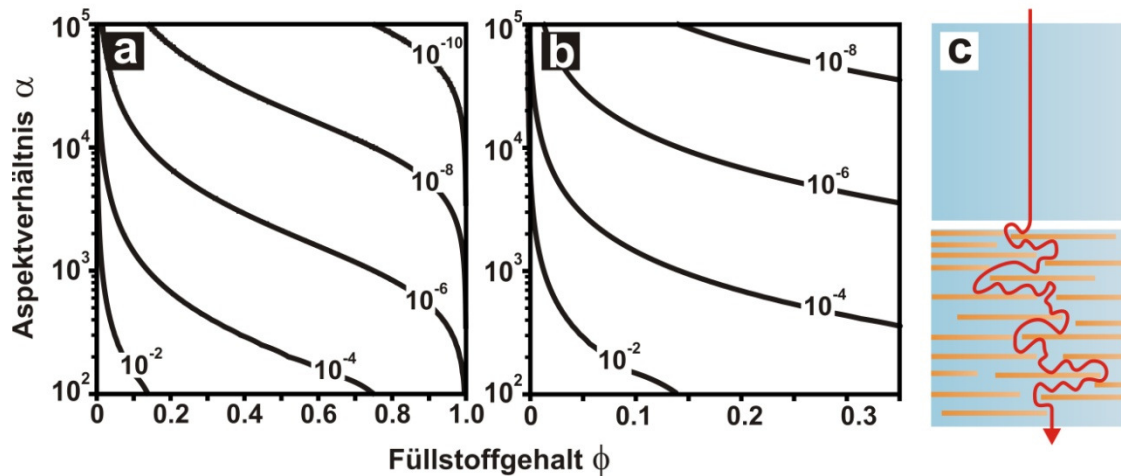


Abbildung 6. Das *Cussler* Modell. a) Ausgewählte relative Permeationsisothermen in Abhängigkeit von Füllstoffgehalt und Aspektverhältnis; b) Ausschnittsvergrößerung der relativen Permeationsisothermen bei realisierbarem Füllstoffgehalt; c) schematische Repräsentation der Diffusion eines Gasmoleküls durch eine pure Polymermatrix (oben) und der reflektiven Diffusion durch eine *Cusslersche* Barrieremembran.

Wie aus obiger Abbildung ersichtlich ist, erhöhen sowohl ein großes Aspektverhältnis als auch eine Steigerung des Füllstoffgehalts die Gasbarriere (**Abbildung 6a**). Rein physikalisch lassen sich jedoch selbst mit kurzkettigen organischen Modifikatoren kaum Füllstoffgehalte jenseits von 0.35<sup>8</sup> realisieren, da prinzipiell jede Organophilierung eine Aufweitung des Zwischenschichtraums aufgrund des erhöhten Platzbedarfs der Moleküle nach sich zieht. Füllstoffgehalte jenseits von 0.3 führen darüber hinaus zu einer signifikanten Versprödung der Nanokompositbeschichtung, was sich negativ auf die Flexibilität auswirken kann. Demnach sind v.a. Füllstoffe mit effektiven Aspektverhältnissen jenseits von ca. 10 000 optimal, um einerseits den OLED Anforderungen zu genügen und andererseits eine ausreichende Flexibilität bei geringerem Füllstoffbedarf (ungefähr um 0.2) zu gewährleisten (**Abbildung 6b**; siehe dazu auch **Kapitel 4.5**).

<sup>8</sup> Kommerzielle organophilisierte Montmorillonite wie CLOISITE<sup>®</sup> 93 zeigen d-Werte von 2.79 nm. Eine Schichtsilicatlamelle besitzt eine Dicke von 0.96 nm.<sup>[13,44]</sup> Folglich weist diese Interkalationsverbindung bereits einen „Füllstoffgehalt“ von etwa 35 vol.% auf, was für Nanokomposite mit delaminierten Füllstoffen als oberes Limit gesehen werden kann.

### 3.3.2 Quasi-Epitaxie zur Steigerung der OLED-Effizienz

Die Lebensdauer von (flexiblen) OLEDs hängt von einer effizienten Einkapselung ab, deren Leistungsfähigkeit hingegen kann durch die externe Quanteneffizienz (*EQE*) beschrieben werden:<sup>[45-47]</sup>

$$EQE = \gamma \cdot \beta \cdot \Phi_{PL} \cdot \eta_{out} \quad (15)$$

EQE besteht aus vier Termen, wobei sich die beiden ersten aus dem Ladungsausgleichsfaktor  $\gamma$ , der die Wahrscheinlichkeit der Ladungsträger-Rekombination und nachfolgende Excitonenbildung beschreibt, und dem Spinstatistikfaktor  $\beta$ , der zwischen den beiden Materialklassen der Singulett- und Triplettmitter unterscheidet, zusammensetzen. Der dritte Faktor stellt Photolumineszenz-Quantenausbeute  $\Phi_{PL}$  dar und der vierte beinhaltet die Auskopplungseffizienz  $\eta_{out}$ , d.h. welcher Anteil intern generierter Photonen die Struktur verlassen kann.

Für eine optimale OLED müssen demnach alle in **Gleichung (15)** erwähnten Faktoren optimiert werden, d.h. nahe 1 sein. In gegenwärtigen OLEDs wird die Rekombination aller Ladungsträger bereits erreicht ( $\gamma = 1$ ), da die Rekombinationszone durch effiziente Blockierungs-Materialien innerhalb einer sehr dünnen Schicht beschränkt ist.<sup>[48]</sup> Weiterhin werden hauptsächlich phosphoreszierende Emitter verwendet, um sowohl Triplett- als auch Singulett-Harvesting zu betreiben, was zu einem Spinstatistikfaktor  $\beta$  von 1 führt.<sup>[49]</sup> Dieser hätte vergleichsweise bei fluoreszierenden Materialien einen Wert von 0.25, da diese lediglich 25% der Excitonen über Singulett-Harvesting bilden können. Somit basieren die ersten beiden Terme auf Material-inhärenten Eigenschaften, während die beiden folgenden von der OLED Kavität beeinflusst werden und stark von der Verteilung und Orientierung der Emitter abhängen. Eine vollständige Photolumineszenz-Quantenausbeute von  $\Phi_{PL} = 1$  ist theoretisch möglich bei Emittern, welche sich durch kurze Triplett-Lebensdauern und reduzierte strahlungsfreie Relaxationsprozesse auszeichnen.<sup>[50]</sup> In dieser Hinsicht besitzen phosphoreszierende Übergangsmetall- (TM-) Komplexe ein großes Potential, da sie, verglichen mit rein organischen Emittern, neben ihrer Vielfältigkeit im Farbspektrum auch über eine effizientere Exciton-Umwandlung in Licht verfügen.<sup>[50]</sup> Schließlich muss die Auskopplungseffizienz  $\eta_{out}$  optimiert werden. Hier hat sich erst in jüngster Zeit gezeigt, dass auch die Orien-

---

tierung der Emitter eine essentielle Rolle spielt.<sup>[51]</sup>

Die Möglichkeit der Orientierung von Emittern hängt von deren Anisotropie ab. Polymere Spezies können durch geeignete Techniken wie Langmuir-Blodgett oder mechanischer Nachbehandlung (Rubbeln, Ziehen) orientiert werden.<sup>[52-56]</sup> Bei molekularen organischen Emittern erfolgt die Orientierung z.B. über epitaktisches Wachstum durch Gasphasenabscheidung. *Yokoyama* diskutiert aktuelle Forschung dazu in einem kürzlichen erschienenen Review-Artikel.<sup>[51]</sup> Im Wesentlichen wird sich bei der Orientierung der meist stäbchenförmigen Anisotropie der Moleküle bedient. Bei den meist hochsymmetrischen effizienteren TM-Komplexe gestaltet sich eine einheitliche Orientierung weitaus schwieriger. Bis dato wurde kein vernünftiger Lösungsansatz gefunden.

Auch hier bieten synthetische Schichtsilicate ein großes Potential, da man positiv geladene TM-Komplexe einerseits durch die hohe Ladungshomogenität äquidistant auf einzelnen Lamellen immobilisieren und diese anschließend aufgrund der großen Aspektverhältnisse texturieren könnte. In grundlegenden Studien wurde die Orientierung von Komplexen auf Schichtsilicatoberflächen bereits theoretisch beleuchtet.<sup>[57-59]</sup> In **Kapitel 4.6** wird die Generierung eines derartigen Nanokomposits gezeigt und dessen Effizienz anhand von polarisierter Emissions-Spektroskopie näher erläutert.

### 3.4 Problemstellung: Vom Festkörper zur Mesotechnologie

Wirft man einen Blick auf die zeitliche Entwicklung der Generierung von Nanomaterialien, so stellt man zwei zentrale Herangehensweisen fest, den meist sehr anspruchsvollen und aufwändigen „Top Down“ Prozess, sowie die effizientere, aber noch nicht ganz ausgereifte „Bottom Up“ Technik (**Abbildung 7**). Der Kurvenschnittpunkt in der Gegenwart deutet auf eine Synergie der beiden Herangehensweisen hin, die in Kombination den Weg zur Mesotechnologie, dem Bindeglied zwischen Nanotechnologie und Werkstoffentwicklung ebnen.

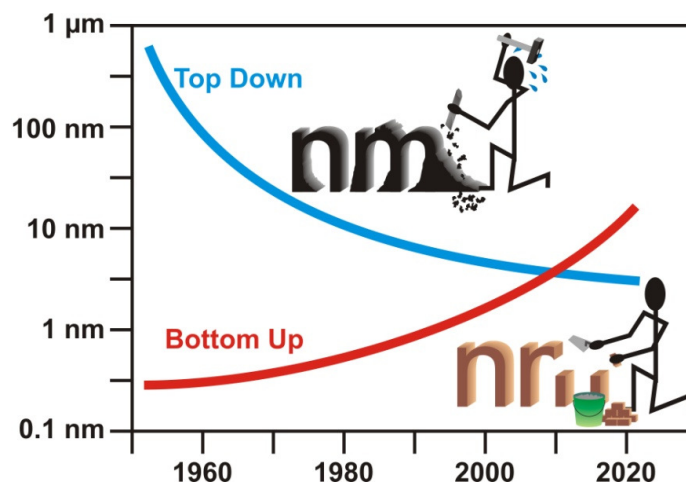


**Abbildung 7.** Entwicklungsverlauf der Nanomaterialien mit der Zeit. Der Kurvenschnittpunkt deutet auf eine Synergie zwischen der „Top Down“ Herangehensweise und der „Bottom Up“ Technik hin.<sup>[60]</sup>

In genau diesem Kontext wird in der vorliegenden Dissertation ein Konzept erarbeitet, das eine Route für die sukzessive Entwicklung effizienter Nanokomposite von der Füllstoffsynthese bis zur möglichen High-End Anwendung beschreibt.

---

Diese Konzeptentwicklung stützt sich im Wesentlichen auf drei Säulen:

1. Synthese eines hochreinen Schichtsilicat-Füllstoffs
  - a. Intrakristalline Reaktivität
  - b. Partikelgröße
  - c. Reinheit
  - d. Skalierbarkeit
2. Eigenschaftscharakterisierung und –optimierung des Füllstoffs
  - a. Aspektverhältnis
  - b. Mechanische Eigenschaften
  - c. Ladungsdichteabgleich
3. Generierung und Charakterisierung neuartiger Nanokomposite mit dem Füllstoff
  - a. Kompatibilisierung mit Polymermatrix
  - b. Texturierungsverfahren
  - c. Charakterisierung hinsichtlich Gasbarriereigenschaften, Emissionseigenschaften
  - d. Skalierbarkeit

Die wesentlichen Schritte sind in **Abbildung 8** schematisch dargestellt. Sie ist zugleich als Übersicht für die Synopsis und den Ergebnisteil gedacht.

## 4 Synopsis

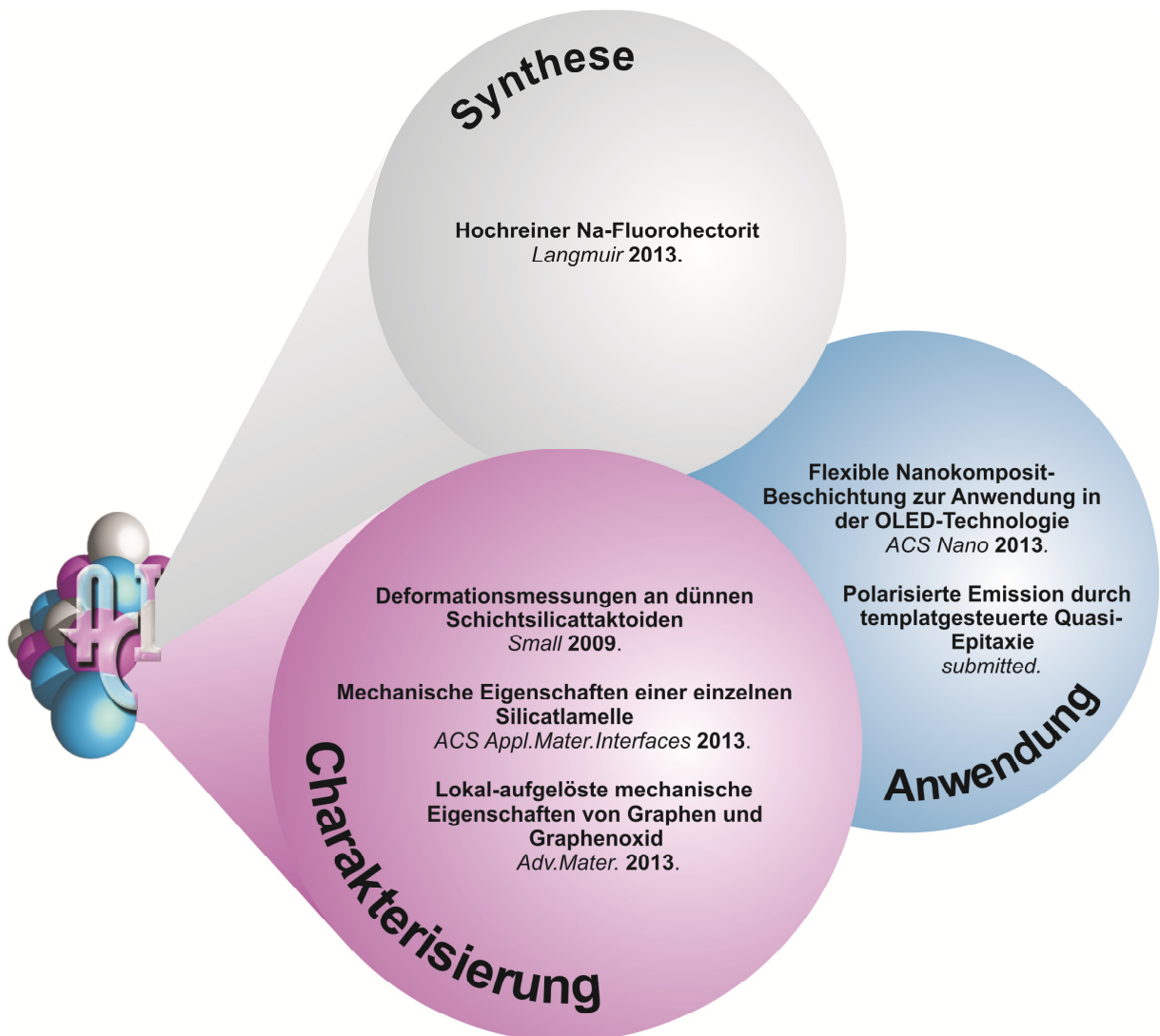


Abbildung 8. Schematische Darstellung der Ergebnisse dieser Dissertation.

Die vorliegende Dissertation enthält sechs Publikationen, welche sich thematisch in drei große Blöcke unterteilen lassen. Im folgenden Kapitel wird die **Synthese** eines neuartigen Natrium-Fluorohectorits vorgestellt, der zugleich das in dieser Arbeit hauptsächlich verwendete Ausgangsmaterial darstellt. Den zweiten Bereich bilden grundlegende mechanische **Charakterisierungen** einzelner Nanoplättchen und im dritten Block werden zwei neuartige **Anwendungen** präsentiert.

#### 4.1 *Hochreiner Natrium-Fluorohectorit*

Ein optimierter Füllstoff ist unabdingbar, um das volle Potential von Polymer-Schichtsilicat-Nanokompositen auszuschöpfen. Die Füllstoffeigenschaften sind hauptsächlich durch dessen Aspektverhältnis, relative Orientierung in der Polymermatrix (Textur), mechanische Eigenschaften und Kompatibilisierung mit der Polymermatrix bestimmt. Während die ersten beiden Faktoren stark von der lateralen Ausdehnung des Füllstoffs abhängen, werden die beiden letzteren stark von der Homogenität und Ladungsdichte beeinflusst, was mit einer einheitlichen intrakristallinen Reaktivität korreliert. Weiterhin sollte der Schichtsilicatfüllstoff frei von Fremdphasen sein und optimale optische Eigenschaften besitzen. Natürliche, kommerziell verfügbare Schichtsilicate können diese Voraussetzungen jedoch nicht aufbringen: Geringe Partikelgrößen ( $< 300$  nm für Montmorillonit) und heterogene Ladungsdichte, in Kombination mit akzessorischen mineralischen Verunreinigungen und verminderter optischer Qualität durch strukturelle farbgebende Übergangsmetalle machen natürliche Schichtsilicate prinzipiell unbrauchbar für High-End-Anwendungen. Vor allem für flexible, transparente Hochbarrierebeschichtungen stellen alle globularen Verunreinigungen Defekte dar, welche die Permeabilität signifikant ansteigen lassen, während die Farbe der Plättchen die optischen Eigenschaften beeinträchtigt.

Durch einen Langzeit-Tempersschritt ließ sich ein Natrium-Fluorohectorit überraschenderweise aktivieren. Es wurde neben größeren Plättchendurchmessern auch ein absolut phasenreines Material gewonnen, welches in deionisiertem Wasser auch spontan delaminierte. Ein derartiger milder anisotroper Top-Down Prozess wäre für die Generierung funktioneller Nanokomposite von größter Bedeutung. In einer detaillierten Studie wurden die strukturellen und physikochemischen Änderungen untersucht und erläutert.

Analysen hinsichtlich der chemischen Zusammensetzung ergaben eine Stöchiometrie nahe der Zielkomposition und eine Bestimmung der Kationenaustauschkapazität lieferte ebenfalls einen Wert nahe der Theorie. Beide Resultate zeigen stichhaltige Hinweise auf ein Material von hoher Reinheit aus.



Auch Röntgenpulverdiffraktometrie bestätigte ein einphasiges Material, das weder Reflexe einer Protoamphibol-Nebenphase noch einen amorphen Halo, die beide im nicht getemperten Hectorit auftraten, zeigte. Weiterhin ließen sich die Diffraktogramme indizieren und mit steigender Luftfeuchtigkeit war eine steigende Ordnung zu erkennen, wie sie bisher nur bei deutlich höher geladenen Schichtsilicaten aufgetreten war. Festkörper-NMR Untersuchungen ergaben, dass auch der amorphe Anteil, welcher durch Röntgenbeugung nur sehr schwer sichtbar war, durch das Langzeit-Tempern verschwand.

Neben strukturellen Analysen konnte darüber hinaus auch eine hervorragende Ladungshomogenität durch Interkalation von Alkylammoniumsalzen verschiedener Kettenlänge gezeigt werden. Die aus der kritischen Kettenlänge bestimmte Schichtladung stimmt hervorragend mit den vorangegangenen Bestimmungen der Kationenaustauschkapazität überein. Vorsichtiges Versetzen des Hectorits mit Wasser lieferte ein zunächst stufenförmiges Quellen des Zwischenschichtraums über das Doppelschichthydrat hinaus und endet schließlich in osmotischer Quellung und Delaminierung.

Mit Hilfe einer Kombination aus Schmelzsynthese und Langzeit-Tempern ließen sich somit homogene und hochreine Hectorit-Nanoplättchen generieren, welche sich hervorragend als Füllstoffe für effiziente Nanokomposite eignen.

## 4.2 *Deformationsmessungen an einzelnen Schichtsilicattaktoiden*

Basierend auf der Generierung hochgefüllter Nanokomposite ist der Beitrag eines einzelnen Schichtsilicattaktoids zur Versteifung von immenser Bedeutung, da dieser eine Abschätzung des Gesamtversteifungsgrades nach *Halpin Tsai*<sup>[28]</sup> ermöglicht. Der intrinsisch-anisotrope Charakter der Schichtsilicate erfordert jedoch eine richtungsabhängige mechanische Charakterisierung. Daher kann auch nicht auf Bulk-Methoden zurückgegriffen werden. Zu diesem Zweck wurde ein AFM-basierter nanoskaliger Biegetest einzelner Schichtsilicattaktoids entwickelt. Ziel war es, die Plättchen dickenabhängig mechanisch zu charakterisieren und einen Biegemodul zu extrahieren. Dabei wurde auf einen Na-Fluorohectorit zurückgegriffen.<sup>h</sup>

Zunächst wurde eine verdünnte Schichtsilicat-Suspension auf ein mikrostrukturiertes Siliciumsubstrat getropft und getrocknet. Die Probe wurde im Anschluss systematisch mit dem AFM abgerastert um Taktoide zu identifizieren, die für den nachfolgenden Biegetest geeignet waren und über einem Spalt lagen. Gleichzeitig konnte deren Höhe bestimmt werden. Anschließend wurde das Plättchen elastisch über ein „Force-Mapping“ deformiert, d.h. ein virtuelles Gitter mit mindestens 625 Knotenpunkten wurde über den Topographie-Scan gelegt und an jedem Knotenpunkt eine Kraft-Abstandskurve aufgenommen. Dabei ergaben sich drei unterschiedliche Arten von Kraft-Abstandskurven, die des eigentlichen Biegetests mit einer Plättchendeformation und die des nicht deformierbaren Substrats bzw. des auf dem Substrat liegenden Taktoids. Die detektierten Deformationen setzen sich über Linearkombination aus Verbiegung des Cantilevers und des Plättchens zusammen. Mit der Kenntnis der Federkonstante der Cantilevers lassen sich hieraus die Taktoidsteifigkeiten extrahieren.

Durch die Charakterisierung etlicher Taktoide unterschiedlicher Dicke konnte schließlich ein Biegemodul bestimmt werden ( $21 \pm 9$  GPa). Dieser ist geringer als die von konventionellen Glimmern in der Literatur vorkommende  $C_{33}$  Konstanten (50-70 GPa),<sup>[61,62]</sup> was auf die geringere Schichtladung und vielmehr auf die Gleitebenen durch die Hydratisierung der Na<sup>+</sup>-Zwischenschichtionen (bei Glimmern befindet sich nicht hydratisierbares K<sup>+</sup> in der Zwischen-

---

<sup>h</sup> Im Gegensatz zum im vorangegangenen Kapitel beschriebenen Hectorit wurde dieser nicht getempert, es lagen also in Suspension neben Monolagen auch bis zu 250 nm dicke Taktoide vor.

schicht) zurückzuführen ist. Taktoide mit hydratisierbaren Kationen in der Zwischenschicht sind demnach nur bedingt als mechanisch verstärkende Füllstoffe in extrusionsfähigen Kompositen einsetzbar.

### 4.3 *Mechanische Eigenschaften einer einzelnen Silicatlamelle*

Bei den in **Kapitel 4.2** durchgeführten Untersuchungen stellte sich heraus, dass Taktoide, welche dünner als 20 nm waren über eine sehr hohe Flexibilität verfügten und beim Trocknungsprozess über Kapillarkräfte in die Spalten des mikrostrukturierten Substrats gesaugt wurden und dadurch eine Messung unmöglich machten. Jedoch sind die mechanischen Eigenschaften innerhalb einer einzelnen Schichtsilicatlamelle beispielsweise für flexible Hochbarrierebeschichtungen von größter Bedeutung.

Aus diesem Grund wurde auch für sehr dünne Plättchen eine Methode entwickelt, die es erlaubt, selbst einzelne Lamellen mechanisch zu charakterisieren. Mittels Computersimulationen wurden kürzlich aus durch thermische Fluktuationen hervorgerufenen Wellungen die elastischen Eigenschaften einer einzelnen Schichtsilicatlamelle extrahiert.<sup>[44]</sup> Analog dazu ist es auch möglich, den in-plane Modul aus kontrollierten, erzwungenen Faltungen abzuleiten. Die generelle Idee hinter dieser Messtechnik, auch „Wrinkling“ genannt, ist die planare Kompression einer dünnen, steifen Schicht auf einem dickeren, gummiartigen Substrat. Dieses Prinzip ist etabliert in der Analyse dünner Filme<sup>[63,64]</sup> und konnte nun erstmals auf etwa 1 nm dicke Plättchen erfolgreich übertragen werden. Dabei wurde eine verdünnte Suspension aus delaminiertem Na-Fluorohectorit auf ein gestrecktes, hydrophilisiertes PDMS-Substrat aufgetropft, getrocknet und im Anschluss die Spannung kontrolliert gelöst. Im Gegensatz zu den in **Kapitel 4.2** beschriebenen Deformationsmessungen reichen bei dieser Messmethode kostengünstigere, rein topographische AFMs vollkommen für die nachfolgenden Untersuchungen aus. AFM Analysen ergaben, dass die Schichtsilicatlamellen deutlich und homogen gefaltet waren, während das PDMS-Substrat glatt blieb. Die Wellenlänge der Falten korreliert dabei mit dem in-plane Modul des Plättchens. Um die Datenevaluation zu beschleunigen, wurde ein Computerprogramm geschrieben, das die topographischen Informationen aus den AFM-Scans einliest und über eine 2D-Fourier Transformation die Wellenlänge extrahiert.

Die Messungen bestätigten die in **Kapitel 4.1** beschriebene Homogenität auch von mechanischer Seite, was auch an einem sehr scharfen Fourier-Peak erkennbar war. Der in-plane Modul einer einzelnen Schichtsilicatlamelle ( $142 \pm 17$  GPa) ist mit den Ergebnissen der oben

---

erwähnten Computersimulationen (230 GPa) durchaus vergleichbar. Auch der Unterschied zum experimentell bestimmten in-plane Modul von Glimmern ( $178.5 \pm 1.5$  GPa) wird klar, wenn man sich vor Augen führt, welche strukturellen Modelle zur Bestimmung herangezogen wurden: Glimmer wurde im Gegensatz zu den Faltungsuntersuchungen als Bulk-Material analysiert, d.h. sein in-plane Modul stellt eine Superposition aus Schichtsilicatlamellen und Zwischenschichtraum dar. Diese Sandwich-Konstruktion kann zu einer gewissen Materialversteifung führen, wie man sie aus dem Leichtbau kennt.

Durch ihre Schnelligkeit mit semiautomatisierter Datenevaluation, sowie durch ihre hohe Sensitivität und kostengünstige Analytik könnte die Wrinkling Methode zukünftig als Standardprozedur für Materialscreening Prozesse an Nanoplättchen herangezogen werden.

#### 4.4 *Lokal-aufgelöste mechanische Eigenschaften von Graphen, Graphenoxid und chemisch erzeugtem Graphen*

Um das Potential der in **Kapitel 4.3** vorgestellten Messtechnik voll auszuschöpfen wurden auch *per se* inhomogene Nanoplättchen auf mechanische Veränderungen auf lokaler Ebene untersucht. Dazu war vor allem Graphenoxid (GO) sehr interessant, da es neben seiner hohen materialwissenschaftlichen Bedeutung auch die Vorstufe zur (bis dato einzigen) Graphen-Massenproduktion darstellt. Aus diesem Grund wurde neben GO auch daraus hergestelltes Graphen und, als interner Standard, CVD Graphen charakterisiert.

GO wird unter harschen Bedingungen üblicherweise nach der Methode von Hummers & Offeman<sup>[65]</sup> aus Graphit hergestellt. Durch den heterogenen Charakter der Oxidation entsteht ein heterogenes Material mit inhomogen verteilten funktionellen Gruppen auf der Oberfläche der Nanoplättchen, welche als Defekte wirken.<sup>[66,67]</sup> Daher ist, um das mechanische Verhalten von GO und seiner reduzierten Spezies zu charakterisieren, eine Messtechnik nötig, welche den heterogenen Charakter dieser Materialien lokal auflösen kann.

Diese Möglichkeit bietet die Wrinkling-Methode. Analog zu dem in **Kapitel 4.3** beschriebenen Procedere wurden in dieser Arbeit GO Nanoplättchen auf hydrophilisiertem PDMS kontrolliert gefaltet. Um Ortsauflösung zu gewährleisten, wurden die über AFM erhaltenen topographischen Aufnahmen in kleinere quadratische Areale von ca. 1  $\mu\text{m}$  Seitenlänge zerlegt und diese separat einer 2D-Fourier Transformation unterzogen. Das Resultat war eine multimodale Wellenlängenverteilung, welche Aufschluss auf unterschiedlich stark oxidierte Domänen im sub- $\mu\text{m}$  Bereich gab. Diese blieben auch nach der Reduktion zu chemisch hergestelltem Graphen existent, wobei insgesamt eine Versteifung festzustellen war. Die gemittelten in-plane Module lagen bei  $0.23 \pm 0.07$  TPa für GO und beim etwa doppelten Wert für chemisch hergestelltes Graphen ( $0.48 \pm 0.06$  TPa). Lokale mechanische Kenndaten lagen jedoch teilweise bis zur Hälfte unterhalb des Mittelwertes. Hier wird die Notwendigkeit einer orts aufgelösten mechanischen Charakterisierung heterogener Nanomaterialien deutlich, da ein über eine größere Fläche gemittelter Wert, wie er etwa durch klassische Deformationsmessungen erzielt wird (vgl. **Kapitel 4.2**) zu einer dramatischen Überschätzung der Leistungsfähigkeit des Materials führen kann. Materialversagen wird in den schwächsten Domänen

stattfinden. Als interner Standard wurde homogenes CVD<sup>i</sup>-Graphen analysiert, was, ähnlich wie in **Kapitel 4.3** eine enge monomodale Wellenlängenverteilung und einen in-plane Modul in sehr guter Übereinstimmung mit dem Literaturwert für Graphen ( $1.0 \text{ TPa}^{[68]}$ ) lieferte ( $0.91 \pm 0.02 \text{ TPa}$ ). Durch die hohe Ortsauflösung konnten sogar geringe Anteile an Bilayers identifiziert werden, welche die doppelte Wellenlänge besitzen. Dies ist charakteristisch für diese Art der Graphenherstellung.

Demnach konnte gezeigt werden, dass die Wrinkling Methode neben den in **Kapitel 4.3** beschriebenen Vorzüge auch durch ihre hohe Ortsauflösung im sub- $\mu\text{m}$  Bereich zur lokalen mechanischen Charakterisierung heterogener Nanoplättchen und sogar zur effizienten Unterscheidung von Mono- und Bilayer Graphen herangezogen werden kann.

---

<sup>i</sup> Chemical Vapor Deposition

#### 4.5 *Flexible Nanokomposit-Beschichtung zur Anwendung in der Optoelektronik*

Der in **Kapitel 4.1** vorgestellte Na-Fluorohectorit eignet sich dank der spontanen Delaminierung in Wasser und der dadurch entstehenden enormen Aspektverhältnisse, seiner Homogenität und seiner hohen optischen Güte hervorragend als Füllstoff für Hoch-Gasbarrierebeschichtungen im Elektronik-Sektor. Laut *Cussler* Modell werden die Barrierevoraussetzungen für eine effiziente OLED/OPV-Einkapselung dadurch erfüllt (**Kapitel 3.3.1**). Auch die durch kontrolliertes Falten gezeigte Flexibilität der einzelnen Schichtsilicatlamellen (**Kapitel 4.3**) spricht für die im Bereich flexibler Elektronik nötige Biegsamkeit der entstehenden Nanokomposit-Beschichtungen.

Die wesentlichen Schritte in diesem Projekt waren zum einen durch gezielte Modifikation die Schichtsilicatplättchen mit einer hydrophoben Polymermatrix zu kompatibilisieren und zum anderen ein skalierbares Beschichtungsverfahren zu etablieren, das eine perfekte Textur garantiert. Diverse Vorversuche und frühere Arbeiten haben das große Potential des Rakeln als Beschichtungsmöglichkeit bereits gezeigt.<sup>[9]</sup>

Eine wässrige Hectoritsuspension musste zunächst mit einem simplen Kationenaustausch mit quaternisiertem DMAEMA (Dimethylaminoethylmethacrylat) organophilisiert und über Flockung in ein organisches, mit der Polymermatrix kompatibles, Lösungsmittel phasentransferiert werden. Bei den realisierten Füllstoffgehalten von mehr als 20 wt.% konnte nicht auf ein Lösungsmittel verzichtet werden, um mit der Viskosität in einem verarbeitbaren Rahmen zu bleiben. Eine Dispergierung in niedrigviskosen Monomeren mit anschließender Polymerisation der Beschichtung war hauptsächlich aus dem Grund nicht möglich, als eine unkontrollierte Vernetzung zum einen eine erhebliche Versprödung des Nanokomposits und eine unnötige Vergrößerung des freien Volumens bewirkt hätte. Ausdampfende Monomerreste würden darüber hinaus der Barrierewirkung durch etwaige Blasenbildung schaden.

Die große Herausforderung lag hierbei bei der Entfernung des Lösungsmittels selbst, da diese durch die gute Barrierewirkung des Schichtsilicatfüllstoffs erheblich erschwert ist. Als Lö-



sungsweg wurden kommerzielle Polyurethan-Precursorpolymere (Desmophen® 670 BA,<sup>j</sup> Desmodur® N 3600<sup>k</sup>) mit geeigneter Topfzeit<sup>l</sup> herangezogen, welche erst nach dem Trocknen vernetzten und in einem gelartigen Zwischenzustand ein Entfernen des Lösungsmittels ohne Blasenbildung ermöglichten. Außerdem brachten sie die für die Flexibilität nötigen mechanischen Eigenschaften mit sich.

Die gehärteten Beschichtungen zeichneten sich durch eine hohe Transparenz aus, was durch Schärfe- und Trübungsmessungen quantifiziert werden konnte. Über den gesamten Bereich des sichtbaren Lichtes konnten Transmissionswerte jenseits von 85 % bestimmt werden. Weiterhin wurden die mechanischen Eigenschaften der Nanokompositbeschichtung im Vergleich zum reinen Polymer um einen Faktor von 10 gesteigert.

Die wichtigsten Erkenntnisse lieferten jedoch Gasbarrieremessungen an den PU-Schichtsilicat-Nanokompositbeschichtungen. Die Sauerstofftransmissionsanalysen erfolgten durch die Firma Mocon, USA (SuperOxTran,<sup>m</sup> unteres Messlimit  $0.0005 \text{ cm}^3 \text{ m}^{-2} \text{ day}^{-1} \text{ bar}^{-1}$ ) bei Umgebungstemperatur und Luftfeuchten von jeweils 0 % r.h. und 50 % r.h. und ergaben mit  $3.7 \cdot 10^{-3} \text{ cm}^3 \text{ m}^{-2} \text{ day}^{-1} \text{ bar}^{-1}$  und  $1.0 \cdot 10^{-2} \text{ cm}^3 \text{ m}^{-2} \text{ day}^{-1} \text{ bar}^{-1}$  die bis dato niedrigsten gemessenen Werte in der Literatur. Wasserdampftransmissionsraten unterhalb der Nachweisgrenze des verfügbaren Gerätes im Hause ( $< 0.05 \text{ g m}^{-2} \text{ day}^{-1}$ ) bestätigten die geringe Anfälligkeit der Nanokompositbeschichtung gegenüber Luftfeuchte. Kombiniert mit der herausragenden Transparenz und der hohen Flexibilität haben diese Nanokompositbeschichtungen auf der Basis kommerziell erhältlicher Polymere großes Potential, als Verkapselungsmaterialien für flexible Optoelektronik zu finden.

---

<sup>j</sup> Schwach verzweigter, hydroxylgruppenhaltiger Polyester, Bayer MaterialScience AG.

<sup>k</sup> Aliphatisches Polyisocyanat, Bayer MaterialScience AG.

<sup>l</sup> Zeitfenster zur Verarbeitung reaktiver Materialien.

<sup>m</sup> Markteinführung 2013 geplant. Alle anderen kommerziell verfügbaren Geräte waren nicht sensitiv genug.

#### 4.6 *Polarisierte Emission durch templatgesteuerte Quasi-Epitaxie*

Aufgrund der Ladungshomogenität des in **Kapitel 4.1** beschriebenen Hectorits lässt sich dieser auch als Templat zur quasi-epitaktischen Strukturierung von TM-Komplexen verwenden.

Wie in **Kapitel 3.3.2** angedeutet, trägt eine Strukturierung der Emitttermoleküle entscheidend zur Steigerung der OLED Effizienz bei. Für TM-Komplexe, die mittlerweile als leistungsfähigste OLED Emmitter in den Fokus gerückt sind, gab es bis dato noch keine geeignete Strukturierungsmöglichkeit. Aus theoretischen Studien von *Breu et al.*<sup>[57-59]</sup> ist jedoch ersichtlich, dass es mit homogen geladenen Schichtsilicaten möglich ist, geladene TM-Komplexe äquidistant und orientiert in den Zwischenschichtraum zu interkalieren. Weiterhin zeigten erste Experimente in der Pulverdiffraktion eine zusätzliche Ordnung der Komplexe in der Zwischenschicht.<sup>[69]</sup>

Basierend auf diesen Erkenntnissen wurde an dem Modellsystem  $[\text{Ru}(\text{bpy})_3]^{2+}$  zum einen eine einheitliche Orientierung der TM-Komplexe zum ersten Mal experimentell nachgewiesen und die Emissionseigenschaften näher analysiert. Bei  $[\text{Ru}(\text{bpy})_3]^{2+}$  handelt es sich um einen symmetrischen oktaedrischen Komplex mit je einer  $C_3$  Schraubenachse senkrecht zu zwei parallelen Dreiecksflächen.

Über einen hydrothermalen Kationenaustausch wurde  $[\text{Ru}(\text{bpy})_3]^{2+}$  interkaliert, was durch eine Aufweitung des Zwischenschichtraums im Pulverdiffraktogramm verfolgt werden konnte. Weiterhin wurde durch die Wahl eines hohen Elektrolythintergrundes eine in den **Kapiteln 4.1, 4.3** und **4.5** beschriebene Delaminierung vermieden wodurch einige bis zu ca. 300  $\mu\text{m}$  große und etwa 20  $\mu\text{m}$  dicke Plättchen erhalten wurden. Diese Partikelgröße war für eine erfolgreiche Justage am Spektrometer nötig. Ein starkes Indiz für die gleichmäßige Orientierung der Komplexe lieferte bereits die röntgenographische Analyse. Der ermittelte Schichtabstand von 17.7 Å setzt sich aus der Höhe einer Silicatlamelle (9.6 Å) und der Höhe des  $[\text{Ru}(\text{bpy})_3]^{2+}$  Komplexes in der Zwischenschicht zusammen. Die resultierende Distanz von 8.1 Å entspricht dabei fast exakt der Höhe des Komplexes entlang seiner  $C_3$  Schraubenachse (8.15 Å).

Bei den nachfolgenden Emissionsstudien wurden die Plättchen und, als Referenz, ein

$[\text{Ru}(\text{bpy})_3](\text{PF}_6)_2$  Einkristall richtungsabhängig vermessen. Ein konfokaler Aufbau des Spektrometers sorgte dabei für eine hohe Ortsauflösung im Mikrometerbereich. Studien an einem  $[\text{Ru}(\text{bpy})_3](\text{PF}_6)_2$  Einkristall von *Yersin et al.*<sup>[70]</sup> zeigten eine richtungsabhängige polarisierte Emission senkrecht zur  $C_3$  Schraubenachse, welche entlang der  $c$ -Achse des Kristallsystems verläuft. Diese konnte bei der Messung in dieser Arbeit auch reproduziert werden. Der Polarisationsgrad lag bei 0.77, was eine sehr einheitliche, für einen Einkristall typische, Orientierung der Komplexe widerspiegelt. Die Plättchenanalysen lieferten entlang der Kante ein identisches Emissionsverhalten mit einem Polarisierungsgrad von 0.35. Die  $[\text{Ru}(\text{bpy})_3]^{2+}$  Komplexe waren auf der Schichtsilicatoberfläche demnach mit der  $C_3$  Schraubenachse entlang der Stapelachse, also senkrecht zu den Plättchenbasalflächen orientiert. Dies stimmte mit den vorangegangenen röntgenographischen Analysen und Simulationen überein. Der geringere Polarisationsgrad ist hauptsächlich auf die ausgefranzten Kanten der Plättchen zurückzuführen, die durch die hydrothermale Behandlung entstanden sind.

Kombiniert mit einem ähnlichen wie in **Kapitel 4.5** beschriebenen Texturierungsverfahren können nun mit orientierten Komplexen belegte Schichtsilicatmonolagen schnell und skalierbar texturiert werden. Der Polarisierungsgrad dürfte erwartungsgemäß höher als beim Plättchen liegen, da bereits erwähnte Kanteneffekte ausgeschlossen werden können. Dadurch eröffnen sich neuartige Möglichkeiten zur Generierung von leistungsfähigen, robusten und dennoch flexiblen, polarisiert emittierenden OLEDs.

## 5 Verwendete Literatur

- [1] [http://www.heliatek.com/wp-content/uploads/2011/12/111205\\_PI\\_Heliatek-mit-Rekordzelle-fuer-organische-Photovoltaik\\_DE.pdf](http://www.heliatek.com/wp-content/uploads/2011/12/111205_PI_Heliatek-mit-Rekordzelle-fuer-organische-Photovoltaik_DE.pdf) **11-10-2012**
- [2] L. A. Goettler, K. Y. Lee, H. Thakkar, *Polym. Rev.* **2007**, *47*, 291-317.
- [3] Z. Y. Tang, N. A. Kotov, S. Magonov, B. Ozturk, *Nat. Mater.* **2003**, *2*, 413-418.
- [4] P. Podsiadlo, A. K. Kaushik, E. M. Arruda, A. M. Waas, B. S. Shim, J. D. Xu, H. Nandivada, B. G. Pumplun, J. Lahann, A. Ramamoorthy, N. A. Kotov, *Science* **2007**, *318*, 80-83.
- [5] M. Kurian, M. E. Galvin, P. E. Trapa, D. R. Sadoway, A. M. Mayes, *Electrochim. Acta* **2005**, *50*, 2125-2134.
- [6] M. R. Schütz, H. Kalo, T. Lunkenbein, J. Breu, C. A. Wilkie, *Polymer* **2011**, *52*, 3288-3294.
- [7] M. R. Schütz, H. Kalo, T. Lunkenbein, A. H. Gröschel, A. H. E. Müller, C. A. Wilkie, J. Breu, *J. Mater. Chem.* **2011**, *21*, 12110-12116.
- [8] M. W. Möller, T. Lunkenbein, H. Kalo, M. Schieder, D. A. Kunz, J. Breu, *Adv. Mater.* **2010**, *22*, 5245-5249.
- [9] M. W. Möller, D. A. Kunz, T. Lunkenbein, S. Sommer, A. Nennemann, J. Breu, *Adv. Mater.* **2012**, *24*, 2142-2147.
- [10] D. A. Laird, *Appl. Clay Sci.* **2006**, *34*, 74-87.
- [11] E. Ferrage, B. Lanson, B. A. Sakharov, N. Geoffroy, E. Jacquot, V. A. Drits, *Amer. Mineral.* **2007**, *92*, 1731-1743.
- [12] J. Breu, W. Seidl, J. Senker, *Z. Anorg. Allg. Chem.* **2004**, 80-90.
- [13] H. Kalo, W. Milius, J. Breu, *RSC Adv.* **2012**, *2*, 8452-8459.
- [14] M. W. Möller, U. A. Handge, D. A. Kunz, T. Lunkenbein, V. Altstädt, J. Breu, *Acs Nano* **2010**, *4*, 717-724.
- [15] J. E. F. C. Gardolinski, G. Lagaly, *Clay Miner.* **2005**, *40*, 547-556.
- [16] G. Lagaly, K. Jasmund, *Tonminerale und Tone*, Steinkopf Verlag, Heidelberg **1993**.
- [17] G. Lagaly, O. Schulz, R. Zimehl, *Dispersionen und Emulsionen*, Steinkopff Verlag Darmstadt, **1997**.
- [18] J. T. Klopogge, S. Komarneni, J. E. Amonette, *Clays Clay Miner.* **1999**, *47*, 529-554.

- 
- [19] R. M. Barrer, D. L. Jones, *Journal of the Chemical Society A -Inorganic Physical Theoretical* **1970**, 1531-&.
- [20] E. Balnois, S. Durand-Vidal, P. Levitz, *Langmuir* **2003**, *19*, 6633-6637.
- [21] H. Tateyama, S. Nishimura, K. Tsunematsu, K. Jinnai, Y. Adachi, M. Kimura, *Clays Clay Miner.* **1992**, *40*, 180-185.
- [22] J. Breu, W. Seidl, A. J. Stoll, K. G. Lange, T. U. Probst, *Chem. Mater.* **2001**, *13*, 4213-4220.
- [23] H. Kalo, M. W. Möller, M. Ziadeh, D. Dolejs, J. Breu, *Appl. Clay Sci.* **2010**, *48*, 39-45.
- [24] H. Kalo, M. W. Möller, D. A. Kunz, J. Breu, *Nanoscale* **2012**, *4*, 5633-5639.
- [25] H. Kalo, W. Milius, M. Bräu, J. Breu, *J. Solid State Chem.* **2013**, *198*, 57-64.
- [26] L. J. Bonderer, A. R. Studart, L. J. Gauckler, *Science* **2008**, *319*, 1069-1073.
- [27] M. W. Möller, T. Lunkenbein, H. Kalo, M. Schieder, D. A. Kunz, J. Breu, *Adv. Mater.* **2010**, *22*, 5245-5249.
- [28] J. C. Halpin, J. L. Kardos, *Polym. Eng. Sci.* **1976**, *16*, 344-352.
- [29] *Fundamentals of Crystallography*, (Ed.: C. Giacovazzo) Oxford University Press, New York **1992**, pp. 599-643.
- [30] L. E. McNeil, M. Grimsditch, *J. Phys. :Condens. Mat.* **1993**, *5*, 1681-1690.
- [31] B. Cappella, G. Dietler, *Surface Science Reports* **1999**, *34*, 1-104.
- [32] Bosio, V., Dissertation thesis, Universität Potsdam, **2003**.
- [33] B. Bhushan, H. Fuchs, S. Hosaka, *Applied Scanning Probe Methods*, Springer Verlag, Heidelberg **2004**.
- [34] R. Garcia, R. Perez, *Surface Science Reports* **2002**, *47*, 197-301.
- [35] M. Tscherner, C. Konrad, M. Bizzarri, M. Suppan, M. Cajlakovic, F. Stelzer, V. Ribitsch, *unpublished* **2011**.
- [36] J. S. Lewis, M. S. Weaver, *IEEE J. Sel. Top. Quant.* **2004**, *10*, 45-57.
- [37] G. Choudalakis, A. D. Gotsis, *Curr. Opin. Colloid. In.* **2012**, *17*, 132-140.
- [38] L. E. Nielsen, *J. Macromol. Sci. A* **1967**, *1*, 929-942.
- [39] W. T. Brydges, S. T. Gulati, G. Baum, *J. Mater. Sci.* **1975**, *10*, 2044-2049.

- [40] E. L. Cussler, S. E. Hughes, W. J. Ward, R. Aris, *J. Membrane Sci.* **1988**, *38*, 161-174.
- [41] G. H. Fredrickson, J. Bicerano, *J. Chem. Phys.* **1999**, *110*, 2181-2188.
- [42] A. A. Gusev, H. R. Lusti, *Adv. Mater.* **2001**, *13*, 1641-1643.
- [43] H. R. Lusti, M. A. Osman, V. Mittal, *Macromol. Rapid Commun.* **2004**, *25*, 1145-1149.
- [44] J. L. Suter, P. V. Coveney, H. C. Greenwell, M. A. Thyveetil, *J. Phys. Chem. C* **2007**, *111*, 8248-8259.
- [45] M. Flämmich, J. Frischeisen, D. S. Setz, D. Michaelis, B. C. Krummacher, T. D. Schmidt, W. Brütting, N. Danz, *Org. Electron.* **2011**, *12*, 1663-1668.
- [46] J. Frischeisen, D. Yokoyama, A. Endo, C. Adachi, W. Brütting, *Org. Electron.* **2011**, *12*, 809-817.
- [47] T. D. Schmidt, D. S. Setz, M. Flämmich, J. Frischeisen, D. Michaelis, B. C. Krummacher, N. Danz, W. Brütting, *Appl. Phys. Lett.* **2011**, *99*.
- [48] M. Pfeiffer, K. Leo, X. Zhou, J. S. Huang, M. Hofmann, A. Werner, J. Blochwitz-Nimoth, *Org. Electron.* **2003**, *4*, 89-103.
- [49] M. A. Baldo, D. F. O'Brien, Y. You, A. Shoustikov, S. Sibley, M. E. Thompson, S. R. Forrest, *Nature* **1998**, *395*, 151-154.
- [50] H. Yersin, A. F. Rausch, R. Czerwieniec, T. Hofbeck, T. Fischer, *Coord. Chem. Rev.* **2011**, *255*, 2622-2652.
- [51] D. Yokoyama, *J. Mater. Chem.* **2011**, *21*, 19187-19202.
- [52] D. Neher, *Macromol. Rapid Commun.* **2001**, *22*, 1366-1385.
- [53] P. Andersson, M. Berggren, T. Kugler, *Appl. Phys. Lett.* **2003**, *83*, 1307-1309.
- [54] M. Hamaguchi, K. Yoshino, *Appl. Phys. Lett.* **1995**, *67*, 3381-3383.
- [55] J. Matsui, S. Yoshida, T. Mikayama, A. Aoki, T. Miyashita, *Langmuir* **2005**, *21*, 5343-5348.
- [56] A. Bolognesi, C. Botta, D. Facchinetti, M. Jandke, K. Kreger, P. Strohriegl, A. Relini, R. Rolandi, S. Blumstengel, *Adv. Mater.* **2001**, *13*, 1072-1075.
- [57] J. Breu, C. R. A. Catlow, *Inorg. Chem.* **1995**, *34*, 4504-4510.
- [58] J. Breu, N. Raj, C. R. A. Catlow, *J. Chem. Soc. Dalton* **1999**, 835-845.
- [59] J. Breu, H. Domel, A. Stoll, *Eur. J. Inorg. Chem.* **2000**, 2401-2408.

- 
- [60] G. A. Ozin, A. C. Arsenault, L. Cademartiri, *Nanochemistry: A Chemical Approach to Nanomaterials*, 2nd ed. RSC Publ., Cambridge **2009**.
- [61] D. R. Collins, C. R. A. Catlow, *Am. Mineral.* **1992**, *77*, 1172-1181.
- [62] D. R. Collins, W. G. Stirling, C. R. A. Catlow, G. Rowbotham, *Phys. Chem. Miner.* **1993**, *19*, 520-527.
- [63] C. M. Stafford, C. Harrison, K. L. Beers, A. Karim, E. J. Amis, M. R. Vanlandingham, H. C. Kim, W. Volksen, R. D. Miller, E. E. Simonyi, *Nat. Mater.* **2004**, *3*, 545-550.
- [64] N. Bowden, S. Brittain, A. G. Evans, J. W. Hutchinson, G. M. Whitesides, *Nature* **1998**, *393*, 146-149.
- [65] W. S. Hummers, R. E. Offeman, *J. Am. Chem. Soc.* **1958**, *80*, 1339.
- [66] U. Hofmann, R. Holst, *Ber. Dtsch. Chem. Ges.* **1939**, *72*, 754-771.
- [67] A. Lerf, H. Y. He, M. Forster, J. Klinowski, *J. Phys. Chem. B* **1998**, *102*, 4477-4482.
- [68] C. Lee, X. D. Wei, J. W. Kysar, J. Hone, *Science* **2008**, *321*, 385-388.
- [69] J. Breu, A. Stoll, K. G. Lange, T. Probst, *Phys. Chem. Chem. Phys.* **2001**, *3*, 1232-1235.
- [70] H. Yersin, E. Gallhuber, A. Vogler, H. Kunkely, *J. Am. Chem. Soc.* **1983**, *105*, 4155-4156.

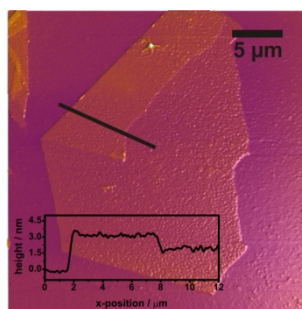
## 6 Ergebnisse

### 6.1 Hochreiner Natrium-Fluorohectorit

Matthias Stöter<sup>†,§</sup>, Daniel A. Kunz<sup>†,§</sup>, Marko Schmidt<sup>‡</sup>, Dunja Hirsemann<sup>†</sup>, Hussein Kalo<sup>†</sup>, Bernd Putz<sup>†</sup>, Jürgen Senker<sup>‡</sup>, and Josef Breu<sup>†,\*</sup>

#### Nanoplatelets of Sodium Hectorite Showing Aspect Ratios of $\approx 20000$ and Superior Purity

Erschienen in: *Langmuir* **2013**, 29, 1280-1285. Reprinted with permission, Copyright (2013) American Chemical Society.



<sup>†</sup> Lehrstuhl für Anorganische Chemie I, Universität Bayreuth, 95447 Bayreuth, Deutschland

<sup>‡</sup> Lehrstuhl für Anorganische Chemie III, Universität Bayreuth, 95447 Bayreuth, Deutschland

<sup>§</sup> Gleicher Beitrag zu je 35 %

\* josef.breu@uni-bayreuth.de

#### Darstellung des Eigenanteils:

Bei dieser Publikation handelt es sich um ein lehrstuhlinternes Gemeinschaftsprojekt zur Optimierung der Eigenschaften der im Hause hergestellten Schichtsilicate. Ich koordinierte zusammen mit Prof. Dr. *Josef Breu* das Projekt und führte grundlegende Experimente durch. *Matthias Stöter* war für den Kationenaustausch mit nachfolgender Analytik verantwortlich. *Bernd Putz* und Dr. *Hussein Kalo* oblagen die Temperversuche. Die Festkörper-NMR-Messungen wurden von *Marko Schmidt* und Dr. *Dunja Hirsemann* mit Prof. Dr. *Jürgen Senker* durchgeführt. Verfasst wurde diese Publikation hauptsächlich von Prof. Dr. *Josef Breu*, *Matthias Stöter* und mir. *Matthias Stöter* und ich haben zu einem Anteil von je 35 % beigetragen.



### 6.1.1 Nanoplatelets of Sodium Hectorite Showing Aspect Ratios of $\approx 20000$ and Superior Purity

# Langmuir

Article


pubs.acs.org/Langmuir

## Nanoplatelets of Sodium Hectorite Showing Aspect Ratios of $\approx 20\,000$ and Superior Purity

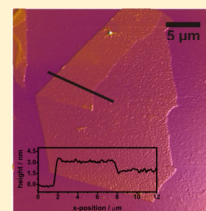
Matthias Stöter,<sup>†,§</sup> Daniel A. Kunz,<sup>†,§</sup> Marko Schmidt,<sup>‡</sup> Dunja Hirsemann,<sup>†</sup> Hussein Kalo,<sup>†</sup> Bernd Putz,<sup>†</sup> Jürgen Senker,<sup>‡</sup> and Josef Breu<sup>\*,†</sup>

<sup>†</sup>Lehrstuhl für Anorganische Chemie I, Universität Bayreuth, D-95440 Bayreuth, Germany

<sup>‡</sup>Lehrstuhl für Anorganische Chemie III, Universität Bayreuth, D-95440 Bayreuth, Germany

 Supporting Information

**ABSTRACT:** Applying a combination of melt synthesis followed by long-term annealing a fluorohectorite is obtained which is unique with respect to homogeneity, purity, and particle size. Counterintuitively, the hectorite undergoes a disorder-to-order transition upon swelling to the level of the bilayer hydrate. Alkylammonium-exchanged samples show at any chain length only a single basal spacing corroborating a nicely homogeneous layer charge density. Its intracrystalline reactivity improves greatly upon annealing, making it capable to spontaneously and completely disintegrate into single clay lamellae of 1 nm thickness. Realizing exceptional aspect ratios of around 20 000 upon delamination, this synthetic clay will offer unprecedented potential as functional filler in highly transparent nanocomposites with superior gas barrier and mechanical properties.



### ■ INTRODUCTION

Plenty of polymer nanocomposites contain platy nanofillers like clays as functional compounds for improvement in gas barrier activity, fire retardancy, and mechanical properties.<sup>1–5</sup> In order to exploit the full potential of these composite materials, it is especially important to optimize the performance of the clay filler, which in turn is mainly determined by its aspect ratio (ratio of particle size and height), textured orientation, mechanical properties, and compatibilization with the polymeric matrix. While texture and aspect ratio are strongly related to the filler's lateral extension, mechanical properties and interface management are crucially dependent on the homogeneity of the charge density of the clay layers which correlates with a uniform intracrystalline reactivity. Applicability of commercially available, natural swelling clays like montmorillonite is severely restricted by both small particle size (<200 nm) and a heterogeneous charge density. Additionally, all natural clays suffer from accessory minerals and poor optical quality due to colored transition metal ions incorporated into the structure. The latter drawbacks are particularly detrimental when aiming at flexible, transparent high-barrier films for optoelectronic packaging. Any globular impurities will act as defects and increase permeability significantly while the color reduces transmission.

Over the past decade we have developed melt synthesis protocols that yield platelets with particularly large lateral extensions and homogeneous charge density.<sup>6–8</sup> The intracrystalline reactivity was found to vary with charge<sup>9,10</sup> and the type of interlayer cation.<sup>11</sup> For instance, while Na-hectorite as obtained by melt synthesis<sup>7</sup> requires large shear forces in order to be exfoliated into thinner platelets,<sup>12</sup> Li-hectorite so far was the only material that spontaneously delaminates into single lamellae of 1 nm thickness by osmotic swelling when immersed

in deionized water.<sup>8</sup> Since in this gentle anisotropic top down process the particle diameter is preserved, such a fully delaminated material exhibits the maximum aspect ratio that may be obtained with given initial lateral dimension of the platelets which is determined by the synthesis conditions. While the Li-hectorite shows huge aspect ratios,<sup>8</sup> it lacks phase purity and needs to be purified before being applied as filler in nanocomposite films.<sup>3,13</sup>

Clearly, for high-barrier applications suitable for flexible optoelectronic packaging there still is a need for perfectly phase pure, transparent clay materials with huge lateral dimensions that spontaneously delaminate into nanoplatelets with aspect ratios >10 000.

Here we show that, surprisingly, a melt synthesized Na-fluorohectorite of medium charge density may be greatly activated in respect to swelling by long-term annealing. While the pristine material, as mentioned above, cannot be delaminated even when applying strong shearing forces, e.g. applying a ball mill, the annealed material spontaneously and completely delaminates. Since by annealing concomitantly the lateral extension of the material is increased, hydrous suspensions of nanoplatelets of huge aspect ratios are obtained. In this paper, changes in respect to structure, phase, and chemical composition are revealed and related to rationalizing the observed unexpected activation.

### ■ RESULTS AND DISCUSSION

**Synthesis of Na<sub>0.5</sub>-Hec.** Na<sub>0.5</sub>-fluorohectorite with nominal composition of [Na<sub>0.5</sub>]<sup>inter</sup>[Mg<sub>2.5</sub>Li<sub>0.5</sub>]<sup>oct</sup>[Si<sub>4</sub>]<sup>tet</sup>O<sub>10</sub>F<sub>2</sub> (Na<sub>0.5</sub>-

Received: November 8, 2012

Revised: December 14, 2012

Published: January 3, 2013

Hec) was synthesized by melt synthesis in a gastight molybdenum crucible according to an already published procedure.<sup>7</sup> 45 g of the as-synthesized dry Na<sub>0.5</sub>-Hec was milled with a planetary ball mill (Retsch PM 100) for 20 min at 250 rpm using a ZrO<sub>2</sub> grinding beaker with 15 ZrO<sub>2</sub> balls. By milling, the particle (aggregates) size was reduced to less than 250 μm. In order to remove the adsorbed humidity, the material was first dried overnight at 150 °C in a drying chamber, then dried under vacuum (10<sup>-2</sup> mbar) at 250 °C for 14 h to remove traces of water, and finally was stored in a glovebox. 35 g of the milled Na<sub>0.5</sub>-Hec was filled into a molybdenum crucible and then sealed under high vacuum (10<sup>-5</sup> mbar) with a molybdenum cap by a high-frequency furnace. In order to prevent the molybdenum from oxidation during the annealing procedure, the crucible was enclosed under vacuum into a quartz glass tube and heated in a chamber furnace (Thermal Technology) at 1045 °C (heating rate 2 °C/min). After annealing for 6 weeks the oven was switched off, and the sample was kept in the oven until the crucible cooled down to room temperature. Analysis by inductively coupled-plasma atomic emission spectroscopy (ICP-AES) and wavelength dispersive X-ray spectroscopy (WDX) (Supporting Information) confirmed that for the annealed material the compositions of both the bulk and individual clay tactoids were close to the target composition, [Na<sub>0.5</sub>]<sup>inter</sup>[Mg<sub>2.5</sub>Li<sub>0.5</sub>]<sup>oct</sup>[Si<sub>4</sub>]<sup>tet</sup>O<sub>10</sub>F<sub>2</sub> (Na<sub>0.5</sub>-Hec,  $x = 0.5$  per formula unit (pfu)). Since WDX is incapable to determine Li, the analytical results were converted into the formula by normalizing to Si = 4 and gave [Na<sub>0.48(1)</sub>]<sup>inter</sup>[Mg<sub>2.57(3)</sub>Li<sub>x</sub>]<sup>oct</sup>[Si<sub>4</sub>] for the composition of cations. Additionally, Li and Na contents were determined by ICP-AES, and the Li content was derived by normalizing to the Na content found with WDX. This way the cation composition was found to be [Na<sub>0.48</sub>]<sup>inter</sup>[Mg<sub>2.57(3)</sub>Li<sub>0.47</sub>]<sup>oct</sup>[Si<sub>4</sub>]. The cation exchange capacity (CEC) was determined to be 126 mequiv/100 g with the barium method and 125 mequiv/100 g with the [Cu(trien)]<sup>2+</sup> method (see Supporting Information for details), which again is very close to the value expected for the target composition (130 mequiv/100 g). Usually for synthetic clays deviations from expectations are found to be much larger due to impurities. For instance, the CEC of the pristine sample is much lower (113 mequiv/100 g determined with the [Cu(trien)]<sup>2+</sup> method). Thus, the good agreement is a first indication for a high-purity material. The small residual difference is most likely due to the still limited size of the tactoids since in melt synthesis some sodium cations are consumed to neutralize tangling bonds at the edges.

Powder X-ray diffraction (PXRD) analysis confirmed a single phase material (Figure 2) while the pristine material, as obtained in the initial melt synthesis, by contrast contained small but detectable amounts of protoamphibole as side phase (Figure 1).<sup>7</sup>

Please note that PXRD is rather insensitive to amorphous materials that only show up in a broad background around 18°–28° 2θ. It is also obvious that by annealing the PXRD pattern develops additional peaks as compared to the pristine material. While the pristine material is almost turbostratically disordered,<sup>14</sup> these extra features are already pinpointing to a less disordered material with fewer stacking faults. The much improved stacking order becomes even more obvious upon hydration of the material. At relative humidities (RH) of 0%, 43%, and 93% well-defined hydration states of zero (0 WL), one (1 WL), and two layer hydrate (2 WL) are obtained. For

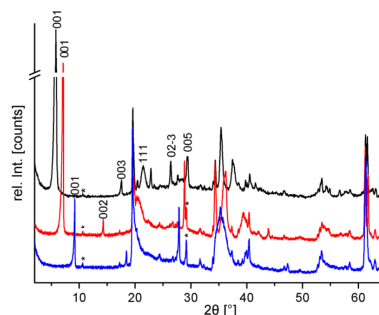


**Figure 1.** PXRD profiles of the nonannealed, pristine Na<sub>0.5</sub>-Hec at different relative humidities (RH): (a) sample heated at 120 °C, resulting in a nonhydrated state (0% RH, 0 WL); (b) sample equilibrated at 43% RH, resulting in a one layer hydrate (1 WL); (c) swelling with water ( $m(\text{water}):m(\text{pristine Na}_{0.5}\text{-Hec}) = 700:1$ ), resulting in a two-layer hydrate (2 WL). Detectable reflexes of the protoamphibole side phase are marked with an asterisk.

all hydration states rational 00l series are observed. No signs for interstratifications of differently hydrated interlayers within the same stack were seen, and this unusual uniform intracrystalline reactivity in turn again indicates a superb homogeneous charge density.

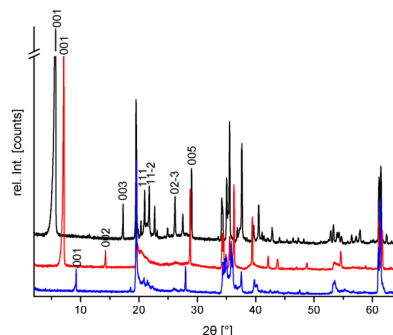


**Figure 2.** PXRD profiles of annealed Na<sub>0.5</sub>-Hec at different relative humidities (RH): (a) sample heated at 120 °C, resulting in a nonhydrated state (0% RH, 0 WL); (b) sample equilibrated at 43% RH, resulting in a one-layer hydrate (1 WL); (c) equilibrated at 93% RH, resulting in a two-layer hydrate (2 WL).

The nonhydrated structure (0 water layer = 0 WL) of Na<sub>0.5</sub>-Hec shows a *d*-spacing of 9.6 Å with a nearly perfect rational 00l series (coefficient of variation = 0.16%; see Supporting Information for details). Although the λ-shaped 11/02-band at around 20°2θ, indicates stacking faults, some peak maxima are visible and the PXRD pattern of the 0 WL can be indexed with a unit cell of  $a = 5.25$  Å,  $b = 9.08$  Å,  $c = 9.82$  Å, and  $\beta = 94.5^\circ$ . The *d*-spacing increases uniformly to 12.4 Å (coefficient of variation = 0.19%) at 43% RH. The PXRD pattern of the 1 WL can be indexed with a unit cell of  $a = 5.24$  Å,  $b = 9.09$  Å,  $c = 12.47$  Å, and  $\beta = 96.0^\circ$ . Finally swelling at a higher relative

## Langmuir

## Article

humidity of 93% yields the 2 WL with  $d_{001} = 15.5 \text{ \AA}$  (coefficient of variation = 0.21%). As seen before for much higher charged swelling clays, e.g.,  $[\text{Na}_{0.7}]^{\text{inter}}[\text{Mg}_{2.3}\text{Li}_{0.7}]^{\text{oct}}[\text{Si}_4]_{\text{tet}}\text{O}_{10}\text{F}_2$ ,<sup>9</sup> for the 2 WL phase the number and the intensity of peaks in the range of the 11/02-band increased significantly. This is related to a disorder-to-order transition which is mediated by specific well-defined hydrogen-bonding networks to basal oxygens by the water molecules involved in octahedral coordination of  $\text{Na}^+$ . Evidently, the occurrence of this disorder-to-order transition is not crucially dependent on high charge densities. The PXRD pattern of the 2 WL can be indexed with the following unit cell:  $a = 5.248 \text{ \AA}$ ,  $b = 9.093 \text{ \AA}$ ,  $c = 15.483 \text{ \AA}$ , and  $\beta = 96.67^\circ$ .

Since PXRD is insensitive to amorphous phases, additionally, the purity of the material was investigated by solid-state NMR spectroscopy. Comparing the  $^{19}\text{F}$  MAS spectra of the pristine material and the annealed  $\text{Na}_{0.5}\text{-Hec}$  (Figure 3), clear

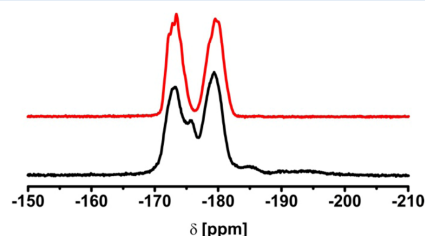


Figure 3.  $^{19}\text{F}$ -MAS spectra of  $\text{Na}_{0.5}\text{-Hec}$  (red line) in comparison with the nonannealed sample (black line).

differences in the environment of the  $^{19}\text{F}$  nuclei become evident. Two main types of fluorine sites with shifts at about  $-172$  and  $-180$  ppm were found. This is in good agreement with shifts reported in the literature for a hectorite of similar composition at  $-176.2$  and  $-182.8$  ppm, which were assigned to  $\text{Mg-Mg-Mg}$  and  $\text{Mg-Mg-Li}$  environments, respectively.<sup>15</sup> In the case of the pristine sample, however, an additional peak arises at ca.  $-175$  ppm. This signal cannot be attributed to protoamphibole, which would be expected at about  $-169$  ppm (Figure S1). Therefore, we propose that the pristine material, in addition to protoamphibole, contains a second, amorphous impurity phase. Clearly, this fluorine containing glass disappears during annealing, most likely by crystallization into Na-hectorite.

The high purity and homogeneity of this single phase material also became apparent applying the layer charge density determination by the alkylammonium method, which is demonstrated in Figure 4. Upon exchange of the interlayer  $\text{Na}^+$  ions with alkylammonium ions of increasing chain length ( $[\text{C}_n\text{H}_{2n+1}\text{NH}_3]^+$ ), the homogeneity of the layer charge can be easily checked by simply measuring the  $d$ -spacing of the intercalation compound. Because of the high selectivity of the alkylammonium ions, the interlayer cations are displaced completely and the negative layer charge is fully neutralized by alkylammonium ions. Depending on the charge density of the clay and the chain length of the alkylammonium ions different interlayer structures are formed. Monolayers ( $d_{001} = 13.4\text{--}13.6 \text{ \AA}$ ) will be realized as long as the charge density of flat-lying alkylammonium ions is higher than the charge density of the clay. At a certain critical chain length, these monolayers will be closely packed and with the next longer

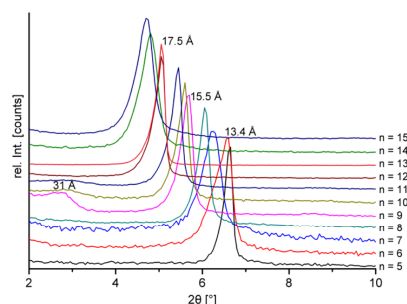


Figure 4. PXRD pattern of annealed  $\text{Na}_{0.5}\text{-Hec}$  exchanged with alkylammonium cations of different chain length ranging from pentyl ( $n = 5$ ) to pentadecylammonium ( $n = 15$ ).

chain lengths, some bilayers with a basal spacing of typically  $17.6 \text{ \AA}$  must be formed to neutralize the charge density of the clay. As already discussed with respect to hydration, heterogeneity in the charge density of clay sample will inevitably result in varying packing densities of the alkylammonium chains in different scattering domains. Consequently, the onset of bilayers being incorporated in the stack will occur at different chain length. This would cause the observation of more than one basal spacing at a given chain length as seen with the pristine material.<sup>7</sup> Contrary to this, for the annealed  $\text{Na}_{0.5}\text{-Hec}$  the basal spacing shifted gradually with increasing chain length, and at any chain length only a single basal spacing was observed, corroborating a nicely homogeneous layer charge density.

Please note that the smooth transition from mono- to bilayer with alkylammonium cations of increasing chain length is an artifact of interstratification. The X-ray beam averages over mono- and bilayer basal spacings in a volume weighted manner and while these basal spacings are fixed, the ratio of mono- and bilayers is varied to meet charge neutrality. This is because the strong coulomb interaction between positively charged interlayers and negatively charged silicate layers strongly favors minimization of the average basal spacing and therefore drives a strict segregation into densely packed mono- and bilayers.

The charge density ( $x$ ) of the clay corresponds directly to the longest alkylammonium ion (chain length  $n$ ) that still is capable to satisfy the charge density of the clay by a monolayer arrangement and can be calculated with a formula defined by Lagaly et al.:<sup>16–18</sup>

$$x = \frac{0.5a \cdot b}{5.67n + 14} \quad (1)$$

where  $a$  and  $b$  are the unit cell axes. Given unit cell parameters of  $a = 5.248 \text{ \AA}$  and  $b = 9.093 \text{ \AA}$  (e.g., for the 2WL state) a layer charge of  $x = 0.5$  should allow a monolayer arrangement up to a chain length of  $n = 5.95$ . The chain lengths must of course be an integer, and consequently charge neutrality with  $n = 6$  already requires very few bilayers. And indeed with  $n = 6$  the basal peak started to shift and the peak width broadens (Figure 4), both signs of beginning interstratification of some bilayers in the predominantly monolayer stacking.

Assuming the same packing density of mono- and bilayer arrangement, the critical chain length should be  $n = 14$  (more precisely  $14.36$ ) for the latter. However, uniform bilayer

## Langmuir

## Article

arrangement is observed only up to tridecylammonium ( $n = 13$ , corresponding to  $x < 0.54$ ), while with  $n = 14$ , the basal peak already started to shift and broaden, indicating interstratification. Thus, with the Lagaly method, the layer charge can be narrowed down to  $\approx 0.5 < x < 0.54$ , which within the limits of the method is in excellent agreement with results from chemical analysis and determination of CEC.

As previously pointed out, with homogeneously charged synthetic clays an ordered interstratification of bilayer and monolayers with Reichweite ( $R$ ) = 1 is found to be the thermodynamically stable state. With some intermediate chain length, moreover, the ratio of mono- and bilayer will be close to 1:1, and indeed with nonadecylammonium ( $n = 9$ ) a superstructure reflection at 31 Å was observed (Figure 4). The plot of basal distance as a function of alkylammonium chain length (Figure S2) for this synthetic clay is therefore not linear but shows a plateau at  $d_{002}^*$  of the superstructure basal series of the ordered interstratification where the probability for a monolayer  $w_1$  is approximately equal to the probability for the bilayer  $w_2$  ( $w_1 = w_2$ ). Please note that the continuous shift of the  $d$ -spacing going from mono- to bilayer with alkylammonium cations of increasing chain length, which was observed by Lagaly and Weiss for a natural montmorillonite,<sup>18</sup> is due to random interstratification ( $R = 0$ ) caused by layer charge heterogeneity. Thus, the reason underlying interstratifications is different; for natural montmorillonites it is charge heterogeneity while for our synthetic clays it is observed for chain lengths where  $w_1 \ll w_2$  or  $w_1 \gg w_2$ .

In summary, both experimental facts—the observations of just one basal spacing with any alkylammonium intercalate and the formation of an ordered interstratification at an intermediate chain length—corroborate an unprecedented homogeneous distribution of the layer charge density.

The osmotic swelling behavior of  $\text{Na}_{0.5}\text{-Hec}$  was investigated in more detail by mixing the  $\text{Na}_{0.5}\text{-Hec}$  with different amounts of deionized water. Similar to what has been reported for synthetic Li-hectorit,<sup>8</sup> with increasing amounts of water the 001 peaks are continuously shifted to lower diffraction angle (higher  $d$ -values, Figure S3). The 001 reflection could, however, only be observed up to a weight ratio of  $m(\text{water}):m(\text{Na}_{0.5}\text{-Hec}) = 4:1$ ; even higher  $d_{001}$  values were out of the measurement range of our instrument. The  $d_{001}$  series for the mixture of 4:1 was rational ( $d_{001} = 115.4$  Å,  $d_{002} = 58.8$  Å,  $d_{003} = 38.8$  Å, and  $d_{004} = 28.8$  Å). Larger basal spacings realized at higher water contents, could, however, still be calculated using higher order reflections. This way a linear increase of the  $d_{001}$ -spacing was obtained as a function of growing amounts of water being added (Figure 5). This linear characteristic resembles swelling of alkylammonium exchanged clays in organic liquids and organic liquid mixtures<sup>19–22</sup> and osmotic swelling of natural montmorillonites with sodium as an interlayer cation.<sup>23,24</sup>

Please note that the pristine  $\text{Na}_{0.5}\text{-Hec}$  shows no osmotic swelling. Even with a much higher water to pristine  $\text{Na}_{0.5}\text{-Hec}$  ratio of 700:1 only swelling to the two-layer hydrate (15.1 Å) was observed (curve c in Figure 1). The linear swelling characteristic, together with the broadening of the reflexes, as compared to “air” measurements, indicate that the tactoids of  $\text{Na}_{0.5}\text{-Hec}$  may delaminate in highly diluted dispersions. A proof for this suggestion could be delivered with AFM. For this, drops of a highly diluted dispersion (0.02 g/L,  $m(\text{water}):m(\text{Na}_{0.5}\text{-Hec}) = 50\,000:1$ ) were deposited and dried on a silicon wafer. Individual, delaminated platelets with a height of about 1 nm and a size between 10 and 20 μm can be seen in the AFM

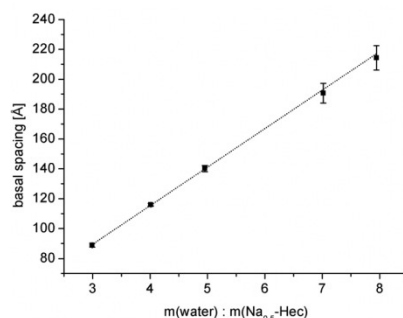


Figure 5. Relation between average  $d_{001}$  and mass ratio of water to  $\text{Na}_{0.5}\text{-Hec}$ .

image, as illustrated in Figure 6. Please note that due to the ambient conditions during measurement a water layer may exist

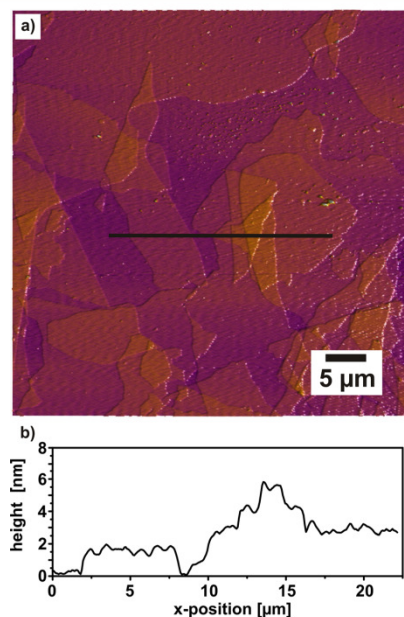


Figure 6. (a) Topographical AFM image of a typical sample of annealed  $\text{Na}_{0.5}\text{-Hec}$  showing the huge lateral extensions. (b) Height profile showing singular lamellae that are partially stacked above each other upon drying yielding discrete steps of about 1 nm height.

between substrate and platelets, causing an apparently larger height. Regardless of this systematic error, since the height of multilayer stacks increases in discrete steps of about 1 nm, all platelets with a thickness thinner than 2 nm can be safely assigned to be monolayers.

Although Figure 6 is a typical representative of many more images recorded, AFM is not a bulk method. In order to obtain



## Langmuir

## Article

more information about the lateral extension of the platelets, the particle size distribution was measured with static light scattering (SLS) of an aqueous dispersion. The number weighted results show a relatively narrow size distribution of the platelets with a mean particle size of about 18  $\mu\text{m}$  (Figure S4). The SLS measurements were performed in aqueous dispersions; the particle size distribution therefore is representative for the bulk material. Moreover, it has been shown by Goossens<sup>25</sup> that the lateral extensions of clay tactoids correlate well with the hydrodynamical radius obtained from SLS. We are, however, aware that the absolute values might be somewhat in error because of the large size and the floppy nature of the nanoplatelets. To account for this high anisotropy of the particles, we therefore cross-checked the value by determining the chord lengths distribution by focused beam reflectance measurement (FBRM) (17  $\mu\text{m}$ ) and by assessing a large number of particles of  $\text{Na}_{0.5}\text{-Hec}$  powders as seen in SEM micrographs (Figure S5) giving a mean tactoid size of 18  $\mu\text{m}$ . Considering a platelet thickness of about 1 nm and a median lateral extension of the clay particles of 18  $\mu\text{m}$  and assuming complete delamination by osmotic swelling as indicated by AFM and PXRD (Figure 5),  $\text{Na}_{0.5}\text{-Hec}$  offers a mean aspect ratio of 18 000.

## CONCLUSIONS

Long-term annealing of melt-synthesized  $\text{Na}_{0.5}\text{-Hec}$  induces crystallization of an amorphous impurity. We propose that this impurity acts as binder in the pristine material and limits its intracrystalline reactivity. As indicated by  $^{19}\text{F}$  MAS solid-state NMR a highly phase pure fluorohectorite is obtained by the additional annealing step. Dispersing this activated  $\text{Na}_{0.5}\text{-Hec}$  in water induces osmotic swelling and finally complete delamination into 1 nm thick platelets with medium aspect ratios of 18 000 as determined by AFM and particle size distributions. Moreover, annealing also results in superb charge characteristics. Both swelling with water and cation exchange with alkylammonium cations suggest a perfectly uniform intracrystalline reactivity corresponding to a degree of homogeneous charge density of the clay platelets not seen before. At last, stacking faults are diminished a great deal by annealing and the highly ordered material can be used for the synthesis of ordered microporous pillared or interstratified inorganic/organic hybrid materials. Most importantly, the combination of high optical transparency, ultrahigh aspect ratio, and the absence of impurities renders this clay the perfect filler for high gas barrier applications and mechanical improvement of nanocomposites which will be studied in future work.

## ASSOCIATED CONTENT

## Supporting Information

All experimental details and the following supporting data:  $^{19}\text{F}$ -MAS spectra of a sample enriched in protoamphibole, plot of  $d$ -spacings as a function of alkylammonium chain length  $n$ , PXRD traces of osmotic swelling, particle size distributions, and SEM micrographs. This material is available free of charge via the Internet at <http://pubs.acs.org>.

## AUTHOR INFORMATION

## Corresponding Author

\*Phone +49 921 55 2531; Fax +49 921 55 2788; e-mail Josef.Breu@uni-bayreuth.de.

## Author Contributions

<sup>§</sup>These authors contributed equally. The manuscript was written through contributions of all authors. All authors have given approval to the final version of the manuscript.

## Notes

The authors declare no competing financial interest.

## ACKNOWLEDGMENTS

This work was supported by the Deutsche Forschungsgemeinschaft (SFB 840). D.A.K. thanks the elite study program "Macromolecular Science" as well as the International Graduate School "Structure, Reactivity and Properties of Oxide Materials" within the Elite Network of Bavaria (ENB) for ongoing support. The authors thank the Bayerisches Geoinstitut, Bayreuth, Germany for the WDX measurements. We also thank Prof. A. Fery, Physikalische Chemie II, Universität Bayreuth, for making AFM equipment available.

## REFERENCES

- (1) Schütz, M. R.; Kalo, H.; Lunkenbein, T.; Gröschel, A. H.; Müller, A. H. E.; Wilkie, C. A.; Breu, J. Shear Stiff, Surface Modified, Mica-Like Nanoplatelets: a Novel Filler for Polymer Nanocomposites. *J. Mater. Chem.* **2011**, *21*, 12110–12116.
- (2) Tang, Z. Y.; Kotov, N. A.; Magonov, S.; Ozturk, B. Nanostructured Artificial Nacre. *Nat. Mater.* **2003**, *2*, 413–418.
- (3) Möller, M. W.; Kunz, D. A.; Lunkenbein, T.; Sommer, S.; Nennemann, A.; Breu, J. UV-Cured, Flexible, and Transparent Nanocomposite Coating with Remarkable Oxygen Barrier. *Adv. Mater.* **2012**, *24*, 2142–2147.
- (4) Podsiadlo, P.; Kaushik, A. K.; Arruda, E. M.; Waas, A. M.; Shim, B. S.; Xu, J. D.; Nandivada, H.; Pumphlin, B. G.; Lahann, J.; Ramamoorthy, A.; Kotov, N. A. Ultrastrong and Stiff Layered Polymer Nanocomposites. *Science* **2007**, *318*, 80–83.
- (5) Schütz, M. R.; Kalo, H.; Lunkenbein, T.; Breu, J.; Wilkie, C. A. Intumescent-like Behavior of Polystyrene Synthetic Clay Nanocomposites. *Polymer* **2011**, *52*, 3288–3294.
- (6) Kalo, H.; Möller, M. W.; Ziadeh, M.; Dolejs, D.; Breu, J. Large Scale Melt Synthesis in an Open Crucible of Na-Fluorohectorite with Superb Charge Homogeneity and Particle Size. *Appl. Clay Sci.* **2010**, *48*, 39–45.
- (7) Breu, J.; Seidl, W.; Stoll, A. J.; Lange, K. G.; Probst, T. U. Charge Homogeneity in Synthetic Fluorohectorite. *Chem. Mater.* **2001**, *13*, 4213–4220.
- (8) Kalo, H.; Möller, M. W.; Kunz, D. A.; Breu, J. How to Maximize the Aspect Ratio of Clay Nanoplatelets. *Nanoscale* **2012**, *4*, 5633–5639.
- (9) Kalo, H.; Milius, W.; Breu, J. Single Crystal Structure Refinement of One- and Two-Layer Hydrate of Sodium-Fluorohectorite. *RSC Adv.* **2012**, *2*, 8452–8459.
- (10) Kalo, H.; Milius, W.; Bräu, M.; Breu, J. Synthesis and Single Crystal Structure Refinement of the One-Layer Hydrate of Sodium Brittle Mica. *J. Solid State Chem.* **2013**, *198*, 57–64.
- (11) Möller, M. W.; Handge, U. A.; Kunz, D. A.; Lunkenbein, T.; Altstadt, V.; Breu, J. Tailoring Shear-Stiff, Mica-Like Nanoplatelets. *ACS Nano* **2010**, *4*, 717–724.
- (12) Ziadeh, M.; Chwalka, B.; Kalo, H.; Schütz, M. R.; Breu, J. A Simple Approach for Producing High Aspect Ratio Fluorohectorite Nanoplatelets Utilizing a Stirred Media Mill (Ball Mill). *Clay Miner.* **2012**, *47*, 341–353.
- (13) Möller, M. W.; Lunkenbein, T.; Kalo, H.; Schieder, M.; Kunz, D. A.; Breu, J. Barrier Properties of Synthetic Clay with a Kilo-Aspect Ratio. *Adv. Mater.* **2010**, *22*, 5245–5249.
- (14) Breu, J.; Seidl, W.; Stoll, A. Disorder in Smectites in Dependence of the Interlayer Cation. *Z. Anorg. Allg. Chem.* **2003**, *629*, 503–515.

## Langmuir

## Article

- (15) Huve, L.; Delmotte, L.; Martin, P.; LeDred, R.; Baron, J.; Saehr, D. F-19 MAS-NMR study of structural fluorine in some natural and synthetic 2:1 layer silicates. *Clays Clay Miner.* **1992**, *40*, 186–191.
- (16) Mermut, A. R.; Lagaly, G. Baseline studies of The Clay Minerals Society source clays: Layer-charge determination and characteristics of those minerals containing 2: 1 layers. *Clays Clay Miner.* **2001**, *49*, 393–397.
- (17) Lagaly, G. Characterization of Clays by Organic-Compounds. *Clay Miner.* **1981**, *16*, 1–21.
- (18) Lagaly, G.; Weiss, A. Arrangement and Orientation of Cationic Tensides on Silicate Surfaces 0.4. Arrangement of Alkylammonium Ions in Low-Charged Silicates of Films. *Kolloid Z. Z. Polym.* **1971**, *243*, 48–55.
- (19) Dekany, I.; Szanto, F.; Nagy, I. G. Sorption and Immersional Wetting on Clay-Minerals Having Modified Surface 0.2. Interlamellar Sorption and Wetting on Organic Montmorillonites. *J. Colloid Interface Sci.* **1986**, *109*, 376–384.
- (20) Kotov, N. A.; Meldrum, F. C.; Fendler, J. H.; Tombacz, E.; Dekany, I. Spreading of Clay Organocomplexes on Aqueous-Solutions - Construction of Langmuir-Blodgett Clay Organocomplex Multilayer Films. *Langmuir* **1994**, *10*, 3797–3804.
- (21) Dekany, I.; Szanto, F.; Weiss, A.; Lagaly, G. Interactions of Hydrophobic Layer Silicates with Alcohol-Benzene Mixtures 0.1. Adsorption-Isotherms. *Ber. Bunsenges. Phys. Chem.* **1986**, *90*, 422–427.
- (22) Dekany, I.; Szanto, F.; Weiss, A.; Lagaly, G. Interactions of Hydrophobic Layer Silicates with Alcohol-Benzene Mixtures 0.2. Structure and Composition of the Adsorption Layer. *Ber. Bunsenges. Phys. Chem.* **1986**, *90*, 427–431.
- (23) Norrish, K. The Swelling of Montmorillonite. *Discuss. Faraday Soc.* **1954**, *120*–134.
- (24) Segad, M.; Hanski, S.; Olsson, U.; Ruokolainen, J.; Akesson, T.; Jonsson, B. Microstructural and Swelling Properties of Ca and Na Montmorillonite: (In Situ) Observations with Cryo-TEM and SAXS. *J. Phys. Chem. C* **2012**, *116*, 7596–7601.
- (25) Goossens, D. Techniques to Measure Grain-Size Distributions of Loamy Sediments: a Comparative Study of Ten Instruments for Wet Analysis. *Sedimentology* **2008**, *55*, 65–96.

## 6.1.2 Supporting Information

**Nanoplatelets of sodium hectorite showing  
aspect ratios of  $\approx 20000$  and superior purity**

*Matthias Stöter,<sup>†,§</sup> Daniel A. Kunz,<sup>†,§</sup> Marko Schmidt,<sup>‡</sup> Dunja Hirsemann,<sup>†</sup> Hussein Kalo,<sup>†</sup>*

*Bernd Putz,<sup>†</sup> Jürgen Senker,<sup>‡</sup> and Josef Breu<sup>†,\*</sup>*

<sup>†</sup>Lehrstuhl für Anorganische Chemie I, Universität Bayreuth, D-95440 Bayreuth, Germany

<sup>‡</sup>Lehrstuhl für Anorganische Chemie III, Universität Bayreuth, D-95440 Bayreuth, Germany

**Supporting Information**

Content:

1. Experimental Details
2. Supporting Data
3. Supporting References

## 1. Experimental Details

### Cation exchange capacity

The cation exchange capacity (CEC) of the non-annealed, pristine hectorite and the annealed material was determined with the  $[\text{Cu}(\text{trien})]^{2+}$  method.<sup>1</sup> A control measurement was done by a threefold exchange of the annealed  $\text{Na}_{0.5}$ -Hec with excess of a  $\text{BaCl}_2$  solution (0.1 mol/L) according to the DIN ISO 11260 standard procedure. The collected washing solutions were analyzed for Na using a Varian SpectrAA-100 atomic absorption spectrometer.

### WDX

The composition of the annealed  $\text{Na}_{0.5}$ -Hec was determined by wavelength dispersive X-ray spectroscopy (WDX) on a Joel JXA 8200 spectrometer, with acceleration voltage 15 kV and 15 nA with a beam spot diameter of 1  $\mu\text{m}$ . Calibration was done using andradite  $\text{Ca}_3\text{Fe}_2\text{Si}_3\text{O}_{12}$  as silicon standard, synthetic enstatite  $\text{Mg}_2[\text{Si}_2\text{O}_6]$  as magnesium standard and albite  $\text{NaAlSi}_3\text{O}_8$  as sodium standard. After polishing only particles with smooth surfaces were chosen for the WDX measurement. The counting time was 20 s at every peak position. The composition was normalized to  $\text{Si}_{4.00}$  because lithium is not detectable with this method.

### ICP-AES

The lithium and sodium content of the bulk material was determined by inductive-coupled-plasma atomic emission spectroscopy (ICP-AES). Two samples of about 20 mg of dry synthetic  $\text{Na}_{0.5}$ -Hec were weighed into clean Teflon flasks of 150 mL volume. After addition of 1.5 mL 30 wt. %  $\text{HCl}$  (Merck), 0.5 mL of 85 wt. %  $\text{H}_3\text{PO}_4$  (Merck), 0.5 mL 65 wt. %  $\text{HNO}_3$  (Merck) and 1 mL of 48 wt. %  $\text{HBF}_4$  (Merck) the sample was digested in a MLS 1200 Mega microwave digestion apparatus for 6.5 min and heated at 600W (MLS GmbH, Mikrowellen-Labor-Systeme, Leutkirch, Germany). The closed sample container was cooled to room temperature and the clear solution was diluted to 100 mL in a volumetric flask and analyzed.



**Layer charge determination**

The layer charge was determined by the alkylammonium method.<sup>2</sup> The alkylammonium salts were prepared by acidification of amines ( $[C_nH_{2n+1}NH_3]^+$ ;  $n = 5-15$ ) dissolved in ethanol by adding aqueous formic acid (2 mol/L). The solutions were adjusted to a pH of 8 and filled up with water to achieve a concentration of 2 mol/L for the pentyl- and hexylamine, 0.5 mol/L for the pentyl- to decylamines and 0.1 mol/L for the corresponding longer chain alkylamines. 90 mg of the annealed  $Na_{0.5}$ -Hec was exchanged 3 times with 3 ml of the different amines in small glass vessels closed with screw caps at 60 °C in an overhead shaker. The products were removed from the solution by centrifugation and washed 6 times with ethanol-water mixture (1:1), 4 times with pure ethanol and finally dried at 60°C.

**Powder X-ray diffraction**

Powder X-ray diffraction (PXRD) was measured in transmission geometry on a STOE Stadi P powder diffractometer equipped with a MYTHENIK detector using Cu  $K\alpha_1$  radiation ( $\lambda = 1.54056 \text{ \AA}$ ). For investigation of the different hydration states the  $Na_{0.5}$ -Hec powder was filled into fused silica capillaries (0.7 mm Hilgenberg) and equilibrated for 30 days in a desiccator at 43% and 93% relative humidity using saturated  $K_2CO_3$  and  $KNO_3$  solutions, respectively. To prevent evaporation of water during the PXRD measurement the capillaries were sealed with high vacuum silicone grease (Merck) immediately after being removing from the selected water vapor atmosphere. For the non-hydrated (0% RH) sample the capillary was stored at 120°C overnight and sealed by melting the top of the capillary.

The osmotic swelling experiments were completed in small glass vessels by mixing a weighted mass of deionized water with a corresponding mass of hectorite powder. After an equilibration time of 48 hours, the resulting gels were mixed with a spatula, placed between two mylar foils using a flat sample holder and then were immediately measured on the XRD within 15 minutes.

**Atomic Force Microscopy**

Atomic Force Microscopy was done by using a MFP3D™ Atomic Force Microscope (Asylum Research, Santa Barbara, California) equipped with silicon cantilevers (silicon tip, type NSC15/AIBS,  $\mu$ mash, Tallin, Estonia) with a scan rate of 1 Hz. The samples were prepared by slowly evaporation of a few drops of a diluted suspension (0.02 g/L) on a Si-wafer under ambient conditions.

#### **Particle size distribution**

Particle size distribution was recorded by static light scattering (SLS) of aqueous dispersions using a Retsch Horiba LA-950 SLS instrument. The refractive index of the solid phase was set to a value of 1.5. A measurement routine called “mica in water” supplied by the manufacturer (Horiba) was applied. Micas have similar lateral extensions as the synthetic hectorites studied here. The routine determines transmission rates and optimizes the concentration of the suspensions.

For comparison the chord length distribution of an aqueous dispersion was additionally investigated by focused beam reflectance measurement (FBRM) with a Mettler Toledo LASENTEC FBRM model D600L-HC22-K. Finally, the crystal size of the solid material was also measured by assessing a large number of hectorite particles as imaged with a LEO 1530 FE-SEM at an operating voltage of 3 kV.

#### **NMR MAS Measurement**

The  $^{19}\text{F}$  shifts are reported with respect to  $\text{CFCl}_3$ . The 1D- $^{19}\text{F}$  MAS NMR spectra were recorded on a Bruker Avance II spectrometer using triple resonance probes ( $\text{ZrO}_2$ , diameter 2.5 mm) at a MAS frequency of 30 kHz. A direct excitation on the  $^{19}\text{F}$  channel with a  $90^\circ$  pulse length of 2  $\mu\text{s}$  was applied. The recycle delay was 20 s, the number of experiments was set to 16. For all experiments, no proton decoupling was used.

## **2. Supporting Data**

**Coefficient of variation (CV)**

The coefficient of variation was calculated according to Bailey:<sup>3</sup>

$$CV = \frac{100s}{X}$$

where  $s$  = standard deviation and  $X$  = mean of the observed  $l^*$   $d_{00l}$  values. Due to overlap, we were only able to unambiguously determine the positions of the  $00l$ -series where  $l_{\max} = 7$  in case of zero-layer hydrate,  $l_{\max} = 9$  in case of one layer hydrate, and  $l_{\max} = 10$  in case of the two-layer hydrate.

The 2WL gives a basal spacing of  $d_{001} = 15.4 \text{ \AA}$  (coefficient of variation = 0.21 %).

Example 2WL:

<i>l</i>	<i>d</i>	<i>l</i> * <i>d</i> (001)
1	15.459	15.46
3	5.130	15.39
4	3.848	15.39
5	3.073	15.36
6	2.563	15.38
7	2.195	15.37
8	1.920	15.36
10	1.537	15.37
Mean		15.39
CV		0.21%

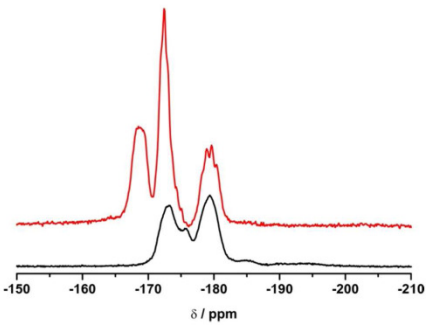


**Figure S1:**  $^{19}\text{F}$ -MAS spectra of a  $\text{Na}_{0.5}$ -Hec sample containing a much increased volume ratio of protoamphibole<sup>4,5</sup> sidephase (red line) as compared to the pristine  $\text{Na}_{0.5}$ -Hec sample. The additional peak at about -169 ppm can be assigned to protoamphibole.

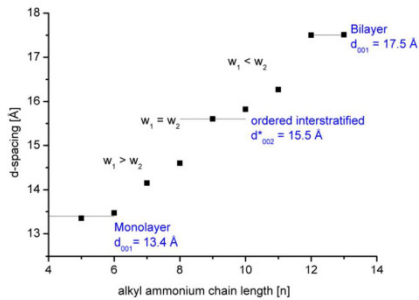


**Figure S2:** Plot of  $d$ -spacings as function of alkylammonium chain length  $n$  ( $[\text{C}_n\text{H}_{2n+1}\text{NH}_3]^+$ ). A plateau for the ordered interstratification where the probability of the monolayer  $w_1$  is approximately equal to the probability of the bilayer  $w_2$  ( $w_1 = w_2$ ) is indicated.

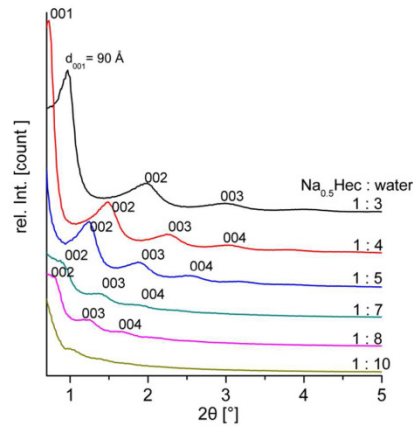


**Figure S3:** PXRD measurement of the osmotic swelling of the  $\text{Na}_{0.5}$ -Hec as function of the mass ratio  $\text{Na}_{0.5}$ -Hec : water.

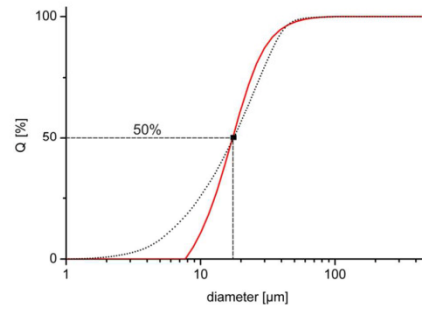


**Figure S4.** Number weighted particle size distribution as determined by SLS measurement of a  $\text{Na}_{0.5}$ -Hec dispersion in water (solid red line) and corresponding unweighted FBRM measurement (dotted black line). Both results agree well with the mean tactoid size of  $\text{Na}_{0.5}$ -Hec powder as seen in SEM micrographs (black square).

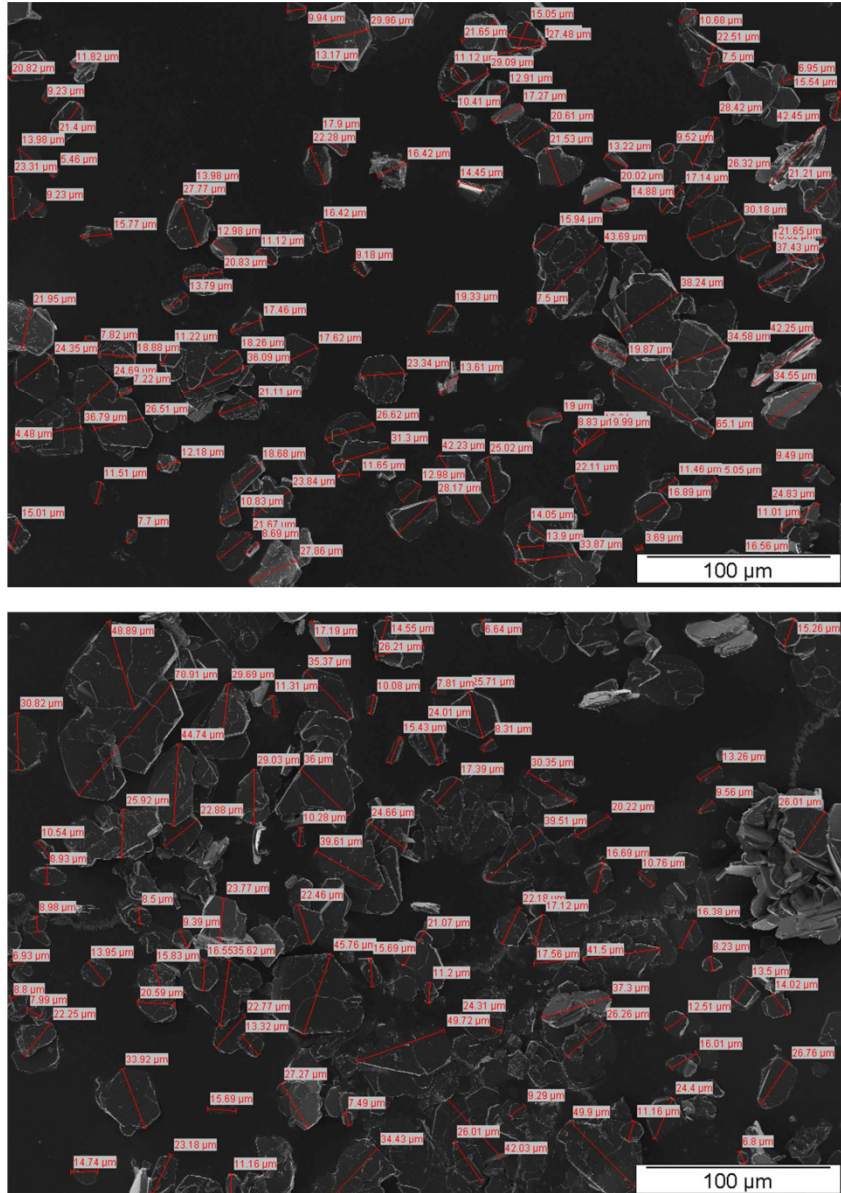


**Figure S5:** SEM micrographs of singular  $\text{Na}_{0.5}\text{-Hec}$  tactoids after annealing. The mean particle size is 18 µm.

### 3. Supporting References

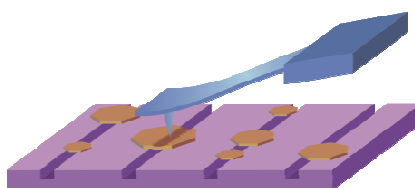
- (1) Ammann, L.; Bergaya, F.; Lagaly, G. Determination of the cation exchange capacity of clays with copper complexes revisited. *Clay Miner.* **2005**, *40*, 441-453.
- (2) Mermut, A. R.; Lagaly, G. Baseline studies of The Clay Minerals Society Source Clays: Layer-charge determination and characteristics of those minerals containing 2 : 1 layers. *Clays Clay Miner.* **2001**, *49*, 393-397.
- (3) Bailey, S. W. Nomenclature for Regular Interstratifications. *Am. Mineral.* **1982**, *67*, 394-398.
- (4) Delevoye, L.; Liu, S. X.; Welch, M. D.; Fernandez, C.; Amoureux, J. P.; Klinowski, J. Triple-quantum Al-27 and Na-23 MAS NMR study of amphiboles. *J. Chem. Soc. Faraday Trans.* **1997**, *93*, 2591-2595.
- (5) Möller, M.; Hirsemann, D.; Haarmann, F.; Senker, J.; Breu, J. Facile Scalable Synthesis of Rectorites. *Chem. Mater.* **2010**, *22*, 186-196.

## 6.2 *Deformationsmessungen an dünnen Schichtsilicattaktoiden*

Daniel A. Kunz<sup>†</sup>, Eva Max<sup>‡</sup>, Richard Weinkamer<sup>§</sup>, Thomas Lunkenbein<sup>†</sup>, Josef Breu<sup>†,\*</sup>, and Andreas Fery<sup>‡,\*</sup>

### Deformation Measurements on Thin Clay Tactoids

Erschienen in: *Small* **2009**, 5, 1816-1820. Copyright © 2009 by John Wiley & Sons, Inc. Reprinted by permission of John Wiley & Sons, Inc.



<sup>†</sup> Lehrstuhl für Anorganische Chemie I, Universität Bayreuth, 95447 Bayreuth, Deutschland

<sup>‡</sup> Lehrstuhl für Physikalische Chemie II, Universität Bayreuth, 95447 Bayreuth, Deutschland

<sup>§</sup> Max Plank Institut für Kolloide und Grenzflächen, 14476 Potsdam-Golm, Deutschland

\* josef.breu@uni-bayreuth.de; andreas.fery@uni-bayreuth.de

### Darstellung des Eigenanteils:

Das Konzept dieser Publikation wurde zusammen mit Prof. Dr. *Josef Breu* und Prof. Dr. *Andreas Fery* erarbeitet. Mein Anteil dieser Veröffentlichung bestand aus der Entwicklung der Messmethode und aus der Durchführung und Auswertung der Messungen. Dr. *Eva Max* unterwies mich in der Kraftspektroskopie. Dr. *Richard Weinkamer* unterstützte in der Interpretation der Daten hinsichtlich der Plattentheorie. *Thomas Lunkenbein* steuerte die REM-Aufnahme bei. Verfasst wurde diese Publikation hauptsächlich von Prof. Dr. *Josef Breu*, Prof. Dr. *Andreas Fery* und mir. Dr. *Richard Weinkamer* hat zum Plattenmechanik-Teil beigetragen.

Mein Eigenanteil beläuft sich auf ca. 70 %.



## 6.2.1 Deformation Measurements on Thin Clay Tactoids

## communications

## Nanocomposites

## Deformation Measurements on Thin Clay Tactoids\*\*

Daniel A. Kunz, Eva Max, Richard Weinkamer, Thomas Lunkenbein, Josef Breu,\*  
and Andreas Fery\*

Many modern composite materials contain clay platelets as functional compounds. The clay filler determines properties like barrier activity,<sup>[1]</sup> fire retardancy,<sup>[2]</sup> electrical properties,<sup>[3]</sup> and mechanical reinforcement.<sup>[4]</sup> Recent work has brought the mechanical properties of polymer-layered silicate nanocomposites (PLSNs) even closer to ultrastrong and stiff natural materials like nacre.<sup>[5–7]</sup> For most of these applications, it is crucial to maximize the aspect ratio (lateral extension divided by height) of the clay platelets, so-called tactoids, which are quasi-crystals consisting of between two and up to several thousands of individual silicate lamellae stacked in a parallel mode along  $c^*$  (Scheme 1). At the same time the stiffness of the tactoids has of course to be preserved. This issue is not trivial because increasing the aspect ratio by exfoliation (definition according to Lagaly et al.<sup>[8]</sup>) necessarily will produce thinner and thinner tactoids and eventually they will be of nanoscale thickness.

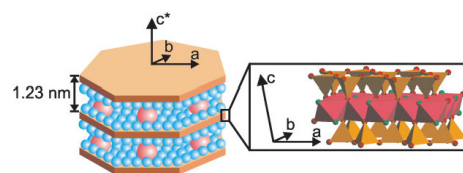
Up to now, very little information has been available about the elastic properties of individual (natural) clay tactoids. The edges of natural clay tactoids are badly fringed and the lateral extension of natural clay platelets is limited to less than 300 nm,<sup>[9,10]</sup> rendering measurements on individual tactoids (typical thickness 10 nm) nearly impossible with conventional procedures. Therefore, bulk values are usually extrapolated to nanoscale dimensions, which might be critical since elastic constants can show size dependencies.<sup>[11]</sup>

Even reliable bulk values of natural swelling clays (e.g., smectites like montmorillonite) are inherently difficult to obtain: it is very tedious to separate auxiliary minerals without affecting the clay structure at the same time and the charge

density of these natural clay minerals is inhomogeneous, leading to interstratified materials, that is, neighboring interlayer galleries within one tactoid exhibit different compositions, for example, different hydration states.<sup>[12]</sup> Consequently, reliable information about elastic constants of “bulk clay” is scarce. In an overview, Chen et al.<sup>[13]</sup> discussed the mechanical properties of clays obtained via experimental or theoretical approaches: the latter include computer simulations on montmorillonite.<sup>[14,15]</sup> Experimental results were, inter alia, achieved by extrapolation of acoustic measurements (dickite, kaolinite, montmorillonite)<sup>[16,17]</sup> or by extrapolation of data of epoxy–clay hybrids<sup>[18]</sup> or via compressibility measurements.<sup>[19–22]</sup>

The most reliable experimental bulk elastic constants of 2:1 layered silicates were obtained via ultrasonic pulse method,<sup>[23]</sup> inelastic neutron scattering,<sup>[24]</sup> and Brillouin scattering<sup>[25,26]</sup> of micas. The values obtained were partially crosschecked by computer simulations.<sup>[27]</sup> Micas are non-hydrated and well-crystalline relatives of smectites within the family of 2:1 layered silicates. Micas, however, carry a two- to threefold higher charge density as compared to smectites. Please note that while the structure of the silicate layers is the same for both micas and smectites, the coulomb attraction between silicate layers and interlayer galleries and the hydration state are distinctly different. Hence the bonding strength between neighboring lamellae along the stacking direction is weaker in smectites as compared to micas, which in turn is expected to considerably influence the mechanical properties, in particular the  $C_{33}$  elastic constant.

In a pioneering work by Piner et al.<sup>[28]</sup> several atomic force microscopy (AFM)-based techniques were employed, including lateral force microscopy (LFM) and force modulation microscopy (FMM), to mechanically characterize individual tactoids of different natural and synthetic clays. However, the measurements were hampered by strong compliance of the clays to the substrates and mobile impurities that were observed. In a recent paper, the elastic modulus and hardness of muscovite and rectorite were determined by nanoindentation.<sup>[29]</sup>



**Scheme 1.** Representation of the structure of a 2:1 silicate layer and the state of hydration at 32% r.h.

[\*] Prof. J. Breu, D. A. Kunz, T. Lunkenbein  
Department of Inorganic Chemistry I, University of Bayreuth  
95447 Bayreuth (Germany)  
E-mail: josef.breu@uni-bayreuth.de

Prof. A. Fery, E. Max  
Department of Physical Chemistry II, University of Bayreuth  
95447 Bayreuth (Germany)  
E-mail: andreas.fery@uni-bayreuth.de

Dr. R. Weinkamer  
Max Planck Institute of Colloids and Surfaces  
14476 Potsdam-Golm (Germany)

[\*\*] D.A.K. would like to acknowledge the graduate school “Structure, Reactivity and Properties of Oxide Materials” and the elite study program “Macromolecular Science” within the Elitenetzwerk Bayern (ENB) as well as the “Write it Right” workshop for ongoing support.

Supporting Information is available on the WWW under <http://www.small-journal.com> or from the author.

DOI: 10.1002/sml.200801710

Rectorite is a regularly interstratified material that contains alternating non-hydrated mica-like and hydrated smectite-like interlayers. Unfortunately, the measurement for rectorite ( $E = 18.3 \pm 4.6$  GPa, where  $E$  is the young's modulus of the material) was somewhat hampered by giant steps observed in the load–displacement curves.

In this paper, we present novel AFM-based measurements on synthetic clays, which for the first time allowed the determination of elastic constants of individual clay platelets in a quantitative fashion. The development of this new method was facilitated by the availability of synthetic clay showing a sufficiently large lateral extension. Over the last decade we have developed high temperature routes for synthetic fluorohectorites. Contrary to what has been stated above for natural clays, melt synthesis in any case yields materials that show a homogenous charge density. Moreover, particularly large lateral extensions (up to  $10\ \mu\text{m}$ ) are observed for clay platelets obtained by melt synthesis. At the same time, the intracrystalline reactivity is not diminished. For instance,  $\text{Na}_{0.5}$ -fluorohectorite ( $[\text{Na}_{0.5}][\text{Li}_{0.5}\text{Mg}_{2.5}][\text{Si}_4]\text{O}_{10}\text{F}_2$ , layer charge per formula unit (p.f.u.)  $x = 0.5$ ) readily swells with water. However, contrary to the interstratified hydrated states observed with natural smectites like montmorillonite,<sup>[9,12]</sup> the synthetic fluorohectorites show discrete and well-defined hydration levels at any given relative humidity.<sup>[30,31]</sup> Furthermore, the morphology of the tactoids is well-defined (Scheme 2 and Scheme S1, Supporting Information). The edges of the tactoids are not fringed but sharp and smooth and all lamellae within a tactoid are oriented perfectly parallel to each other. As a consequence, the apparent density of such a synthetic tactoid is close to the real density. Please note that unlike natural clays, this synthetic fluorohectorite does not show osmotic swelling and subsequent delamination into single lamellae when immersed into water. Due to the somewhat larger layer charge ( $x = 0.5$  p.f.u.) as compared to typical montmorillonites ( $0.3\text{--}0.4$  p.f.u.), upon immersion in water, the synthetic Na-fluorohectorite instead only disaggregates into individual tactoids and partially exfoliates into thinner tactoids. Hence clay tactoids with different thicknesses and lateral extensions are electrostatically stabilized in dilute suspensions and may thus easily be cast as singular platelets onto a substrate (Scheme 2).

These specific features of the synthetic material paved the way to the development of a new method that enables the measurement of the elastic constants of individual clay tactoids—a bending test applying AFM, which is a method perfectly suited for platelets thinner than  $80\ \text{nm}$ . Using AFM, a clay platelet that was positioned over a gap of the substrate was bent, and then applying the theory of plates,<sup>[32]</sup> the  $C_{33}$  elastic constant could be determined. This constant is a measure for the bending elasticity of the material. In highly anisotropic matter like clays, the elastic modulus is a tensor and the crystal symmetry of the system determines the exact number of independent elastic constants. In the case of the applied  $\text{Na}_{0.5}$ -fluorohectorite, the  $C_{33}$  constant represents the elasticity along the  $c^*$ -axis that is perpendicular to the basal planes of a tactoid and is a kind of bending modulus (Scheme 1).<sup>[25,33]</sup>

A powder X-ray diffraction analysis of the employed  $\text{Na}_{0.5}$ -fluorohectorite confirmed that at the relative humidity prevailing in measurement environment (32% r. h.), the first

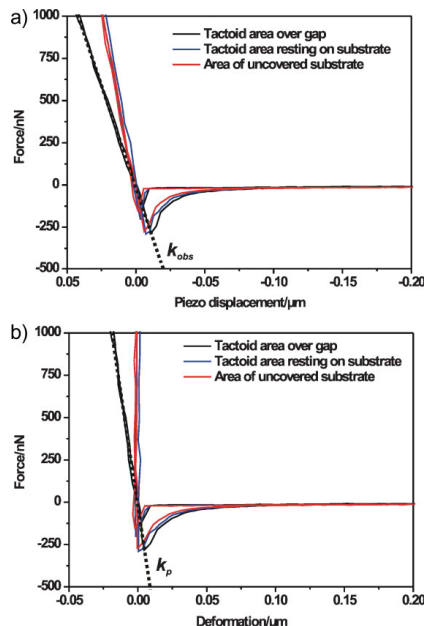
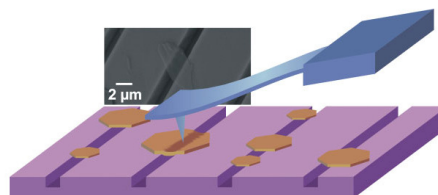


Figure 1. a) Three representative force–piezo-displacement curves for tactoid areas positioned adequately above a gap, tactoid areas resting on substrate, and pure uncovered substrate. b) The three resulting force–deformation curves after subtraction of the cantilever deflection. The perpendicular reference curves show that no further deformation, either from the tactoid resting on the substrate or from the substrate itself, are observed.

state of hydration is realized ( $d_{001} = 1.23\ \text{nm}$ ) with  $\text{Na}^+$  (enthalpy of hydration  $-406\ \text{kJ mol}^{-1}$ <sup>[34]</sup>) as an interlayer cation. According to Lagaly et al.<sup>[35]</sup> this corresponds to a monolayer of water in the interlayer gallery (Scheme 1). Please note that this interlayer water may act as a lubricant introducing additional shear planes when pressing on the clay platelet.

For the elastic measurements a sample was prepared on a structured substrate (Scheme 2). Initially, a large area was imaged with the AFM to identify the positions of the clay tactoids. As expected for such highly anisometric particles, a perfectly textured sample was obtained by drying the



Scheme 2. Measurement setup; imaging appropriately positioned tactoids of fluorohectorite that may be used for bending over the  $2\text{-}\mu\text{m}$ -wide channels; SEM micrograph of a tactoid lying across a channel.

## communications

suspensions on the flat substrate with all platelets lying flat and with their  $c^*$ -axis oriented perpendicular to the substrate. Tactoids lying exactly across a channel (see scanning electron microscopy (SEM) micrograph, Scheme 2) were selected for the bending test. Additionally, the tactoid heights of the selected platelets were determined by cross sections of the AFM images. Finally, a force-mapping of selected regions was performed. Here, a virtual net with at least 625 nodes was placed over the region that was chosen for the bending test. At each of these nodes a force–piezo-displacement curve was recorded. With the acquired data a new quasi-topographical image could be generated with each pixel representing one force–piezo-displacement curve (Scheme S1, Supporting Information). From this image the relevant data could be easily filtered out. On the basis of this image, for each particular clay tactoid, 10 curves were selected from areas not covered by clay (pure substrate), areas where clay platelets are resting on the substrate, and areas of clay platelets clearly positioned over the gap (Scheme S1, Supporting Information). To avoid irreversible damage of the smectite platelets and/or the cantilever tip, forces were limited to 100 nN for tactoids thinner than 25 nm.

The force-mapping resulted in three different kinds of force–piezo-displacement curves: the ones that stem from the genuine bending test of tactoid areas positioned above a gap and two types of references, namely platelet resting on substrate and pure uncovered substrate. Those places could be exactly distinguished since the shape of the tactoid and the gap can be seen clearly in the image generated after force mapping. Figure 1a shows a typical example of the obtained raw data (force versus piezo-displacement). The force increases linearly with piezo position. An effective spring constant  $k_{\text{obs}}$ , representing the combined deformation resistance of cantilever and sample, can be assigned to each measurement. Since the bare substrate is known to be non-deformable under the experimental conditions, the raw data can be converted into a force versus substrate-deformation plot shown in Figure 1b. This clearly shows that within the accuracy of the experiment, the elastic properties of bare substrate and tactoids resting on the substrate are identical, indicating that indentation of the tactoid can be safely ruled out, while the free-standing tactoid is deforming significantly – as we assume in the following – due to bending. Providing full experimental information, we will now discuss the dependency of  $k_{\text{obs}}$  on the tactoid thickness.

For each clay tactoid measured,  $k_{\text{obs}}$  of 10 force–piezo-displacement curves of each kind were averaged and the root mean square (rms) values were determined. A plot of the slopes of the genuine bending test, namely  $k_{\text{obs}}$ , versus the tactoid height reveals the sensitivity of the cantilever (Figure 2). Note that  $k_{\text{obs}}$  is actually the spring constant of the combined cantilever-tactoid system because the observed displacement has contributions of both. The two reference areas are shown in the Supporting Information. Moreover, corresponding plots of the reference values (Figure S1, Supporting Information), indicate that a possible indentation of the clay tactoids can be safely ruled out. The slope of the bending test force curves  $k_{\text{obs}}$  contains the spring constant of the platelet  $k_p$  as well as the cantilever spring constant  $k_c$ . The system can be described as a linear combination of two springs as it is schematically shown in

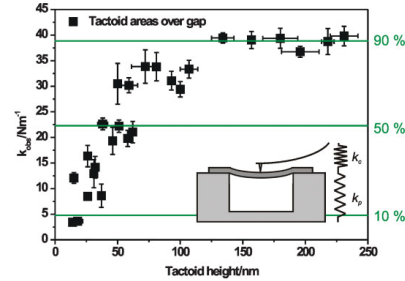


Figure 2. Observed slope  $k_{\text{obs}}$  of the bending test force–piezo-displacement curves in dependency on the platelet height. The percentages represent the ratios of the cantilever spring constant  $k_c$  in  $k_{\text{obs}}$ . Inset: scheme for the description of the contributions of  $k_{\text{obs}}$  (linear combination of the cantilever spring and the platelet spring).

the inset of Figure 2. Hence the observed spring constant is given by the product of the single spring constants divided by their sum. Resolving this equation yields:

$$k_p = \frac{k_{\text{obs}} k_c}{k_c - k_{\text{obs}}} \quad (1)$$

Based on Equation (1) the spring constant  $k_p$  of every clay platelet could be experimentally obtained. The relation between the  $C_{33}$  elastic constant of the platelet and the measured value  $k_p$  for a plate clamped at two opposite edges under a concentrated load  $P$  is given by plate theory<sup>[32]</sup> as

$$k_p = \frac{P}{w_{\text{max}}} = \frac{D}{\alpha a^2} = \frac{C_{33} h^3}{12 \alpha a^2 (1 - \nu^2)} \quad (2)$$

where  $h$  denotes the thickness of the plate,  $a$  is the smaller edge length of the plate,  $w_{\text{max}}$  is the maximum deflection of the plate,  $D$  is the bending stiffness of the plate, and  $\nu$  is Poisson's ratio. Due to the experimental setup  $a$  is fixed at 2  $\mu\text{m}$ . The factor  $\alpha$  depends only on the aspect ratio and boundary conditions, which in this particular context is the ratio between the lateral expansions of the platelets. For an aspect ratio larger than 3, as typically encountered in the experiments, the aspect ratio dependency is negligibly small, since the stiffness of the platelet is dominated by the smallest dimension, that is, by the width of the channel  $a$ . Deviations from the rectangular shape are of minor importance once it is secured that the lengths of the platelets are significantly larger than  $a$ . For a plate clamped at two opposite edges under a concentrated load,  $\alpha$  has the value 0.00724.<sup>[32]</sup> Assuming alternatively a simply supported elongated plate, Equation (2) is still valid, but with a larger value for  $\alpha$  (0.01695).<sup>[32]</sup> The best value found in literature for  $\nu$  of our material is 0.3.<sup>[36]</sup> Modifying Equation (2) yields

$$\sqrt[3]{k_p} = \sqrt[3]{\frac{C_{33}}{12 \alpha a^2 (1 - \nu^2)}} \cdot h \quad (3)$$

The linear fit of a plot of the third root of the platelet stiffness  $k_p$  against the tactoid height gives the  $C_{33}$  elastic

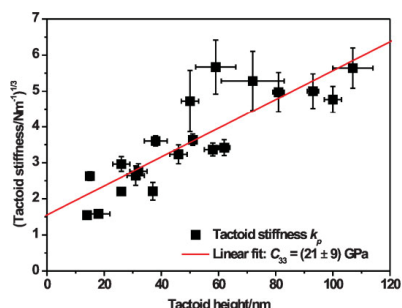


Figure 3. Determination of the  $C_{33}$  elastic constant of the  $\text{Na}_{0.5}$ -fluorohectorite applying a linear regression according to Equation (3).

constant of the material (Figure 3). Here it was  $21 \pm 9$  GPa assuming that the platelet is clamped at two opposite edges corresponding to a strong bonding (adhesion) between tactoid and substrate. A weaker interaction between platelet and substrate has the consequence of an increased stiffness of the platelet. In the extreme case of no interaction between platelet and substrate corresponding to a simply supported plate, the value of the platelet stiffness would be about  $48 \pm 20$  GPa. Recent measurements with nanoindentation on rectorite, for which half of the interlayers are comparable to the synthetic fluorohectorite in respect to charge density and hydration, gave a elastic modulus of  $18.3 \pm 4.6$  GPa.<sup>[29]</sup> Under the assumption of a strong interaction between tactoid and substrate, this value is in good agreement with our measurements.

As outlined in the introduction, reliable experimental values of  $C_{33}$  elastic constants are only available for some natural di- and trioctahedral micas of varying composition. The published values as determined by different methods vary between 54.9 and 70.5 GPa.<sup>[24,27]</sup> Most of this scatter is certainly due to the variation of composition. Furthermore, it is important to realize that the bonding along the stacking direction of smectites and micas is quite different. The layer charge of micas is twice as high as that of the employed  $\text{Na}_{0.5}$ -fluorohectorite. In addition, the dominating interlayer cation of micas is  $\text{K}^+$ , which possesses an ionic radius that perfectly fits with the hexagonal cavities in the Kagome net of the tetrahedral basal planes. Moreover, the enthalpy of hydration of  $\text{K}^+$  ( $-322 \text{ kJ mol}^{-1}$ <sup>[34]</sup>) is lower than that of  $\text{Na}^+$  ( $-406 \text{ kJ mol}^{-1}$ <sup>[34]</sup>). Because of all this, micas come in non-hydrated, macroscopically large, and well-crystalline platelets. The interlayer distance of micas is 0.99 nm instead of 1.23 nm as observed for the hydrated  $\text{Na}_{0.5}$ -fluorohectorite investigated here. All the factors listed above, the perfect fit, more interlayer cations, smaller interlayer distance, and no interlamellar water, contribute to a much increased Coulomb interaction between consecutive layers in tactoids of mica as compared to the fluorohectorites used here. Consequently, it is expected that the  $C_{33}$  elastic constant of  $\text{Na}_{0.5}$ -fluorohectorite is indeed significantly lower than the ones reported for micas. In that respect, the value of  $21 \pm 9$  GPa falls exactly within the expected trend. For hydrated (synthetic) smectites with a layer charge in the range of  $x = 0.5$  p.f.u. there is no reliable data about bending properties of individual tactoids available so far with which to compare.

Within the range of thicknesses investigated here, we find no evidence for a systematic dependency of the elastic constants on thickness. As already observed by Piner et al.,<sup>[28]</sup> tactoids thinner than 20 nm turned out to be very compliant, tended to be sucked into the gaps, and tended to be huddled against the walls of the microstructured substrate. Therefore, further measurements using substrates with finer submicrometer structures are currently underway.

Future work will certainly also have to probe the influence of the nature of the interlayer galleries. Starting with  $\text{Na}_{0.5}$ -fluorohectorite, the degree of hydration can be easily varied either as a function of relative humidity or of the interlayer cation. Furthermore, the mechanical properties of organophilized materials or porous hybrid materials (pillared clays<sup>[37–39]</sup>) are of special interest regarding their utilization as fillers in PLSNs.

It would be highly desirable to extend the measurements to natural montmorillonites, which currently represent the most widely used filler materials for PLSNs, in order to improve our understanding of the reinforcement. However, due to their small tactoid diameter and thickness, measurements on the currently available substrates were not possible so far. Regardless, the results for montmorillonites will be inherently hampered by their inhomogeneous charge density and non-removable auxiliary minerals.

Finally the mechanical characterization with this novel method can easily be extended to other nanoplatelets such as layered chalcogenides or layered double hydroxides. The latter are also used as functional compounds in polymer nanocomposites<sup>[40]</sup> and some theoretical work has already been published.<sup>[41]</sup>

## Experimental Section

**Synthesis of fluorohectorite:** The employed  $\text{Na}_{0.5}$ -fluorohectorite with the stoichiometry  $[\text{Na}_{0.5}][\text{U}_{0.5}\text{Mg}_{2.5}][\text{Si}_4\text{O}_{10}\text{F}_2]$  was synthesized via a melt synthesis described earlier.<sup>[30,42]</sup> In a typical procedure, high purity reagents of  $\text{SiO}_2$  (Merck, fine granular, washed and calcined quartz p.a.),  $\text{LiF}$  (Chempur, 99.9%, powder),  $\text{MgF}_2$  (Chempur, 99.9%, 3–6 mm pieces),  $\text{MgO}$  (Alfa Aesar, 99.95%, 1–3 mm, fused lumps), and  $\text{NaF}$  (Alfa Aesar, Puratronic, 99.995%, powder) were carefully weighed out ( $\approx 0.1 \text{ mol}$ ) according to the required composition. All reagents are kept in a glovebox under Argon to keep them absolutely dry.

The Mo-crucibles (25-mm outer diameter, 21-mm inner diameter, 180-mm overall length) were manufactured by eroding from a rod of pure Mo (Plansee, Austria). The crucible was heated in a radio frequency induction furnace applying two differently designed water-cooled coils. While the “reaction-coil” extends over of the full length of the crucible with 22 equally spaced windings, with the “melting-coil” the energy is concentrated by only 4 tight windings in a double-layer arrangement to a narrow zone, which allows the generation of temperatures of nearly 3000 °C, enough to melt Mo. To protect the crucible from oxidation at high temperatures it is placed in a quartz tube under high vacuum ( $< 10^{-4}$  Torr). The quartz tube itself is cooled with a flow of air to prevent crystallization caused by the high heat radiation during synthesis.

Prior to synthesis, the crucible and the conical lid were heated in a vertical position with the reaction-coil to approximately



## communications

1600 °C for cleaning purposes. After stocking with reagents and prior to closing the crucible, residual water adsorbed on the surfaces was removed by heating the upper rim of the crucible to approximately 700 °C for 20 min applying the melting-coil followed by cooling under vacuum. Applying short radiation pulses of less than 40 s the lid is then welded onto the crucible, yielding a gas-tight reaction vessel.

After sealing, the crucible is heated with the reaction-coil at 1900 °C for 20 min and then the melt is quenched by switching off the radio frequency. To minimize inhomogeneities in composition within the product volume, the crucible was subsequently transferred to an Argon floated graphite rotary kiln (60 rpm) and heated to 1750 °C for 60 min. Finally, the fluorohectorites were crystallized by switching off the power supply and letting it slowly cool in the graphite oven while continuing rotation.

**Sample Preparation and Force Measurements:** The dry smectite as obtained by melt synthesis was immersed in deionized water to swell. The suspensions were washed thoroughly to remove the colloidal fraction and the coarse fraction was collected by centrifugation. To confirm the hydration state, a textured sample was prepared on a glass substrate by drying a suspension at 120 °C. Finally, the sample was equilibrated for two days at room conditions (25 °C, 32% r.h.). The powder X-ray diffraction pattern was collected in Bragg–Brentano geometry (X'Pert Pro (PANalytical)) using CuK $\alpha$  radiation. The microstructured silicon substrates for the bending tests were purchased from GeSiM, (Großberkmannsdorf, Germany). The structure was obtained with lithography and exhibited 10- $\mu$ m broad bars separated by channels 2  $\mu$ m in diameter. For force spectroscopy measurements an MFP3D™ AFM (Asylum Research, Santa Barbara, California) with Silicon cantilevers (Silicon tip, type NSC15/ALBS, typical  $k_c = 46$  Nm<sup>-1</sup>,  $\mu$ mash, Tallinn, Estonia) was used. Field-emission SEM (FESEM) was performed using a LEO Gemini microscope 1530 equipped with a field emission cathode. In order to prepare a sample for the bending test a very dilute suspension of Na<sub>0.5</sub>-fluorohectorite (<10  $\mu$ g L<sup>-1</sup>) was dropped onto the microstructured substrate that was previously cleaned according to the RCA-method.<sup>[43]</sup> Finally it was slowly dried in a closed Petri dish.

**Keywords:**

atomic force microscopy · bending tests · clays · elastic constants · nanocomposites

- [1] B. Xu, Q. Zheng, Y. H. Song, Y. Shanguan, *Polymer* **2006**, *47*, 2904–2910.
- [2] G. Beyer, *J. Fire Sci.* **2005**, *23*, 75–87.
- [3] M. Kurian, M. E. Galvin, P. E. Trapa, D. R. Sadoway, A. M. Mayes, *Electrochim. Acta* **2005**, *50*, 2125–2134.
- [4] L. A. Goettler, K. Y. Lee, H. Thakkar, *Polym. Rev.* **2007**, *47*, 291–317.
- [5] Z. Y. Tang, N. A. Kotov, S. Magonov, B. Ozturk, *Nat. Mater.* **2003**, *2*, 413–418.
- [6] P. Podsiadlo, A. K. Kaushik, E. M. Arruda, A. M. Waas, B. S. Shim, J. D. Xu, H. Nandivada, B. G. Pumplun, J. Lahann, A. Ramamoorthy, N. A. Kotov, *Science* **2007**, *318*, 80–83.
- [7] P. Podsiadlo, Z. Y. Tang, B. S. Shim, N. A. Kotov, *Nano Lett.* **2007**, *7*, 1224–1231.
- [8] J. E. F. C. Gardolinski, G. Lagaly, *Clay Miner.* **2005**, *40*, 547–556.
- [9] D. A. Laird, *Appl. Clay Sci.* **2006**, *34*, 74–87.
- [10] A. Cadene, S. Durand-Vidal, P. Turq, J. Brendle, *J. Colloid Interface Sci.* **2005**, *285*, 719–730.
- [11] B. Kracke, B. Damaschke, *Appl. Phys. Lett.* **2000**, *77*, 361–363.
- [12] K. Devineau, I. Bihannic, L. Michot, F. Villieras, F. Masrouji, O. Cuisinier, G. Fragneto, N. Michau, *Appl. Clay Sci.* **2006**, *31*, 76–84.
- [13] B. Q. Chen, J. R. G. Evans, *Scr. Mater.* **2006**, *54*, 1581–1585.
- [14] O. L. Manevitch, G. C. Rutledge, *J. Phys. Chem. B* **2004**, *108*, 1428–1435.
- [15] J. L. Suter, P. V. Coveney, H. C. Greenwell, M. A. Thyveetil, *J. Phys. Chem. C* **2007**, *111*, 8248–8259.
- [16] M. Prasad, M. Kopycinska, U. Rabe, W. Arnold, *Geophys. Res. Lett.* **2002**, *29*, 1172–1175.
- [17] T. Vanorio, M. Prasad, A. Nur, *Geophys. J. Int.* **2003**, *155*, 319–326.
- [18] Z. J. Wang, H. Wang, M. E. Cates, *Geophysics* **2001**, *66*, 428–440.
- [19] A. R. Pawley, S. M. Clark, N. J. Chinnery, *Am. Mineral.* **2002**, *87*, 1172–1182.
- [20] A. Pavese, G. Ferraris, V. Pischedda, M. Mezouar, *Phys. Chem. Miner.* **1999**, *26*, 460–467.
- [21] J. R. Smyth, S. D. Jacobsen, R. J. Swope, R. J. Angel, T. Arlt, K. Domanik, J. R. Holloway, *Eur. J. Mineral.* **2000**, *12*, 955–963.
- [22] J. Faust, E. Knittle, *J. Geophys. Res.* **1994**, *99*, 19785–19792.
- [23] K. S. Aleksandrov, T. V. Ryzhova, *Bull. Acad. Sci. USSR, Geophys. Ser.* **1961**, *12*, 1165–1168. Cited after Reference [13].
- [24] D. R. Collins, W. G. Stirling, C. R. A. Catlow, G. Rowbotham, *Phys. Chem. Miner.* **1993**, *19*, 520–527.
- [25] L. E. Mcneil, M. Grimsditch, *J. Phys. Condens. Matter* **1993**, *5*, 1681–1690.
- [26] M. T. Vaughan, S. Guggenheim, *J. Geophys. Res.* **1986**, *91*, 4657–4664.
- [27] D. R. Collins, C. R. A. Catlow, *Am. Mineral.* **1992**, *77*, 1172–1181.
- [28] R. D. Piner, T. T. Xu, F. T. Fisher, Y. Qiao, R. S. Ruoff, *Langmuir* **2003**, *19*, 7995–8001.
- [29] G. Zhang, Z. Wei, R. E. Ferrell, *Appl. Clay Sci.* **2009**, *43*, 271–281.
- [30] N. Malikova, A. Cadene, E. Dubois, V. Marry, S. Durand-Vidal, P. Turq, J. Breu, S. Longeville, J. M. Zanotti, *J. Phys. Chem. C* **2007**, *111*, 17603–17611.
- [31] V. Marry, N. Malikova, A. Cadene, E. Dubois, S. Durand-Vidal, P. Turq, J. Breu, S. Longeville, J. M. Zanotti, *J. Phys. Condens. Matter* **2008**, *20*, 104205.
- [32] S. Timoshenko, S. Woinowsky-Krieger, *Theory of Plates and Shells*, 2nd ed. McGraw-Hill Book Company, Singapore **1959**, p. 143.
- [33] *Fundamentals of Crystallography*, (Ed.: C. Giacovazzo), Oxford University Press, New York **1992**, pp. 599–643.
- [34] A. F. Holleman, E. Wiberg, N. Wiberg, *Lehrbuch der Anorganischen Chemie*, 102 nd ed., Walter de Gruyter & Co, Berlin **2007**.
- [35] *Tonminerale und Tone: Struktur, Eigenschaften, Anwendungen und Einsatz in Industrie und Umwelt*, (Eds: G. Jasmund, G. Lagaly), Steinkopff Verlag GmbH & Co. KG, Darmstadt **1993**.
- [36] J. Y. Park, N. Lee, *J. Reinf. Plast. Compos.* **2007**, *26*, 601–616.
- [37] R. Mariychuk, A. Baumgartner, F. E. Wagner, A. Lerf, A. Dubbe, R. Moos, J. Breu, *Chem. Mater.* **2007**, *19*, 5377–5387.
- [38] M. Stöcker, W. Seidl, L. Seyfarth, J. Senker, J. Breu, *Chem. Commun.* **2008**, 629–631.
- [39] A. Baumgartner, K. Sattler, J. Thun, J. Breu, *Angew. Chem. Int. Ed.* **2008**, *47*, 1640–1644.
- [40] F. Leroux, J. P. Besse, *Chem. Mater.* **2001**, *13*, 3507–3515.
- [41] M. A. Thyveetil, P. V. Coveney, J. L. Suter, H. C. Greenwell, *Chem. Mater.* **2007**, *19*, 5510–5523.
- [42] J. Breu, W. Seidl, A. J. Stoll, K. G. Lange, T. U. Probst, *Chem. Mater.* **2001**, *13*, 4213–4220.
- [43] B. C. Donose, E. Taran, I. U. Vakarelski, H. Shinto, K. Higashitani, *J. Colloid Interface Sci.* **2006**, *299*, 233–237.

Received: November 17, 2008  
 Revised: March 10, 2009  
 Published online: April 21, 2009

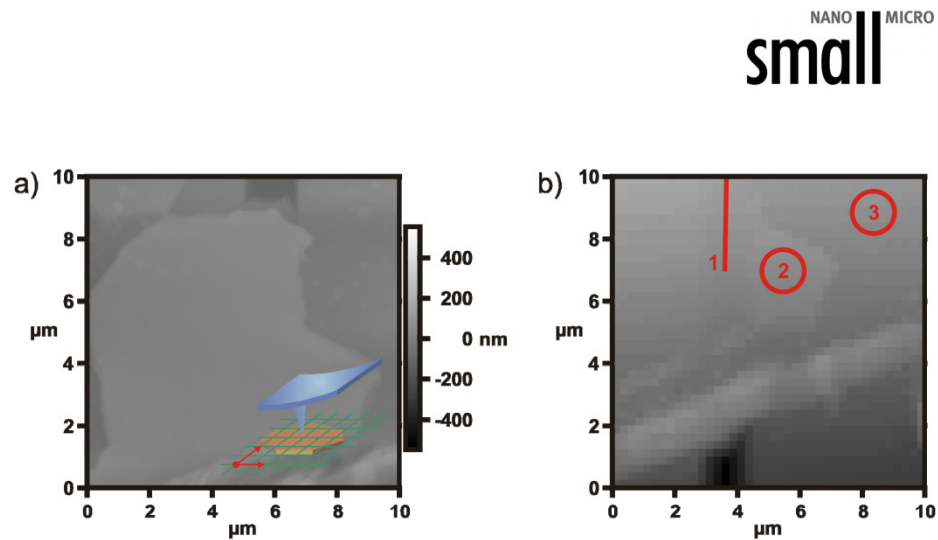
6.2.2 Supporting Information



## Supporting Information

### Deformation Measurements on Thin Clay Tactoids

*Daniel A. Kunz, Eva Max, Richard Weinkamer, Thomas Lunkenbein,  
Josef Breu,\* and Andreas Fery\**



**Scheme S1.** a) AFM height image of a tactoid lying over a gap; inset: scheme of the force mapping procedure; b) reconverted quasi-topographical image after the force mapping; each pixel represents a force- deformation curve; red: investigated areas, tactoid areas positioned above a gap (1) and the two references, namely platelet resting on substrate (2) and pure uncovered substrate (3).

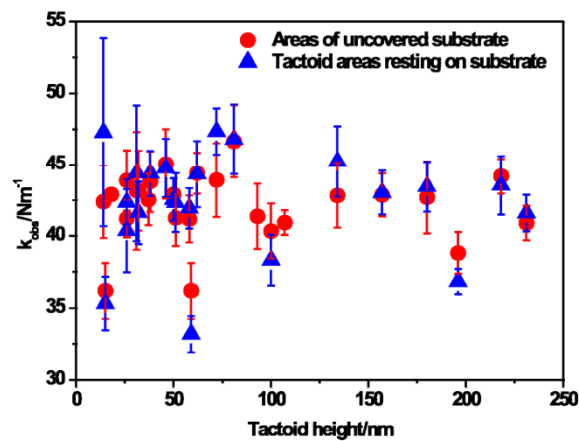


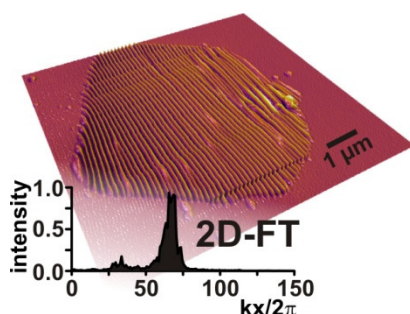
**Figure S1.** Reference plot of the averaged slopes of the force-piezo displacement curves at different tactoid heights; indentation can be ruled out.

### 6.3 *Mechanische Eigenschaften einer einzelnen Silicatlamelle durch kontrollierte Faltung*

Daniel A. Kunz<sup>†</sup>, Daniel Kluge<sup>‡</sup>, Herbert Thurn<sup>§</sup>, Andreas Fery<sup>‡,\*</sup>, and Josef Breu<sup>†,\*</sup>

#### **In-plane Modulus of Singular 2:1-Clay Lamellae Applying a Simple Wrinkling Technique**

Erschienen in: *ACS Applied Materials and Interfaces* **2013**, 5, 5851-5855. Reprinted with permission, Copyright (2013) American Chemical Society.



<sup>†</sup> Lehrstuhl für Anorganische Chemie I, Universität Bayreuth, 95447 Bayreuth, Deutschland

<sup>‡</sup> Lehrstuhl für Physikalische Chemie II, Universität Bayreuth, 95447 Bayreuth, Deutschland

<sup>§</sup> Rechenzentrum, Universität Bayreuth, 95447 Bayreuth, Deutschland

\* josef.breu@uni-bayreuth.de; andreas.fery@uni-bayreuth.de

#### **Darstellung des Eigenanteils:**

Das Konzept dieser Publikation wurde von Prof. Dr. *Andreas Fery* und mir selbst entwickelt. Weiterhin etablierte ich die Methode hinsichtlich der untersuchten Materialien und führte sämtliche Messungen durch. Dr. *Herbert Thurn* unterstützte mich in der Entwicklung eines Programmes zur automatisierten Datenauswertung. *Daniel Kluge* lieferte Beiträge zur Plattentheorie, *Johann Erath* half bei der E-Modul Bestimmung des Substrates und *Bernd Putz* synthetisierte das Rohmaterial. Verfasst wurde diese Publikation hauptsächlich von Prof. Dr. *Josef Breu*, Prof. Dr. *Andreas Fery* und mir.

Mein Eigenanteil beläuft sich auf ca. 80 %.



### 6.3.1 In-plane Modulus of Singular 2:1-Clay Lamellae Applying a Simple Wrinkling Technique

ACS **APPLIED MATERIALS**  
& **INTERFACES**


Research Article

www.acsami.org

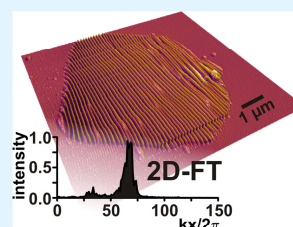
## In-Plane Modulus of Singular 2:1 Clay Lamellae Applying a Simple Wrinkling Technique

Daniel A. Kunz,<sup>†</sup> Johann Erath,<sup>†</sup> Daniel Kluge,<sup>‡</sup> Herbert Thurn,<sup>§</sup> Bernd Putz,<sup>†</sup> Andreas Fery,<sup>\*,‡</sup> and Josef Breu<sup>\*,†</sup>

<sup>†</sup>Department of Inorganic Chemistry I, <sup>‡</sup>Department of Physical Chemistry II, and <sup>§</sup>Computing Center, University of Bayreuth, Universitätsstraße 30, D-95440 Bayreuth, Germany

 Supporting Information

**ABSTRACT:** Knowledge of the mechanical properties of singular clay lamellae is of crucial importance for the optimization of clay–polymer nanocomposites. On the basis of controlled stress release, singular 2:1 clay lamellae show regular wrinkles on a deformable substrate. A subsequent two-dimensional Fourier transformation gives an in-plane modulus of the clay lamella of approximately 150 GPa. Only readily-available topographical atomic force microscopy is required for analysis rendering that fast and facile procedure generally applicable for nanoplatelet characterization.



**KEYWORDS:** nanomechanics, wrinkling, nanoplatelet, clay, nanocomposite, AFM

### ■ INTRODUCTION

A plethora of nanocomposites contain clay platelets as functional compounds embedded in a variety of polymer matrixes. Besides electric,<sup>1</sup> fire-retardant,<sup>2,3</sup> and gas-barrier properties,<sup>4,5</sup> the most prominent function of clay fillers is mechanical reinforcement of nanocomposites.<sup>6</sup> Along that line, tremendous improvements of mechanical performance have been reported for ultrastrong, clay-based artificial nacre.<sup>7,8</sup>

In general, with fixed filler content, the performance of nanocomposites may be optimized by tuning four crucial factors regarding the clay filler: perfect texture, maximized aspect ratio, smart interface management, and excellent mechanical properties. The aspect ratio of layered 2:1 silicates may be easily modified for swelling clays like montmorillonite or hectorite by exfoliation or delamination,<sup>9</sup> which is fostered by the extensive intercalation chemistry. Contrary to swelling clays, structurally related nonswelling micas come with nonadjustable thickness of the platelets. As a consequence of the stronger interaction along the stacking direction, micas can, however, be obtained in crystals of appreciable thickness (>10 μm). The potential reinforcement of platy fillers, as given, e.g., by the Halpin–Tsai equations,<sup>10</sup> is determined by the aspect ratio and the ratio of the moduli of filler and matrix. However, clays, as any layered filler, are highly anisotropic, and the elastic constants differ by more than a factor of 3. While the elastic moduli of coarse-grained materials like mica have been determined, constants for completely delaminated singular clay lamellae, which are advantageous because of their maximized aspect ratio, would actually be needed. Usually bulk methodologies have been applied to obtain information on the mechanical properties of different types of clays,<sup>11</sup> ranging

from compressibility measurements<sup>12–15</sup> to the extrapolation of data from epoxy–clay hybrids,<sup>16</sup> or acoustic measurements.<sup>17,18</sup>

Not surprisingly, the most reliable bulk elastic constants of 2:1 layered silicates have been obtained for coarse-grained micas via ultrasonic measurements,<sup>19</sup> inelastic neutron scattering,<sup>20</sup> and Brillouin scattering.<sup>21,22</sup> Results of computer simulations agree well with these experimental constants.<sup>23</sup> Knowledge about the elastic properties of swelling clay platelets that are actually used as fillers in nanocomposites because of the superior aspect ratio, however, is scarce. We recently determined, for the first time, the bending modulus of single hectorite tactoids, which represent semiordered crystals consisting of randomly oriented stacks of several individual 2:1 lamellae separated by hydrated interlayer cations. Atomic force microscopy (AFM)-based deformation measurements gave a significantly lower bending modulus for these hydrated clays than values reported for other types of nonswelling clays.<sup>24</sup> We proposed that the main reason for the surprisingly low modulus was the combination of hydration of interlayer cations and the decreased layer charge compared to that of micas in these swelling clays. Both effects lead to an increased contribution of shearing to bending deformations and therefore to a lower apparent bending modulus.<sup>25</sup> Because this effect will also be effective in composites, it will therefore reduce the efficiency of tactoids as filler material. In particular, tactoids thinner than 20 nm were found to be very flexible, and reinforcement of nanocomposites in a direction perpendicular

Received: April 24, 2013

Accepted: May 29, 2013

Published: May 29, 2013



ACS Publications

© 2013 American Chemical Society

5851

dx.doi.org/10.1021/am4015204 | ACS Appl. Mater. Interfaces 2013, 5, 5851–5855

to the platelets would be expected to be rather low. To calculate the reinforcement potential for real nanocomposites with more or less randomly oriented fillers, knowledge of the in-plane moduli of delaminated 2:1 lamellae, where no interlayer shearing can occur, is needed as well.

Such measurements, however, require a metrology that allows for orientation of singular 2:1 lamellae and that is able to cope with the compliant nature of such 1 nm thin nanoplatelets. In very demanding and impressive computer simulations of a single montmorillonite lamella by Suter et al.,<sup>26</sup> undulations caused by thermal fluctuations were observed, from which they were able to derive the in-plane modulus (230 GPa).

Analogously, it is possible to determine the in-plane modulus from forced undulations, which are also called wrinkles. The general idea of buckling-based metrology is the planar compression of a thin, stiff coating on a thicker, compliant substrate like poly(dimethylsiloxane) (PDMS). The wrinkling technique is well established for thin-film metrology<sup>27,28</sup> and in structure formation and patterning.<sup>29–31</sup> More recently, Reyes-Martinez et al. revealed in an intriguing investigation the elastic constants of rubrene microcrystals by the same technique.<sup>32</sup> Here we show that the wrinkling approach can even be transferred to single nanoplatelets of clays. The sought-after in-plane modulus of the nanoplatelet  $E_p$  depends on the characteristic wrinkling wavelength  $\lambda$ , on the platelet thickness  $h$ , and on Young's modulus  $E_s$  of the substrate:<sup>33,34</sup>

$$E_p = \frac{3E_s(1 - \nu_p^2)}{(1 - \nu_s^2)} \left( \frac{\lambda}{2\pi h} \right)^3 \quad (1)$$

where  $\nu_p$  and  $\nu_s$  refer to Poisson's ratios of nanoplatelet and substrate, respectively.

Simple topographical AFM imaging of the wrinkled platelets is sufficient to retrieve the in-plane modulus (Figure 1).

## ■ RESULTS AND DISCUSSION

Melt synthesis,<sup>35–37</sup> followed by long-time annealing, yielded sodium fluorohectorite ( $\text{Na}_{0.5}\text{Li}_{0.5}\text{Mg}_{2.5}\text{Si}_4\text{O}_{10}\text{F}_2$ , Na-hec) with lateral extensions of several micrometers and high intracrystalline reactivity.<sup>38</sup> This Na-hec spontaneously delaminates in water by osmotic swelling.<sup>39</sup> The van der Waals height of the silicate lamella deprived of hydrated counterions can be derived from the basal spacing of nonhydrated sodium hectorite to be 0.96 nm<sup>37</sup> (Figure 2).

A droplet of a diluted Na-hec suspension was placed onto a hydrophilized slab of PDMS that was uniaxially stretched with a customer-made apparatus (Figure S1, Supporting Information). After gentle drying and stress release, the sample was analyzed via AFM imaging. The results are shown in Figure 1. The hectorite lamella exhibited a uniformly wrinkled morphology, while the noncovered surface areas of the PDMS substrate remained featureless (Figure 1a). To recover the wavelength of the wrinkles, the recorded image was processed with a discrete two-dimensional Fourier transformation (2D-FT; see the Supporting Information for details). Figure 1b shows an intensity profile in reciprocal space along the axis of stress release ( $kx$ ). It was integrated over a range of  $-5$  to  $+5$   $ky$  values considering also the wrinkles that are slightly tilted away from  $90^\circ$ . The main peak corresponds to a wrinkling wavelength of 149 nm. Taking the same layer thickness as Suter et al.<sup>26</sup> and Kalo et al.<sup>37</sup> (0.96 nm) and applying eq 1 yielded an in-plane modulus of 143 GPa. Poisson's ratios of

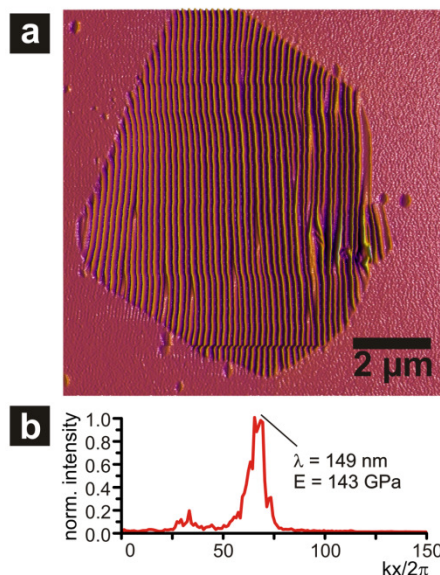


**Figure 1.** (a) AFM topographical image of a typical wrinkled Na-hec nanoplatelet on a featureless PDMS surface. (b) Normalized intensity profile after 2D-FT along  $kx$ , integrated over a range of  $-5$  to  $+5$   $ky$  values, that considers also the wrinkles that are slightly tilted away from  $90^\circ$ . The peak represents a wrinkling wavelength of 149 nm corresponding to an in-plane modulus of 143 GPa.

0.5<sup>40</sup> and 0.3<sup>41</sup> for substrate and clay, respectively, were used. The Young's modulus of the PDMS substrate was measured to be  $2.6 \pm 0.1$  MPa by applying a standard tensile test (see the Supporting Information). It has, however, been reported in the literature that low-molecular-weight species, e.g., non-cross-linked precursors, slowly migrate to the surface of PDMS and soften the local modulus.<sup>42</sup> Because this local surface modulus is actually the relevant modulus for the wrinkling metrology, it was additionally measured with a surface-selective metrology (colloidal-probe AFM<sup>43–45</sup>). While for a PDMS substrate aged for some months, the surface modulus was found to have decreased by 50%, for freshly prepared samples the bulk Young's modulus determined by tensile tests and the surface modulus determined by colloidal-probe AFM agree within experimental error. Therefore, it is strongly recommended to either use freshly prepared PDMS slabs (<2 weeks) for wrinkling metrology or determine the Young's modulus of the substrate's surface via colloidal-probe AFM.

In a recent work, Fu et al.<sup>46</sup> determined the minimum radius of curvature for a single clay lamella before failure to be 3 nm. That suggests that the deformations induced by wrinkling were clearly within the elastic regime. For instance, the radius of curvature of the wavelength observed in Figure 1 approximated by a sine wave with a wavelength of 149 nm and an amplitude of 18 nm yields a value of 31 nm (see the Supporting Information for details). A cross section of a wrinkled nanoplatelet (Figure S2, Supporting Information) shows a sine-wave profile, indicating that the clay lamella is completely adhered to the PDMS substrate by a strong cohesion.

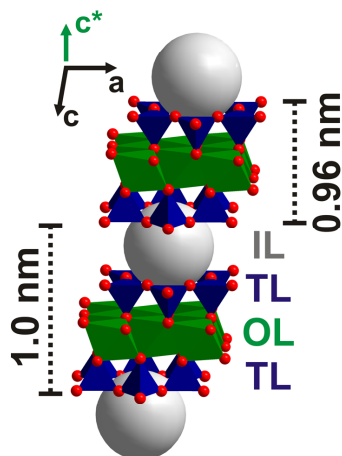


**Figure 2.** Structural representation of a mica crystal showing the two-dimensional, partially covalent Kagome network of basal oxygen atoms (TL) in combination with the trioctahedral layer (OL) connecting the two tetrahedral layers; the van der Waals height of the silicate lamella deprived of hydrated counterions is 0.96 nm.<sup>26,37</sup> The periodicity (basal spacing) of mica is, however, slightly larger (1.0 nm<sup>48</sup>) than the height of the 2:1 lamella because the structure represents a sandwich with the interlayer space (IL). The view is along the *b* axis; *c\** represents the stacking direction of the crystal.

The FT peak indicated a uniform wrinkling wavelength throughout the whole lamella. The whole set of investigated platelets showed a uniform stiffness, suggesting that they were defect-free and are structurally homogeneous, with no clustering of isomorphous substitution. The latter statement is in line with a homogeneous charge density, as proven by a uniform intracrystalline reactivity of all interlayer spaces (ILs) reported earlier.<sup>35,36,47</sup>

Averaging the values of 16 hectorite monolayers yielded a mean in-plane modulus of  $142 \pm 17$  GPa. The in-plane modulus found for a singular hectorite lamella is somewhat lower than those reported for in-plane moduli of various micas (average of  $C_{11}$  and  $C_{22}$  constants:  $178.5 \pm 1.5$  GPa).<sup>19–22</sup> The mica structure can be regarded as a sandwich of relatively soft ILs and stiff silicate lamellae, resulting in a total basal spacing *d* of 1.0 nm<sup>48</sup> (Figure 2).

This sandwich construction might therefore lead to a certain stiffening of the bulk material,<sup>49</sup> as is known from light-weight construction materials.

Although it has been reported in the literature that hydrophilization of the PDMS substrate by HCl treatment does not affect the bulk modulus of PDMS significantly,<sup>40</sup> a minor change in the bulk modulus cannot be ruled out. A study with different durations of HCl treatment showed that the systematic error introduced would, however, be insignificant compared to possible errors related to uncertainties in the determination of the height of the platelets (Figure S4, Supporting Information). Averaging the values of five hectorite monolayers suspended on PDMS hydrophilized for 32 h instead of 16 h yielded a mean in-plane modulus of  $154 \pm 11$  GPa.

The wrinkling wavelength is dependent on the strain, and eq 1 applied by us may be regarded as a first-order approximation. Because of the platelet thickness of  $<1$  nm, the wrinkling metrology is pushed to its limit. Because the amplitude of the sine wave is directly related to the ratio of the Young's moduli of the substrate and clay platelet and the platelet height, a strain of  $>30\%$  was necessary for a reliable measurement of the wavelength for these thin platelets. Unfortunately, no experimental values for the in-plane modulus of a single hectorite lamella are available in the literature to serve as a benchmark. We were, however, recently able to determine in-plane moduli of graphene oxide, chemically derived graphene, and CVD-graphene nanoplatelets by applying the very same method.<sup>50</sup> For these materials, independently measured reference values were available and could be reproduced with the wrinkling metrology with high accuracy. Moreover, in molecular dynamics simulations, spontaneous undulations were observed, and upon analysis of this buckling of clay nanoplatelets,<sup>26</sup> an in-plane modulus in fair agreement with our measurements could be derived (230 GPa).

When the strain-corrected models published by Rogers et al.<sup>51</sup> were applied, the effective wrinkling wavelength would be drastically enhanced, corresponding to a significantly higher in-plane modulus of  $357 \pm 42$  GPa for hectorite platelets. However, our own preliminary results suggest that the strain dependency is significantly lower than those suggested by Rogers et al. Given the reasonable agreement with benchmark values available for other materials and with simulation results on clays, we refrain from applying corrections to eq 1.

The stiffness of the silicate lamella is assured by the two-dimensional, partially covalent Kagome network of basal oxygen atoms in combination with the trioctahedral layer connecting the two tetrahedral layers (Figure 2). Nevertheless, typical purely covalent two-dimensional networks like graphene still have an in-plane modulus approximately 8 times as high.<sup>52</sup>

Most of the moderate scatter of the wrinkling wavelengths is attributed to the slight tilt of the wavevector away from the axis of stress release. Another cause of scatter inherent to the wrinkling metrology is stochastically occurring local stress release by platelet breakage instead of wrinkling (Figure S3, Supporting Information), in particular, because additional edges are generated by the line defects, which can be attributed to defects in the platelet under tension (Poisson's expansion upon compression of the PDMS). It has been shown that these cracks do not directly influence the wrinkling wavelength.<sup>31,53</sup> These line defects, as well as the edges of the platelets, are, of course, expected to show lower moduli compared to undisturbed core areas, which is realized in a certain full width at half-maximum of the FT peak (Figure 1b).

## CONCLUSION

The wrinkling method can easily be applied to any kinds of nanoplatelets, such as transition-metal sulfides and selenides,<sup>54–56</sup> layered double hydroxides, and, as already mentioned, graphene materials.<sup>50,52</sup> The great appeal of a simple approach requiring only standard and affordable AFM analytics renders the presented method a powerful tool that could be used as a quite ubiquitous, fast, low-cost, and facile standard method for large-scale mechanical characterization of nanoplatelets.<sup>50</sup>

## ■ ASSOCIATED CONTENT

## ■ Supporting Information

Materials and methods, additional analytical details, and supplementary figures and references. This material is available free of charge via the Internet at <http://pubs.acs.org>.

## ■ AUTHOR INFORMATION

## Corresponding Author

\*E-mail: andreas.fery@uni-bayreuth.de (A.F.), josef.breu@uni-bayreuth.de (J.B.). Phone: +49 921 55 2753 (A.F.), +49 921 55 2531 (J.B.). Fax: +49 921 55 2059 (A.F.), +49 921 55 2788 (J.B.).

## Author Contributions

The manuscript was written through contributions of all authors. All authors have given approval to the final version of the manuscript.

## Notes

The authors declare no competing financial interest.

## ■ ACKNOWLEDGMENTS

This work was supported by the German Science Foundation (Grant SFB 840). D.A.K. thanks the elite study program "Macromolecular Science" as well as the International Graduate School "Structure, Reactivity and Properties of Oxide Materials" within the Elite Network of Bavaria for ongoing support. Kai-Uwe Claussen and Andreas Schedl are gratefully acknowledged for helping with the PDMS tensile tests.

## ■ DEDICATION

Dedicated to Professor Wolfgang Bensch on the occasion of his 59th birthday.

## ■ REFERENCES

- (1) Kurian, M.; Galvin, M. E.; Trapa, P. E.; Sadoway, D. R.; Mayes, A. M. *Electrochim. Acta* **2005**, *50*, 2125–2134.
- (2) Schutz, M. R.; Kalo, H.; Lunkenbein, T.; Breu, J.; Wilkie, C. A. *Polymer* **2011**, *52*, 3288–3294.
- (3) Schutz, M. R.; Kalo, H.; Lunkenbein, T.; Groschel, A. H.; Müller, A. H. E.; Wilkie, C. A.; Breu, J. *J. Mater. Chem.* **2011**, *21*, 12110–12116.
- (4) Moller, M. W.; Kunz, D. A.; Lunkenbein, T.; Sommer, S.; Nennemann, A.; Breu, J. *Adv. Mater.* **2012**, *24*, 2142–2147.
- (5) Kunz, D. A.; Schmid, J.; Feicht, P.; Erath, J.; Fery, A.; Breu, J. *ACS Nano* **2013**, *7*, 4275–4280.
- (6) Goettler, L. A.; Lee, K. Y.; Thakkar, H. *Polym. Rev. (Philadelphia, PA, U. S.)* **2007**, *47*, 291–317.
- (7) Tang, Z. Y.; Kotov, N. A.; Magonov, S.; Ozturk, B. *Nat. Mater.* **2003**, *2*, 413–418.
- (8) Podsiadlo, P.; Kaushik, A. K.; Arruda, E. M.; Waas, A. M.; Shim, B. S.; Xu, J. D.; Nandivada, H.; Pumphlin, B. G.; Lahann, J.; Ramamoorthy, A.; Kotov, N. A. *Science* **2007**, *318*, 80–83.
- (9) Gardolinski, J. E. F. C.; Lagaly, G. *Clay Miner.* **1985**, *40*, 547–556.
- (10) Halpin, J. C.; Kardos, J. L. *Polym. Eng. Sci.* **1976**, *16*, 344–352.
- (11) Chen, B. Q.; Evans, J. R. G. *Scr. Mater.* **2006**, *54*, 1581–1585.
- (12) Pawley, A. R.; Clark, S. M.; Chinnery, N. J. *Am. Mineral.* **2002**, *87*, 1172–1182.
- (13) Pavese, A.; Ferraris, G.; Pischedda, V.; Mezouar, M. *Phys. Chem. Miner.* **1999**, *26*, 460–467.
- (14) Smyth, J. R.; Jacobsen, S. D.; Swope, R. J.; Angel, R. J.; Arlt, T.; Domanik, K.; Holloway, J. R. *Eur. J. Mineral.* **2000**, *12*, 955–963.
- (15) Faust, J.; Knittle, E. J. *Geophys. Res.: Solid Earth* **1994**, *99*, 19785–19792.
- (16) Wang, Z. J.; Wang, H.; Cates, M. E. *Geophysics* **2001**, *66*, 428–440.
- (17) Prasad, M.; Kopycinska, M.; Rabe, U.; Arnold, W. *Geophys. Res. Lett.* **2002**, *29*, 1172–1175.
- (18) Vanorio, T.; Prasad, M.; Nur, A. *Geophys. J. Int.* **2003**, *155*, 319–326.
- (19) Aleksandrov, K. S.; Ryzhova, T. V. *Bull. Acad. Sci. USSR, Geophys. Ser.* **1961**, *12*, 1165–1168.
- (20) Collins, D. R.; Stirling, W. G.; Catlow, C. R. A.; Rowbotham, G. *Phys. Chem. Miner.* **1993**, *19*, 520–527.
- (21) McNeil, L. E.; Grimsditch, M. *J. Phys.: Condens. Matter* **1993**, *5*, 1681–1690.
- (22) Vaughan, M. T.; Guggenheim, S. *J. Geophys. Res.: Solid Earth* **1986**, *91*, 4657–4664.
- (23) Collins, D. R.; Catlow, C. R. A. *Am. Mineral.* **1992**, *77*, 1172–1181.
- (24) Kunz, D. A.; Max, E.; Weinkamer, R.; Lunkenbein, T.; Breu, J.; Fery, A. *Small* **2009**, *5*, 1816–1820.
- (25) Whitney, J. M. *Structural Analysis of Laminated Isotropic Plates*; Technomic Publishing Company, Inc.: Philadelphia, PA, 1987; p 263.
- (26) Suter, J. L.; Coveney, P. V.; Greenwell, H. C.; Thyveetil, M. A. *J. Phys. Chem. C* **2007**, *111*, 8248–8259.
- (27) Stafford, C. M.; Harrison, C.; Beers, K. L.; Karim, A.; Amis, E. J.; Vanlandingham, M. R.; Kim, H. C.; Volksen, W.; Miller, R. D.; Simonyi, E. E. *Nat. Mater.* **2004**, *3*, 545–550.
- (28) Bowden, N.; Brittain, S.; Evans, A. G.; Hutchinson, J. W.; Whitesides, G. M. *Nature* **1998**, *393*, 146–149.
- (29) Lu, C. H.; Mohwald, H.; Fery, A. *Soft Matter* **2007**, *3*, 1530–1536.
- (30) Genzer, J.; Groenewold, J. *Soft Matter* **2006**, *2*, 310–323.
- (31) Pretzl, M.; Schweikart, A.; Hanske, C.; Chiche, A.; Zettl, U.; Horn, A.; Böker, A.; Fery, A. *Langmuir* **2008**, *24*, 12748–12753.
- (32) Reyes-Martinez, M. A.; Ramasubramanian, A.; Briseno, A. L.; Crosby, A. J. *Adv. Mater.* **2012**, *24*, 5548–5552.
- (33) Huang, R. J. *Mech. Phys. Solids* **2005**, *53*, 63–89.
- (34) Groenewold, J. *Physica A* **2001**, *298*, 32–45.
- (35) Breu, J.; Seidl, W.; Stoll, A. J.; Lange, K. G.; Probst, T. U. *Chem. Mater.* **2001**, *13*, 4213–4220.
- (36) Kalo, H.; Möller, M. W.; Ziadeh, M.; Dolejs, D.; Breu, J. *Appl. Clay Sci.* **2010**, *48*, 39–45.
- (37) Kalo, H.; Milius, W.; Breu, J. *RSC Adv.* **2012**, *2*, 8452–8459.
- (38) Stöter, M.; Kunz, D. A.; Schmidt, M.; Hirsemann, D.; Kalo, H.; Putz, B.; Senker, J.; Breu, J. *Langmuir* **2013**, 1280–1285.
- (39) *Tomminerale und Tone: Struktur, Eigenschaften, Anwendungen und Einsatz in Industrie und Umwelt*; Jasmund, K., Lagaly, G., Eds.; Steinkopff Verlag GmbH & Co. KG: Darmstadt, Germany, 1993; p 110.
- (40) Huang, H.; Chung, J. Y.; Nolte, A. J.; Stafford, C. M. *Chem. Mater.* **2007**, *19*, 6555–6560.
- (41) Park, J. Y.; Lee, N. J. *Reinf. Plast. Compos.* **2007**, *26*, 601–616.
- (42) Hillborg, H.; Tomczak, N.; Olah, A.; Schönherr, H.; Vancso, G. J. *Langmuir* **2004**, *20*, 785–794.
- (43) Carrillo, F.; Gupta, S.; Balooch, M.; Marshall, S. J.; Marshall, G. W.; Pruitt, L.; Puttlitz, C. M. *J. Mater. Res.* **2005**, *20*, 2820–2830.
- (44) Trenkenschuh, K.; Erath, J.; Kuznetsov, V.; Gensel, J.; Boulmedais, F.; Schaaf, P.; Papastavrou, G.; Fery, A. *Macromolecules* **2011**, *44*, 8954–8961.
- (45) Gensel, J.; Dewald, L.; Erath, J.; Bethausen, E.; Müller, A. H. E.; Fery, A. *Chem. Sci.* **2013**, *4*, 325–334.
- (46) Fu, Y. T.; Zartman, G. D.; Yoonessi, M.; Drummy, L. F.; Heinz, H. J. *Phys. Chem. C* **2011**, *115*, 22292–22300.
- (47) Moller, M. W.; Hirsemann, D.; Haarmann, F.; Senker, J.; Breu, J. *Chem. Mater.* **2010**, *22*, 186–196.
- (48) Brigatti, M. F.; Guggenheim, S. *Micas: Crystal Chemistry & Metamorphic Petrology*; Mottana, A., Sassi, F. P., Thompson, J. B., Jr., Guggenheim, S., Eds.; Mineralogical Society of America: Washington, DC, 2002; p 1.
- (49) Möller, M. W.; Handge, U. A.; Kunz, D. A.; Lunkenbein, T.; Alstädt, V.; Breu, J. *ACS Nano* **2010**, *4*, 717–724.
- (50) Kunz, D. A.; Feicht, P.; Gödrich, S.; Thurn, H.; Papastavrou, G.; Fery, A.; Breu, J. *Adv. Mater.* **2012**, *25*, 1337–1341.

## ACS Applied Materials &amp; Interfaces

## Research Article

- (51) Jiang, H. Q.; Khang, D. Y.; Song, J. Z.; Sun, Y. G.; Huang, Y. G.; Rogers, J. A. *Proc. Natl. Acad. Sci. U.S.A.* **2007**, *104*, 15607–15612.
- (52) Lee, C.; Wei, X. D.; Kysar, J. W.; Hone, J. *Science* **2008**, *321*, 385–388.
- (53) Lee, J. H.; Chung, J. Y.; Stafford, C. M. *ACS Macro Lett.* **2011**, *1*, 122–126.
- (54) Coleman, J. N.; Lotya, M.; O'Neill, A.; Bergin, S. D.; King, P. J.; Khan, U.; Young, K.; Gaucher, A.; De, S.; Smith, R. J.; Shvets, I. V.; Arora, S. K.; Stanton, G.; Kim, H. Y.; Lee, K.; Kim, G. T.; Duesberg, G. S.; Hallam, T.; Boland, J. J.; Wang, J. J.; Donegan, J. F.; Grunlan, J. C.; Moriarty, G.; Shmeliov, A.; Nicholls, R. J.; Perkins, J. M.; Grievson, E. M.; Theuwissen, K.; McComb, D. W.; Nellist, P. D.; Nicolosi, V. *Science* **2011**, *331*, 568–571.
- (55) Zhon, K. G.; Mao, N. N.; Wang, H. X.; Peng, Y.; Zhang, H. L. *Angew. Chem., Int. Ed.* **2011**, *50*, 10839–10842.
- (56) Zeng, Z.; Yin, Z.; Huang, X.; Li, H.; He, Q.; Lu, G.; Boey, F.; Zhang, H. *Angew. Chem., Int. Ed.* **2011**, *50*, 11093–11097.



## 6.3.2 Supporting Information

## In-plane Modulus of Singular 2:1-Clay Lamellae

## Applying a Simple Wrinkling Technique

*Daniel A. Kunz,<sup>†</sup> Johann Erath,<sup>‡</sup> Daniel Kluge,<sup>‡</sup> Herbert Thurn,<sup>§</sup> Bernd Putz,<sup>†</sup> Andreas Fery,<sup>\*‡</sup>  
and Josef Breu<sup>\*†</sup>*

<sup>†</sup> Department of Inorganic Chemistry I, University of Bayreuth, Universitätsstraße 30, D-95440 Bayreuth, Germany.

<sup>‡</sup> Department of Physical Chemistry II, University of Bayreuth, Universitätsstraße 30, D-95440 Bayreuth, Germany.

<sup>§</sup> Computing Center, University of Bayreuth, Universitätsstraße 30, D-95440 Bayreuth, Germany

\* To whom correspondence should be addressed: andreas.fery@uni-bayreuth.de; josef.breu@uni-bayreuth.de

## Supplementary Information

## Contents:

1. Materials and Methods
2. Additional Analytical Details
3. Supplementary Figures
4. Supplementary References

## 1 Materials and Methods

*Preparation of substrates.* PDMS precursor (Dow Corning Sylgard 184) was mixed in a 10:1 mass ratio of oligomeric base to curing agent, degassed and poured into  $(60 \times 10 \times 2) \text{ mm}^3$  Teflon boats. After prehardening for 20 h at room temperature, the samples were post-treated for 2 h at  $150^\circ\text{C}$ . Tensile tests were carried out on an Instron 5565 universal tester with pneumatic clamps and a 100 N load cell (clamping distance 30 mm, strain rate  $200 \text{ mm min}^{-1}$ , see ISO 37:2005). The elastic moduli are calculated from the initial slope and averaged over 10 different samples ( $E_s = 2.6 \pm 0.1 \text{ MPa}$ ). While this tensile test yields the modulus of the bulk sample, additionally, the local modulus of the surface was determined by colloidal probe AFM measurements. To cross-check a possible dependency of the modulus on the duration of HCl-treatment, PDMS substrates (see *preparation of the wrinkles*) were treated for 16 h and 32 h. Again applying colloidal probe AFM measurements, the same elastic modulus ( $E_s = 2.6 \pm 0.1 \text{ MPa}$ ) was found at the surface of both samples, indicating that the duration of treatment has no significant influence.

*Synthesis of  $\text{Na}_{0.5}$ -fluorohectorite.* The employed  $\text{Na}_{0.5}$ -fluorohectorite with stoichiometry  $[\text{Na}_{0.5}][\text{Li}_{0.5}\text{Mg}_{2.5}][\text{Si}_4]\text{O}_{10}\text{F}_2$  was synthesized via melt synthesis as described earlier.<sup>1,2</sup> In a typical procedure, high purity reagents of  $\text{SiO}_2$  (Merck, fine granular, washed and calcined quartz p.a.), LiF (Chempur, 99.9%, powder),  $\text{MgF}_2$  (Chempur, 99.9%, 3–6 mm pieces), MgO (Alfa Aesar, 99.95%, 1–3 mm, fused lumps), and NaF (Alfa Aesar, Puratronic, 99.995%, powder) were carefully weighed out ( $\approx 0.1 \text{ mol}$ ) in a glovebox under Argon according to the required composition. The Mo-crucibles (Plansee, Austria) were heated in a radio frequency induction furnace. The crucible is placed in a quartz tube under high vacuum ( $<104 \text{ Torr}$ ) to prevent oxidation. The quartz tube itself is cooled with a flow of air to prevent crystallization caused by the high heat radiation during synthesis. Prior to synthesis, the crucible and the conical lid were heat-cleaned. After sealing, the crucible is heated with the reaction-coil at  $1900^\circ\text{C}$  for 20 min

and then the melt is quenched by switching off the radio frequency. To minimize inhomogeneities in composition within the product volume, the crucible was subsequently transferred to an Argon floated graphite rotary kiln (60 rpm) and heated to 1750 °C for 60 min. Finally, the fluorohectorite was crystallized by switching off the power supply and letting it slowly cool in the graphite oven while continuing rotation. To improve intracrystalline reactivity and to increase the lateral extension of the platelets, the fluorohectorite was at last annealed at 1045 °C for 6 weeks.<sup>3</sup>

*Preparation of the wrinkles.* Firstly, the coarse-grained fluorohectorite powder was immersed into Millipore water (typical concentrations in the range of 0.04 mgmL<sup>-1</sup>) and placed in a rotary shaker. Because of the improved intracrystalline reactivity, strong osmotic swelling spontaneously caused complete delamination of the tactoids. Successful delamination was proven by AFM; for this a droplet of the nanoplatelet suspension was placed onto a RCA-cleaned<sup>4</sup> silicon wafer, gently dried and analyzed topographically.

The PDMS substrates were hydrophilized by immersing them in 10 vol % aqueous HCl solution for 16 h, thoroughly washed with deionized water and dried, as reported in the literature.<sup>5</sup> The PDMS substrates were uniaxially stretched in a customer-made apparatus<sup>6</sup> (see Figure S1) to a strain of 33% to their length. In the stretched stage a droplet of the nanoplatelet suspension was added to the center and dried gently. Finally, the stress was released uniformly and the sample was investigated with AFM. 16 platelets suspended on PDMS substrates hydrophilized for 16 h were analyzed and the error was calculated by taking the standard deviation of the 2D-FT peaks. Additionally, 5 platelets suspended on PDMS substrates hydrophilized for 32 h were analyzed accordingly.

*Analytics.* The wrinkled samples were investigated with an MFP3D AFM (Asylum Research, Santa Barbara, California) operating in intermittent contact mode. Silicon cantilevers with a force



constant of typically  $42 \text{ Nm}^{-1}$  (Olympus, typical frequency of 300 kHz) were utilized. The scan rate was 1 Hz.

To cross-check the Young's modulus at the surface of the PDMS substrates, it was determined locally on each substrate next to where the samples were placed via indentation experiments using the colloidal probe (CP) technique.<sup>7-9</sup> Hereby, a Nanowizard I AFM (JPK Instruments AG, Germany) was used.

To determine the Young's modulus, the detected force-distance curves were transformed into force-indentation curves by subtraction of the cantilever deflection. The approach curves were fitted by the Hertz model.

As probes, colloidal glass beads (Polysciences, Germany) of approximately  $50 \mu\text{m}$  in diameter were attached with epoxy resin (UHU schnellfest, Germany) on pre-calibrated AFM cantilevers (tipless NSC 12, Micromash, Estonia). The force constant was detected applying the thermal noise method.<sup>10</sup> For the presented measurements a cantilever with a force constant of  $4.75 \text{ N m}^{-1}$  and a colloidal probe with a diameter of  $42.8 \mu\text{m}$  was used.

Measurements were performed for each PDMS substrate on 100 different positions on a digital  $20 \times 20 \mu\text{m}^2$  grid using the force mapping mode. The force-distance curves were analyzed using the JPK Image Processing software.

## 2 Additional Analytical Details

### Discrete 2D Fourier Transformation

To analyze the wavelength of the wrinkles, the recorded AFM images were processed with a discrete 2D Fourier transformation (2D-FT). This was done applying Scilab (<http://www.scilab.org/>). Hereby the program routine performs the following steps:

- **Read matrix** of AFM scan (typical image size:  $1024 \times 1024$  pixel)

- **Conduct a 2D-FT** of the matrix
- **Construct and rearrange a 2x2 submatrix** from the 2D-FT area (essential for the analysis of all four quadrants in reciprocal space (+kx,+ky; +kx,-ky; -kx,+ky; -kx,-ky), see below)
- **Integrate** within a range of appropriate ky-values (-5 to +5)
- **Normalize** to a range of 0-1 within an image
- **Plot** intensity profiles

The consideration of the direction of the wave-vector  $k$  is an important issue. In the case  $k$  is not pointing exactly into the main direction  $[1,0]$  but is slightly tilted in  $-y$  direction, the information would get lost applying a simple 2D-FT. Hence it is necessary to consider all four quadrants in the 2D-FT analysis.

#### Calculation of the radius of curvature

The observed wrinkles are approximated by a sine wave. The wavelength of 149 nm was obtained with 2D-FT and the amplitude was determined from the topographical image (difference between substrate and maxima of the wrinkles) to be 18 nm. Consequently, the function of the sine wave reads as follows:

$$y = a \cdot \sin(bx) = 18 \cdot \sin\left(\frac{2\pi}{149}x\right)$$

The extreme value of the radius of curvature  $r_c$  is reached at the maxima of the sine wave and

$$\text{reads: } r_c = \frac{1}{ab^2} = 31 \text{ nm}$$

### 3 Supplementary figures

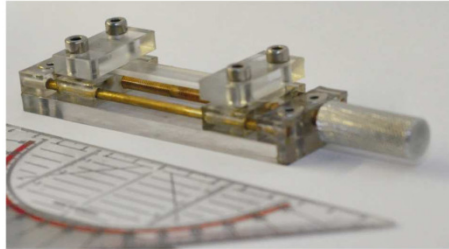


Figure S1. Home-built stretching stage providing reproducible wrinkling conditions.

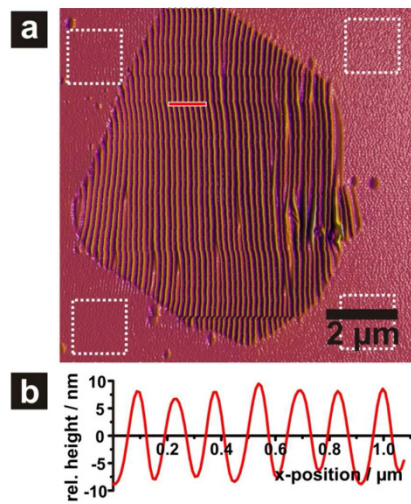


Figure S2. a) Wrinkled nanoplatelet taken from Figure 1 with a surface roughness of  $1.1 \pm 0.1$  nm (white dotted squares); the surface roughness of the PDMS substrate in the stretched stage (not shown) is within the same range; b) cross section of the wrinkled nanoplatelet showing a sinoidal curvature with uniform wavelength.

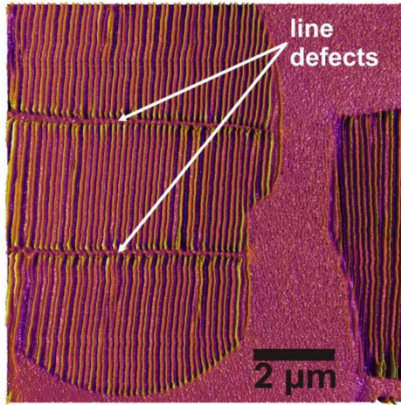


Figure S3. Wrinkled hectorite lamella showing line defects that can occur using the wrinkling metrology. They occur in most of the cases perpendicular to the wrinkling direction.

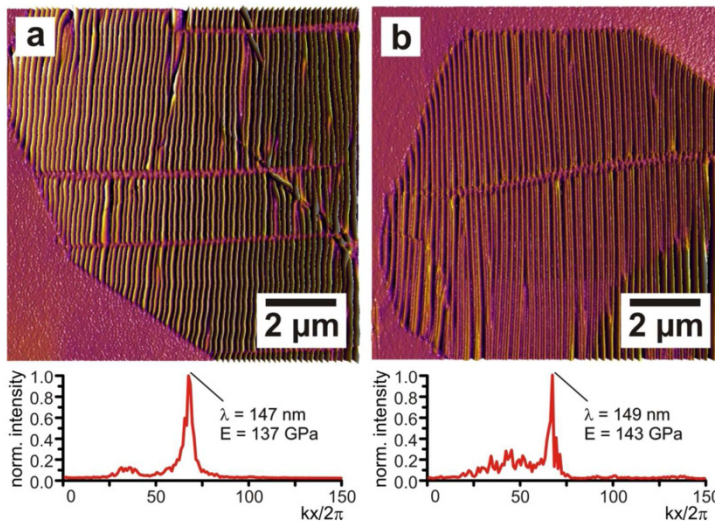


Figure S4. Wrinkled hectorite lamellae on PDMS substrates that were hydrophilized via HCl treatment for a) 16 h and b) 32 h, respectively. No trend in the wrinkling wavelengths depending on the duration of the treatment was detectable. The Young's modulus of the PDMS substrate's surface was cross-checked with colloidal probe AFM measurements and did also not change. The

PDMS slab that was treated with HCl for only 8h was still too hydrophobic to obtain valuable measurements on single hectorite lamellae.

#### 4 Supplementary references

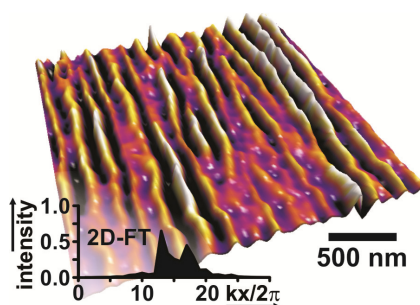
- (1) Breu, J.; Seidl, W.; Stoll, A. J.; Lange, K. G.; Probst, T. U. *Chem. Mater.* **2001**, *13*, 4213-4220.
- (2) Malikova, N.; Cadene, A.; Dubois, E.; Marry, V.; Durand-Vidal, S.; Turq, P.; Breu, J.; Longeville, S.; Zanotti, J. M. *J. Phys. Chem. C* **2007**, *111*, 17603-17611.
- (3) Stöter, M.; Kunz, D. A.; Schmidt, M.; Hirsemann, D.; Kalo, H.; Putz, B.; Senker, J.; Breu, J. *Langmuir* **2013**, 1280-1285.
- (4) Donose, B. C.; Taran, E.; Vakarelski, I. U.; Shinto, H.; Higashitani, K. *J. Colloid Interface Sci.* **2006**, *299*, 233-237.
- (5) Huang, H.; Chung, J. Y.; Nolte, A. J.; Stafford, C. M. *Chem. Mater.* **2007**, *19*, 6555-6560.
- (6) Pretzl, M.; Schweikart, A.; Hanske, C.; Chiche, A.; Zettl, U.; Horn, A.; Böker, A.; Fery, A. *Langmuir* **2008**, *24*, 12748-12753.
- (7) Ducker, W. A.; Senden, T. J.; Pashley, R. M. *Nature* **1991**, *353*, 239-241.
- (8) Kappl, M.; Butt, H. J. *Part. Part. Syst. Char.* **2002**, *19*, 129-143.
- (9) Butt, H. J.; Cappella, B.; Kappl, M. *Surf. Sci. Rep.* **2005**, *59*, 1-152.
- (10) Hutter, J. L.; Bechhoefer, J. *Rev. Sci. Instrum.* **1993**, *64*, 1868-1873.

## 6.4 Lokal-aufgelöste mechanische Eigenschaften von Graphen, Graphenoxid und chemisch erzeugtem Graphen

Daniel A. Kunz<sup>†</sup>, Patrick Feicht<sup>†</sup>, Sebastian Gödrich<sup>‡</sup>, Herbert Thurn<sup>§</sup>, Georg Papastavrou<sup>‡</sup>, Andreas Fery<sup>‡,\*</sup>, and Josef Breu<sup>†,\*</sup>

### Space-Resolved In-Plane Moduli of Graphene and Graphene Oxide Applying a Simple Wrinkling Procedure

Erschienen in: *Advanced Materials* **2013**, 25, 1337-1341. Copyright © 2013 by John Wiley & Sons, Inc. Reprinted by permission of John Wiley & Sons, Inc.



<sup>†</sup> Lehrstuhl für Anorganische Chemie I, Universität Bayreuth, 95447 Bayreuth, Deutschland

<sup>‡</sup> Lehrstuhl für Physikalische Chemie II, Universität Bayreuth, 95447 Bayreuth, Deutschland

<sup>§</sup> Rechenzentrum, Universität Bayreuth, 95447 Bayreuth, Deutschland

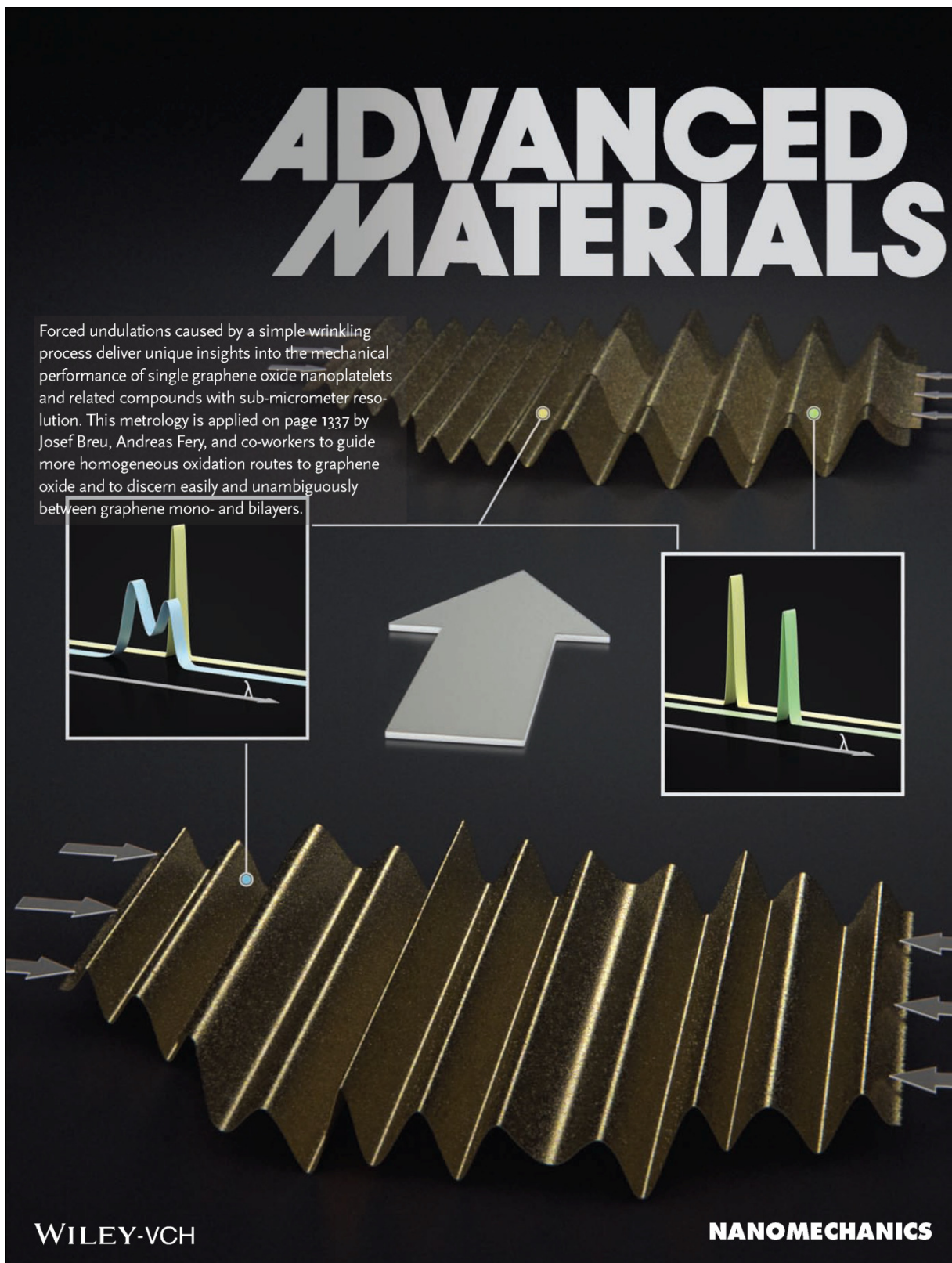
\* josef.breu@uni-bayreuth.de; andreas.fery@uni-bayreuth.de

#### Darstellung des Eigenanteils:

Das Konzept dieser Publikation wurde von mir selbst erarbeitet. Weiterhin etablierte ich die Methode hinsichtlich der untersuchten Materialien und führte sämtliche Messungen durch, bis auf die Leitfähigkeitsmessung, die *Sebastian Gödrich* in Zusammenarbeit mit Prof. Dr. *Georg Papastavrou* übernahm. *Patrick Feicht* half mir bei der Herstellung der Nanoplättchen. Dr. *Herbert Thurn* unterstützte mich in der Entwicklung eines Programmes zur automatisierten Datenauswertung. Verfasst wurde diese Publikation hauptsächlich von Prof. Dr. *Josef Breu*, Prof. Dr. *Andreas Fery* und mir. Mein Eigenanteil beläuft sich auf ca. 80 %.



### 6.4.1 Space-Resolved In-Plane Moduli of Graphene and Graphene Oxide Applying a Simple Wrinkling Procedure



# Space-Resolved In-Plane Moduli of Graphene Oxide and Chemically Derived Graphene Applying a Simple Wrinkling Procedure

Daniel A. Kunz, Patrick Feicht, Sebastian Gödrich, Herbert Thurn, Georg Papastavrou, Andreas Fery,\* and Josef Breu\*

Almost 50 years after its first description in 1962 by H.P. Boehm,<sup>[1]</sup> the unique properties of graphene, a single carbon layer of the graphitic structure,<sup>[2]</sup> were unraveled by A. K. Geim and K. S. Novoselov<sup>[3]</sup> who were awarded the Nobel prize for physics in 2010. Besides the novel electronic and thermal properties, the exceptionally high mechanical strength triggered various applications as reinforcing fillers in nanocomposites,<sup>[4,5]</sup> and for fabrication of carbon-based paper-like<sup>[6]</sup> and fibrous materials.<sup>[7]</sup> The only established up-scalable procedure for graphene production is via reduction of graphene oxide (GO).<sup>[8–9]</sup> The process implies several steps: oxidation of bulk graphite to graphite oxide, delamination of graphite oxide into GO by osmotic swelling, and finally reduction of GO to chemically derived graphene. Conditions for the oxidation of graphite are rather harsh and, due to the heterogeneous character of the oxidation, gradients in the local concentration of reactants are inherent to the process. Accordingly, the degree of oxidation achieved is heterogeneous within the material and, moreover, critically depends on the kinetics of the reaction. The type and number of functional groups introduced/removed by the redox-chemistry vary spatially. Consequently, properties of GO and graphene derived thereof vary from sample to sample and even within domains of a single nanoplatelet. The functional groups act as local defects and, for instance, electrical conductivity is critically influenced by defect concentration and distribution.<sup>[10]</sup>

Since both GO and chemically derived graphene are structurally heterogeneous materials, space-resolved mechanical characterization of monolayers would be of crucial interest. Ideally, the method should be facile and fast enough to allow a real-time quality control in an industrial production process which

is indispensable because of the decisive influence of reaction kinetics.

Hence, in order to study the development of the mechanical behavior of GO and graphene, an approach visualizing the mechanical homogeneity of single nanoplatelets is highly desirable.

Here we present a method that meets all these requirements. Based on a straightforward wrinkling process on a deformable substrate, readily available topographical atomic force microscopy (AFM) imaging is sufficient to retrieve the in-plane modulus with a spatial resolution down to the sub-micrometer range. The use of surface wrinkles is well-established for thin film metrology<sup>[11–12]</sup> and these wrinkles have also found applications in structure formation and patterning,<sup>[13–15]</sup> with a validity from the nano- to the macroscale.<sup>[16]</sup>

The general idea of the buckling-based metrology is the planar compression of a thin, stiff coating on a thicker, compliant substrate like poly(dimethylsiloxane) (PDMS). Recent studies quite parallel to our findings revealed the elastic constants of rubrene micro-crystals via wrinkling.<sup>[17]</sup> We succeeded in transferring this technique to single nanoplatelets with a thickness even thinner than 1 nm (Figure 1). The characteristic wrinkling wavelength observed depends on the platelet thickness  $h$  as well as on the ratio of moduli of platelet and substrate.<sup>[18–19]</sup>

$$\lambda = 2\pi h \left[ \frac{(1 - \nu_s^2) E_p}{3(1 - \nu_p^2) E_s} \right]^{1/3} \quad (1)$$

where  $E_p$  and  $\nu_p$  are in-plane modulus and Poisson's ratio of the platelet, respectively;  $E_s$  and  $\nu_s$  refer to Young's modulus and Poisson's ratio of the substrate, respectively. Rearranging Equation 1 yields the desired in-plane modulus of the nanoplatelet:

$$E_p = \frac{3E_s(1 - \nu_p^2)}{(1 - \nu_s^2)} \left( \frac{\lambda}{2\pi h} \right)^3 \quad (2)$$

In order to apply wrinkling metrology to GO/graphene, the following procedure was used: A droplet of diluted GO suspension was placed onto a hydrophilized slab of PDMS that was stretched uniaxially with a customer-made apparatus (Figure S2 of the Supporting Information (SI)). After gentle drying, the stress was released and the sample was analyzed with imaging AFM. Figure 1a shows AFM topographical images of the same GO monolayer before and after stress release. The strain could be directly read out by comparing the distances  $d$  and  $d'$  in the

D. A. Kunz, P. Feicht, Prof. J. Breu  
Department of Inorganic Chemistry  
University of Bayreuth  
Universitätsstr. 30, 95440 Bayreuth, Germany  
E-mail: josef.breu@uni-bayreuth.de

S. Gödrich, Prof. G. Papastavrou, Prof. A. Fery  
Department of Physical Chemistry  
University of Bayreuth  
Universitätsstr. 30, 95440 Bayreuth, Germany  
E-mail: andreas.fery@uni-bayreuth.de

Dr. H. Thurn  
Computing Center  
University of Bayreuth  
Universitätsstr. 30, 95440 Bayreuth, Germany

DOI: 10.1002/adma.201204049





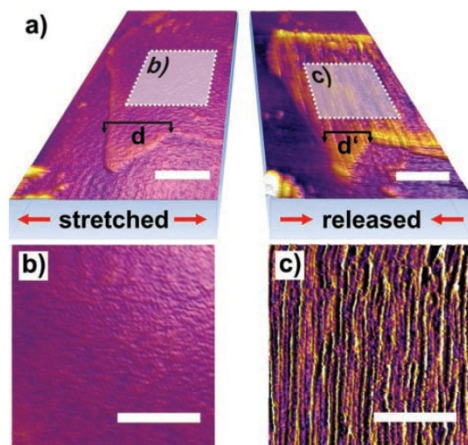


**Figure 1.** Wrinkling a GO monolayer on PDMS. a) shows an AFM topographical image of the nanoplatelet in the stretched state (left) and after stress release (right). The strain can be easily read out from the marked distances  $d$  and  $d'$ . A higher magnification of the dotted squares clearly shows a smooth platelet surface (b) and the wrinkled pattern (c). All scale bars are 1  $\mu\text{m}$ .

image. At higher magnification (Figure 1b and c) the generation of a wrinkled topography clearly became visible. In order to analyze the wavelength of these wrinkles, the image was processed with a discrete 2D Fourier transformation (2D-FT, see SI for details). 2D-FT improves the sensitivity for periodic domains within the platelet. To probe for heterogeneity, several wrinkled GO nanoplatelets were systematically analyzed. Moreover, images of individual nanoplatelets were subdivided into smaller areas that were analyzed with respect to homogeneity of periodicity. Results for GO nanoplatelets are visualized in Figure 2. The recorded image, a  $10\text{ }\mu\text{m} \times 10\text{ }\mu\text{m}$  scan (Figure 2a), was subdivided into  $8 \times 8$  sub-areas of  $1.25\text{ }\mu\text{m}$  each that were subsequently Fourier transformed. Figures 2b–d show selected sub-areas at higher magnification representing areas with higher in-plane modulus (b), lower in-plane modulus (c), and typical in-plane modulus (d), while an area of unloaded and therefore featureless PDMS is given in Figure 2e as a reference.

Next to each image a contour plot of the FT-intensities along the  $k_x$ -axis in reciprocal space is shown. Unfortunately, the wrinkles are not aligned perfectly perpendicular to the axis of stress release ( $k_x$ ). Rather some wrinkles are slightly tilted away from  $90^\circ$  and consequently, the FT-peak maxima are not always projected exactly onto the  $k_x$ -axis but are randomly displaced in  $\pm k_y$ -direction. In order to include all orientations in the analysis, 2D-FT-intensities were integrated within a range of appropriate  $k_y$  values (see SI for details). To assist comparison of different areas the integrated intensities were finally normalized to a range of 0–1 within a given image.

The 2D-FTs of chosen areas differ in the position of peak maxima, the number of peak maxima, and the widths of the peaks. The widths of the FT-peaks are determined by periodic domain sizes but also by small modulations in the periodicity.

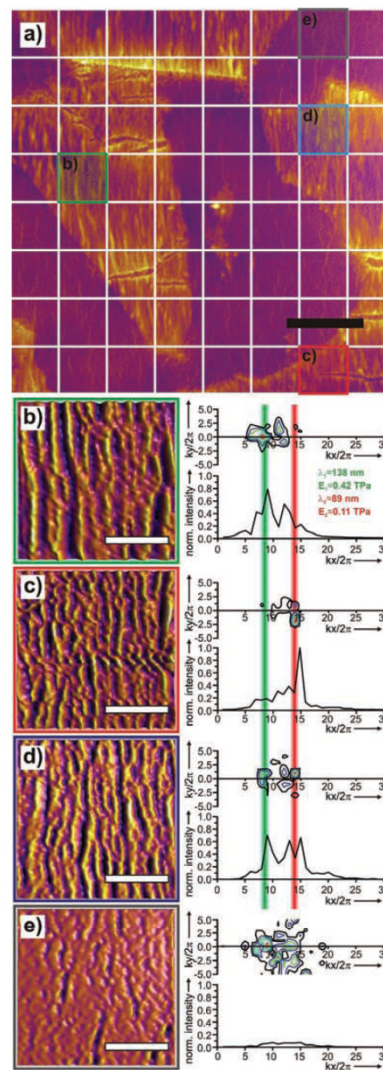


**Figure 2.** GO platelet analysis. a) The recorded AFM image ( $10\text{ }\mu\text{m} \times 10\text{ }\mu\text{m}$  scan) with wrinkled GO nanoplates was subdivided into  $8 \times 8$  sub-areas. For each area a 2D-FT was conducted. b–d) Representative areas at higher magnification: b) high elastic modulus (green square), c) low elastic modulus (red square), d) typical region showing both features (blue square). e) The unloaded and therefore featureless PDMS as a reference (grey square). Next to the images, the contour-plots and averaged intensity profiles of the areas after 2D-FT are shown. The green and red lines mark the typical range of wrinkling wavelengths corresponding to in-plane moduli of 0.42 and 0.11 TPa, respectively. The color code for the contour plot ranges from blue (low intensity) to red (high intensity). The scale bars represent 2  $\mu\text{m}$  (black) and 500 nm (white).

Occurrence of more than one peak maximum indicated that within the selected sub-area different wavelengths of wrinkles are realized which in turn suggest that domains with different in-plane moduli were present. Since clearly distinct peak maxima are realized within a sub-area of  $1.25\ \mu\text{m}$ , the spatial resolution of derived in-plane moduli is in the sub-micrometer range. Finally, applying Equation 2 the positions of the peak maxima were converted into in-plane moduli (see SI).

GO is known to be a non-stoichiometric material. The type, number, and distribution of functional groups is highly heterogeneous.<sup>[20]</sup> Moreover, depending on the local degree of oxidation, defects are generated in the covalent 2D framework as proposed by Lerf and Klinowski.<sup>[21]</sup>

Heterogeneities in GO lead to heterogeneities in deformability of the platelets and these can be detected by scatter of the wrinkling wavelength. Deformability is determined by both scatter in thickness and scatter in the in-plane modulus. At an atomistic level, chemical heterogeneities, as expressed by a varying density of functional groups, are inevitably connected to changes in the thickness of the layer. Since thickness and chemical heterogeneity cannot be separated from each other at this level, for simplicity we kept the thickness constant and interpreted the experimentally observed heterogeneities as being purely related to variations in the in-plane modulus.

In agreement with this structural heterogeneity, the wavelength of wrinkles varied in a certain range. 2D-FTs of the selected areas show different peak maxima (Figure 2) whereby an upper and lower limit of around  $138\ \text{nm}$  (green vertical line) and around  $89\ \text{nm}$  (red vertical line) became obvious. These wrinkling periodicities correspond to in-plane moduli of around  $0.42\ \text{TPa}$  and  $0.11\ \text{TPa}$ , respectively. Some areas even show a trimodal 2D-FT intensity distribution (Figure 2b and d) with an additional wrinkling wavelength of approximately  $100\ \text{nm}$  corresponding to an in-plane modulus of  $0.16\ \text{TPa}$ . Most likely, the spread of in-plane moduli is related to defect concentration or clustering of different functional groups. These variations become only obvious, if the spatial resolution of the mechanical testing is below  $1\ \mu\text{m}$ . Furthermore, conductive AFM (C-AFM) was applied as an independent complementary method to probe inhomogeneities in GO nanoplatelets (Figure S3 of the SI). Recently, applying this technique, defect patterning of GO and reduced GO was visualized via local current-mapping.<sup>[22,23]</sup> Similar to these published results, current-mapping clearly indicated local clustering of domains in the range of  $500\ \text{nm}$  with higher and lower conductivity corresponding to areas with lower and higher degrees of oxidation (Figure S3 of the SI) that are in line with the mechanical characterization. While both techniques confirm heterogeneities in the material, clearly the spatial resolution of wrinkling metrology and C-AFM is profoundly different. The lateral resolution of C-AFM is well below  $100\ \text{nm}$  and thus much higher than the observed wrinkling wavelengths for GO. Therefore both techniques can be considered as complementary and confirm both the existence of heterogeneities.

Classical deformation measurements will average over larger areas and median moduli are observed. To compare our results with published in-plane moduli we had to average over larger areas. This way, an overall average in-plane modulus could be determined to be  $(0.23 \pm 0.07)\ \text{TPa}$  which is in excellent

agreement with the in-plane modulus reported by J.W. Suk et al. via contact-force-measurements  $((0.21 \pm 0.02)\ \text{TPa})$ .<sup>[24]</sup> In both cases a nanoplatelet thickness of  $0.7\ \text{nm}$  was assumed to calculate the modulus. Mechanical failure will, however, be dominated by the weak areas. Averaging the modulus of heterogeneous materials will lead to a dramatic overestimation of the mechanical performance since the area with highest defect concentration, and hence lowest in-plane modulus will determine material failure. Our spatially resolved results show that the weakest domains have an in-plane modulus of some 50% lower than the average.

By random stacking of single layers in GO multilayers the in-plane distribution of defect domains will be averaged leading to an apparently more homogeneous structure. Indeed, with increasing number of layers the wrinkling becomes more homogeneous which is underlined by the shape of the 2D-FT profile (Figure S4 of the SI). Consequently, the information on defect variation will be lost. Therefore, when the mechanical characteristics should be used for instance to guide a production process it will be crucial to analyze monolayers.

To measure chemically derived graphene a sample with well-separated GO nanoplatelets on PDMS in the stretched state was exposed to hydrazine vapor for 14 hours according to an established literature procedure.<sup>[25]</sup> After this reduction, the stress was released. Raman spectra (Figure S6 of the SI) reveal typical features of graphene obtained from GO via hydrazine treatment.<sup>[8]</sup> Topographical AFM showed no significant reduction in the height of the nanoplatelets upon hydrazine treatment (Figure S5 of the SI) which can be rationalized by the persistence of some functional groups even after reduction. Therefore, the same monolayer thickness as for GO was applied in calculations.

AFM images of wrinkled chemically derived graphene nanoplatelets evince a much better contrast relating to higher wrinkling amplitudes as compared to the pristine GO giving a first indication of stiffening due to a regraphitization (compare Figure 2 and Figure 3). For studying the homogeneity within a platelet, the same approach as for GO was applied. The smaller images again show, like in Figure 2, representative sub-areas at a higher magnification.

While the wavelength of wrinkles increased as compared to pristine GO corresponding to higher in-plane moduli of chemically derived graphene, the spread of wrinkling wavelengths did not narrow significantly. The higher and lower ends, as indicated by vertical green and red lines in Figure 3, correspond to in-plane moduli of approximately  $0.82\ \text{TPa}$  and  $0.36\ \text{TPa}$ , respectively. The average in-plane modulus of all domains is  $(0.48 \pm 0.06)\ \text{TPa}$ , which is twice as high as that of GO. Apparently, the heterogeneities introduced during synthesis of GO were not removed by the reduction and the material still exhibits a domain structure. Nevertheless, the spread of in-plane moduli observed by wrinkling is considerably lower than the scattering of the mechanical properties of chemically derived graphene reported by Gómez-Navarro et al.<sup>[26]</sup> via AFM-based nano-mechanical bending tests, suggesting that this scatter includes also contributions originating from the deformation-based measurement method.

The observed higher absolute values of in-plane moduli confirm that regraphitization enforces the 2D framework and



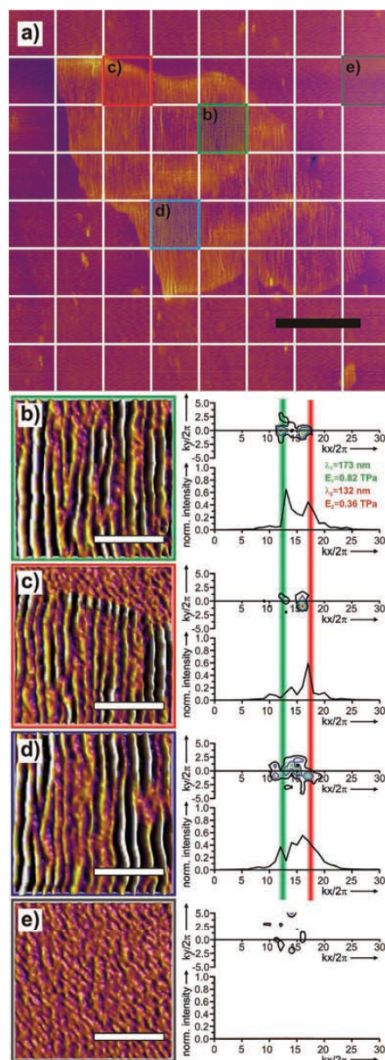


**Figure 3.** Graphene platelet analysis. a) The recorded AFM image ( $18\ \mu\text{m} \times 18\ \mu\text{m}$  scan) with a wrinkled chemically derived graphene monolayer was subdivided into  $8 \times 8$  sub-areas. For each square a 2D-FT was conducted. b–d) Representative areas at higher magnification: b) high elastic modulus (green square), c) low elastic modulus (red square), d) typical region showing both features (blue square). e) Unloaded and therefore featureless PDMS as a reference (grey square). Next to the images, the contour-plots and averaged intensity profiles of the areas after 2D-FT are shown. The green and red lines mark the typical range of wrinkling wavelengths corresponding to in-plane moduli of 0.82 and 0.36 TPa, respectively. The color code for the contour plot ranges from blue (low intensity) to red (high intensity). The scale bars represent  $4\ \mu\text{m}$  (black) and  $1\ \mu\text{m}$  (white).

stiffens the nanoplatelets. Interestingly, for some domains the aromatic character seems to be fully restored and the in-plane modulus approached that of high quality graphene (1.0 TPa via AFM deformation tests and 1.1 TPa for bulk graphite).<sup>[27,28]</sup> However, as mentioned before, mechanical failure will be determined by the weakest domains. Moreover, since the electrical conductivity of chemically derived graphene is lower by a few orders of magnitude, the graphene-like domains most likely are not connected to a percolation path but represent isolated domains.<sup>[10]</sup> This is in excellent agreement with our observation of domain-dependant mechanical properties.

In order to validate the measurements presented above we carried out control experiments applying the wrinkling method to commercial graphene obtained by chemical vapor deposition (CVD graphene, “Trivial Transfer Graphene” obtained from ACS Materials LLC). Contrary to what has been observed for GO and chemically derived graphene (Figures 2 for CVD graphene a very homogeneous microstructure of the wrinkles throughout the whole image was observed (Figure S7 of the SI). Representative sub-areas at a higher magnification (Figure S7b–d of the SI), all show a narrow wavelength distribution resulting in a sharp and well-defined Fourier peak at  $84\ \text{nm}$  which corresponds to an in-plane modulus of  $0.9\ \text{TPa}$ . Averaging over all sub-areas yielded an in-plane modulus of  $(0.91 \pm 0.02)\ \text{TPa}$  which is in very good agreement with reported literature values for graphene produced by the scotch tape method ( $1.0\ \text{TPa}$ <sup>[27]</sup>) and about twice as high as the value found for chemically derived graphene. The slightly lower value might be related to the quality differences between mechanically exfoliated graphene and CVD graphene.

Interestingly, in Figure S7c of the SI a second wavelength is visible in the 2D-FT profile which is twice as long ( $167\ \text{nm}$ ). Under special situations period doubling can occur but would result in a different shape of the wrinkles.<sup>[29]</sup> Their shape would strongly deviate from a sinusoidal pattern unlike the findings in this study. Therefore the feature observed here can be assigned to the occurrence of a small fraction of bilayer graphene which is quite typical for the CVD processing.<sup>[30]</sup>

This underlines the power of the method to distinguish unambiguously and quite easily between mono- and bilayer graphene. Due to the discrete wavelengths and the sharp peaks it is possible to distinguish quickly via the wrinkling method between mono- and bilayer graphene in a much easier way than TEM electron diffraction and Raman analysis.<sup>[31,32]</sup>

Applying the wrinkling method to GO and chemically derived graphene monolayers we could successfully determine their mechanical properties with sub-micrometer resolution. The resolution revealed the heterogeneous nature of the chemically modified carbon nanomaterials. The method allows for direct visualization of the shortcomings of chemically derived graphene over high quality genuine graphene. Moreover, it has the potential to guide the development of more sophisticated and milder synthetic routes to more homogeneous, less defect carrying GO. With analytical processing in the range of a few hours it is about ten times faster than conventional deformations measurements and hence also suitable for real-time quality control.

The wrinkling method can easily be applied to other nanoplatelets, such as transition-metal sulfides and selenides,<sup>[33–35]</sup> layered double-hydroxides (LDHs), clays, and so forth. The

great advantage of a simple approach with subsequent standard AFM analytics renders the presented method a powerful tool that could be used as a quite ubiquitous, fast, low-cost and facile standard method for mechanical characterization of nanoplatelets with sub-micrometer spatial resolution. Moreover, for uniform nanoplatelets, wrinkling might be applied as an appealing method to unambiguously discern between mono- and bilayers.

### Experimental Section

All experimental details are given in the SI.

### Supporting Information

Supporting Information is available from the Wiley Online Library or from the author.

### Acknowledgements

This work was supported by the German Science Foundation (SFB 840). D.A.K. thanks the elite study program "Macromolecular Science" as well as the International Graduate School "Structure, Reactivity and Properties of Oxide Materials" within the Elite Network of Bavaria (ENB) for ongoing support. Kai-Uwe Claussen is gratefully acknowledged for helping with the tensile tests. We also thank Prof. Hans Keppler for the support with the Raman spectra.

Received: September 26, 2012

Revised: November 7, 2012

Published online: December 13, 2012

- [1] H. P. Boehm, A. Clauss, U. Hofmann, G. O. Fischer, *Z. Naturforsch. (B)* **1962**, *B* 17, 150.
- [2] H. P. Boehm, R. Setton, E. Stumpp, *Pure Appl. Chem.* **1994**, *66*, 1893.
- [3] A. K. Geim, K. S. Novoselov, *Nat. Mater.* **2007**, *6*, 183.
- [4] N. A. Kotov, I. Dekany, J. H. Fendler, *Adv. Mater.* **1996**, *8*, 637.
- [5] S. Stankovich, D. A. Dikin, G. H. B. Dommett, K. M. Kohlhaas, E. J. Zimney, E. A. Stach, R. D. Piner, S. T. Nguyen, R. S. Ruoff, *Nature* **2006**, *442*, 282.
- [6] D. A. Dikin, S. Stankovich, E. J. Zimney, R. D. Piner, G. H. B. Dommett, G. Evmenenko, S. T. Nguyen, R. S. Ruoff, *Nature* **2007**, *448*, 457.
- [7] Z. Dong, C. Jiang, H. Cheng, Y. Zhao, G. Shi, L. Jiang, L. Qu, *Adv. Mater.* **2012**, *24*, 1856.
- [8] S. Stankovich, D. A. Dikin, R. D. Piner, K. A. Kohlhaas, A. Kleinhammes, Y. Jia, Y. Wu, S. T. Nguyen, R. S. Ruoff, *Carbon* **2007**, *45*, 1558.
- [9] D. Li, M. B. Muller, S. Gilje, R. B. Kaner, G. G. Wallace, *Nat. Nanotechnol.* **2008**, *3*, 101.
- [10] A. B. Kaiser, C. Gomez-Navarro, R. S. Sundaram, M. Burghard, K. Kern, *Nano Lett.* **2009**, *9*, 1787.
- [11] C. M. Stafford, C. Harrison, K. L. Beers, A. Karim, E. J. Amis, M. R. Vanlandingham, H. C. Kim, W. Volksen, R. D. Miller, E. E. Simonyi, *Nat. Mater.* **2004**, *3*, 545.
- [12] N. Bowden, S. Brittain, A. G. Evans, J. W. Hutchinson, G. M. Whitesides, *Nature* **1998**, *393*, 146.
- [13] C. H. Lu, H. Mohwald, A. Fery, *Soft Matter* **2007**, *3*, 1530.
- [14] J. Genzer, J. Groenewold, *Soft Matter* **2006**, *2*, 310.
- [15] M. Pretzl, A. Schweikart, C. Hanske, A. Chiche, U. Zettl, A. Horn, A. Böker, A. Fery, *Langmuir* **2008**, *24*, 12748.
- [16] H. Vandeparre, M. Pineirua, F. Brau, B. Roman, J. Bico, C. Gay, W. Z. Bao, C. N. Lau, P. M. Reis, P. Damman, *Phys. Rev. Lett.* **2011**, *106*, 224301.
- [17] M. A. Reyes-Martinez, A. Ramasubramaniam, A. L. Briseno, A. J. Crosby, *Adv. Mater.* **2012**, *24*, 5548.
- [18] R. Huang, *J. Mech. Phys. Solids* **2005**, *53*, 63.
- [19] J. Groenewold, *Physica A* **2001**, *298*, 32.
- [20] U. Hofmann, R. Holst, *Ber. Dtsch. Chem. Ges.* **1939**, *72*, 754.
- [21] A. Lerf, H. Y. He, M. Forster, J. Klinowski, *J. Phys. Chem. B* **1998**, *102*, 4477.
- [22] S. Fujii, T. Enoki, *Angew. Chem. Int. Edit.* **2012**, *51*, 7236.
- [23] J. M. Mativetsky, E. Treossi, E. Orgiu, M. Melucci, G. P. Veronese, P. Samori, V. Palermo, *J. Am. Chem. Soc.* **2010**, *132*, 14130.
- [24] J. W. Suk, R. D. Piner, J. H. An, R. S. Ruoff, *ACS Nano* **2010**, *4*, 6557.
- [25] S. C. Youn, J. Geng, B. S. Son, S. B. Yang, D. W. Kim, H. M. Cho, H. T. Jung, *J. Nanosci. Nanotechnol.* **2011**, *11*, 5959.
- [26] C. Gomez-Navarro, M. Burghard, K. Kern, *Nano Lett.* **2008**, *8*, 2045.
- [27] C. Lee, X. D. Wei, J. W. Kysar, J. Hone, *Science* **2008**, *321*, 385.
- [28] O. L. Blakslee, *J. Appl. Phys.* **1970**, *41*, 3373.
- [29] F. Brau, H. Vandeparre, A. Sabbah, C. Poulard, A. Boudaoud, P. Damman, *Nat. Phys.* **2011**, *7*, 56.
- [30] C. Mattevi, H. Kim, M. Chhowalla, *J. Mater. Chem.* **2011**, *21*, 3324–3334.
- [31] Y. Hernandez, V. Nicolosi, M. Lotya, F. M. Blighe, Z. Y. Sun, S. De, I. T. McGovern, B. Holland, M. Byrne, Y. K. Gun'ko, J. J. Boland, P. Niraj, G. Duesberg, S. Krishnamurthy, R. Goodhue, J. Hutchison, V. Scardaci, A. C. Ferrari, J. N. Coleman, *Nat. Nanotechnol.* **2008**, *3*, 563.
- [32] A. C. Ferrari, J. C. Meyer, V. Scardaci, C. Casiraghi, M. Lazzeri, F. Mauri, S. Piscanec, D. Jiang, K. S. Novoselov, S. Roth, A. K. Geim, *Phys. Rev. Lett.* **2006**, *97*, 187401.
- [33] J. N. Coleman, M. Lotya, A. O'Neill, S. D. Bergin, P. J. King, U. Khan, K. Young, A. Gaucher, S. De, R. J. Smith, I. V. Shvets, S. K. Arora, G. Stanton, H. Y. Kim, K. Lee, G. T. Kim, G. S. Duesberg, T. Hallam, J. J. Boland, J. J. Wang, J. F. Donegan, J. C. Grunlan, G. Moriarty, A. Shmeliov, R. J. Nicholls, J. M. Perkins, E. M. Grievson, K. Theuwissen, D. W. McComb, P. D. Nellist, V. Nicolosi, *Science* **2011**, *331*, 568.
- [34] K. G. Zhou, N. N. Mao, H. X. Wang, Y. Peng, H. L. Zhang, *Angew. Chem. Int. Ed.* **2011**, *50*, 10839.
- [35] Z. Zeng, Z. Yin, X. Huang, H. Li, Q. He, G. Lu, F. Boey, H. Zhang, *Angew. Chem. Int. Ed.* **2011**, *50*, 11093.

---

6.4.2 Supporting Information

Copyright WILEY-VCH Verlag GmbH & Co. KGaA, 69469 Weinheim, Germany, 2012.

# ADVANCED MATERIALS

## Supporting Information

for *Adv. Mater.*, DOI: 10.1002/adma.201204049

Space-Resolved In-Plane Moduli of Graphene Oxide and  
Chemically Derived Graphene Applying a Simple Wrinkling  
Procedure

*Daniel A. Kunz, Patrick Feicht, Sebastian Gödrich, Herbert  
Thurn, Georg Papastavrou, Andreas Fery,\* and Josef Breu\**

Submitted to **ADVANCED  
MATERIALS**

DOI: 10.1002/adma.201204049

**Space-Resolved In-Plane Moduli of Graphene Oxide and Chemically Derived Graphene  
Applying a Simple Wrinkling Procedure**

*By Daniel A. Kunz, Patrick Feicht, Sebastian Gödrich, Herbert Thurn, Georg Papastavrou,  
Andreas Fery,\* and Josef Breu\**

## **Supporting Information**

Contents:

1. Materials and Methods
2. Analytical Details
3. Supplementary Graphs and Figures
4. Supplementary References

## 1 Materials and Methods

**Preparation of substrates.** PDMS precursor (Dow Corning Sylgard 184) was mixed in a 10:1 mass ratio of oligomeric base to curing agent, degassed and poured into (60 x 10 x 2) mm<sup>3</sup> Teflon boats. After prehardening for 20 h at room temperature, the samples were post-treated for 2 h at 150 °C. Tensile tests were carried out on an Instron 5565 universal tester with pneumatic clamps and a 100 N load cell (clamping distance 30 mm, strain rate 200 mm min<sup>-1</sup>, see ISO 37:2005). The Young's moduli are calculated from the initial slope and averaged over 15 different samples.

**Preparation of graphene oxide (GO), graphene.** GO suspensions were prepared according to the method described by Hummers and Offeman.<sup>[1]</sup> Chemically derived graphene was obtained by exposure of the dried drop-casted GO suspension on the stretched PDMS substrate for 14 hours to hydrazine vapor that was generated by hydrazine monohydrate (Aldrich) under reduced pressure and at room temperature.

**Preparation of the wrinkles.** Firstly, the PDMS substrates were hydrophilized by immersing them in 10 vol % aqueous HCl solution for 16 h, afterwards they were thoroughly washed with Millipore water and dried, as reported in the literature.<sup>[2]</sup> Care was taken to ensure that the mechanical properties of the surface were not affected by this procedure. The PDMS substrates were stretched uniaxially in a customer-made apparatus<sup>[3]</sup> (**Figure S2**) to a strain of 33% of their length. In the stretched stage a droplet of diluted GO suspension (typically 0.04 mgmL<sup>-1</sup>) was added to the center and dried gently to obtain samples with isolated nanoplatelets.

CVD-graphene wrinkles were generated by immobilization of "Trivial Transfer Graphene" (ACS Material LLC, monolayer graphene which has been coated on one face with a thin PMMA layer) on a stretched, non-treated PDMS substrate. The un-coated face of the graphene was pointing towards the PDMS substrate. To ensure adhesion the sample was

**ADVANCED  
MATERIALS**

Submitted to

heated beyond the glass transition temperature of PMMA for several minutes to allow the trivial transfer sample to relax and adhere strongly to the PDMS substrate. After cooling the PMMA coating on the top of the CVD-graphene was carefully removed by repeated washing with acetone and finally was allowed to dry. At last, the stress was gently released.

**Analytics.** The wrinkled samples were investigated under ambient conditions with an MFP3D AFM (Asylum Research) operating in intermittent contact mode. Silicon cantilevers with a force constant of typically  $42 \text{ Nm}^{-1}$  (Olympus, typical resonance frequency of 300 kHz) were utilized. The scan rate was 0.5-1 Hz.

Conductive AFM was performed with an MFP3D AFM (Asylum Research) operating in contact mode. Cantilevers with all-platinum tip and a force constant of typically  $18 \text{ Nm}^{-1}$  (Bruker RMN-25PT300B, typical resonance frequency of 20 kHz) were utilized. The scan rate was 0.4 Hz. During the imaging, a force below 100 nN and a bias voltage of + 1.0 V were maintained. Care was taken to ensure that no redox-processes took place during scanning.

According to J.M. Mativetsky et al. tip-induced reduction of GO only occurs at negative voltages beyond  $(-3.7 \pm 0.3) \text{ V}$ .<sup>[4]</sup> As substrates, template-stripped gold supports prepared according to D. Stamou et al.<sup>[5]</sup> were chosen because of their small surface roughness.

Raman spectra were collected with a Horiba Labram HR spectrometer using the 514 nm line of an argon laser for excitation.



## 2 Analytical Details

### 2.1 Data processing

In order to obtain the wavelength of the wrinkles, the image data was processed with a discrete 2D Fourier transformation (2D-FT). This was done applying Scilab.<sup>[6]</sup>

The program routine performs the following steps:

- **Read matrix** of AFM scan (typical image sizes were 1024x1024 pixel)
- **Generate submatrices** (Enables the analysis of small areas on the platelet; please note that the submatrices still must be sufficiently larger than the wavelength of the wrinkles)
- **Conduct a 2D-FT** for the desired area
- **Construct and rearrange a 2x2 submatrix** from the 2D-FT area (indispensable in order to analyze all four quadrants in reciprocal space (+k<sub>x</sub>,+k<sub>y</sub>; +k<sub>x</sub>,−k<sub>y</sub>; −k<sub>x</sub>,+k<sub>y</sub>; −k<sub>x</sub>, −k<sub>y</sub>), see example below)
- **Integrate** within a range of appropriate k<sub>y</sub>-values (see example below)
- **Normalize** to a range of 0-1 within a given image
- **Plot** intensity profiles and contour plots

An important issue is the consideration of the direction of the wave-vector  $k$ . In a simple 2D-FT only the positive  $k$ -values are regarded. However, since the wave-vector of the investigated wrinkles is slightly tilted away from the main direction  $k \approx [1,0]$ , information of  $k$  pointing in  $-y$  direction would be lost. The following Figure S1a shows a realistic simulation of a wrinkled surface as it was found in the present study. The wave-vector  $k = [1,0]$  was subjected to a small randomized uncertainty in  $\pm x$  and  $\pm y$  direction resulting in a broad intensity profile after 2D-FT (Figure S1b). That uncertainty is in the real system caused by the variation of the stiffness within single nanoplatelets due to a variation of domains with higher and lower defect concentration. However, in the real system the variation is not

Submitted to  
**ADVANCED  
MATERIALS**

randomized but happens domain-dependent in a certain range as depicted in **Figures 2 and 3**.

A better view of the spread of periodicities in the simulation is given in the contour plot shown in **Figure S1c**. In that case, the intensities would be integrated from  $-4$  to  $+4$   $k_y$ -values to generate the intensity profile.

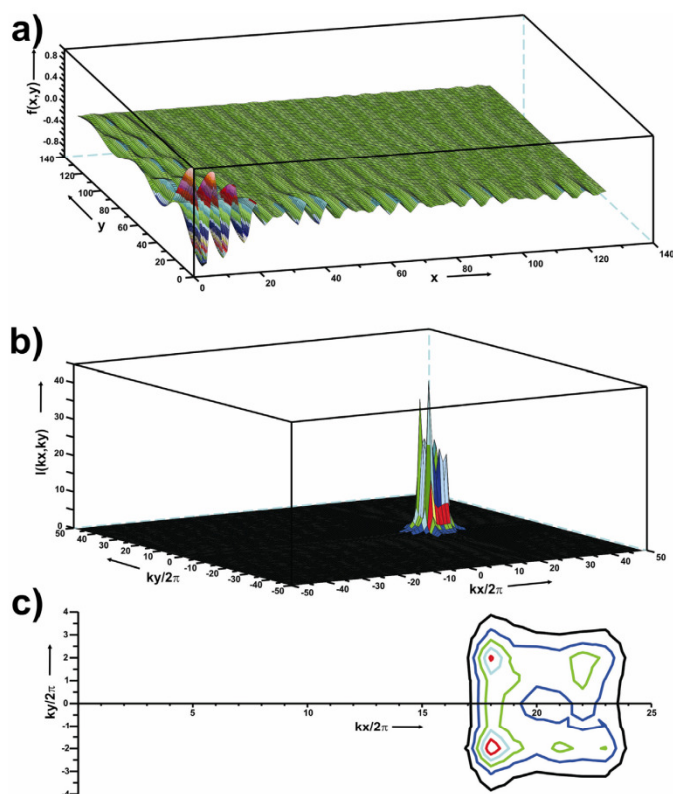


**Figure S 1.** Realistic wrinkling simulation. (a) Simulation of a typical wrinkled surface with a small randomized uncertainty in  $\pm x$  and  $\pm y$  direction of the wave-vector  $k$ . (b) Overall intensity profile after 2D-FT. (c) Contour plot of the intensity along the  $kx$ -axis.

## 2.2 Calculation of the In-Plane Moduli

Together with the extracted wrinkling wavelength the following values were used to calculate the in-plane moduli:

$$E_s = 3.46 \pm 0.09 \text{ MPa}$$

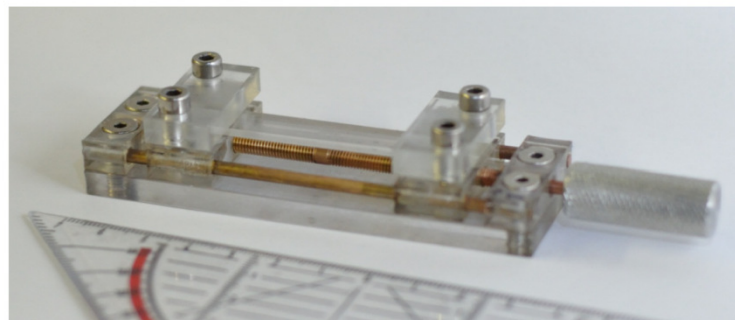
$$\nu_s = 0.5, \text{ see ref.}^{[2]}$$

$$\nu_p = 0.165, \text{ see ref.}^{[7,8]}$$

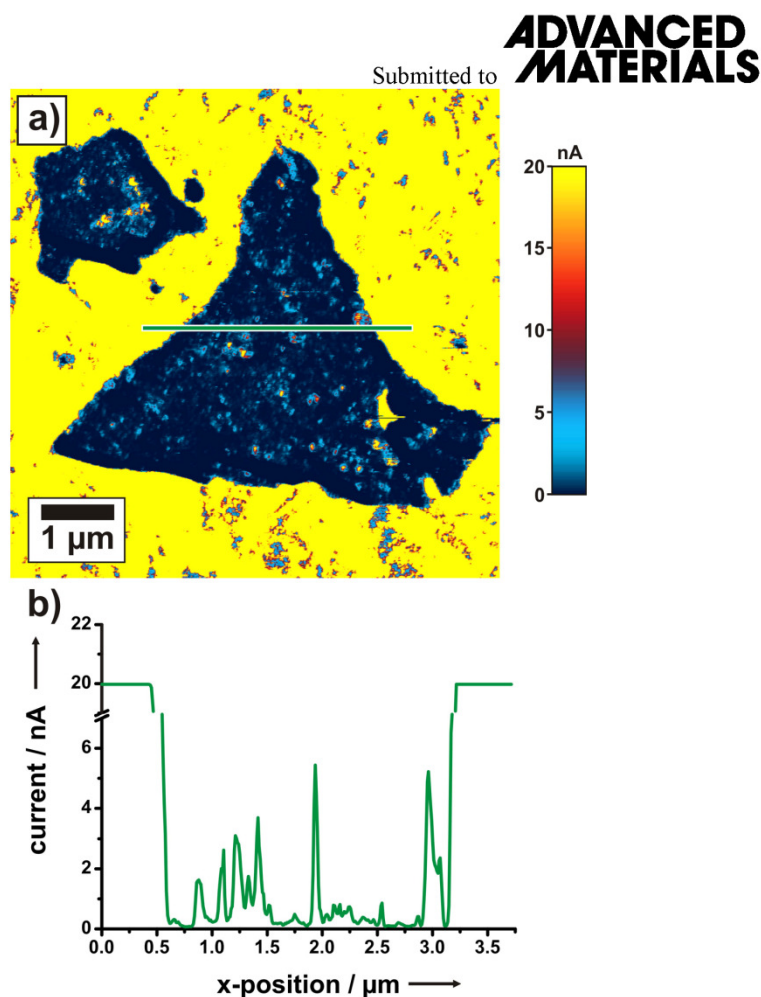
$$h = 0.7 \text{ nm}, \text{ see ref.}^{[9]}$$

$E_s$  was obtained by averaging the Young's moduli measured from 15 different samples (see chapter 1).

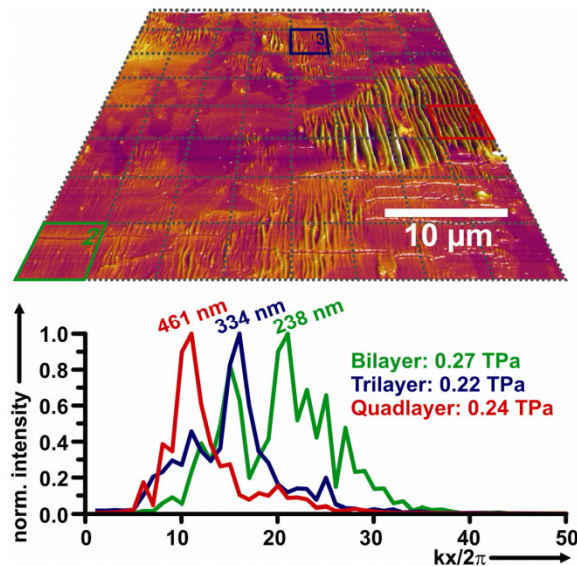
## 3 Supplementary Graphs and Figures



**Figure S 2.** Home-built stretching stage to provide reproducible wrinkling conditions.



**Figure S 3.** a) Conductive AFM image of GO monolayers lying on a template-stripped gold substrate. The color code ranges from yellow (high conductivity/gold) to dark blue (low conductivity/GO). For the highly conductive gold substrate the current goes into saturation (20 nA) due to the necessary amplification factor for imaging the conductivity of the platelets. Within one platelet, various domains with different conductivity become visible (brighter dots). Their distribution is, however, not statistical but shows a certain clustering. A partial cross-section through the conductivity data (b)) shows that the size of single defect domains is typically 80 – 100 nm while the clusters exhibit expansions around 500 – 750 nm which are detected as defects by the wrinkling method.

Submitted to **ADVANCED MATERIALS**

**Figure S 4.** AFM topographical image of wrinkled GO multi-layers at a higher platelet concentration. Some nanoplatelets are deposited above each other yielding thicker stacks. Below, the intensity profiles are given for a bilayer (green), trilayer (blue), and a quadlayer (red). Since the in-plane modulus of monolayer GO is related to the wrinkling wavelength, it is easy to distinguish between monolayer, bilayers and multilayers due to significant, stepwise increases in wavelengths and amplitudes. Assuming a multiple monolayer thickness for these higher wavelengths cases we obtained a constant in-plane modulus which, in turn, shows self-consistency of the assumptions within the continuum mechanics theory. No thickness dependence of the in-plane modulus was observed. The intensity profiles, however, become more homogeneous with increasing number of layers. Please note, that all intensities were scaled to 1. Unfortunately, the contrast of the monolayers (middle of image) was too low to be resolved properly.

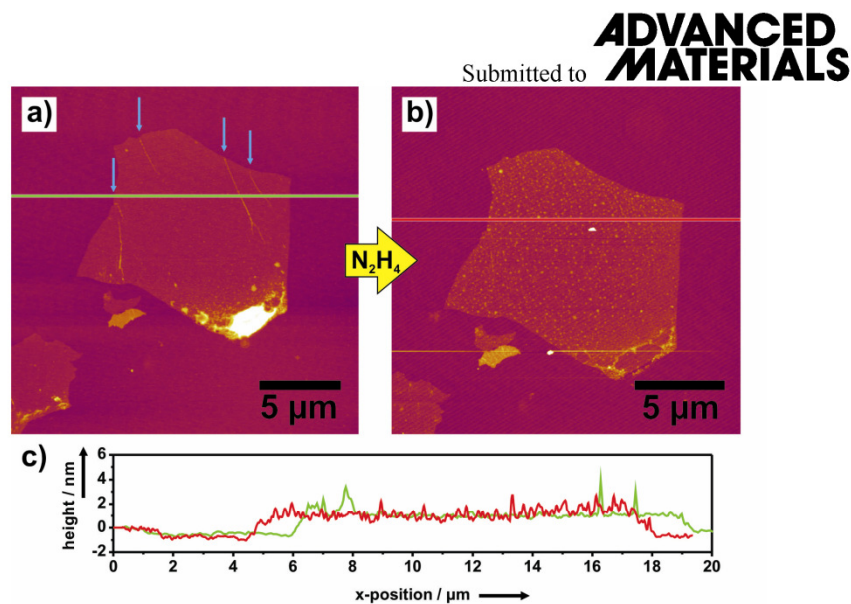


**Figure S 5.** AFM topographical images of the identical GO monolayer on a Silicon wafer, (a) before and (b) after reduction with hydrazine vapor. The cross-sections (green and red lines) show no significant decrease in height due to reduction. The blue arrows indicate wrinkles that are caused by sedimentation and drying procedure. Their absence after the reduction process strongly suggests a toughening of the platelet's in-plane moduli.

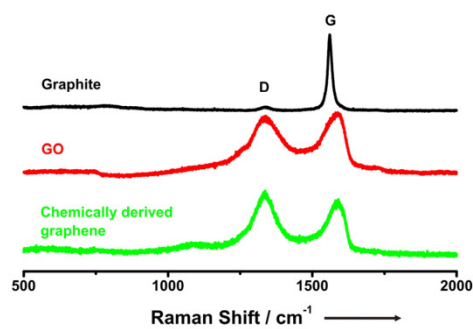


**Figure S 6.** Raman spectra of the graphite raw material (black line), GO (red line), and chemically derived graphene after reduction with hydrazine (green line).

**ADVANCED  
MATERIALS**

Submitted to

The Raman spectra show the typical changes accompanying the different steps of the synthesis of chemically derived graphene, as described in the literature.<sup>[10]</sup> Starting from graphite, the spectrum shows a prominent and narrow G band at  $1560\text{ cm}^{-1}$ , that corresponds to the first-order scattering of the  $E_{2g}$  mode<sup>[11]</sup>. Upon oxidation the D band becomes prominent which indicates the reduction of the size of the in-plane  $sp^2$  domains. The G band is blue-shifted to  $1588\text{ cm}^{-1}$  and becomes broader. The Raman spectrum of the chemically derived graphene also contains both D and G bands ( $1337\text{ cm}^{-1}$  and  $1590\text{ cm}^{-1}$ , respectively). The D band, however, becomes narrower and the D/G intensity ratio changes as well. A plausible explanation is that due to the generation of new graphitic domains by reduction the size of defect domains decreases while their number increases.<sup>[10]</sup> The persistent domain-structure is in excellent agreement with the results of the wrinkling method.



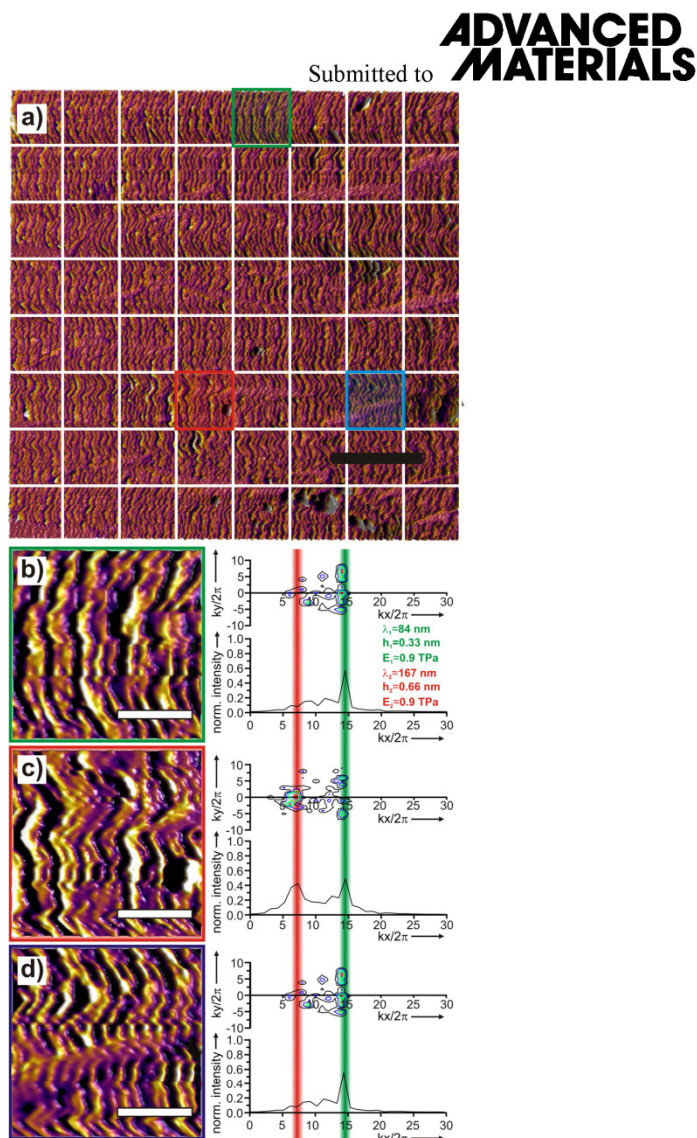


**Figure S 7.** CVD graphene analysis. The recorded AFM image (10  $\mu\text{m} \times 10 \mu\text{m}$  scan) with the wrinkled CVD monolayer graphene (a) was subdivided into 8  $\times$  8 sub-areas. For each area a 2D-FT was conducted. Figures (b) to (d) show representative areas at higher magnification: (b) pure monolayer graphene (green square), (c) mono- and bilayer cotributions (red square), (d) typical region showing monolayer graphene and a typical line defect (blue square); Next to the images, the contour-plots and averaged intensity profiles of the areas after 2D-FT are



**ADVANCED  
MATERIALS**

Submitted to

shown. The green and red lines mark the positions of wrinkling wavelengths for monolayer and bilayer graphene, respectively. The color code for the contour plot ranges from blue (low intensity) to red (high intensity). The scale bars represent 2  $\mu\text{m}$  (black) and 500 nm (white).

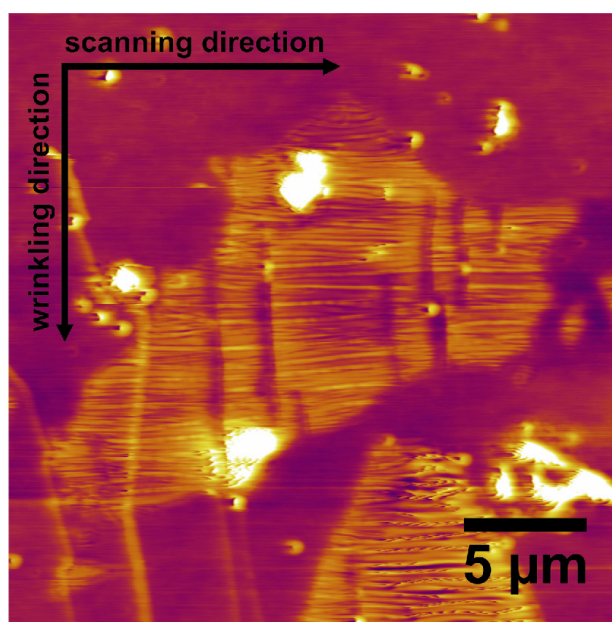


**Figure S 8.** AFM topographical image of a wrinkled graphene platelet that was rotated  $90^\circ$  to rule out the possibility of undulatory artifacts caused by scanning in intermittent contact mode.

Submitted to **ADVANCED  
MATERIALS**

#### 4 Supplementary References

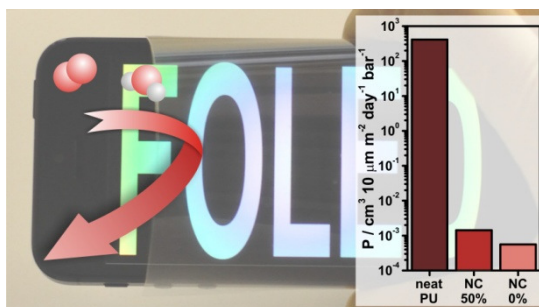
- [1] W. S. Hummers, R. E. Offeman, *J. Am. Chem. Soc.* **1958**, *80*, 1339.
- [2] H. Huang, J. Y. Chung, A. J. Nolte, C. M. Stafford, *Chem. Mater.* **2007**, *19*, 6555-6560.
- [3] M. Pretzl, A. Schweikart, C. Hanske, A. Chiche, U. Zettl, A. Horn, A. Böker, A. Fery, *Langmuir* **2008**, *24*, 12748-12753.
- [4] J. M. Mativetsky, E. Treossi, E. Orgiu, M. Melucci, G. P. Veronese, P. Samori, V. Palermo, *J. Am. Chem. Soc.* **2010**, *132*, 14130-14136.
- [5] D. Stamou, D. Gourdon, M. Liley, N. A. Burnham, A. Kulik, H. Vogel, C. Duschl, *Langmuir* **1997**, *13*, 2425-2428.
- [6] <http://www.scilab.org/>, 1-3-2012
- [7] C. Lee, X. D. Wei, J. W. Kysar, J. Hone, *Science* **2008**, *321*, 385-388.
- [8] O. L. Blakslee, *J. Appl. Phys.* **1970**, *41*, 3373-3382.
- [9] J. W. Suk, R. D. Piner, J. H. An, R. S. Ruoff, *ACS Nano* **2010**, *4*, 6557-6564.
- [10] S. Stankovich, D. A. Dikin, R. D. Piner, K. A. Kohlhaas, A. Kleinhammes, Y. Jia, Y. Wu, S. T. Nguyen, R. S. Ruoff, *Carbon* **2007**, *45*, 1558-1565.
- [11] F. Tuinstra, J. L. Koenig, *J. Chem. Phys.* **1970**, *53*, 1126-1130.

## 6.5 Flexible Nanokomposit-Beschichtung zur Anwendung in der Optoelektronik

Daniel A. Kunz<sup>†</sup>, Jasmin Schmid<sup>†</sup>, Patrick Feicht<sup>†</sup>, Johann Erath<sup>‡</sup>, Andreas Fery<sup>‡</sup>, and Josef Breu<sup>†,\*</sup>

### Clay-Based Nanocomposite Coating for Flexible Electronics Applying Commercial Polymers

Erschienen in: *ACS Nano*, **2013**, 7, 4275-4280. Reprinted with permission, Copyright (2013) American Chemical Society.



<sup>†</sup> Lehrstuhl für Anorganische Chemie I, Universität Bayreuth, 95447 Bayreuth, Deutschland

<sup>‡</sup> Lehrstuhl für Physikalische Chemie II, Universität Bayreuth, 95447 Bayreuth, Deutschland

\* josef.breu@uni-bayreuth.de

### Darstellung des Eigenanteils:

Das Konzept dieser Publikation wurde von mir selbst erarbeitet. Weiterhin führte ich alle grundlegenden Experimente durch, die dann von *Jasmin Schmid* weitergeführt und unter meiner Anleitung erweitert wurden. *Patrick Feicht* unterstützte bei der Wahl der Polymermatrix. Die finalen Gasbarrieremessungen wurden extern über die Firma Lippke bei Mocon Inc. USA durchgeführt und von *Jasmin Schmid* und mir ausgewertet. Die Nanoindentationsmessung übernahm *Johann Erath* in Zusammenarbeit mit Prof. Dr. *Andreas Fery*. Verfasst wurde diese Publikation hauptsächlich von Prof. Dr. *Josef Breu* und mir. Mein Eigenanteil beläuft sich auf ca. 80 %.

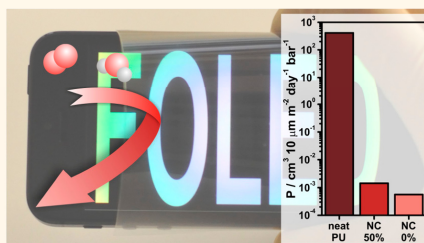
### 6.5.1 Clay-Based Nanocomposite Coating for Flexible Optoelectronics Applying Commercial Polymers

## Clay-Based Nanocomposite Coating for Flexible Optoelectronics Applying Commercial Polymers

Daniel A. Kunz,<sup>†</sup> Jasmin Schmid,<sup>†</sup> Patrick Feicht,<sup>†</sup> Johann Erath,<sup>‡</sup> Andreas Fery,<sup>‡</sup> and Josef Breu<sup>†,\*</sup>

<sup>†</sup>Department of Inorganic Chemistry I, University of Bayreuth, Universitätsstraße 30, 95440 Bayreuth, Germany and <sup>‡</sup>Department of Physical Chemistry II, University of Bayreuth, Universitätsstraße 30, D-95440 Bayreuth, Germany

**ABSTRACT** Transparency, flexibility, and especially ultralow oxygen (OTR) and water vapor (WVTR) transmission rates are the key issues to be addressed for packaging of flexible organic photovoltaics and organic light-emitting diodes. Concomitant optimization of all essential features is still a big challenge. Here we present a thin (1.5  $\mu\text{m}$ ), highly transparent, and at the same time flexible nanocomposite coating with an exceptionally low OTR and WVTR ( $1.0 \times 10^{-2} \text{ cm}^3 \text{ m}^{-2} \text{ day}^{-1} \text{ bar}^{-1}$  and  $<0.05 \text{ g m}^{-2} \text{ day}^{-1}$  at 50% RH, respectively). A commercially available polyurethane (Desmodur N 3600 and Desmophen 670 BA, Bayer MaterialScience AG) was filled with a delaminated synthetic layered silicate exhibiting huge aspect ratios of about 25 000. Functional films were prepared by simple doctor-blading a suspension of the matrix and the organophilized clay. This preparation procedure is technically benign, is easy to scale up, and may readily be applied for encapsulation of sensitive flexible electronics.



**KEYWORDS:** OLED · OPV · oxygen barrier · water vapor barrier · nanocomposite · coating · layered silicate

Efficient and thin coatings with a high barrier to various gases and fluids are needed for a wide range of applications stretching from food packaging<sup>1,2</sup> to high-tech applications such as flexible display packaging.<sup>3–5</sup> Flexible organic photovoltaics (FOPVs) and flexible organic light-emitting diodes (FOLEDs) are superior to conventional devices with respect to their multifunctionality, high durability, and impact resistance and are currently intensively studied. Molecular compounds applied in both FOPVs and FOLEDs suffer, however, from oxygen and moisture sensitivity. Efficient and sufficiently flexible barrier coatings are consequently a major challenge faced by the flexible electronics industry.<sup>6</sup> In order to achieve sufficient performance and lifetime, it has been estimated that transparent coatings need to limit the oxygen transmission rate (OTR) below  $10^{-5} \text{ cm}^3 \text{ m}^{-2} \text{ day}^{-1} \text{ bar}^{-1}$  and a water vapor transmission rate (WVTR) below  $10^{-6} \text{ g m}^{-2} \text{ day}^{-1}$  for application in reliable FOLEDs.<sup>7</sup> The requirements for FOPV are slightly less stringent (OTR  $< 10^{-3} \text{ cm}^3 \text{ m}^{-2} \text{ day}^{-1} \text{ bar}^{-1}$

and WVTR  $< 10^{-4} \text{ g m}^{-2} \text{ day}^{-1}$ , respectively). State of the art encapsulation with vapor-deposited thin films consisting of  $\text{SiO}_x$  or  $\text{Al}_2\text{O}_3$  provide a sufficient barrier but are prone to cracks when flexed.

It has been shown that nanocomposites consisting of platy inorganic fillers such as clays embedded in a polymeric matrix provide sufficient flexibility and excellent mechanical properties mimicking nacre.<sup>8,9</sup> According to tortuous path theory, the performance of nanocomposite coatings as gas barriers is determined by the aspect ratio and the filler content. The maximum reduction that may theoretically be achieved by impermeable platelets due to the elongation of the diffusion path is described by various tortuous path models, e.g., the Cussler model (Figure 1). Here the relative permeability ( $P_{\text{rel}}$ ) is determined as

$$P_{\text{rel}} = \frac{P}{P_0} = \left( 1 + \mu \frac{\alpha^2 \phi^2}{1 - \phi} \right)^{-1} \quad (1)$$

where  $P/P_0$  is the ratio of the permeability of the filled and unfilled polymer matrix,

\* Address correspondence to josef.breu@uni-bayreuth.de.

Received for review February 14, 2013 and accepted April 1, 2013.

Published online April 02, 2013  
10.1021/nn400713e

© 2013 American Chemical Society

KUNZ ET AL.

VOL. 7 ■ NO. 5 ■ 4275–4280 ■ 2013 ACS NANO  
www.acsnano.org

4275

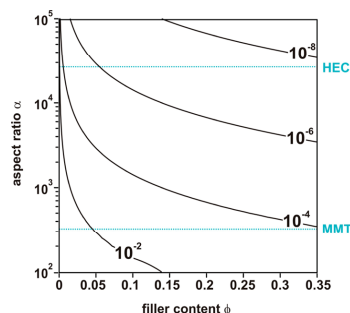


Figure 1. Relative permeability as function of aspect ratio and filler content according to Cussler's model. Dashed turquoise lines mark maximum aspect ratios of natural montmorillonite (MMT, <300) and the applied synthetic hectorite (HEC, ~25 000), respectively.

respectively.  $\phi$  represents the filler content and  $\alpha$  the aspect ratio of the filler.  $\mu$  is a geometric factor with a value of 4/9 in the case of hexagonal platelets.<sup>10</sup>

The most efficient and elegant way to maximize the aspect ratio is to take advantage of the intracrystalline reactivity of layered compounds. At best, so-called osmotic swelling of interlayer cations in materials such as graphene oxide or clay minerals leads to spontaneous delamination into singular platelets of thickness smaller than 1 nm.<sup>11–14</sup> In this fortunate case, the aspect ratio is limited only by the lateral extension of the tactoids, which is determined by crystallization/synthesis conditions. While synthetic hectorites can be obtained in dimensions up to 20  $\mu\text{m}$ <sup>14</sup> and are perfectly transparent, tactoids of natural clays such as montmorillonite are smaller than 300 nm and are colored due to iron impurities. In roll-to-roll processing, nanocomposite film thicknesses of typically <10  $\mu\text{m}$  can be applied. A neat film of the commercial polyurethane applied here shows an OTR of 409.4  $\text{cm}^3 \text{ m}^{-2} \text{ day}^{-1} \text{ bar}^{-1}$  (normalized to 10  $\mu\text{m}$ ). For a functional film to meet the FOLED criteria cited above, the relative permeability must be reduced to  $10^{-8}$ .

Organically modified montmorillonites such as Cloisite 93 show a  $d$ -spacing of 2.79 nm. A singular clay layer itself is 0.96 nm.<sup>15,16</sup> Thus for this intercalation compound, with a strictly alternating sequence of clay layer and organic alkylammonium counterions, the “filler content” is 35 vol %. This filler content may therefore be regarded as an upper limit for nanocomposites of delaminated clays that may be processed. Practically, for processability reasons this value will be even further reduced. Consequently, as depicted in Figure 1, composites containing natural clays such as montmorillonite (MMT) cannot meet the relative permeability requirements due to their limited lateral dimension. Even at maximum filler content and with perfectly delaminated MMT, only a maximum

reduction of the permeability of the polymer matrix by 4 orders of magnitude can be achieved. Furthermore, natural clays often carry significant amounts of globular accessory impurities, which may act as defects that will further enhance the permeability. Reduction of the relative permeability by 8 orders of magnitude would require an effective aspect ratio of 35 000 at a filler content of 35 vol %.

Tortuous path theory assumes that the OTR of the matrix volume in composites is not affected by the presence of the filler. This assumption is of course a rather crude approximation in such highly filled nanocomposites. Completely delaminated clay typically will show some 800  $\text{m}^2 \text{ g}^{-1}$  surface, which is transformed into interface when perfectly dispersed into the polymer matrix. Possible changes of free volume at the interface are therefore expected to crucially affect the OTR of the composite.<sup>17</sup> This is, however, completely neglected by tortuous path theory. Furthermore, the hydrophilic nature of the pristine clay minerals requires hydrophobization of the surfaces for two reasons: to reduce water vapor solubility in the composite and to avoid defects between filler and matrix due to marked differences in the surface tension. Along this line, dip-coating allows for composite formation and organophilization via “Umladung” (charge reversal) in consecutive dipping steps.<sup>8,9,18–22</sup> A bilayer thickness is, however, typically limited to about 5 nm,<sup>21</sup> and sufficiently thick functional films require many dipping steps.

In this work we report on a highly efficient, transparent, and flexible nanocomposite coating consisting of organophilized synthetic clay nanoplatelets embedded in a commercially available polyurethane matrix.

## RESULTS AND DISCUSSION

On the basis of a recent breakthrough in the synthesis of a  $\text{Na}_{0.5}$ -fluorohectorite ( $\text{Na}_{0.5}(\text{Mg}_{2.5}\text{Li}_{0.5})\text{Si}_4\text{O}_{10}\text{F}_2$ , denoted as Na-hec) we were able to apply a filler material that is unique with respect to homogeneity, purity, and particle size.<sup>14</sup> Furthermore, Na-hec shows osmotic swelling when thrown into deionized water, causing spontaneous delamination, *i.e.*, disintegration into single clay lamellae. Due to this gentle and elegant anisotropic top-down process, unprecedented ultra-high aspect ratios can be easily achieved.

The number-weighted lateral extension of the batch of clay platelets used as filler was determined by focused beam reflectance measurements (FBRM).<sup>23</sup> The measurements were first performed in aqueous dispersions; the particle size distribution therefore is representative for the bulk material. Moreover, it has been shown by Goossens<sup>24</sup> that the lateral extensions of clay tactoids correlate well with the hydrodynamical radius. We are, however, aware that the absolute values might be somewhat in error because of the large size

and the floppy nature of the nanoplatelets. Considering a platelet thickness of about 1 nm and a median lateral extension of the clay particles of 25  $\mu\text{m}$  (Figure S1, Supporting Information) and assuming complete delamination by osmotic swelling,  $\text{Na}_{0.5}\text{-Hec}$  offers a mean aspect ratio of 25 000, which is about 80 times higher than the largest platelets of MMT.

As mentioned before, incorporation of these platelets into the polymer matrix, however, requires compatibilization of the filler. Insufficient adjustment of the interface is expected to increase the free volume and/or foster aggregation of platelets, resulting in a lower barrier activity. Organophilization was achieved by a simple cation exchange, replacing  $\text{Na}^+$  against quaternized dimethylaminoethyl methacrylate (TMAEMA). This particular modifier allows for a subtle adjustment of surface tension. While cation exchange with standard modifiers such as quaternary ammonium cations causes immediate flocculation, this particular modifier allows maintaining a good dispersibility in water with no signs of aggregation. Rather flocculation of the organophilized fluorohectorite (O-hec) can be triggered in a controlled way by adding the hydrous dispersion into a 10/1 THF/butanone mixture. The precipitate is filtered and can then be completely redispersed in a polar organic solvent such as acetonitrile. The quality of the redispersion was cross-checked by FBRM particle size analysis. No larger aggregates were found (24  $\mu\text{m}$  median value; see Figure S1, Supporting Information).

The O-hec suspension in acetonitrile (8.8  $\text{mg mL}^{-1}$ ) was subsequently mixed with a standard, commercially available two-component polyurethane precursor polymer system (Desmodur N 3600 and Desmophen 670 BA, Bayer MaterialScience AG). The amount of suspension added corresponded to a final filler content of 50 wt % (ca. 30 vol %) based on solvent-free nanocomposite and pristine, nonmodified filler. The nanocomposite suspension was doctor-bladed on a 100  $\mu\text{m}$  thick polyethylene terephthalate (PET) foil and finally dried and hardened. Figure 2 summarizes the critical steps involved in the described procedure.

Doctor-blading as a coating technique is advantageous compared to conventional layer-by-layer techniques since it allows for preparation of larger area coatings in a fraction of the time because film thicknesses of 1–2  $\mu\text{m}$  can be achieved in one step. Moreover, a highly lamellar orientation of the nanoplatelets is achieved by shear forces acting during the coating process and by the ultrahigh aspect ratio of the filler. A cross sectional scanning microscopy (SEM) image underlines the very good texture (Figure 3a).

Unfortunately, due to the relatively high filler content aimed at, the filler cannot be dispersed in the neat precursor polymer, and additional solvent is indispensable to maintain a viscosity of the nanocomposite suspension that allows processing. While in layer-by-layer fabrication, bilayers of 5 nm have to be dried between

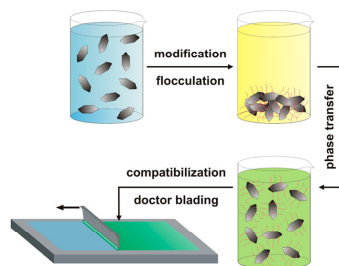


Figure 2. Experimental procedure for fabrication of large-scale nanocomposite coatings. An organophilization (modification and flocculation) step, followed by a phase transfer into a compatible solvent, is conducted. After mixing with commercially available polyurethane precursor polymers the coating is generated via scalable doctor-blading with subsequent drying and hardening.

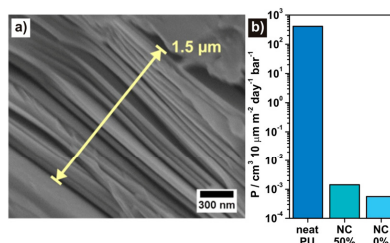


Figure 3. (a) SEM cross section of the nanocomposite coating. (b) Measured permeabilities of the neat polyurethane coating (neat PU) and of the nanocomposite coating (NC) at 50% and 0% RH, respectively. All values are decoupled from the supporting PET foil according to a literature procedure.<sup>25</sup>

steps, in doctor-blading 300 times more solvent has to be able to escape from the 1.5  $\mu\text{m}$  thick film. Drying of the film is therefore a very critical step, even more so, as the barrier film is self-sealing as drying and hardening proceeds from the outer layers to the core. Too fast and uncontrolled drying can cause blisters in the coating, which act as defects and ruin the gas barrier properties.<sup>25</sup> The commercial two-component polyurethane system was deliberately chosen with these difficulties in mind. The gel-like behavior of the non-hardened precursor polymers freezes the orientation and location of the nanoplatelets but allows for outgassing of the volatile solvent within the given curing time (3 days at 80 °C) of the precursors. With that approach blister-free nanocomposite coatings with no detectable amounts of entrapped solvent were obtained.

OTR measurements of the nanocomposite coating were conducted at 25 °C and relative humidities of 0% and 50%, respectively. It is noteworthy that absolute OTR values of  $3.7 \times 10^{-3} \text{ cm}^3 \text{ m}^{-2} \text{ day}^{-1} \text{ bar}^{-1}$  are below the detection limit of commercially available equipment and had to be measured with a new

**TABLE 1. OTR Values and Calculated Permeability (*P*) of the Nanocomposite Coating at Different RH in Comparison with Neat PET Foil and Neat Polyurethane Coating on PET<sup>a</sup>**

sample	RH/%	thickness/ μm	$P/\text{cm}^3 \cdot 10 \mu\text{m m}^{-2} \text{day}^{-1} \text{bar}^{-1}$		
			OTR/ $\text{cm}^3 \text{m}^{-2} \text{day}^{-1} \text{bar}^{-1}$	PET foil + coating	coating
neat PET	50	100	15	$1.5 \times 10^2$	
neat polyurethane	50	80	11.6	$2.1 \times 10^2$	$4.1 \times 10^2$
nanocomposite	50	1.5	$1.0 \times 10^{-2}$	$1.0 \times 10^{-1}$	$1.4 \times 10^{-3}$
	0	1.5	$3.7 \times 10^{-3}$	$3.8 \times 10^{-2}$	$5.6 \times 10^{-4}$

<sup>a</sup> The coating permeability was decoupled from the total values using a method described in the literature.<sup>26</sup>

prototype at Mocon Inc., USA. Relative permeabilities normalized to 10 μm thick films in comparison with neat polyurethane are given in Figure 3b).

It is obvious that the nanocomposite coating led to a significant decrease of the oxygen transmission. Furthermore, the nanocomposite coating is quite insusceptible to humidity. The OTR values for 0% and 50% RH differ by a factor of 2. To underline the good water vapor barrier, WVTR measurements were conducted on neat PET as well as on the nanocomposite samples on our in-house equipment. At 50% RH PET exhibited a WVTR of  $3.7 \text{ g m}^{-2} \text{day}^{-1}$ , whereas the nanocomposite coating was below the detection limit ( $<0.05 \text{ g m}^{-2} \text{day}^{-1}$ ).

The thickness of the coatings was  $1.5 \pm 0.3 \mu\text{m}$  in the case of the nanocomposite (Figure 3a) and  $80 \pm 5 \mu\text{m}$  in the case of neat polyurethane. Table 1 lists the measured OTR values together with the permeability for PET foil, for the nanocomposite coating, and for the neat polyurethane coating, respectively, normalized to 10 μm thickness for comparison.

From the ratio of permeability values of nanocomposite coating and neat polyurethane matrix, the relative permeability ( $P_{\text{rel}}$ ) can be calculated ( $3.4 \times 10^{-6}$ ). According to Cussler's model (eq 1), this relative permeability corresponds to an effective aspect ratio that is about 1 order of magnitude lower than the aspect ratios derived from FBRM measurements. We assume that the remaining discrepancy might be mainly related to inclusions of dust particles (Figure S2, Supporting Information) since the film production was not conducted under clean-room conditions. Additionally, observed partial phase segregation (Figure S3, Supporting Information) of filler and polymer matrix upon film drying lead to partial restacking of the nanoplatelets, resulting in a lower effective aspect ratio. Furthermore, alterations of the polymer's free volume that are neglected in the tortuous path theory could have led to a higher permeability and therefore lower apparent effective aspect ratio. Finally, TMAEMA intercalated into hectorite shows a *d*-spacing of 17.7 Å,

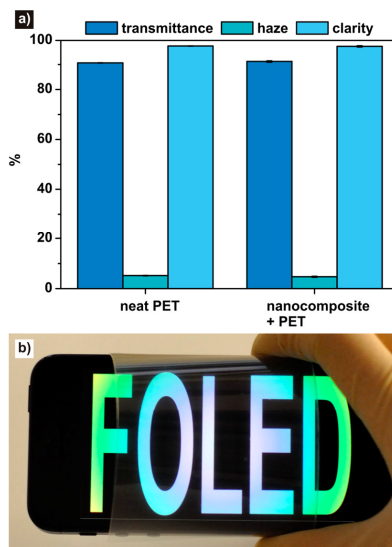


**Figure 4.** (a) Optical transmittance, haze, and clarity of neat PET foil and nanocomposite coating with PET foil as substrate. (b) Image of a bent nanocomposite coating on PET foil in front of a smartphone.

suggesting that the interface volume occupied by the surface modifier of the delaminated nanoplatelets is on the same order of magnitude as the volume of hectorite filler itself. The grafting density will be limited by the cation exchange capacity, and it may well be that the permeability of this interface region is larger than that of a bulk matrix and consequently will also contribute to the observed cut back in effective aspect ratio.

Nevertheless, this coating has improved the gas barrier efficiency by about 3 orders of magnitude compared to our previous best results ( $0.85 \text{ cm}^3 \cdot 10 \mu\text{m m}^{-2} \text{day}^{-1} \text{bar}^{-1}$ ).<sup>27</sup> Moreover, while in previous work we used a special cationic polyurethane modifier that was cured by UV light and that limited the maximum filler content to some 10 vol % due to its bulky nature, here we resort to a readily available and affordable commercial two-component polyurethane system (Desmodur N 3600 and Desmophen 670 BA were provided by Bayer MaterialScience AG) and a slim monomolecular modifier that allowed filler contents of 30 vol %.

Another important feature of the synthetic hectorite-based coatings with respect to applications in display packaging is their superb optical transparency. Since some scattering is caused by surface roughness, first a clear-coat of unfilled polyurethane was applied previous to measurements. Figure 4a compares optical transmittance, clarity, and haze of neat PET foil



(substrate) and the nanocomposite coating on PET foil. The barrier films exhibited almost the same level of optical transmittance and clarity as the untreated PET foil serving as substrate. Haze values were even improved.

Additionally, to check for color fastness on displays, absorption spectra covering the range of visible light were recorded (Figure S3, Supporting Information). Comparing the spectra of PET support and the nanocomposite barrier film shows that light transmission in the visible range is limited only by the PET support.

## CONCLUSION

A highly transparent, strong, and at the same time flexible nanocomposite coating on the basis of an ultrahigh aspect ratio clay was obtained applying a commercially available polyurethane matrix. Fabrication by doctor-blading is a technically benign and

scalable process. At the same time, oxygen and water vapor transmission rates were among the lowest reported in the literature so far. Moreover, the coating is almost insusceptible to humidity. Altogether, this barrier coating possesses great potential for flexible display packing, e.g., rollable electronic newspapers, pen-sized smartphones, and the like.

Moreover, as suggested by the recently measured in-plane moduli ( $\sim 200$  GPa),<sup>26</sup> the incorporation of these nanosheets into a tough polyurethane matrix is expected to significantly increase the Young's modulus. Preliminary nanoindentation measurements on samples of neat polyurethane and nanocomposite coated on glass slides revealed an increase of the Young's modulus from  $1.0 \pm 0.3$  GPa (neat polyurethane) to  $40 \pm 5$  GPa (nanocomposite). A detailed characterization of the mechanical properties of the nanocomposite films is in progress.

## METHODS

**Synthesis of Na<sub>0.5</sub>-fluorhectorite.** The employed Na<sub>0.5</sub>-fluorhectorite (Na-hec) with stoichiometry  $[\text{Na}_{0.5}][\text{Li}_{0.5}\text{Mg}_{2.5}][\text{Si}_4\text{O}_{10}]\text{F}_2$  was synthesized *via* melt synthesis according to an established literature procedure.<sup>14,29,30</sup> The material featured a cation exchange capacity (CEC) of  $1.27 \text{ mval g}^{-1}$ .

**Preparation of Modifier.** Trimethylammonium ethylmethacrylate iodide was used for surface modification of the hectorite. Hereby, dimethylaminoethyl methacrylate (DMAEMA, Sigma Aldrich) was quaternized according to a procedure described in the literature.<sup>31</sup> In a typical procedure, DMAEMA was dissolved in acetone and methyl iodide was added at a molar ratio of 1.5 compared to amino groups. Ensuring complete conversion, the mixture was stirred overnight. The precipitate was washed several times with acetone and finally dried using high vacuum. <sup>1</sup>H NMR spectroscopy revealed a quantitative quaternization.

**Nanocomposite Preparation.** For the surface modification of the clay a double excess of TMAEMA compared to the CEC of the Na-hec was dissolved in Millipore water, added dropwise to an aqueous suspension of Na-hec ( $2.5 \text{ g L}^{-1}$ ), and placed into an overhead shaker for 24 h. Afterward the clay was washed with Millipore water and the procedure was repeated. The aqueous dispersion of modified clay (O-hec) was flocculated in a 10/1 THF/butanone mixture, filtered over a  $90 \mu\text{m}$  sieve, and redispersed in acetonitrile. THF, butanone, and acetonitrile were purchased from Sigma Aldrich in p.a. quality.

As a polymer matrix a two-component polyurethane system was used. The precursor polymers Desmodur N 3600 and Desmophen 670 BA were provided by Bayer MaterialScience AG, Leverkusen, Germany, and were mixed 1/1 according to the equivalent weight (ratio of reactive groups).

For preparation of the nanocomposite mixture with 50 wt % hectorite the polymer matrix and the modifier were counted as organic compound. So the 50 wt % content refers only to the neat hectorite. Matrix and modified filler were homogenized by using the SilentCrusher M (Heidolph Instruments GmbH & Co. KG) at 12 000 rpm for 2 min. Solid content (neat hectorite) was about  $40 \text{ mg mL}^{-1}$ .

The nanocomposites were deposited on PET foils *via* doctor-blading (blade speed  $0.9 \text{ cm s}^{-1}$ ). The obtained films were dried at  $80^\circ\text{C}$  for 3 days.

**Nanocomposite Characterization.** Oxygen transmission rates were acquired by Mocon (Minneapolis, MN, USA) on a Mocon OX-TRAN 2/21 XL instrument with a lower detection limit of  $0.0005 \text{ cm}^3 \text{ m}^{-2} \text{ day}^{-1} \text{ bar}^{-1}$ . The measurements were

conducted at  $25^\circ\text{C}$  and relative humidities of 0% RH and 50% RH, respectively, applying the standards ASTM D-3985, ASTM F-1927, DIN 53380, JIS K-7126, and ISO CD 15105-2.

Water vapor transmission rates were measured at a Mocon PERMATRAN-W model 333 at  $25^\circ\text{C}$  and a relative humidity of 50% RH. The lower detection limit of the device was  $0.05 \text{ g m}^{-2} \text{ day}^{-1}$ .

SEM images were obtained on a LEO 1530 FESEM (Zeiss). The cross section polished sample was prepared by Leica Microsystems GmbH, Germany, using ion-etching.

TEM images were obtained on a JEM-2100 TEM (JEOL GmbH, Germany). Cross sections of the nanocomposite coatings were prepared with an Ion Slicer EM-09100IS (JEOL GmbH, Germany). These preparation and analytical steps were conducted by JEOL GmbH, Germany.

Transmittance, clarity, and haze of the coatings were measured on a BYK-Gardner Haze-Gard Plus, BYK Additives & Instruments (Altana AG, Germany).

Visible light transmission spectra were recorded on a Cary 300 Scan UV/vis spectrometer (Varian/Agilent Tech., CA, USA).

Nanoindentation measurements were conducted using an MFP-3DT (Asylum Research, CA, USA) equipped with a nano-indenter (Berkovich tip geometry). Hereby samples of neat polyurethane and nanocomposite film were coated onto microscopy glass slides and hardened as described above.

**Conflict of Interest:** The authors declare no competing financial interest.

**Supporting Information Available:** Supplementary Figures S1–S4. This material is available free of charge *via* the Internet at <http://pubs.acs.org>.

**Acknowledgment.** This work was supported by the German Science Foundation (SFB 840). D.A.K. thanks the elite study program "Macromolecular Science" as well as the International Graduate School "Structure, Reactivity and Properties of Oxide Materials" within the Elite Network of Bavaria (ENB) for ongoing support. Bayer MaterialScience AG is gratefully acknowledged for providing polymer samples. We are particularly indebted to Dr. F. Richter, Bayer MaterialScience AG, Leverkusen, Germany, for valuable discussions regarding the choice of commercial polyurethane system. The authors would also like to thank Paul Lippke Handels-GmbH, Germany, and Mocon Inc., USA, for conducting the permeation measurements at the SuperOxTran device. The authors thank JEOL GmbH, Germany, for the preparation and analytics of the TEM samples.



## REFERENCES AND NOTES

- Lange, J.; Wyser, Y. Recent Innovations in Barrier Technologies for Plastic Packaging - a Review. *Packag. Technol. Sci.* **2003**, *16*, 149–158.
- Arora, A.; Padua, G. W. Review: Nanocomposites in Food Packaging. *J. Food Sci.* **2010**, *75*, 43–49.
- Choi, M. C.; Kim, Y.; Ha, C. S. Polymers for Flexible Displays: From Material Selection to Device Applications. *Prog. Polym. Sci.* **2008**, *33*, 581–630.
- Lewis, J. Material Challenge for Flexible Organic Devices. *Mater. Today* **2006**, *9*, 38–45.
- Logothetidis, S. Flexible Organic Electronic Devices: Materials, Process and Applications. *Mater. Sci. Eng. B* **2008**, *152*, 96–104.
- Burrows, P. E.; Graff, G. L.; Gross, M. E.; Martin, P. M.; Shi, M. K.; Hall, M.; Mast, E.; Bonham, C.; Bennett, W.; Sullivan, M. B. Ultra Barrier Flexible Substrates for Flat Panel Displays. *Displays* **2001**, *22*, 65–69.
- Kumar, R. S.; Auch, M.; Ou, E.; Ewald, G.; Jin, C. S. Low Moisture Permeation Measurement through Polymer Substrates for Organic Light Emitting Devices. *Thin Solid Films* **2002**, *417*, 120–126.
- Tang, Z. Y.; Kotov, N. A.; Magonov, S.; Ozturk, B. Nanostructured Artificial Nacre. *Nat. Mater.* **2003**, *2*, 413–418.
- Podsiadlo, P.; Kaushik, A. K.; Arruda, E. M.; Waas, A. M.; Shim, B. S.; Xu, J. D.; Nandivada, H.; Pimplin, B. G.; Lahann, J.; Ramamoorthy, A.; et al. Ultrastrong and Stiff Layered Polymer Nanocomposites. *Science* **2007**, *318*, 80–83.
- DeRocher, J. P.; Gettelfinger, B. T.; Wang, J. S.; Nuxoll, E. E.; Cussler, E. L. Barrier Membranes With Different Sizes of Aligned Flakes. *J. Membr. Sci.* **2005**, *254*, 21–30.
- Möller, M. W.; Handge, U. A.; Kunz, D. A.; Lunkenbein, T.; Altstädt, V.; Breu, J. Tailoring Shear-Stiff, Mica-Like Nanoplatelets. *ACS Nano* **2010**, *4*, 717–724.
- Kalo, H.; Möller, M. W.; Ziadeh, M.; Dolejš, D.; Breu, J. Large Scale Melt-Synthesis in an Open Crucible of Na-Fluorohectorite with Superb Charge Homogeneity and Particle Size. *Appl. Clay Sci.* **2010**, *48*, 39–45.
- Kalo, H.; Möller, M. W.; Kunz, D. A.; Breu, J. How to Maximize the Aspect Ratio of Clay Nanoplatelets. *Nanoscale* **2012**, *4*, 5633–5639.
- Stöter, M.; Kunz, D. A.; Schmidt, M.; Hirsemann, D.; Kalo, H.; Putz, B.; Senker, J.; Breu, J. Nanoplatelets of Sodium Hectorite Showing Aspect Ratios of 20000 and Superior Purity. *Langmuir* **2013**, *29*, 1280–1285.
- Suter, J. L.; Coveney, P. V.; Greenwell, H. C.; Thyveetil, M. A. Large-Scale Molecular Dynamics Study of Montmorillonite Clay: Emergence of Undulatory Fluctuations and Determination of Material Properties. *J. Phys. Chem. C* **2007**, *111*, 8248–8259.
- Kalo, H.; Millius, W.; Breu, J. Single Crystal Structure Refinement of One- and Two-Layer Hydrate of Sodium-Fluorohectorite. *RSC Adv.* **2012**, *2*, 8452–8459.
- Choudalakis, G.; Gotsis, A. D. Free Volume and Mass Transport in Polymer Nanocomposites. *Curr. Opin. Colloid Interface Sci.* **2012**, *17*, 132–140.
- Kotov, N. A.; Haraszti, T.; Turi, L.; Zavala, G.; Geer, R. E.; Dekany, I.; Fendler, J. H. Mechanism of and Defect Formation in the Self-Assembly of Polymeric Polycation-Montmorillonite Ultrathin Films. *J. Am. Chem. Soc.* **1997**, *119*, 6821–6832.
- Podsiadlo, P.; Michel, M.; Lee, J.; Verploegen, E.; Kam, N. W. S.; Ball, V.; Lee, J.; Qi, Y.; Hart, A. J.; Hammond, P. T.; et al. Exponential Growth of LBL Films with Incorporated Inorganic Sheets. *Nano Lett.* **2008**, *8*, 1762–1770.
- Priolo, M. A.; Gamboa, D.; Holder, K. M.; Grunlan, J. C. Super Gas Barrier of Transparent Polymer-Clay Multi layer Ultrathin Films. *Nano Lett.* **2010**, *10*, 4970–4974.
- Priolo, M. A.; Holder, K. M.; Greenlee, S. M.; Grunlan, J. C. Transparency, Gas Barrier, and Moisture Resistance of Large-Aspect-Ratio Vermiculite Nanobrick Wall Thin Films. *ACS Appl. Mater. Interfaces* **2012**, *4*, 5529–5533.
- Yang, Y. H.; Bolling, L.; Priolo, M. A.; Grunlan, J. C. Super Gas Barrier and Selectivity of Graphene Oxide-Polymer Multi-layer Thin Films. *Adv. Mater.* **2013**, *25*, 503–508.
- Heath, A. R.; Fawell, P. D.; Bahri, P. A.; Swift, J. D. Estimating Average Particle Size by Focused Beam Reflectance Measurement (FBRM). *Part. Part. Syst. Charact.* **2002**, *19*, 84–95.
- Goossens, D. Techniques to Measure Grain-Size Distributions of Loamy Sediments: A Comparative Study of Ten Instruments for Wet Analysis. *Sedimentology* **2008**, *55*, 65–96.
- Möller, M. W.; Lunkenbein, T.; Kalo, H.; Schieder, M.; Kunz, D. A.; Breu, J. Barrier Properties of Synthetic Clay with a Kilo-Aspect Ratio. *Adv. Mater.* **2010**, *22*, 5245–5249.
- Roberts, A. P.; Henry, B. M.; Sutton, A. P.; Grovenor, C. R. M.; Briggs, G. A. D.; Miyamoto, T.; Kano, A.; Tsukahara, Y.; Yanaka, M. Gas Permeation in Silicon-Oxide/Polymer (SiOx/PET) Barrier Films: Role of the Oxide Lattice, Nano-Defects and Macro-Defects. *J. Membr. Sci.* **2002**, *208*, 75–88.
- Möller, M. W.; Kunz, D. A.; Lunkenbein, T.; Sommer, S.; Nennemann, A.; Breu, J. UV-Cured, Flexible, and Transparent Nanocomposite Coating with Remarkable Oxygen Barrier. *Adv. Mater.* **2012**, *24*, 2142–2147.
- Kunz, D. A.; Erath, J.; Kluge, D.; Thurn, H.; Putz, B.; Fery, A.; Breu, J. In-Plane Modulus of Singular 2:1-Clay Lamellae Applying a Simple Wrinkling Technique. Unpublished work.
- Breu, J.; Seidl, W.; Stoll, A. J.; Lange, K. G.; Probst, T. U. Charge Homogeneity in Synthetic Fluorohectorite. *Chem. Mater.* **2001**, *13*, 4213–4220.
- Malikova, N.; Cadene, A.; Dubois, E.; Marry, V.; Durand-Vidal, S.; Turq, P.; Breu, J.; Longeville, S.; Zanotti, J. M. Water Diffusion in a Synthetic Hectorite Clay Studied by Quasi-Elastic Neutron Scattering. *J. Phys. Chem. C* **2007**, *111*, 17603–17611.
- Plamper, F. A.; Schmalz, A.; Penott-Chang, E.; Drechsler, M.; Jusufi, A.; Ballauff, M.; Müller, A. H. E. Synthesis and Characterization of Star-Shaped Poly(*N,N*-dimethylaminoethyl methacrylate) and its Quaternized Ammonium Salts. *Macromolecules* **2007**, *40*, 5689–5697.

---

6.5.2 Supporting Information

1 Clay-Based Nanocomposite Coating for Flexible  
2 Optoelectronics Applying Commercial Polymers

3 *Daniel A. Kunz,<sup>†</sup> Jasmin Schmid,<sup>†</sup> Patrick Feicht,<sup>†</sup> Johann Erath,<sup>‡</sup> Andreas Fery,<sup>‡</sup> and Josef*  
4 *Breu<sup>†,\*</sup>*

5 <sup>†</sup> Department of Inorganic Chemistry I, University of Bayreuth, Universitätsstr. 30, 95440  
6 Bayreuth, Germany

7 <sup>‡</sup> Department of Physical Chemistry II, University of Bayreuth, Universitätsstraße 30, D-95440  
8 Bayreuth, Germany

9 \* To whom correspondence should be addressed: andreas.fery@uni-bayreuth.de; josef.breu@uni-  
10 bayreuth.de

11

12 Supplementary Information

13

## Supplementary figures

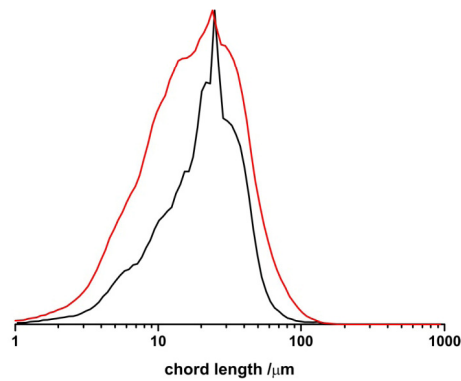


**Figure S1.** Number-weighted focused beam reflectance measurements (FBRM) for an aqueous Na-hec suspension (black curve) and for an O-hec suspension in acetonitrile (red curve). The median values are 25  $\mu\text{m}$  for Na-hec and 24  $\mu\text{m}$  for O-hec, respectively.

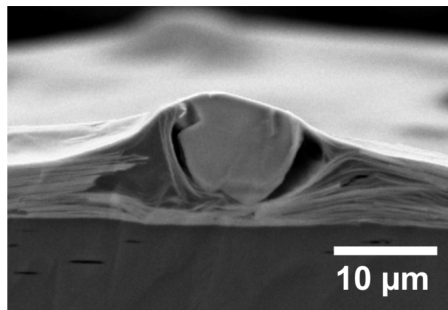
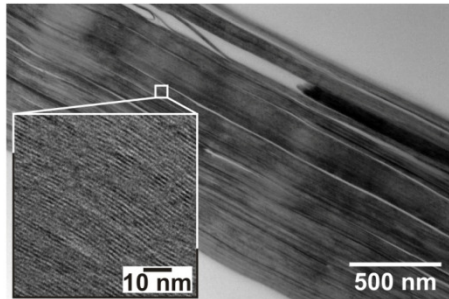


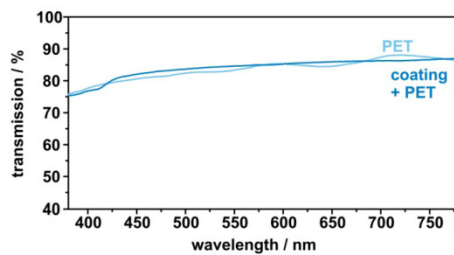
**Figure S2.** Cross-section polished SEM image of the inclusion of a dust particle. Please note that the coating is fanned out in this region which may limit the gas barrier performance.



25

26 **Figure S3.** Cross-section TEM image of the nanocomposite coating prepared with the ion-  
27 slicer. Brighter regions in the cross-section denote phase segregated polymer. It seems that phase  
28 segregation took place upon film drying while the suspension *per se* was stable. The inset  
29 underlines the perfect texture of the nanoplatelets.

30



31

32 **Figure S4.** Visible light transmission as a function of the wavelength for the neat PET foil and  
33 the nanocomposite coating on PET.

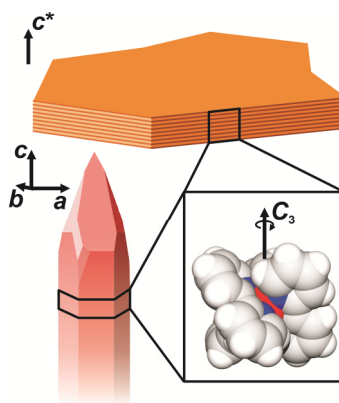
34

## 6.6 *Polarisierte Emission durch templatgesteuerte Quasi-Epitaxie*

Daniel A. Kunz<sup>†</sup>, Markus Leitl<sup>‡</sup>, Lukas Schade<sup>§</sup>, Jasmin Schmid<sup>†</sup>, Beate Bojer<sup>†</sup>, Ulrich T. Schwarz<sup>§</sup>, Geoffrey A. Ozin<sup>⊥,\*</sup>, Hartmut Yersin<sup>‡,\*</sup>, and Josef Breu<sup>†,\*</sup>

### **Quasi-Epitaxy of $[\text{Ru}(\text{bpy})_3]^{2+}$ by Confinement in Clay Nanoplatelets Yields Polarized Emission**

*Submitted to Small.*



<sup>†</sup> Lehrstuhl für Anorganische Chemie I, Universität Bayreuth, 95447 Bayreuth, Deutschland

<sup>‡</sup> Lehrstuhl für Physikalische Chemie, Universität Regensburg, 93053 Regensburg, Deutschland

<sup>§</sup> Institut für Mikrosystemtechnik IMTEK, Universität Freiburg, 79110 Freiburg, Deutschland

<sup>⊥</sup> Materials Chemistry and Nanochemistry Research Group, Center for Inorganic and Polymeric Nanomaterials, Chemistry Department, University of Toronto, Toronto M5S 3H6, Canada

\* josef.breu@uni-bayreuth.de, hartmut.yersin@ur.de, gozin@chem.utoronto.ca

#### **Darstellung des Eigenanteils:**

Das Konzept dieser Publikation wurde von mir selbst erarbeitet. Weiterhin führte ich die grundlegenden Experimente durch, die dann von *Jasmin Schmid* weitergeführt wurden. *Markus Leitl* war mit mir in Zusammenarbeit mit Prof. Dr. *Hartmut Yersin* für die ersten

Emissionsmessungen verantwortlich und stellte den Kontakt mit *Lukas Schade* und Prof. Dr. *Ulrich T. Schwarz* her, die die Messungen am hauseigenen Gerät finalisierten. *Beate Bojer* unterstützte bei der Synthese der Einkristalle. Prof. Dr. *Geoffrey A. Ozin* war an der Diskussion der Resultate beteiligt und betreute meine Experimente in Kanada. Verfasst wurde die Publikation hauptsächlich von Prof. Dr. *Josef Breu* und mir.

Mein Eigenanteil beläuft sich auf ca. 80 %.

---

6.6.1      Quasi-Epitaxy of  $[\text{Ru}(\text{bpy})_3]^{2+}$  by Confinement in Clay Nanoplatelets  
             Yields Polarized Emission

**Quasi-Epitaxy of  $[\text{Ru}(\text{bpy})_3]^{2+}$  by Confinement in Clay Nanoplatelets Yields Polarized Emission**

*Daniel A. Kunz, Markus J. Leidl, Lukas Schade, Jasmin Schmid, Beate Bojer, Ulrich T. Schwarz, Geoffrey A. Ozin\*, Hartmut Yersin\*, and Josef Breu\**

Dedicated to Prof. Geoffrey A. Ozin on the occasion of his 70th birthday

D.A. Kunz, J. Schmid, B. Bojer, Prof. J. Breu  
Department of Inorganic Chemistry I, University of Bayreuth, Universitätsstraße 30, 95440  
Bayreuth, Germany  
E-mail: josef.breu@uni-bayreuth.de

M. J. Leidl, Prof. H. Yersin  
Department of Physical Chemistry, University of Regensburg, Universitätsstraße 31, 93053  
Regensburg, Germany  
E-mail: hartmut.yersin@ur.de

L. Schade, Prof. U.T. Schwarz  
Department of Microsystems Engineering IMTEK, University of Freiburg, Georges-Köhler-  
Allee 103, 79110 Freiburg, Germany

Prof. G.A. Ozin  
Materials Chemistry and Nanochemistry Research Group, Center for Inorganic and Polymeric  
Nanomaterials, Chemistry Department, University of Toronto, 80 St. George Street, Toronto,  
M5S 3H6, Ontario, Canada  
E-mail: gozin@chem.utoronto.ca

Keywords: clay nanoplatelets, host-guest nano-confinement, polarized emission, OLED, oriented intercalation of  $[\text{Ru}(\text{bpy})_3]^{2+}$

Recently, significant progress has been made with the development and improvement of organic light emitting diodes (OLEDs).<sup>[1, 2]</sup> Their use in cell phone displays has paved the way to a mass market and lighting applications with a potentially even larger market within reach. However, so far only about 20 % of generated photons can be out-coupled and extracted as light.<sup>[1-3]</sup> The overall efficiency of OLEDs can be described by the external quantum efficiency ( $\eta_{ext}$ ) which is defined as the ratio of photons emitted compared to the number of electron-hole pairs injected. Four factors determine the magnitude of  $\eta_{ext}$ <sup>[1, 2, 4, 5]</sup>

$$\eta_{ext} = \gamma \cdot \beta \cdot \Phi_{PL} \cdot \eta_{out} \quad (1)$$

In this equation,  $\gamma$  represents the charge balance factor,  $\beta$  the spin statistics factor,  $\Phi_{PL}$  the photoluminescence quantum yield, and  $\eta_{out}$  the optical out-coupling factor. It has already been demonstrated that an internal quantum yield (expressed by  $\eta_{int} = \gamma \beta \Phi_{PL}$ ) of almost 100 % can be obtained.<sup>[3]</sup> This can be achieved with an optimized recombination zone ( $\gamma = 1$ ),<sup>[6]</sup> an optimized photoluminescence quantum yield ( $\Phi_{PL} \approx 1$ ),<sup>[7, 8]</sup> and a triplet harvesting<sup>[7, 9]</sup> instead of a singlet harvesting<sup>[7, 10]</sup> effect ( $\beta = 1$ ).

The optical out-coupling factor  $\eta_{out}$  is, however, significantly lower than all the other factors contributing to  $\eta_{ext}$  and therefore carries the largest potential for optimization. Without improvements in light extraction efficiency, currently the out-coupling factor is limited to  $\eta_{out} \approx 0.2$ .<sup>[1-3]</sup> Enhancing light extraction techniques have demonstrated that this factor can be significantly increased.<sup>[11]</sup> One loss mechanism that causes a low  $\eta_{out}$  involves excitation of surface plasmons at the metallic cathode by coupling to the electric dipole transitions of the emitting molecules. The quenching strength depends on the orientation of the transition dipole and is minimized for emitters that exhibit a polarization of the electric field vector  $\vec{E}$  lying parallel to the plane of the cathode.<sup>[12-16]</sup> Thus, by controlling the orientation of the transition dipole of the emitter molecule adequately, this loss channel can be reduced and the out-coupling factor



can increase up to  $\eta_{out} \approx 0.3$ . Methods to achieve orientation of organic fluorescent emitters<sup>[17]</sup> include Langmuir-Blodgett deposition,<sup>[18]</sup> mechanical alignment,<sup>[19, 20]</sup> and liquid crystalline self-assembly.<sup>[21, 22]</sup> Highly symmetrical and approximately spherical transition metal compounds can prove more difficult to be oriented. Physical vapor deposition is generally of limited suitability. In this context, intercalation of emitters into highly anisotropic layered host lattices, such as synthetic clays and layered double-hydroxides (LDHs),<sup>[23-26]</sup> has been shown to have potential for controlling molecule alignment on the nano-scale. Due to spatial restrictions in the interlayer space and the structure directing effect of the surface corrugation of the host lattice, emitters, as generally any molecule, will be inevitably intercalated in a well-defined orientation.<sup>[27-29]</sup> Furthermore, the adsorption onto clay platelets has been applied to create compatibility of dyes with usually incompatible dispersion media.<sup>[30]</sup> For a potential application in OLED devices, however, sufficiently large (several  $\mu\text{m}$ ) and delaminated (singular lamellae of 1 nm thickness) nanoplatelets are needed for two crucial reasons: First, clay platelets are dielectric materials but it has been shown that electrons can tunnel through thin clay platelets ( $< 5 \text{ nm}$ )<sup>[31]</sup> which is critical for their usage as carriers for electroluminescent emitters. Second, large lateral extensions are needed to gain a large aspect ratio (ratio of lateral extension to height) of the clay hosts, which will lead to a textured, parallel orientation of the clay lamellae when applying a suspension e.g. in a roll to roll process to a planar device substrate. This in turn, will inevitably lead to a well-defined alignment of the emitter molecules which are attached to the clay in a well-defined orientation and if favorable, quasi-epitaxial growth might enhance  $\eta_{out}$ .

In this article, we demonstrate that oriented intercalation of an archetype luminophor between the layers of well-ordered, high-aspect ratio clay nanoplatelets enables polarization emission control and provides a quasi-epitaxial strategy for future work directed at enhancing the efficiency of OLEDs. For a proof-of-principle, the model system  $[\text{Ru}(\text{bpy})_3]^{2+}$  ( $\text{bpy} = 2,2'$ -

bipyridine) intercalated into well-ordered, synthetic Na-fluorohectorite platelets<sup>[32]</sup> was chosen.

Films that exhibit typical thicknesses of emitter layers of OLEDs (tens of nanometers) cannot be analyzed. Therefore, to probe the quality of orientation of the intercalated transition metal complex, the polarization degree of emitted light was studied with macroscopic crystals of the  $[\text{Ru}(\text{bpy})_3]\text{-fluorohectorite}$ .  $[\text{Ru}(\text{bpy})_3]^{2+}$  was chosen because its electronic structure has been well characterized<sup>[33-36]</sup> and because it has been shown to adopt well defined patterns in the interlayer of a clay host.<sup>[37]</sup>

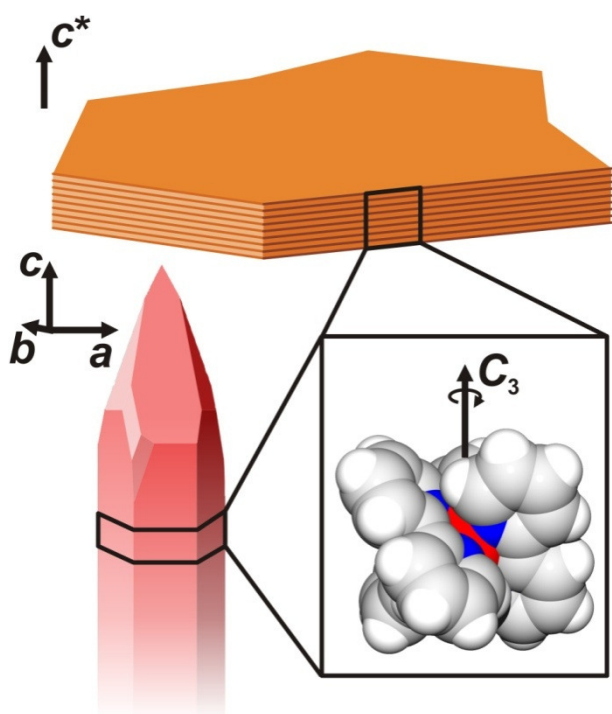


**Figure 1.** Orientation of the  $\vec{C}_3$ -axis of  $[\text{Ru}(\text{bpy})_3]^{2+}$  in a single-crystal needle of  $[\text{Ru}(\text{bpy})_3](\text{PF}_6)_2$  (red) and when sandwiched between clay platelets (orange) as suggested by computer simulations,<sup>[38, 39]</sup>  $a$ ,  $b$ , and  $c$  mark the crystallographic axes of  $[\text{Ru}(\text{bpy})_3](\text{PF}_6)_2$ , while  $\vec{c}^*$  represents the stacking direction of the clay platelet.

The emission properties of  $[\text{Ru}(\text{bpy})_3]^{2+}$  are essentially determined by the electronic structures of the lowest excited states. They have been assigned as being largely of metal-to-ligand

charge transfer (MLCT) character being related to  $4d(\text{Ru})-\pi^*(\text{bpy})$  excitations. Transitions between the lowest  $^3\text{MLCT}$  states and the singlet ground state are forbidden without spin-orbit coupling (SOC). However, efficient SOC to higher lying states of  $^1\text{MLCT}$  character (that carry  $\vec{E} \perp \vec{C}_3$  allowedness) is active and thus, the transitions become allowed and an emission can result. It turns out that above  $T \approx 10$  K and up to ambient temperature, a triplet sub-state (of group theoretical E character in a trigonal point group with a totally symmetric ground state) emits while being polarized with the electric field vector  $\vec{E}$  perpendicularly to the molecular  $\vec{C}_3$ -axis.<sup>[33-36, 40]</sup> For the sake of completeness it should be mentioned that it has been shown by Yersin *et al.* that at ambient temperature a higher lying singlet state (of group theoretical  $^1\text{A}_2$  character) is thermally populated and leads to a weak thermally activated delayed fluorescence (TADF). According to the selection rules, the emission  $\vec{E}$  corresponding to this TADF sub-state is polarized parallel to the  $\vec{C}_3$ -axis. It therefore contributes only a small, negligible fraction to the  $\vec{E} \perp \vec{C}_3$  emission intensity.<sup>[40]</sup>

Ambient temperature structure determination reveals for  $[\text{Ru}(\text{bpy})_3](\text{PF}_6)_2$  single crystals a  $P\bar{3}c$  space group with all  $[\text{Ru}(\text{bpy})_3]^{2+}$  complexes having a  $D_3$  point symmetry with their  $\vec{C}_3$ -axes aligned in the direction of the  $\vec{c}$ -axis (**Figure 1** and **Figure S1**) which is also the main growth direction of the crystal needles.<sup>[41, 42]</sup> Consequently, the main emission intensity for this compound is polarized with the electric field vector  $\vec{E}$  perpendicularly to the  $\vec{c}$ -axis of the crystal.

Because of the cationic nature of  $[\text{Ru}(\text{bpy})_3]^{2+}$ , the complex can be immobilized on any negatively charged surface. It has already been shown that such compounds can be readily intercalated as pillars into clays.<sup>[37, 43]</sup> Clays are lamellar compounds consisting of permanently negatively charged silicate layers that are stacked parallel to each other and form one-

dimensional crystals, so-called tactoids (see **Figure S2**, supporting information). The stacking direction is perpendicular to the basal planes and is denoted as the  $\vec{c}^*$ -axis.

The negatively charged clay lamellae are neutralized by interlayer cations of any type. The inorganic  $\text{Na}^+$  present in the pristine synthetic Na-hectorite applied here, can readily and completely be exchanged by  $[\text{Ru}(\text{bpy})_3]^{2+}$ .

Detailed experimental proof about the orientation of  $[\text{Ru}(\text{bpy})_3]^{2+}$  complexes immobilized on clay basal surfaces is, however, missing. In sophisticated computer simulation studies of  $[\text{Ru}(\text{bpy})_3]^{2+}$  complexes intercalated into different kinds of clays, Breu *et al.*<sup>[38, 39]</sup> identified a energetically strongly preferred orientation of the complexes with their  $\vec{C}_3$ -axes parallel to the  $\vec{c}^*$ -axis as depicted in **Figure 1**. Furthermore, an additional two-dimensional ordering of the complexes within a given interlayer was detected, whereby various packing patterns, depending on the charge density of the host clay, were realized.

Applying a combination of melt synthesis and long-time annealing according to a recently published procedure,<sup>[32]</sup> a medium charged hectorite ( $\text{Na}_{0.5}\text{Li}_{0.5}\text{Mg}_{2.5}\text{Si}_4\text{O}_{10}\text{F}_2$ , Na-hec) with excellent charge homogeneity has recently become available that crystallizes in macroscopic, optically transparent tactoids. Few tactoids, like the one displayed in Fig. 3a, show even lateral extensions of 300  $\mu\text{m}$  and 20  $\mu\text{m}$  thickness enabling an orientation-dependent spectroscopic study. Furthermore, Na-hec, unlike natural clays, is free from accessory paramagnetic impurities. This clay type therefore represents a perfectly suited layered host system for any cationic molecular emitter.

Via a hydrothermal cation exchange,  $[\text{Ru}(\text{bpy})_3]^{2+}$  complexes were intercalated into the interlayer space. The intercalation can be monitored via X-ray diffraction (**Figure S3**, supporting information) by an increase in the interlayer spacing upon intercalation. The periodicity in  $\vec{c}^*$  direction is represented by the  $d_{001}$  value of 17.7 Å. It consists of the clay lamella itself with 9.6 Å<sup>[44, 45]</sup> and the space required by the intercalated complex (8.1 Å). For comparison,

single crystal data of  $[\text{Ru}(\text{bpy})_3](\text{PF}_6)_2$  indicate a height of 8.15 Å for  $[\text{Ru}(\text{bpy})_3]^{2+}$  along its  $\vec{C}_3$ -axis. In line with the simulations mentioned above, the observed  $d_{001}$  value strongly supports a similar orientation of the complexes within the clay and the  $[\text{Ru}(\text{bpy})_3](\text{PF}_6)_2$  crystal (see supporting information for details) with the  $\vec{C}_3$ -axis oriented along  $\vec{c}^*$  and  $\vec{c}$ .<sup>[46]</sup> Additionally, a new lambda-shaped peak ( $hk$ -band,  $d$ -value 7.8 Å) appeared upon intercalation. This can be assigned to an in-plane long range order of the complexes, i.e. an ordered packing pattern in the interlayer space of the clay.<sup>[37]</sup> Both features, the well-defined packing of the complexes within a given interlayer and the perfect periodicity along the stacking direction, indicating the same orientation of the emitter molecules in every interlayer, are prerequisites for the proposed nano-scale quasi-epitaxy.

The distinct orientation of the  $[\text{Ru}(\text{bpy})_3]^{2+}$  complexes within the host clay should result in a polarized emission similar to the one observed for pristine single crystals of  $[\text{Ru}(\text{bpy})_3](\text{PF}_6)_2$ . A  $[\text{Ru}(\text{bpy})_3]^{2+}$  intercalated tactoid of hectorite ( $[\text{Ru}(\text{bpy})_3]^{2+}$ -hec) was therefore investigated by spatially resolved orientation-dependent polarized emission spectroscopy. Applying a confocal microscope, the emission spectra of  $[\text{Ru}(\text{bpy})_3]^{2+}$ -hec platelets were recorded in high spatial resolution at two different directions of observation, namely with an observation along the stacking direction of the clay lamellae and along the edges (**Figure 2**). Additionally, the emission spectra of a  $[\text{Ru}(\text{bpy})_3](\text{PF}_6)_2$  single crystal was recorded as a reference (compare also Yersin *et al.*<sup>[40]</sup>). The degree of polarization  $P$  is defined here as commonly used by:<sup>[47]</sup>

$$P = \frac{I(\vec{E} \perp \vec{c}) - I(\vec{E} \parallel \vec{c})}{I(\vec{E} \perp \vec{c}) + I(\vec{E} \parallel \vec{c})} \quad (2)$$

where  $I(\vec{E} \perp \vec{c})$  and  $I(\vec{E} \parallel \vec{c})$  define the emission intensity with the electric field vector  $\vec{E}$  oriented perpendicularly and parallel to the  $\vec{c}$ -axis. Applying equation (2) to the measured results of  $[\text{Ru}(\text{bpy})_3](\text{PF}_6)_2$  single crystals,  $P$  was determined to be 0.77, indicating, in agree-

ment with previous work,<sup>[40]</sup> a very high degree of optical polarization, i.e. a strongly perpendicularly polarized emission (**Figure 2a**).

In the case of  $[\text{Ru}(\text{bpy})_3]^{2+}$ -hec, direction dependent emission measurements showed a distinctly different polarization behavior when comparing the spectra recorded from the basal surface of the platelet and along its edges (compare **Figure 2b** with **Figure 2c**). For an observation direction parallel to the  $\vec{c}^*$ -axis of the tactoids no polarized emission could be detected and the emission spectra for all orientations of the electric field vector  $\vec{E}$  were almost identical (**Figure 2c**). However, the light emitted from the edges of the platelets is highly polarized (**Figure 2b**) and reaches a degree of polarization  $P$  of approximately 0.35. This demonstrates a uniform orientation of the emitters. Much like the crystal field in  $[\text{Ru}(\text{bpy})_3](\text{PF}_6)_2$  single-crystals, the nano-confinement on the clay basal surfaces compels an arrangement of the emitters with their  $\vec{C}_3$ -axis oriented perpendicular to the silicate lamellae. This provides experimental evidence for the orientations of  $[\text{Ru}(\text{bpy})_3]^{2+}$  suggested by computer simulation studies.<sup>[38, 39]</sup>

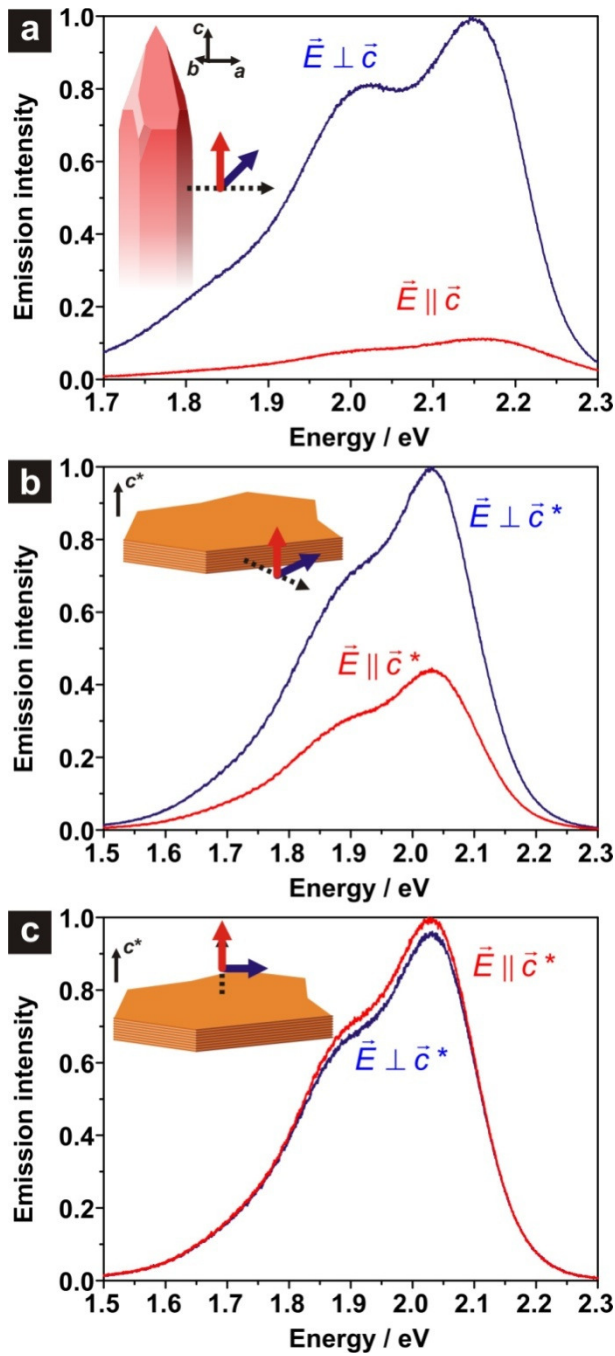


**Figure 2.** **a** Polarized emission spectra of single-crystal  $[\text{Ru}(\text{bpy})_3](\text{PF}_6)_2$ , **b** polarized emission with the direction of observation perpendicular to the edges of  $[\text{Ru}(\text{bpy})_3]^{2+}$ -hec, and **c** non-polarized emission with the direction of observation along the stacking direction  $\vec{c}^*$  of  $[\text{Ru}(\text{bpy})_3]^{2+}$ -hec. The dotted black arrow marks the direction of light detection (observation). The red and blue arrows represent the electric field vector  $\vec{E}$  parallel and perpendicular to the directions of observation. The excitation wavelength was 408 nm.

The observed difference in the degree of polarization between single crystal and intercalation compound may most likely be attributed to the fringed and fanned out nature of the edges of the tactoid that develops upon hydrothermal intercalation (**Figure 3 a and b**). Due to the dramatic volume increase of each interlayer space which is required to expand from 0.3 Å to 8.1 Å to accommodate the large emitter molecule, intracrystalline stresses cause the tactoid then to splinter. Spatially resolved maps of  $P$  (**Figure 3 c**) show a high sensitivity to the misalignment of domains within a tactoid. Well aligned areas show values of  $P \approx 0.45$ , while in areas dominated by defects and cracks,  $P$  is lowered to values of about 0.2. The resolution limit of the measurement is about 1  $\mu\text{m}$ . This means that more than 500 layers of  $[\text{Ru}(\text{bpy})_3]^{2+}$ -hec are measured simultaneously per scan, rendering measurement of defect-free domains without any disorientations impossible. Still, the measured polarized emission is remarkably high. Hence, it is expected that the polarization  $P$  of  $[\text{Ru}(\text{bpy})_3]^{2+}$  oriented on a single lamella would be close to the value of single crystals.



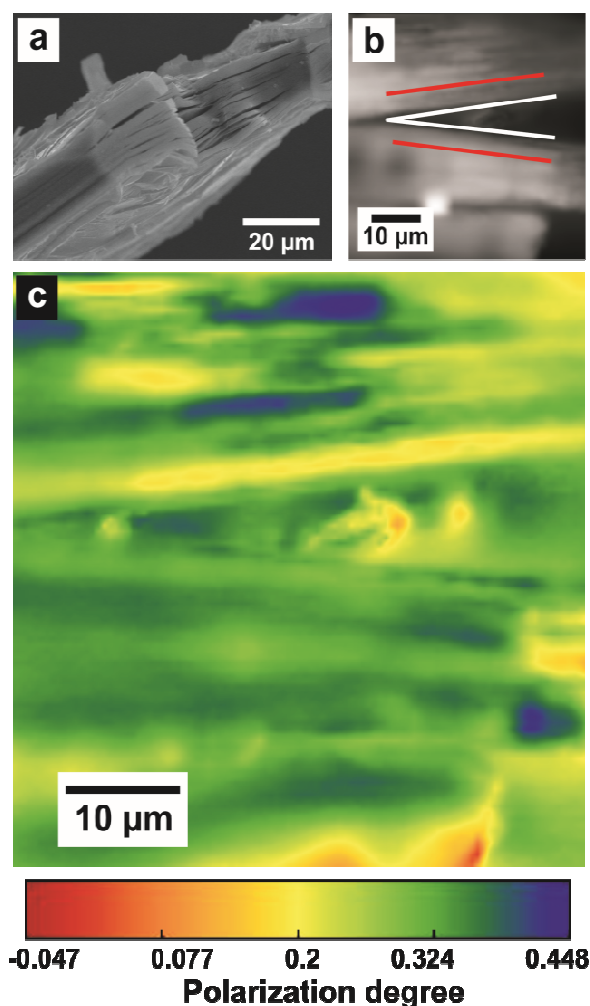


**Figure 3.** **a** SEM micrograph of an edge of a  $[\text{Ru}(\text{bpy})_3]^{2+}$ -hec platelet. Due to stress caused by the expansion during cation exchange the tactoids splinter and cracks (white lines in **b**) develop with misalignments of neighboring domains (red lines in **b**); **b** Optical microscopic image of a typical area of the platelet's edge that was used for emission studies. **c** False-color, spatially resolved map of an edge of a  $[\text{Ru}(\text{bpy})_3]^{2+}$ -hec platelet showing spatially varying degrees of polarization. The  $P$ -values turn out to be much lower on defect sites and cracks due to disturbed orientations of the clay lamellae and therefore of the axes of the  $[\text{Ru}(\text{bpy})_3]^{2+}$  complexes with observed  $P$  values of 0.1 – 0.2.

It is important to note that macroscopic tactoids as applied here for analytical reasons to prove polarized emission are of course not suitable for incorporation into OLED devices. However, as has been demonstrated, the applied synthetic hectorites can easily be completely delaminated into singular clay lamellae with a thickness of 1 nm.<sup>[32]</sup> For OLED applications,

emitter complexes oriented on single lamellae would be applied to yield a homogeneous and well-textured area of equidistant emitters. A simple doctor-blade process from suspension with subsequent drying is sufficient to retrieve highly textured composite films of the functional nanoplatelets.<sup>[48]</sup>

Moreover, packing of sensitive emitters by the perfectly transparent inorganic nanoplatelets might offer the additional benefit of stabilizing and protecting the emitters against oxidation and hydrolysis and thus, increasing the device lifetime of an OLED. Composites manufactured applying the same clay nanoplatelets, though not loaded with emitter guest molecules, have been shown to provide very high gas barrier activity.<sup>[49, 50]</sup>

Preliminary tests to illustrate the feasibility of such processing showed that delaminated nanoplatelets with immobilized  $[\text{Ru}(\text{bpy})_3]^{2+}$  complexes attached to their surface yield a stable dispersion in butanone. After blending with a poly(methyl methacrylate) (PMMA) solution in butanone the mixture was coated onto a microscope glass slide and visually homogeneous films were obtained after drying (**Figure 4**). A cryo-ion-etched SEM cross section of such a nanocomposite film (prepared by Leica Microsystems Inc.) showing perfect texture is depicted in **Figure 4a**. Each of the parallel textured nanoplatelets carries uniformly oriented  $[\text{Ru}(\text{bpy})_3]^{2+}$  complexes (**Figure 4b**) that exhibit a transition dipole shown as small arrows. Uniform orientation of the complexes on the clay platelets, which in turn then are perfectly textured due to the huge aspect ratios of the nanoplatelets, delivers a quasi-epitaxy of the emitters. A kind of macroscopic transition dipole (large arrow) results yielding polarized emission from the edges of the film. It happens that the nano-confinement for the particular shape of this emitter delivers a favorable orientation of the transition dipole that would be expected to enhance the out-coupling factor  $\eta_{out}$ . Under UV light (**Figure 4c**), the emission is optically homogeneous throughout the whole film. Furthermore, the coating *per se* reveals very good optical properties and is also flexible and highly transparent to daylight (**Figure 4d**). For making an OLED device, a suspension of single lamella nanoplatelets packed with

emitting guest complexes would have to be blended with materials that possess good hole and electron transport or bipolar transport properties (compare ref.<sup>[51]</sup>).

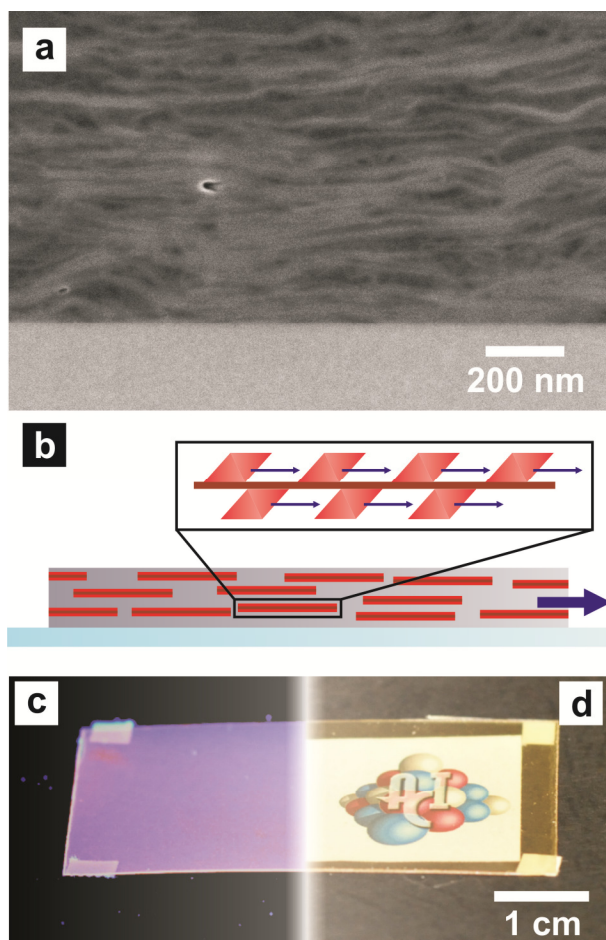


**Figure 4.** **a** Cryo-ion-etched cross section of a nanocomposite film with textured  $[\text{Ru}(\text{bpy})_3]^{2+}$ -hec nanoplatelets embedded in a PMMA matrix; **b** sketch of individually oriented  $[\text{Ru}(\text{bpy})_3]^{2+}$  complexes on the textured nanoplatelets; the blue arrows show the transition dipole moments of the singular complexes that result in a macroscopic moment yielding polarized emission. **c** Nanocomposite film with textured  $[\text{Ru}(\text{bpy})_3]^{2+}$ -hec nanoplatelets embedded in a PMMA matrix under UV light and **d** at daylight. To visualize the transparency, a print-out of a logo was placed under the film at daylight. To show substrate variability, the film in **c** and **d** was coated onto a PET foil.

## Conclusion

The work presented herein represents a proof-of-principle that the orientation of a transition metal luminophor intercalated within the interlayer spaces of well-organized clay nanoplatelets can be controlled, enabling command over the polarization of emitted light. Furthermore, we demonstrate that the composite nanoplatelets can be assembled using a doctor-blade method to form an oriented luminescent film, showing that this quasi-epitaxial strategy could be explored as a means to improve the performance of different kinds of electroluminescent displays and stereoscopic imaging systems.<sup>[52, 53]</sup>

## Supporting Information

Supporting Information is available from the Wiley Online Library or from the author.

## Acknowledgements

This work was supported by the German Science Foundation (SFB 840). D.A.K. thanks the elite study program “Macromolecular Science” as well as the International Graduate School “Structure, Reactivity and Properties of Oxide Materials” within the Elite Network of Bavaria (ENB) for ongoing support. G.A.O. is Government of Canada Research Chair in Materials Chemistry and Nanochemistry. He is deeply grateful to the Natural Sciences and Engineering Council of Canada for strong and sustained support of his research. The authors also gratefully acknowledge Dr. W. Grünewald, Leica Microsystems Inc, for the preparation of the cryo-ion-etched SEM samples and Dr. Beate Förster, BIMF, for the analysis of these samples.

Received: ((will be filled in by the editorial staff))

Revised: ((will be filled in by the editorial staff))

Published online: ((will be filled in by the editorial staff))

[1] *Highly Efficient OLEDs with Phosphorescent Materials* (Ed.: H. Yersin), Wiley-VCH, Weinheim, Germany **2008**.

[2] *Physics of Organic Semiconductors* (Eds.: W. Brütting, C. Adachi), Wiley-VCH, Weinheim, Germany **2012**.

- 
- [3] C. Adachi, M. A. Baldo, M. E. Thompson, S. R. Forrest, *J. Appl. Phys.* **2001**, *90*, 5048.
- [4] T. Tsutsui, E. Aminaka, C. P. Lin, D. U. Kim, *Philos. T. R. Soc. A* **1997**, *355*, 801.
- [5] R. H. Friend, R. W. Gymer, A. B. Holmes, J. H. Burroughes, R. N. Marks, C. Taliani, D. D. C. Bradley, D. A. Dos Santos, J. L. Bredas, M. Logdlund, W. R. Salaneck, *Nature* **1999**, *397*, 121.
- [6] M. Pfeiffer, K. Leo, X. Zhou, J. S. Huang, M. Hofmann, A. Werner, J. Blochwitz-Nimoth, *Org. Electron.* **2003**, *4*, 89.
- [7] H. Yersin, A. F. Rausch, R. Czerwieniec, T. Hofbeck, T. Fischer, *Coord. Chem. Rev.* **2011**, *255*, 2622.
- [8] T. Hofbeck, H. Yersin, *Inorg. Chem.* **2010**, *49*, 9290.
- [9] H. Yersin, *Top. Curr. Chem.* **2004**, *241*, 1.
- [10] R. Czerwieniec, J. B. Yu, H. Yersin, *Inorg. Chem.* **2011**, *50*, 8293.
- [11] Y. S. Tyan, *J. Photon. Energy.* **2011**, *1*, 1.
- [12] W. Brütting, J. Frischeisen, T. D. Schmidt, B. J. Scholz, C. Mayr, *Phys. Status Solidi A* **2013**, *210*, 44.
- [13] J. Frischeisen, D. Yokoyama, A. Endo, C. Adachi, W. Brütting, *Org. Electron.* **2011**, *12*, 809.
- [14] W. Brütting, J. Frischeisen in: *Physics of Organic Semiconductors* (Eds.: W. Brütting, C. Adachi), Wiley-VCH, Weinheim, Germany **2012**, pp. 497-539.
- [15] M. T. Tsai, D. T. Wu in: *Physics of Organic Semiconductors* (Eds.: W. Brütting, C. Adachi), Wiley-VCH, Weinheim, Germany **2012**, pp. 541-574.
- [16] D. Yokoyama, *J. Mater. Chem.* **2011**, *21*, 19187.
- [17] M. Grell, D. D. C. Bradley, *Adv. Mater.* **1999**, *11*, 895.
- [18] V. Cimrova, M. Remmers, D. Neher, G. Wegner, *Adv. Mater.* **1996**, *8*, 146.
- [19] P. Dyreklev, M. Berggren, O. Inganäs, M. R. Andersson, O. Wennerström, T. Hjertberg,

---

*Adv. Mater.* **1995**, 7, 43.

- [20] M. Hamaguchi, K. Yoshino, *Appl. Phys. Lett.* **1995**, 67, 3381.
- [21] K. S. Whitehead, M. Grell, D. D. C. Bradley, M. Jandke, P. Strohriegel, *Appl. Phys. Lett.* **2000**, 76, 2946.
- [22] D. Neher, *Macromol. Rapid Commun.* **2001**, 22, 1366.
- [23] D. Yan, J. Lu, M. Wei, J. Ma, D. G. Evans, X. Duan, *Chem. Commun.* **2009**, 6358.
- [24] D. Yan, J. Lu, M. Wei, D. G. Evans, X. Duan, *J. Phys. Chem. B* **2009**, 113, 1381.
- [25] V. Martínez Martínez, F. López Arbeloa, J. Banuelos Prieto, I. López Arbeloa, *Chem. Mater.* **2005**, 17, 4134.
- [26] R. Sasai, N. Iyi, T. Fujita, F. Arbeloa López, V. Martínez Martínez, K. Takagi, H. Itoh, *Langmuir* **2004**, 20, 4715.
- [27] W. Seidl, J. Breu, *Z. Kristallogr.* **2005**, 220, 169.
- [28] M. Stöcker, W. Seidl, L. Seyfarth, J. Senker, J. Breu, *Chem. Commun.* **2008**, 629.
- [29] A. Baumgartner, K. Sattler, J. Thun, J. Breu, *Angew. Chem.* **2008**, 120, 1664, *Angew. Chem. Int. Ed.* **2008**, 47, 1640.
- [30] M. M. Lezhnina, T. Grewe, H. Stoehr, U. Kynast, *Angew. Chem.* **2012**, 124, 10805, *Angew. Chem. Int. Ed.* **2012**, 51, 10671.
- [31] M. McColl, C. A. Mead, *Trans. Metal. Soc. AIME* **1965**, 233, 502.
- [32] M. Stöter, D. A. Kunz, M. Schmidt, D. Hirsemann, H. Kalo, B. Putz, J. Senker, J. Breu, *Langmuir* **2013**, 1280.
- [33] A. Ceulemans, L. G. Vanquickenborne, *J. Am. Chem. Soc.* **1981**, 103, 2238.
- [34] E. M. Kober, T. J. Meyer, *Inorg. Chem.* **1982**, 21, 3967.
- [35] H. Yersin, W. Humps, J. Strasser, *Top. Curr. Chem.* **1997**, 191, 153.
- [36] H. Yersin, W. Humps, J. Strasser, *Coord. Chem. Rev.* **1997**, 159, 325.

- 
- [37] J. Breu, A. Stoll, K. G. Lange, T. Probst, *Phys. Chem. Chem. Phys.* **2001**, 3, 1232.
- [38] J. Breu, C. R. A. Catlow, *Inorg. Chem.* **1995**, 34, 4504.
- [39] J. Breu, N. Raj, C. R. A. Catlow, *J. Chem. Soc. Dalton* **1999**, 835.
- [40] H. Yersin, E. Gallhuber, A. Vogler, H. Kunkely, *J. Am. Chem. Soc.* **1983**, 105, 4155.
- [41] D. P. Rillema, D. S. Jones, H. A. Levy, *J. Chem. Soc. Chem. Comm.* **1979**, 849.
- [42] J. Breu, C. Kratzer, H. Yersin, *J. Am. Chem. Soc.* **2000**, 122, 2548.
- [43] P. K. Ghosh, A. J. Bard, *J. Phys. Chem.* **1984**, 88, 5519.
- [44] H. Kalo, W. Milius, J. Breu, *RSC Adv.* **2012**, 2, 8452.
- [45] J. L. Suter, P. V. Coveney, H. C. Greenwell, M. A. Thyveetil, *J. Phys. Chem. C* **2007**, 111, 8248.
- [46] J. Breu, H. Domel, A. Stoll, *Eur. J. Inorg. Chem.* **2000**, 2401.
- [47] L. Schade, U. T. Schwarz, T. Wernicke, J. Rass, S. Ploch, M. Weyers, M. Kneissl, *Appl. Phys. Lett.* **2011**, 99.
- [48] M. W. Möller, D. A. Kunz, T. Lunkenbein, S. Sommer, A. Nennemann, J. Breu, *Adv. Mater.* **2012**, 24, 2142.
- [49] M. W. Möller, T. Lunkenbein, H. Kalo, M. Schieder, D. A. Kunz, J. Breu, *Adv. Mater.* **2010**, 22, 5245.
- [50] D. A. Kunz, J. Schmid, P. Feicht, J. Erath, A. Fery, J. Breu, *ACS Nano* **2013**, 7, 4275.
- [51] M. Flämmich, J. Frischeisen, D. S. Setz, D. Michaelis, B. C. Krummacher, T. D. Schmidt, W. Brütting, N. Danz, *Org. Electron.* **2011**, 12, 1663.
- [52] S. Aruga, H. Horiguchi, *US Patent* **1999**, 6 005 644.
- [53] M. B. Wolk, Y. Hsu, R. J. Pechman, H. Sahouani, J. S. Staral, *US. Pat. Appl. Publ.* **2002**, 0 158 574 A1.

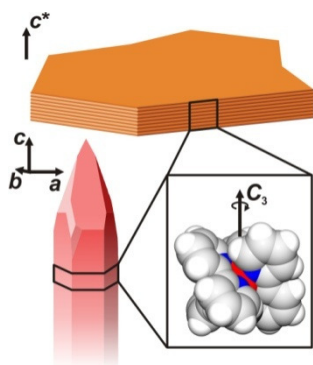
**A nano confinement strategy is presented to control the spatial orientation and emission polarization of phosphorescent metal complexes.** Described herein, we have demonstrated that through nano-confinement of the phosphorescent metal complex  $[\text{Ru}(\text{bpy})_3]^{2+}$  by attaching it to anionic clay nanoplatelets, it is possible to simultaneously lock the spatial orientation of the complex and fix its emission polarization. This quasi-epitaxial approach may provide a strategy for an enhancement of light out-coupling of OLEDs.

**Keyword: Polarized Emission**

Daniel A. Kunz, Markus J. Leidl, Lukas Schade, Jasmin Schmid, Beate Bojer, Ulrich T. Schwarz, Geoffrey A. Ozin\*, Hartmut Yersin\*, and Josef Breu\*

### Quasi-Epitaxy of $[\text{Ru}(\text{bpy})_3]^{2+}$ by Confinement in Clay Nanoplatelets Yields Polarized Emission

ToC figure





## 6.6.2 Supporting Information

## Supporting Information

**Quasi-Epitaxy of  $[\text{Ru}(\text{bpy})_3]^{2+}$  by Confinement in Clay Nanoplatelets Yields Polarized Emission**

*Daniel A. Kunz, Markus J. Leidl, Lukas Schade, Jasmin Schmid, Beate Bojer, Ulrich T. Schwarz, Geoffrey A. Ozin\*, Hartmut Yersin\*, and Josef Breu\**

**Experimental Details**

*Synthesis of single crystals of  $\text{Ru}(\text{bpy})_3(\text{PF}_6)_2$ .* Racemic  $\text{Ru}(\text{bpy})_3(\text{PF}_6)_2$  salt was obtained by metathesis of the corresponding chloride salt and prepared by mixing with  $\text{NH}_4\text{PF}_6$  in aqueous solution according to a literature procedure.<sup>[1]</sup> The raw product was crystallized from an ethanol/water (2:1) solution<sup>[2]</sup> and single-crystal needles with a length of about 1 mm were recovered. All chemicals were purchased from Sigma Aldrich and used without further purification.

*Synthesis of  $\text{Na}_{0.5}$ -fluorohectorite.*  $\text{Na}_{0.5}$ -fluorohectorite with nominal composition of  $[\text{Na}_{0.5}]^{\text{inter}}[\text{Mg}_{2.5}\text{Li}_{0.5}]^{\text{oct}}[\text{Si}_4]^{\text{tet}}\text{O}_{10}\text{F}_2$  (Na-hec) was synthesized via melt synthesis according to an already published procedure.<sup>[3]</sup> Typically, high purity reagents of  $\text{SiO}_2$  (Merck),  $\text{LiF}$  (Chempur),  $\text{MgF}_2$  (Chempur),  $\text{MgO}$  (Alfa Aesar),  $\text{NaF}$  (Alfa Aesar) were weighed in a glovebox under Argon according to the required composition, filled in a cleaned Mo-crucible (Plansee, Austria) and carefully sealed. The crucible is heated in a radio frequency induction furnace at 1900 °C for 20 min, quenched and heated again in a graphite rotary kiln to 1750 °C for 60 min to minimize inhomogeneities. Finally it was allowed to cool down slowly while continuing rotation. The raw product was grinded using a planetary ball mill (Retsch PM 100)

to a particle size of  $< 250 \text{ }\mu\text{m}$ . Absorbed humidity was removed and the powder was transferred to a Mo-crucible, sealed and annealed in a chamber furnace (Thermal Technology) at  $1045 \text{ }^{\circ}\text{C}$  for six weeks.

*Preparation of  $\text{Ru}(\text{bpy})_3^{2+}$  intercalation compounds.* Prior to intercalation the cation exchange capacity (CEC) of Na-hec was determined to be  $127 \text{ meq } 100\text{g}^{-1}$ .<sup>[4]</sup> For intercalation 100 mg of as-synthesized Na-hec powder were mixed with a solution of  $[\text{Ru}(\text{bpy})_3]\text{Cl}_2$  (2x CEC) and NaCl (0.5x CEC) in 5 mL Millipore water and reacted at  $220 \text{ }^{\circ}\text{C}$  for 4-5 days under autogenous water pressure (Parr acid digestion bombs, Type 4764). The NaCl was needed to increase the electrolytic background preventing spontaneous exfoliation due to osmotic swelling of the Na-hec when adding the aqueous solution.<sup>[3]</sup> To replace the  $\text{Na}^+$  interlayer cations completely by  $(\Delta, \Lambda)\text{-}[\text{Ru}(\text{bpy})_3]^{2+}$  ions the procedure had to be repeated five times. After the second repetition, no NaCl was added to the solution. In the last two steps stoichiometric amounts of 2.2.2-cryptand (Merck) were added to remove the residual  $\text{Na}^+$  cations from the equilibrium. Finally, the material was washed five times with Millipore water and two times with acetone.

*Preparation of nanocomposite films.* The as-synthesized Na-hec was immersed into deionized water yielding a 0.1 wt.% suspension. Osmotic swelling caused a spontaneous disintegration of the crystallites into their single lamellae of 1 nm thickness.<sup>[3]</sup> The clay was exchanged twice with  $[\text{Ru}(\text{bpy})_3]\text{Cl}_2$  solution (1.5x CEC each time) at ambient temperature for ca. 10 h using screw-capped vessels and an overhead shaker. The resulting  $[\text{Ru}(\text{bpy})_3]^{2+}$ -hec was washed with Millipore water via centrifugation until supernatant was colorless. After washing with acetone p.a. and three times with butanone p.a. a stable dispersion was yielded in butanone. A mixture of  $[\text{Ru}(\text{bpy})_3]^{2+}$ -hec and PMMA (1:4 by weight with respect to the pure, non-modified Na-hec) in butanone was coated on a PET foil and on a microscope glass cover slip (VWR, thickness:  $150 \text{ }\mu\text{m}$ ) and subsequently dried at  $80 \text{ }^{\circ}\text{C}$ . The sample on the glass substrate was used for preparation of the SEM cross section.

*Analytics.* Powder X-ray patterns of Na-hec and  $[\text{Ru}(\text{bpy})_3]^{2+}$ -hec samples were recorded in transmission geometry with a STOE Stadi P powder diffractometer equipped with a MYTHEN1K detector using  $\text{Cu-K}_{\alpha 1}$  radiation ( $\lambda = 1.54056 \text{ \AA}$ ). The samples were grinded before measurement and placed in glass capillaries. SEM cross sections were obtained using a Leica EM TIC 3X / VCT ion beam cutter system provided by Leica Microsystems Inc. The samples were analyzed with a Zeiss Ultra plus FE-SEM. For visualization purposes, the contrast of the images was enhanced using Adobe Photoshop.

*Spectroscopic analysis.* A confocal micro-photoluminescence setup was used for polarized emission studies. The samples were optically excited by a semiconductor laser at 408 nm. The emitted light was collimated and polarized using a Glan-Thompson polarizer mounted on a motorized stage. A thick optical fiber in the image plane led the detected light to a monochromator of 550 cm focal length and an attached CCD.

## Analytical Details

### Size of a $[\text{Ru}(\text{bpy})_3]^{2+}$ complex along its $\vec{C}_3$ - axis

Since  $[\text{Ru}(\text{bpy})_3]^{2+}$  complexes are slightly ellipsoidal in shape with the shorter axis along its  $\vec{C}_3$  - axis (Fig. S1), a first indication of the orientation in the interlayer space with respect to the clay lamellae may be deduced by comparing the basal spacing observed by X-ray diffraction with the unit cell parameters of the  $\text{Ru}(\text{bpy})_3(\text{PF}_6)_2$  single crystal.

In the case of the single-crystal needle, the crystal system exhibits trigonal symmetry, i.e. hexagonally packed  $[\text{Ru}(\text{bpy})_3]^{2+}$  complexes are stacked with their  $\vec{C}_3$  - axis along the  $\vec{c}$  - axis of the crystal system in perpendicular direction to the  $ab$ -plane.  $[\text{Ru}(\text{bpy})_3]^{2+}$  is a chiral complex; layers of  $\Delta$ - and  $\Lambda$ - $[\text{Ru}(\text{bpy})_3]^{2+}$  are stacked along  $\vec{c}$ . Hence the  $d_{002}$ -value (8.15  $\text{\AA}$ ) corresponds to the van-der-Waals size of one complex along its  $\vec{C}_3$  - axis.<sup>[2]</sup>

The periodic stacking of the layers along  $\vec{c}^*$  into the one-dimensional crystal is represented by the  $00l$  series (**Figure S 2**). The periodicity contains one silicate lamella and one layer of intercalated  $[\text{Ru}(\text{bpy})_3]^{2+}$  complexes and is given by the  $d_{001}$ -value (17.7 Å). The van-der-Waals height of one silicate lamella is 9.6 Å<sup>[5, 6]</sup> which results in a complex height of 8.1 Å.

The nearly perfect agreement of the size demanded of the  $[\text{Ru}(\text{bpy})_3]^{2+}$  complexes in the two different systems strongly suggests the same orientation in single-crystals of  $[\text{Ru}(\text{bpy})_3](\text{PF}_6)_2$  and in  $[\text{Ru}(\text{bpy})_3]^{2+}$ -hec relative to the stacking direction.

### Supplementary Graphs and Figures

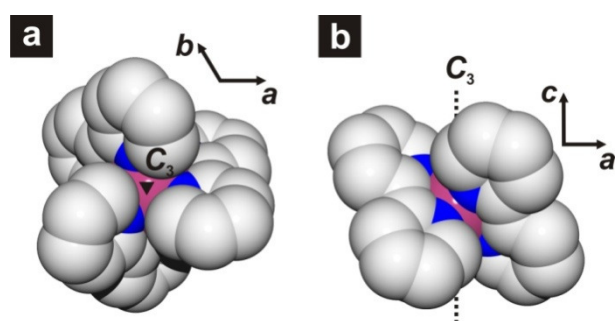


**Figure S1.** The  $[\text{Ru}(\text{bpy})_3]^{2+}$  species in a  $[\text{Ru}(\text{bpy})_3](\text{PF}_6)_2$  single crystal. **a** view along the  $\vec{c}$ -axis, **b** view along the  $b$  axis. The  $\vec{C}_3$ -axis lying parallel to the  $\vec{c}$ -axis is also shown.

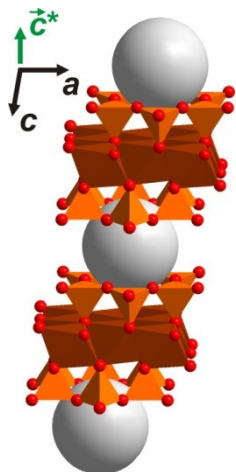


**Figure S2.** A structural representation of the hectorite clay that was utilized in this study.

Negatively charged 2:1 lamellae are stacked upon each other ( $\vec{c}^*$ -axis). The negative charge is balanced by intercalated  $\text{Na}^+$  ions that can be exchanged against other cations in aqueous media.

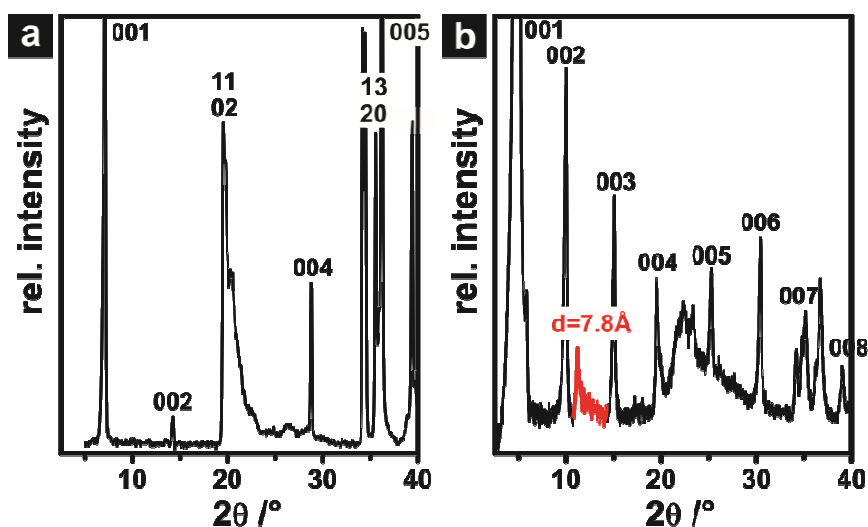


**Figure S3.** Powder X-ray patterns of **a** neat Na-hec host material and **b**  $[\text{Ru}(\text{bpy})_3]^{2+}$ -hec.

After intercalation of the  $[\text{Ru}(\text{bpy})_3]^{2+}$ -complexes that are larger than the  $\text{Na}^+$  ions the  $00l$  series shifts to higher  $d$ -values. The additional  $hk$ -band that appears upon intercalation indicates a 2D ordering within the interlayer space and is marked in red.

### Supplementary References

- [1] M. M. T. Khan, R. C. Bhardwaj, C. Bhardwaj, *Polyhedron* **1990**, 9, 1243.
- [2] J. Breu, H. Domel, A. Stoll, *Eur. J. Inorg. Chem.* **2000**, 2401.
- [3] M. Stöter, D. A. Kunz, M. Schmidt, D. Hirsemann, H. Kalo, B. Putz, J. Senker, J. Breu, *Langmuir* **2013**, 1280.
- [4] M. W. Möller, D. Hirsemann, F. Haarmann, J. Senker, J. Breu, *Chem. Mater.* **2010**, 22, 186.
- [5] H. Kalo, W. Milius, J. Breu, *RSC Adv.* **2012**, 2, 8452.
- [6] J. L. Suter, P. V. Coveney, H. C. Greenwell, M. A. Thyveetil, *J. Phys. Chem. C* **2007**, 111, 8248.

## 7 Publikationsliste

### 7.1 Publikationen

**D.A. Kunz**, A. Fery, J. Breu, *Z. Anorg. Allg. Chem.* **2008**, 634, 2056.

**D. A. Kunz**, E. Max, R. Weinkamer, T. Lunkenbein, J. Breu, A. Fery, *Small* **2009**, 5 1816-1820.

M. W. Möller, U. A. Handge, **D. A. Kunz**, T. Lunkenbein, V. Altstädt, J. Breu, *ACS Nano* **2010**, 4 717-724.

M. W. Möller, T. Lunkenbein, H. Kalo, M. Schieder, **D. A. Kunz**, J. Breu, *Adv. Mater.* **2010**, 22 5245-5249.

F. Polzer, **D. A. Kunz**, J. Breu, M. Ballauff, *Chem. Mater.* **2010**, 22 2916-2922.

G. V. Manohara, **D. A. Kunz**, P. V. Kamath, W. Milius, J. Breu, *Langmuir* **2010**, 26 15586-15591.

M. W. Möller, **D. A. Kunz**, T. Lunkenbein, S. Sommer, A. Nennemann, J. Breu, *Adv. Mater.* **2012**, 24 2142-2147.

H. Kalo, M. W. Möller, **D. A. Kunz**, J. Breu, *Nanoscale* **2012**, 4 5633-5639.

**D.A. Kunz**, A. Fery, J. Breu, *Z. Anorg. Allg. Chem.* **2012**, 638, 1564.

M. Stöter, **D. A. Kunz**, M. Schmidt, D. Hirsemann, H. Kalo, J. Senker, J. Breu, *Langmuir* **2013**, 29 1280-1285.

**D. A. Kunz**, J. Erath, D. Kluge, H. Thurn, B. Putz, A. Fery, J. Breu, *ACS Appl. Mat. Interf.* **2013**, 5 5851-5855.

**D. A. Kunz**, P. Feicht, S. Gödrich, H. Thurn, G. Papastavrou, A. Fery, J. Breu *Adv. Mater.* **2013**, 25 1337-1341.

**D. A. Kunz**, J. Schmid, P. Feicht, J. Erath, A. Fery, J. Breu, *ACS Nano* **2013** 7 4275-4280.

**D. A. Kunz**, M. Leitl, L. Schade, J. Schmid, U.T. Schwarz, H. Yersin, G.A. Ozin, J. Breu, *submitted*.

S. You, **D. A. Kunz**, M. Stöter, A. Talyzin, J. Breu, *Angew. Chem. Int. Ed.* **2013**, 52 3891-3895.

V. Kutsnetsov, **D. A. Kunz**, N. Helfricht, H. Kalo, J. Breu, G. Papastavrou, *to be submitted*.

P. Feicht, **D. A. Kunz**, A. Lerf, J. Breu, *to be submitted*.

## 7.2 Konferenzbeiträge

2008 GDCh Jahrestagung Festkörperchemie (Bayreuth, Poster)

2009 AFM Forum (Garching, Poster, Posterpreis (1. Platz))

2009 International Clay Conference, ICC XIV (Castellaneta Marina, Italien, Poster)

2010 Layered Materials (Bochum, Vortrag)

2010 EuChemS (Nürnberg, Poster)

2011 Fachgruppensitzung DGM Bioinspired Materials, (Thurnau, Vortrag)

2012 GDCh Jahrestagung Festkörperchemie (Darmstadt, Vortrag)

## 7.3 Pressemitteilungen

2012 **D.A. Kunz**, M.W.Möller, J.Breu, C. Wissler,

„Nanokomposite schützen High-Tech-Elektronik“, erschienen in:

**Spektrum der Wissenschaft**, 09.07.2012,

<http://www.spektrum.de/alias/materialforschung/nanokomposite-machen-displays-bruchssicher/1156739>

**Besser lackieren!**, Newsletter, Juli 2012,

<http://www.besserlackieren.de/newsletter/detail.cfm?id=5601>

**Der Wiesentbote**, 04.07.2012,

<http://www.wiesentbote.de/2012/07/04/nanokomposite-schuetzen-high-tech-elektronik/>

**UBT Medienmitteilung**, Nr.227/2012, 02.07.2012,

[http://www.bzkg.uni-bayreuth.de/pdf-ressources/Prof\\_\\_BreuNanokomposite.pdf](http://www.bzkg.uni-bayreuth.de/pdf-ressources/Prof__BreuNanokomposite.pdf)



## 8 Danksagung

Am Ende der Dissertation möchte ich mich bei all denjenigen bedanken, die durch ihre Unterstützung zum Erfolg meiner Arbeit beigetragen haben.

Mein aufrichtiger Dank gilt als erstes meinem akademischen Ziehvater, Prof. Dr. Josef Breu. Ich hatte die letzten Jahre eine überaus produktive Zeit in einer sehr angenehmen Atmosphäre. Besonders bedanken möchte ich mich für das mir entgegengebrachte Vertrauen und die damit verbundene Möglichkeit der freien Entfaltung. So war es mir möglich, weitgehend selbstständig in die facettenreiche Welt der Schichtverbindungen einzutauchen, konnte mich jedoch gleichzeitig auf einen stets kompetenten Ratschlag in jeglicher Situation verlassen. Die zahlreichen wissenschaftlichen Diskussionen haben meinen wissenschaftlichen Horizont entscheidend erweitert. Weiterhin bedanke ich mich für die vielen Möglichkeiten, die mir während meiner Promotion offeriert wurden. Ich konnte meine Forschungsergebnisse auf zahlreichen internationalen Tagungen präsentieren und meinen wissenschaftlichen Werdegang mit einem Auslandsaufenthalt bereichern.

Auch meinem zweiten akademischen Lehrer, Prof. Dr. Andreas Fery möchte ich an dieser Stelle herzlich danken, der mich ebenfalls durchwegs, insbesondere im Bereich der Rasterkraftmikroskopie, tatkräftig unterstützte. Ich bedanke mich für die barrierefreie Integration in den Lehrstuhl und für die tolle, fruchtbare Kooperation. Es war mir eine Ehre, unter der Betreuung eines sehr kompetenten Zweiergespanns in einem so reibungslos funktionierenden und einzigartigen Netzwerk mitgearbeitet haben zu dürfen.

Allen kooperierenden Lehrstühlen und Forschungsgruppen danke ich für deren tatkräftige Unterstützung bei der Durchführung meiner Forschungsvorhaben. Dazu gehören Prof. Dr. Georg Papastavrou, Prof. Dr. Ulrich Schwarz, Prof. Dr. Jürgen Senker, Prof. Dr. Hartmut Yersin und ihre Mitarbeiter, sowie Prof. Dr. Nicholas Kotov und Prof. Dr. Geoffrey Ozin, denen ich zusätzlich für ihre Gastfreundlichkeit und Hilfsbereitschaft während meines Auslandsaufenthalts danken möchte.

Weiterhin möchte ich mich bei allen Freunden und Kollegen der Lehrstühle Anorganische

Chemie I und III für die sehr schöne Zeit bedanken. Es war mir eine Freude, sowohl bei fachlichen Gesprächen als auch beim gemütlichen Tratsch in der Kaffeeküche oder bei den legendären Grillabenden. Ich danke Prof. Dr. Jürgen Senker, Dr. Wolfgang Milius, den Technikern Beate, Bernd, Dieter, Lena und Sonja, den Sekretärinnen Iris, Petra und Sybille für die Unterstützung während meiner Zeit hier am Lehrstuhl. Besonders hervorgehoben sei hier an dieser Stelle Bernd Putz, der die Synthese des in dieser Arbeit wesentlichen Schichtsilicats entscheidend vorangetrieben hat. Dem Lehrstuhl Physikalische Chemie II sei an dieser Stelle auch für die Hilfsbereitschaft und Integration in das Lehrstuhlgeschehen gedankt.

Meinen Freunden aus Bayreuth, lehrstuhlintern oder –extern, aus der Chemie, Physik oder anderen Disziplinen, ob (noch) hier in Bayreuth oder schon verstreut in allen Ecken der Welt, danke ich von Herzen für eine tolle Zeit, viele gemeinsame Unternehmungen und spaßige Abende – diese Jahre bleiben definitiv unvergesslich für mich!

Bedanken möchte ich mich außerdem beim Elitenetzwerk Bayern (ENB). Ich hatte während meiner Doktorarbeit die Ehre, über ein Forschungsstipendium, über das internationale Graduiertenkolleg „Struktur, Reaktivität und Eigenschaften oxidischer Materialien“ und über das Elitestudienprogramm „Macromolecular Science“ aktiv an dem reichhaltigen Zusatzangebot innerhalb des ENBs teilnehmen zu können. Dies hat mich sowohl in den Soft-Skills bereichert als auch entscheidend zur Erweiterung meines fachlichen Horizonts beigetragen.

Dank gebührt auch der Chemiker Spaßgesellschaft e.V. (CSG e.V.) für die zahlreichen Engagements innerhalb und außerhalb der Universität. Als Gründungsmitglied freue ich mich über das stetige Wachstum und wünsche dem Verein für die Zukunft weiterhin gutes Gelingen.

Mein größter Dank gilt zu guter Letzt einem Netzwerk, das während all der Jahre für viele unsichtbar blieb, jedoch den größten Anteil am Erfolg meiner Arbeit besitzt: Meine Familie. Es ist unbezahlbar, wenn man in jeglicher Situation auf 100 Prozent Rückhalt zählen kann und ununterbrochen ein derart hohes Maß an Liebe und Unterstützung erfährt. Meiner Familie sei daher auch diese Arbeit gewidmet.

## **9 Erklärung des Verfassers**

Hiermit erkläre ich, dass ich die vorliegende Arbeit selbstständig verfasst und keine anderen als die angegebenen Quellen und Hilfsmittel benutzt habe.

Ferner erkläre ich, dass ich anderweitig mit oder ohne Erfolg nicht versucht habe, eine Dissertation einzureichen. Ich habe keine gleichartige Doktorprüfung an einer anderen Hochschule endgültig nicht bestanden.

Cambridge, 11. April 2014

---

Daniel A. Kunz